Observations and Modelling of Joule heating in the Sub-Auroral Ionosphere

Elliott Keith Day, MPhys

Department of Physics and Astronomy

Lancaster University

A thesis submitted for the degree of

Doctor of Philosophy

October, 2024

Observations and Modelling of Joule heating in the Sub-Auroral Ionosphere

Elliott Keith Day, MPhys.

Department of Physics, Lancaster University

A thesis submitted for the degree of *Doctor of Philosophy.* October, 2024.

Abstract

Collisional interactions between plasmas and neutrals in Earth's upper atmosphere results in one of the largest sinks of magnetosphere-ionosphere-thermosphere energy: Joule heating. At mid, and specifically sub-auroral latitudes, a combination of electrodynamical and neutral wind drivers contribute to the produced Joule heating. The individual drivers are less well understood than at high-latitudes. The Thermosphere-Ionosphere Electrodynamic General Circulation Model (TIEGCM) is one of the most used within the scientific community to study Joule heating. Due to limited validation and the uncertainties in the mid-latitude drivers, little is known about its performance at the mid-latitudes. This thesis investigates the mid-latitude ion and neutral interactions and resulting Joule heating, while comparing our findings to outputs from TIEGCM.

In Chapter 3 we identify an interval of co-located ion and neutral observations by the Blackstone (BKS) Super Dual Auroral Radar Network (SuperDARN) radar and the Ann Arbor (ANN) North American Thermosphere Ionosphere Observing Network (NATION) Fabry-Perot interferometer (FPI) respectively, and compare our outputs to the TIEGCM model. Despite geomagnetically quiet conditions, we observe strong sub-auroral ion and neutral flows, which TIEGCM does not model due to a lack of dynamic sub-auroral drivers in the model. In Chapter 4, we estimate the local Joule heating rates from the observations in Chapter 3. We find that the excited ion motion drives Joule heating enhancements and that the neutrals account for between 24% and 42% of the total Joule heating, while the Joule heating

magnitudes produced by TIEGCM are smaller and driven by the neutrals instead. Finally in Chapter 5, we statistically analyse observed sub-auroral ion velocities and find that while low velocity events are modelled well, extreme Joule heating events cannot be represented in TIEGCM. Furthermore the direction of the neutral wind effectively modulates the total Joule heating, by up to 4 orders of magnitude.

Acknowledgements

Firstly, I am forever grateful to the Natural Environment Research Council and the ENVISION doctoral training partnership who have provided me with the funding to pursue this opportunity.

I would like to thank my Supervisor, Prof. Adrian Grocott, for the guidance, tutoring and constant willingness to aid me over the course of my 3.5 years in Lancaster. Not only have you taught me an awful lot of physics, but you have also made me a much better scientist to boot. I would also like to send my thanks to Dr. Maria-Theresia Walach and Prof. Jim Wild for their efforts as well.

My thanks goes to the PI's of the SuperDARN and NATION networks and the TIEGCM modellers at NCAR for providing not just their data but also their expertise that allowed me to not just perform my research but also obtain results. I also extend my thanks to the AMPERE, POES & DMSP missions, the IGRF modellers and the CCMC, GNSS TEC & OMNIweb services for their data too.

My thanks to the SPP Office for making my time spent there thoroughly enjoyable, through which I learnt a lot of geography, and we managed to do some physics as well!

I wish to send some personal thanks to the people who have in one-way or another shaped me and put myself on the path that has led me here. My two brothers, Liam and Scott. My housemates of 165 for the many laughs. Dr. Joe Mayes and Dr. Max Bedford, without whose inspiration I doubt I ever would have embarked on this journey in the first place. Soon to be Dr. Tom Brophy for the many memes, and my DnD groups for allowing me to escape to less scientifically bound worlds.

Lastly, but most importantly, I would like to send my love and appreciation to my Mum and Dad. Although I am long past the stage where you have been able to help me with my homework, there is no chance I would be where I am today without your unwavering love, support and for always being there for me when I have needed you.

Declaration

I declare that the work presented in this thesis is, to the best of my knowledge and belief, original and my own work. The material has not been submitted, either in whole or in part, for a degree at this, or any other university. This thesis does not exceed the maximum permitted word length of 80,000 words including appendices and footnotes, but excluding the bibliography. A rough estimate of the word count is: 45,773

Elliott Keith Day

Contents

List of Tables

List of Figures

Abbreviations

AACGM	Altitude-Adjusted Corrected Geomangetic
AE	Auroral Electrojet
AL	Auroral Lower
AU	Auroral Upper
AMPERE	Active Magnetosphere and Planetary Electrodynamics Response Experiment
ANN	ANN Arbor
BKS	Blackstone
DMSP	Defence Meteoroligical Satellite Program
EUV	Extreme Ultra-Violet Radiatoin
FAC	Field-Aligned Current
FPI	Fabry-Perot Interferometer
GNSS	Global Navigation Satellite System
GPS	Global Positioning System
GSE	Geocentric Solar Ecliptic
GSM	Geocentric Solar Magnetospheric
HF	High Frequency
HMB	Heppner-Maynar Boundary
IGRF	International Geomagnetic Reference Field
IMF	Interplanetary Magnetic Field
LOS	Line-of-Sight
MLAT	Magnetic Latitude
MLON	Magnetic Longiutde

MLT	Magnetic Local Time
NATION	North-American Thermosphere Ionosphere Observing Network
POES	Polar Operational Environmental Satellites
RST	Radar Software Toolkit
SuperDARN	Super Dual Auroral Radar Network
TEC	Total Electron Content
TIEGCM	Thermosphere-Ionosphere Electrodynamic General Circulation Model
UT	Universal Time

Chapter 1

Introduction

1.1 Motivation

Earth's upper atmosphere is a playground for plasmas, a form of dissociated matter which is a gaseous mixture of electrons and positive ion which feel the effects of electric and magnetic fields. The plasma in Earth's upper atmosphere interacts with the neutral atoms in Earth's atmosphere through a process known as Joule heating. This heating causes parts of Earth's atmosphere to expand (Fuller-Rowell et al., 1997; Knipp et al., 1998; Lu et al., 2016; Rishbeth et al., 1969; Zhang et al., 2017) which can result in increased outflow of matter from the atmosphere and increased satellite drag that can reduce their operational lifetime.

The awareness and importance of studying and understanding Joule heating in Earth's atmosphere has been increasing recently. In February 2022, SpaceX lost approximately 40 Starlink satellites due to an unexpected increase in Joule heating (Dang et al., 2022; Fang et al., 2022; Lin et al., 2022; SpaceX, 2022). While physical models can be deployed to model and predict Joule heating, these models need validating in order to assess their performance. Typically these models are validated for high-latitude regions, which is where Joule heating deposits most energy, however little is known about their performances at mid-latitudes despite being of arguably greater societal impact. Much of the challenge that comes with validating mid-

latitude Joule heating models is the difficulty in obtaining accurate estimations of the Joule heating through observations (Palmroth et al., 2021). The dynamics and the drivers of plasma at the mid-latitudes are different and often, more complex than at high-latitudes. This thesis explores the mid-latitude plasma dynamics, assess the Joule heating that occurs in the mid-latitudes and compare our findings to model Joule heating predictions.

1.2 Physics of Magnetised Plasmas

Earth's magnetic field is coupled to the upper atmosphere, the thermosphere, where ionisation forms a low density plasma known as the ionosphere. The plasma is in turn coupled and driven by Earth's magnetic field (see section 1.2.4), which drives much of the plasma motion that results in Joule heating. In order to understand the driving processes behind the plasma, we must describe the fundamental principles of magnetised plasma. Due to the plasma's low density over the majority of the altitude range of the ionosphere, we are able to assume that microscale plasma move as individual particles, coined single particle motion, which we shall proceed to discuss.

1.2.1 Maxwell's Equations

First, it is necessary to briefly mention Maxwell's equations, which govern the guiding principles of the behaviour of electromagnetic fields: **Faraday-Maxwell Law**

$$\nabla \times \mathbf{E} = -\frac{d\mathbf{B}}{dt} \tag{1.1}$$

states that any change in magnetic flux induces an electric field (and by proxy, a current) in a closed conductor. **Amperès Law,**

$$\nabla \times \mathbf{B} = \mu_0 \mathbf{J} + \frac{1}{c^2}\frac{d\mathbf{E}}{dt} \tag{1.2}$$

is symmetrical to Faradays law, in that a time varying electric field also produces a magnetic field. **Gauss's Law,**

$$\nabla \cdot \mathbf{E} = \frac{\rho_q}{\epsilon_0} \tag{1.3}$$

states that the flux of an electric field through a closed surface is proportional to the charge enclosed by the surface. **No Monopoles** is given by,

$$\nabla \cdot \mathbf{B} = 0 \tag{1.4}$$

which states that no magnetic monopoles exist and that the total magnetic flux through a closed surface must be zero.

In all cases $\mathbf{E}$ is the electric field, $\mathbf{B}$ is the magnetic field. μ_0 is the permeability of free space. ρ_q is the charge density and ϵ_0 is the permittivity of free space. $\mathbf{J}$ is the current density and c^2 is the identity $1/\mu_0\epsilon_0$.

1.2.2 Single Particle Motion

A single particle at rest, with charge q produces an electric field, $\mathbf{E}$, otherwise known as the Coulomb force per unit charge, $\mathbf{F_c}$ towards other nearby charged particles:

$$\mathbf{F_c} = q\mathbf{E} \tag{1.5}$$

The charge of the particle determines whether the Coulomb force is attractive or repulsive to other charge carriers. A particle with charge q, moving with a velocity $\mathbf{v}$ through a magnetic field $\mathbf{B}$, experiences a Lorentz force, $\mathbf{F_l}$:

$$\mathbf{F_l} = q(\mathbf{v} \times \mathbf{B}) \tag{1.6}$$

where $\mathbf{v} \times \mathbf{B}$ produces an additional electric field relative to the moving particle. A moving charged particle will experience both the Coulomb and the Lorentz force therefore, and by applying Newton's second law of motion, the total force on a charged particle in motion may be written as,

$$\mathbf{F} = m\mathbf{a} = m\frac{d\mathbf{v}}{dt} = q(\mathbf{E} + \mathbf{v} \times \mathbf{B}) \tag{1.7}$$

where m is the mass of the charged particle.

Let us take the case where a charged particle travels in a constant magnetic field, $\mathbf{B} = (0, 0, Bz)$, with no electric field and a velocity, $\mathbf{v} = (v_x, v_y, v_z)$ in a standard cartesian coordinate system. Equation 1.7 becomes:

$$\mathbf{F} = m\frac{d}{dt}\begin{bmatrix} v_x \\ v_y \\ v_z \end{bmatrix} = \begin{bmatrix} qB_z v_y \\ -qB_z v_x \\ 0 \end{bmatrix} \tag{1.8}$$

which shows that the charged particle is accelerated in the x and y directions, perpendicular to the magnetic field, while no acceleration occurs in the direction of the magnetic field.

If we take the time derivates of the perpendicular components of equation 1.8, then the x and y directions of equation 1.8 becomes 1.9.

$$m\frac{d^2}{dt^2}\begin{bmatrix} v_x \\ v_y \end{bmatrix} = \begin{bmatrix} qB_z\frac{dv_y}{dt} \\ -qB_z\frac{dv_x}{dt} \end{bmatrix} \tag{1.9}$$

If we substitute the same components from equation 1.8 into equation 1.9 then get equation 1.10.

$$\frac{d^2}{dt^2}\begin{bmatrix} v_x \\ v_y \end{bmatrix} = \begin{bmatrix} -\frac{q^2{B_z}^2}{m^2}\frac{dv_x}{dt} \\ -\frac{q^2{B_z}^2}{m^2}\frac{dv_y}{dt} \end{bmatrix} \tag{1.10}$$

which is the form of the equation for a simple harmonic oscillator, with the oscillation frequency, otherwise known as the gyrofrequency given by Ω.

$$\Omega = \left|\frac{qB_z}{m}\right| \tag{1.11}$$

Equation 1.10 indicates that charged particles move in a circular motion perpendicular to the direction of a magnetic field.

If we equate the magnitude of the Lorentz force with the centripetal force of a circularly moving particle,

$$\frac{mv^2}{r} = qvB \tag{1.12}$$

then we result in equation 1.13,

$$r_g = \frac{mv}{qB} = \frac{v}{\Omega} \tag{1.13}$$

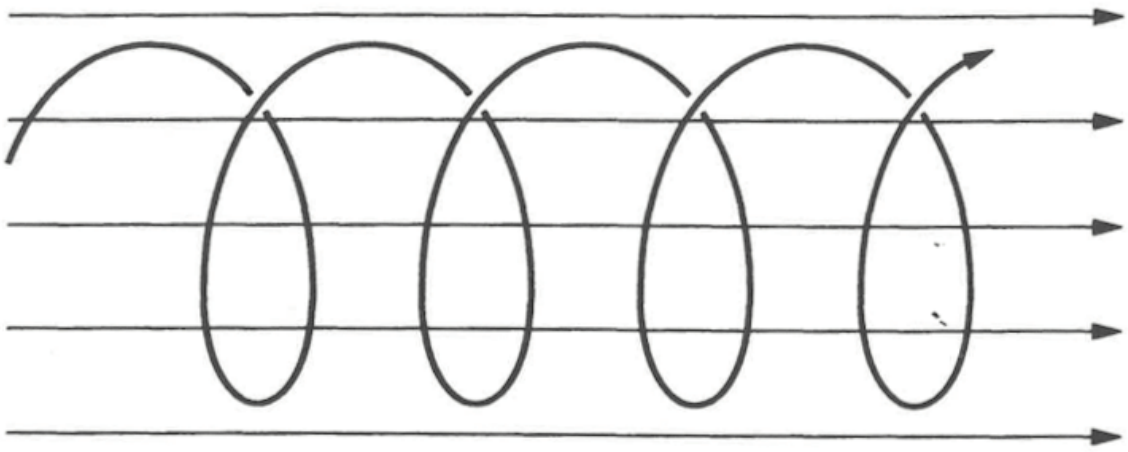

Figure 1.1: Schematic of a charged particle gyrating areound magnetic field lines in a helicoidal trajectory. The horizontal lines are the magnetic field lines, while the curves is the particle. From Baumjohann and Treumann (1996)

where r_g is the radius of gyromotion, otherwise known as the gyroradius. We can use this to generate the solutions to equation 1.10 as

$$\begin{aligned} x - x_0 &= r_g \sin \Omega_g t \\ y - y_0 &= r_g \cos \Omega_g t \end{aligned} \tag{1.14}$$

Where x_0 and y_0 are the initial positions of the particle in the x and y directions.

Figure 1.1 shows the trajectory of a charged particle gyrating around mangetic field lines, which appears helical. We can see through equation 1.13, that the gyration of the particles is dependent on their mass. Heavier particles such as ions will gyrate over a larger radius with a slower frequency, whereas smaller particles such as electrons gyrate over smaller radii with a greater frequency. Meanwhile, the charge determines the direction of gyration, such that positive and negatively charged particles will gyrate in opposite directions.

1.2.2.1 E × B Drift

We previously assumed the presence of no electric field, however in real environments, especially within Earth's magnetosphere and ionosphere this is rarely the

case. If we look at equation 1.7, this tells us that the electric field, **E** imposes an additional force to the motion of charged particles. The total particle velocity may be composed of the vector components parallel, $v_{\parallel}$, and perpendicular to the magnetic field ,$v_{\perp}$, such that

$$\mathbf{v} = \mathbf{v}_{\parallel} + \mathbf{v}_{\perp} \tag{1.15}$$

If we consider the parallel velocity under the effects of a constant magnetic and electric field, $\mathbf{v}_{\parallel} \times \mathbf{B} = 0$, therefore equation 1.7 becomes:

$$\frac{d\mathbf{v}_{\parallel}}{dt} = \frac{q}{m}\mathbf{E}_{\parallel} \tag{1.16}$$

indicating that particles are accelerated in the direction of, or against the magnetic field according to the charge of the particle and at a magnitude respective to its mass.

In the presence of a uniform perpendicular electric and magnetic field, a particle, regardless of mass or charge, drifts with a velocity, $\mathbf{v_E}$, perpendicular to **E** and **B** and is given by equation 1.17.

$$\mathbf{v_E} = \frac{\mathbf{E} \times \mathbf{B}}{B^2} \tag{1.17}$$

This is often referred to as the $\mathbf{E} \times \mathbf{B}$ drift. As there is no charge dependency, electrons and ions drift at the same velocity, resulting in no charge separation, thus in a collisionless system, no current is produced. A particle experiencing $\mathbf{E} \times \mathbf{B}$ drift, still gyrates perpendicular to **B** according to their charge and mass. Ions are accelerated in the direction of **E**, increasing their gyroradius, before being decelerated in the second half of their orbit, decreasing the gyroradius during this period. The opposite but same effect occurs with electrons, resulting in a drift pattern as shown in Figure 1.2.

Finally, we note that we can generate an expression for a generalised force drift by replacing the Coulomb force, **E** with a general force, **F**, (equation 1.5):

$$\mathbf{v_d} = \frac{\mathbf{F} \times \mathbf{B}}{qB^2} \tag{1.18}$$

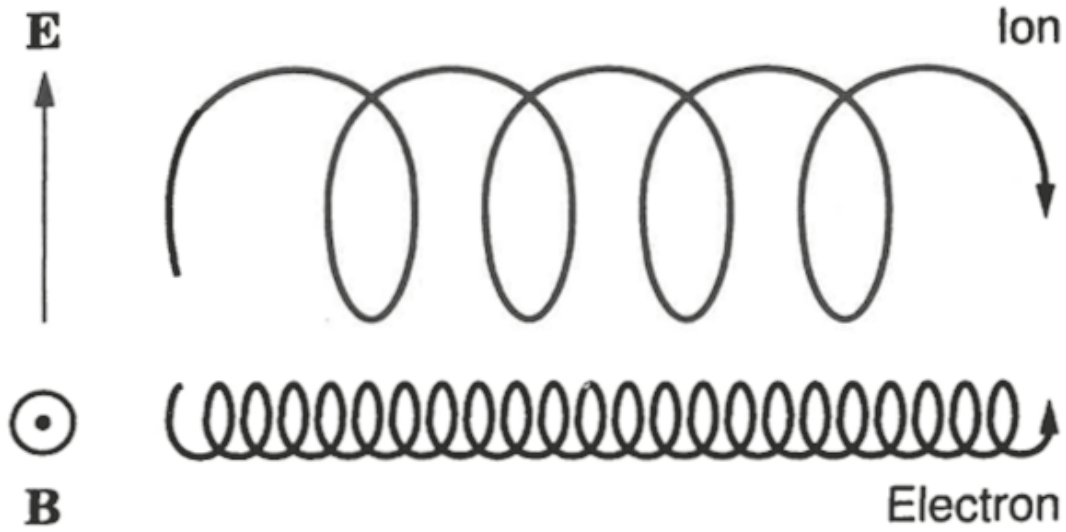

Figure 1.2: An illustration of both ions and electrons experiencing $\mathbf{E} \times \mathbf{B}$ drift. The magnetic field is directed out of the page while the electric field is upwards. From Baumjohann and Treumann (1996).

1.2.2.2 Magnetic Gradient Drift

Previously, we have assumed that the magnetic field is constant, however this is often not the case. If we take a charged particle to be moving through an inhomogenous magnetic field, and assume that the particle gyrates on a much smaller scale than the scale length of a typical magnetic field, then,

$$\mathbf{v}_{\nabla} = \frac{m{v_{\perp}}^2}{2qB^3}(\mathbf{B} \times \nabla B) \tag{1.19}$$

showing that the presence of a magnetic field gradient leads to a gradient drift perpendicular to both the magnetic field and its gradient. The direction and magnitude of the drift is determined by the charge and mass of the particle.

1.2.3 Bulk Particle Motion

While the density of most plasmas in space are small enough that we can consider them to be collisionless. Earth's ionosphere is embedded within the neutral

thermosphere, where the neutral density is often much higher than the plasma, we therefore need to explore the motion of both the neutrals and the plasmas as they interact with each other.

1.2.3.1 Conservation of Mass

Conservation of mass dictates that the flux into or out of a closed surface must remain constant;

$$\frac{\partial \rho}{\partial t} + \nabla \cdot (\rho \mathbf{u}) = 0 \tag{1.20}$$

Where ρ is the mass density of the medium and $\mathbf{u}$ the is the velocity vector of the medium. For neutral mediums, such as Earth's thermosphere, this constitutes the continuity equation. When referring to velocity fields, $\mathbf{u}$ shall be used to denote neutral velocities, while $\mathbf{v}$ will be used for ion velocities.

Assumptions about the medium of which the continuity equation applies to can provide us with useful relationships to be used later. By expanding the divergence operator using $\nabla \cdot (\psi \mathbf{A}) = \psi(\nabla \cdot \mathbf{A}) + \mathbf{A} \cdot (\nabla \psi)$, equation 1.20 becomes

$$\frac{\partial \rho}{\partial t} = -\rho(\nabla \cdot \mathbf{u}) - \mathbf{u} \cdot (\nabla \rho) \tag{1.21}$$

If we use the total time derivative operation,

$$\frac{d}{dt} = \frac{\partial}{\partial t} + \mathbf{u} \cdot \nabla \tag{1.22}$$

then equation 1.21 becomes,

$$\frac{d\rho}{dt} + \rho(\nabla \cdot \mathbf{u}) = 0 \tag{1.23}$$

If the fluid is incompressible, then the mass density remains constant, $d\rho/dt = 0$, therefore from equation 1.23, $\nabla \cdot \mathbf{u} = 0$ indicating that an incompressible fluid is divergence free.

In Earth's ionosphere we consider the plasma to be partially ionised in order to accurately capture its motion. In this case, ion and electron pairs may be produced by photoionisation, energetic particle collisions or lost through recombination

between oppositely charged particles, in which case the continuity equation for ionised species becomes

$$\frac{\partial \rho}{\partial t} + \nabla \cdot (\rho \mathbf{v}) = (P_i - L_i) M_i \tag{1.24}$$

where P_i represents the ion (and electron) production rate per cubic metre per second, L_i the loss rate and M_i the mass of each species. Since electric charge is conserved, the total number of electrons gained or lost must equal the total number of ions gained or loss, therefore

$$\sum_{i=1}^{N} (P_i - L_i) = P_e - L_e \tag{1.25}$$

Negative ions can be ignored as they need only be considered below 80 km altitude. The neutral density is much greater than the ion and electron densities for altitudes less than several thousand kilometres so we can ignore the loss of neutral particles when ion-electron pairs are formed. If we assume the neutral mass density remains constant then equation 1.20 represents the conservation of mass for the neutral atmosphere, while equation 1.24 is the conservation of mass for ionized regions.

1.2.3.2 Equation of state

For an ideal gas, the mass density is related to the pressure, p_i by

$$p_i = \frac{\rho_i \kappa_B T_i}{M_i} = n_i \kappa_B T_i \tag{1.26}$$

which is the equation of state for each fluid that we consider (ions, neutrals and electrons), where n_i is the number density and $\rho_i = n_i M_i$ and κ_B is Boltzmann's constant.

1.2.3.3 Momentum of Neutral Fluids in a Magnetized Plasma

Conservation of momentum states that the total momentum within a closed volume must be equal to the pressure gradient force plus the total external force field, **F**

applied on the fluid within the volume and the momentum flux across the volume surface. The momentum equation is given by

$$\frac{\partial(\rho\mathbf{u})}{\partial t} = -\nabla p + \mathbf{F} - \nabla \cdot \pi_m - \nabla \cdot \pi_w \tag{1.27}$$

where $\mathbf{F}$ is the external force, p, the pressure, π_m the momentum flux density due to material motions and π_w the momentum flux density due to waves in the medium. First we shall consider the material momentum term, π_m. For a particle with mean mass density ρ, travelling at velocity $\mathbf{u}$ in a fluid with velocity $\mathbf{u}$ (Kelley, 2009).

$$\pi_m = \rho\mathbf{u}\mathbf{u} \tag{1.28}$$

Using the vector identity $\nabla \cdot (\mathbf{AB}) = \mathbf{A}(\nabla \cdot \mathbf{B}) + \mathbf{B} \cdot (\nabla \mathbf{A})$, this becomes

$$\nabla \cdot \pi_m = \rho\mathbf{u}(\nabla \cdot \mathbf{u}) + \mathbf{u} \cdot \nabla(\rho\mathbf{u}) \tag{1.29}$$

and using the total time derivative (equation 1.22) we have

$$\frac{d(\rho\mathbf{u})}{dt} = \frac{\partial(\rho\mathbf{u})}{\partial t} + \mathbf{u} \cdot (\nabla\rho\mathbf{u}) \tag{1.30}$$

therefore, and assuming that the fluid is incompressible so that $\nabla \cdot \mathbf{u} = 0$,

$$\nabla \cdot \pi_m = \frac{\rho d\mathbf{u}}{dt} \tag{1.31}$$

Substituting this into equation 1.27 gives us

$$\frac{\rho d\mathbf{u}}{dt} = -\nabla p + \mathbf{F} - \nabla \cdot \pi_w \tag{1.32}$$

It is necessary for us to consider cases where shears arise in the neutral wind flows. In such instances, particles travelling with a mean velocity in the x direction, that randomly move perpendicular to x, and into a region with a different x mean velocity will contribute a different x momentum. The particle will experience collisional interactions, resulting in a momentum transfer that will affect the mediums x velocity gradient. We can account for this with the use of the viscous force, $\mathbf{F_v}$,

$$\mathbf{F_v} = \eta\nabla^2\mathbf{U} + \eta^{'}\nabla(\nabla \cdot \mathbf{u}) \tag{1.33}$$

where η and $\eta^{'}$ are viscosity coefficients of the medium. We add this term to equation 1.32, while for incompressible flows, $\nabla \cdot \mathbf{u} = 0$, so

$$\frac{\rho d\mathbf{u}}{dt} = -\nabla p + \mathbf{F} - \nabla \cdot \pi_w + \eta \nabla^2 \mathbf{u} \tag{1.34}$$

where η is a dynamic viscosity coefficient. For large scale flow patterns, $\nabla \cdot \mathbf{u} = 0$ is a good approximation and is applicable where molecular collisions dominate against turbulent eddies in the flow, which holds true above ($\sim$ 100km altitude).

Now we must consider the effect of external forces on the fluid. All particles that have mass experience gravitational forces, $\mathbf{F_g}$,

$$\mathbf{F_g} = \rho \mathbf{g} \tag{1.35}$$

which must be accounted for. Furthermore, there is an electromagnetic force which is transferred to a neutral medium when charged particles travel through it. In a continuous medium, such as Earth's atmosphere, the electromagnetic force, $\mathbf{F_{EM}}$ is given by

$$\mathbf{F_{EM}} = \mathbf{J} \times \mathbf{B} \tag{1.36}$$

where $\mathbf{J}$ is the current density, $\rho \mathbf{v}$. The total external force field $\mathbf{F} = \mathbf{F_g} + \mathbf{F_{EM}}$, so equation 1.34 becomes (Kelley, 2009).

$$\frac{\rho d\mathbf{u}}{dt} = -\nabla p + \rho \mathbf{g} - \nabla \cdot \pi_w + \eta \nabla^2 \mathbf{u} + \mathbf{J} \times \mathbf{B} \tag{1.37}$$

The velocity term, $\mathbf{u}$, at the left hand side of equation 1.37 is for the velocity given at Earth's surface. At high altitudes, Earth's atmosphere experiences the Coriolis force, which deflects the neutrals to the right in the northern hemisphere and to the left in the southern hemisphere. We must therefore relate the velocity on the left hand side to the reference frame of the rotating atmosphere as observed by the inertial frame of reference, Earth's surface. Transport theorem relates time derivatives of rotating and non-rotating vectors by,

$$\frac{d}{dt}\mathbf{f} = \left[\left(\frac{d}{dt}\right)_R + \Omega\times\right]\mathbf{f} \tag{1.38}$$

where $\mathbf{f}$ is the vector evaluated in both the rotating and non-rotating coordinate systems. Here, R refers to the rotating reference frame, I will be used to refer to the inertial frame. It follows then, that for a radial position vector $\mathbf{r}$,

$$\frac{d}{dt}\mathbf{r} = \left[\left(\frac{d}{dt}\right)_R + \Omega\times\right]\mathbf{r} = \left(\frac{d\mathbf{r}}{dt}\right)_R + \Omega \times \mathbf{r} \tag{1.39}$$

and since $d\mathbf{r}/dt = \mathbf{u}$, we can rewrite the above equation as

$$\mathbf{u_I} = \mathbf{u_r} + \Omega \times \mathbf{r} \tag{1.40}$$

In equation 1.37, $\mathbf{u}$ on the left hand side is considered to be $\mathbf{u_I}$, where we want to replace it by $\mathbf{u_r}$. taking the time derivative of equation 1.40:

$$\frac{d}{dt}\mathbf{u_I} = \frac{d}{dt}\mathbf{u_r} + \Omega \times \frac{d}{dt}\mathbf{r} \tag{1.41}$$

and by once more applying the transport theorem (equation 1.38),

$$\frac{d\mathbf{u_I}}{dt} = \left[\left(\frac{d}{dt}\right)_r + \Omega\times\right]\mathbf{u_r} + \Omega \times \left[\left(\frac{d}{dt}\right)_r + \Omega\times\right]\mathbf{r} \tag{1.42}$$

we know that $d\mathbf{r}/dt = \mathbf{u}$, therefore the previous becomes:

$$\frac{d\mathbf{u_I}}{dt} = \frac{d\mathbf{u_r}}{dt} + 2(\Omega \times \mathbf{u_r}) + \Omega \times (\Omega \times \mathbf{r}) \tag{1.43}$$

The term $\Omega \times (\Omega \times \mathbf{r})$ is known as the centripetal force, which is generally already considered for within gravitational forces, therefore we can ignore it as it is part of $\mathbf{g}$. Thus, substituting 1.43 into the left hand side of 1.37 and rearranging gives us the full equation of motion for the neutral fluid in a rotating frame:

$$\rho\frac{d\mathbf{u}}{dt} = -\nabla p + \rho\mathbf{g} - \nabla \cdot \pi_w + \eta\nabla^2\mathbf{u} + \mathbf{J} \times \mathbf{B} - 2\rho(\Omega \times \mathbf{u}) \tag{1.44}$$

1.2.3.4 Momentum of Magnetized Plasmas

In section 1.2.3.3 the only effect of a coexisting plasma embedded within the neutral atmosphere was the $\mathbf{J} \times \mathbf{B}$ force that would be transferred to the neutrals. Although the coriolis force has a great affect on neutral fluids in Earth's atmosphere, the

magnetic force applied to plasma is far greater and so the coriolis force can be ignored. The important forces, **F** that act on the charged particles are:

$$\begin{aligned} \text{Gravitational}: \ & \rho_i \mathbf{g} \\ \text{Electric}: \ & n_i q_i \mathbf{E} \\ \text{Magnetic}: \ & n_i q_i (\mathbf{v} \times \mathbf{B}) \end{aligned}$$

where q_i is the charge of each species. Furthermore, each species may experience collisional interactions with each other species, including other neutrals. The force is respective to the collisional frequency and the difference between the velocities of each species and can be written as:

$$\mathbf{F_j} = -\sum_{\substack{k=1 \\ i \neq k}} \rho_i v_{ik} (\mathbf{v_i} - \mathbf{v_k}) \tag{1.45}$$

where v_{ik} are momentum transfer collision frequencies between species i and k, with units of s^{-1}. The momentum equation for ionised species is then

$$\rho_i \frac{d\mathbf{v_i}}{dt} = -\nabla p + \rho_i \mathbf{g} + n_i q_i (\mathbf{E} + \mathbf{V_i} + \mathbf{B}) - \sum_{\substack{k=1 \\ i \neq k}} \rho_i v_{ik} (\mathbf{v_i} - \mathbf{v_k}) \tag{1.46}$$

For most situations and as is appropriate for this work, viscosity and momentum transfer by waves can be ignored so are not included.

1.2.3.5 Collisions in a magnetised Plasma

If we assume that the fluid velocity of a magnetised plasma is unchanging, the left hand side of equation 1.46 goes to zero. For simplicity we can consider a single ion species, use the relationship $\rho = n_i \kappa_B T_i$ and rearrange into

$$q_i n_i \mathbf{v_i} = -\nabla (n_i \kappa_B T_i) + n_i M_i \mathbf{g} + q_i n_i (\mathbf{E} + \mathbf{v_i} \times \mathbf{B}) \tag{1.47}$$

If we divide through by $n_i M_i \nu_i k_B$ and use the following relationships:

$$\begin{aligned} \kappa_i &= \frac{q_i B}{M_i \nu_i k_B} &= \frac{\Omega}{\nu} \\ D_i &= \frac{\kappa_B T_i}{M_i \nu_i k_B} \\ b_i &= \frac{q_i}{M_i \nu_i k_B} \\ H_i &= \frac{\kappa_B T_i}{M_i \mathbf{g}} \end{aligned} \tag{1.48}$$

where κ_i is the ratio of gyrofrequency to collision frequency, D_i is the diffusion coefficient, b_i is the mobility and H_i is the scale height, equation 1.47 becomes

$$\mathbf{v_i} - \kappa_i(\mathbf{v_i} \times \hat{\mathbf{B}}) = -D_i \frac{\nabla n}{n} + b_i \mathbf{E} + \frac{D_i}{H_i} \hat{\mathbf{g}} \equiv \mathbf{W_i} \tag{1.49}$$

where we have assumed that $n_i = n_e = n$ and $\hat{\mathbf{B}}$ is the unit vector of $\mathbf{B}$. $\mathbf{W_i}$ is the fluid velocity of an unmagnetised plasma subject to the same forces.

Equation 1.49 describes the motion of charged particles in the presence of an electric and magnetic field according to their gyro to collision frequency ratio, κ_i. For high collision rate plasma, $\kappa_i << 1$, therefore equation 1.49 simply becomes $\mathbf{v_i} = \mathbf{W_i}$. The particle will move parallel to the electric field as if there was no magnetic field present. $\mathbf{W}$ then, can be described as the fluid velocity of an unmagnetised plasma. For $\kappa_i >> 1$ we need to consider the parallel and perpendicular directions separately. In the parallel direction, $\kappa_i(\mathbf{v_i} \times \hat{\mathbf{B}})$ goes to 0, thus $v_{i\|} = \mathbf{W} \cdot \hat{\mathbf{B}}$. In the perpendicular direction, $\mathbf{v}_\perp = \kappa_i(\mathbf{v_i} \times \hat{\mathbf{B}}) >> \mathbf{v}_\|$, so we only consider $\mathbf{v}_\perp$, equation 1.49 becomes

$$\mathbf{v}_\perp = \frac{1}{B^2} \left(\mathbf{E} - \frac{\kappa_B T}{q_i} \frac{\nabla n}{n} + \frac{M_i}{q_i} \mathbf{g} \right) \times \mathbf{B} \tag{1.50}$$

which can be resolved into,

$$\mathbf{v}_\perp = \frac{\mathbf{E} \times \mathbf{B}}{B^2} \left(\frac{M_i}{q_i} \mathbf{g} - \frac{\kappa_B T}{q_i} \right) \times \mathbf{B} \tag{1.51}$$

which shows that collisionless plasmas move with the $\mathbf{E} \times \mathbf{B}$ drift velocity. For an intermediate case, e.g. $\kappa \approx 1$,

$$\mathbf{v_i} = \mathbf{W_i} + \kappa_i(\mathbf{v_i} \times \mathbf{B}) \tag{1.52}$$

which, with a velocity $\mathbf{v_i} = (v_{ix}, v_{iy}, v_{iz})$ and a magnetic field, $\mathbf{B} = (0, 0, B_z)$,

$$\mathbf{v_i} = \begin{bmatrix} v_{ix} \\ v_{iy} \\ v_{iz} \end{bmatrix} = \begin{bmatrix} W_{ix} \\ W_{iy} \\ W_{iz} \end{bmatrix} \kappa_i \begin{bmatrix} v_{iy}B_z \\ -v_{ix}B_z \\ 0 \end{bmatrix} \tag{1.53}$$

substituting, v_{ix} and v_{iy} back into each other yields

$$v_{i\parallel} = W_{i\parallel} \tag{1.54}$$

and

$$\mathbf{v_{i\perp}} = \frac{\mathbf{W_{i\perp}}}{1 + \kappa_i^2} + \frac{\kappa_i \mathbf{W_{i\perp}}}{1 + \kappa_i^2} \tag{1.55}$$

where v_{iz} is the component parallel to $\mathbf{B}$ and v_{ix} and v_{iy} the components perpendicular. We see then that particle will drift in both the $\mathbf{E} \times \mathbf{B}$ direction and parallel to $\mathbf{E}$. An illustration of the trajectories of ions and electrons for different collision frequency to gyrofrequency ratios is visible in Figure 1.3. Equations 1.54 and 1.55 can also be used as the general expressions for the motion of collisional plasma with varying κ_i.

The conductivity of a plasma can be calculated through the relationship

$$\mathbf{J} = ne(\mathbf{v_i} - \mathbf{v_e}) = \sigma \cdot \mathbf{E} \tag{1.56}$$

where σ is the electrical conductivity and e the charge of an electron. Using equations 1.49 and 1.54, while noting that the electric field force in equation 1.49 dominates the other terms, we obtain

$$\mathbf{v_i} = \mathbf{W_i} = b_i \mathbf{E} \tag{1.57}$$

substituting the above into equation 1.56 tells us the parallel conductivity:

$$\sigma_\parallel = ne(b_i - b_e) \tag{1.58}$$

Electrons exhibit a much higher mobility than ions in the ionosphere, so we can discount b_e, leaving us with the definition for the parallel conductivity,

$$\sigma_\parallel = \frac{ne^2}{M_e \nu_e} \tag{1.59}$$

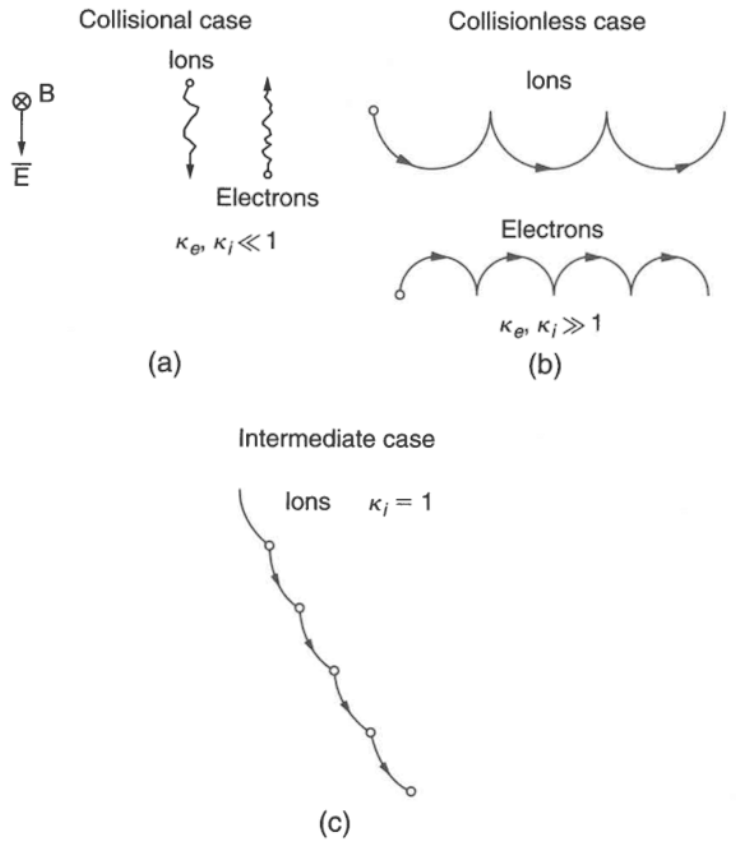

Figure 1.3: Illustrations of the trajectories of ions and electrons with different gyrofrequency to collision frequency ratios, κ. (a) is for when the collision frequency dominates ($\kappa << 1$), (b) when the gyrofrequency dominates ($\kappa >> 1$) and (c) when the terms are approximately equal ($\kappa \approx 1$). From Kelley (2009)

Similarly, if we substitute equation 1.57 into 1.55

$$\mathbf{v_{i\perp}} = \frac{b_i \mathbf{E}}{1+\kappa_i^2} + \frac{\kappa_i b_i \mathbf{E}}{1+\kappa^2} \tag{1.60}$$

and so from 1.56, the parallel conductivity must be

$$\sigma_\perp = ne\left(\frac{b_i}{1+\kappa_i^2} - \frac{b_e}{1+\kappa_e^2} + \frac{\kappa b_i}{1+\kappa_i^2} + \frac{\kappa b_e}{1+\kappa_e^2}\right) \tag{1.61}$$

which we can use tensor notation to split into σ_P and σ_H,

$$\sigma_P = ne\left(\frac{b_i}{1+\kappa_i^2} - \frac{b_e}{1+\kappa_e^2}\right) \tag{1.62}$$

and,

$$\sigma_H = ne\left(\frac{\kappa_i b_i}{1+\kappa_i^2} - \frac{\kappa_e b_e}{1+\kappa_e^2}\right) \tag{1.63}$$

where the full tensor for the conductivity is given as σ,

$$\sigma = \begin{pmatrix} \sigma_P & -\sigma_H & 0 \\ \sigma_H & \sigma_P & 0 \\ 0 & 0 & \sigma_\parallel \end{pmatrix} \tag{1.64}$$

Depending on the ratio of collision frequency to gyrofrequencies, either the Hall or Pedersen conductivities can dominate in the ionosphere.

1.2.4 The Frozen-In Theorem

If we take the motion of ions and electrons from equation 1.46 separately, and replace the collisional term with χ

$$\begin{aligned} \rho\frac{d\mathbf{v_i}}{dt} &= -\nabla \mathbf{p}_i + n_i i(\mathbf{E} + \mathbf{v_i} \times \mathbf{B}) + \chi \\ \rho\frac{d\mathbf{v_e}}{dt} &= -\nabla \mathbf{p}_e + n_e q_e(\mathbf{E} + \mathbf{v_e} \times \mathbf{B}) - \chi \end{aligned} \tag{1.65}$$

where we have neglected the gravity term due to it being minute. In plasma environment with no neutrals the collisional term, χ, refers to the ion-electron and electron-ion collisions. Conservation of momentum means that $\chi = \chi_{\mathbf{ie}} = -\chi_{\mathbf{ei}}$. If

we subtract the ion part of the above with the electron part, divide throughout by m_i and use the identity 1.56 then we have

$$\frac{m_e}{e}\frac{d\mathbf{J}}{dt} = \nabla\left(\mathbf{p_e} - \frac{m_e}{m_i}\mathbf{p_i}\right) + \left(1 + \frac{m_e}{m_i}\right)\chi - ne(\mathbf{E} + \mathbf{v_e} \times \mathbf{B}) + ne\frac{m_e}{m_i}(\mathbf{E} + \mathbf{v_i} \times \mathbf{B}) \quad (1.66)$$

where we have assumed quasi neutrality, $n \approx n_i \approx n_e$. Since m_e/m_i is small, we can remove most of the terms:

$$\frac{m_e}{e}\frac{d\mathbf{J}}{dt} = \nabla\mathbf{p_e} - \chi + ne(\mathbf{E} + \mathbf{v_e} \times \mathbf{B}) \quad (1.67)$$

The fluid velocity of a plasma is given as

$$\mathbf{v} = \frac{m_i n_i \mathbf{v_i} + m_e n_e \mathbf{v_e}}{m_e n_e + m_i n_i} \quad (1.68)$$

which using the previous assumptions and equation 1.56 gives us an identity relating the velocities and current density,

$$\mathbf{v_e} = \mathbf{v} - \frac{\mathbf{J}}{ne} \quad (1.69)$$

substituting this into equation 1.67 gives us

$$\frac{m_e}{e}\frac{d\mathbf{J}}{dt} = \nabla\mathbf{p_e} + ne(\mathbf{E} + \mathbf{v} \times \mathbf{B}) - \mathbf{J} \times \mathbf{B} - \chi \quad (1.70)$$

Finally, using resistivity as the inverse of the conductivity (equation 1.59) and applying the cross product with $\mathbf{B}$, we arrive at the general form of Ohm's law, which relates the current density, $\mathbf{J}$, with the electric field, $\mathbf{E}$, through the relationship:

$$\mathbf{E} + \mathbf{v} \times \mathbf{B} = R\mathbf{J} + \frac{\mathbf{J} \times \mathbf{B}}{R_e e} + \frac{\nabla\mathbf{P_e}}{R_e e} + \frac{m_e}{R_e e^2}\frac{d\mathbf{J}}{dt} \quad (1.71)$$

where R is the resistivity of the medium. The second, third and fourth terms on the right hand side represent electric fields due to the Hall effect, ambipolar diffusion and electron inertia respectively. In an ideal magnetic field environment, such as found in the solar wind, these terms are negligble and can be ignored. We can swap the inverse of the resistivity for the conductiviy, $\sigma_\parallel$, and in ideal magnetic field environments, the conductivity tends to infinity, therefore we can say

$$\mathbf{E} = -\mathbf{v} \times \mathbf{B} \quad (1.72)$$

Equation 1.72 tells us that bulk plasma motion in a magnetic field, produces a convective electric field. If we substitute this into Faraday's law, (equation 1.1) then,

$$\frac{d\mathbf{B}}{dt} = \nabla \times (\mathbf{v} \times \mathbf{B}) \tag{1.73}$$

which shows that the magnetic field is changed by convective motion of the plasma. Since the plasma moves with $\mathbf{E} \times \mathbf{B}$ drift, the plasma and the magnetic field lines are intrinsically linked, the plasma is "frozen-in" with the magnetic field.

1.3 The Solar Wind Interaction with the Magnetosphere

1.3.1 The Solar Wind

The outermost layer of the Sun's atmosphere, the corona, is highly ionised plasma with temperatures of the order of 10^6 K and densities to the order of 10^{17}cm^{-3}. Such high pressures cannot be contained within the corona, even with the Sun's gravitational force, so it flows radially outwards, forming the solar wind, a collisionless plasma with speeds typically around 400kms^{-1}.

The Sun also has an extremely complex magnetic field structure. At the equator, one rotation of its surface takes roughly 24.5 days, while at the poles a rotation takes 38 days. This rotation causes twists in its magnetic field. Where the magnetic field lines are "closed" in a loop, plasma is not allowed to escape from the Sun due to frozen-in flow, however, regions exist where one end of the magnetic field lines are not tied to the sun and instead flow into open space, known as "open" field lines. These open regions are called coronal holes. Plasma flows outwards from the sun from coronal holes alongside the open magnetic field lines that convect across interplanetary space. This is known as the interplanetary magnetic field (IMF).

The solar wind has a near infinite conductivity due to the negligible presence of neutral particles and low density plasmas, therefore due to frozen-in flow, the

plasma from the solar wind moves with the IMF.

The ratio of plasma pressure to magnetic pressure is known as the plasma beta quantity, β, which tells us whether the plasma or the magnetic field is dominant:

$$\beta = \frac{P_{plasma}}{P_{field}} = \frac{n\kappa_B T}{B^2/2\mu_0} \tag{1.74}$$

In the solar wind, the magnetic field pressure is weaker than the plasma pressure, $\beta > 1$, so the plasma drags the field with it radially outwards from the Sun. The base of the magnetic field is however tied to the Sun which is rotating, therefore the magnetic field line bends as the footprint moves with the Sun's rotation. Assuming a uniform outflow from the surface of the Sun, the IMF takes the form of a spiral (Parker, 1958) known as the Parker spiral.

Various coordinate systems are utilised to describe positions in near-Earth space, including the solar wind and orientation of the IMF. Two of the most commonly used coordinate system, which are geocentric, meaning the Earth is at the centre of (0, 0, 0) for an (x, y, z) coordinate system, are the following Hapgood (1992) and Laundal and Richmond (2017):

- Geocentric Solar Ecliptic (GSE) - x is directed towards the Sun, y is in the ecliptic plane opposite to the direction of Earth's orbit and z is perpendicular to both

- Geocentric Solar Magnetospheric (GSM) - x is the same as in GSE, however y is perpendicular to both the magnetic dipole axis x, (positive y values point towards dusk). z is aligned with the projection of Earth's magnetic dipole (positive z values point North) and is perpendicular to both x and y.

1.3.2 Earth's Magnetosphere

Earth has an intrinsic global scale magnetic field, generated by the continual flow of liquid iron in Earth's outer core. Earth's magnetic field is *approximately* dipolar, where the field lines flow into and out of the poles much like a bar magnet's do.

The poles of Earth's magnetic field are fairly well aligned with its geographic poles (although in opposite hemispheres) but an approximate 10° difference exists between the two. As Earth rotates, the magnetic dipole rotates alongside it, effectively causing it to rock back and forth as viewed along the x axis. The difference between GSE and GSM is then a rotation around the x axis, where instances of the magnetic dipole being perpendicular to the ecliptic plane result in the two systems being equal.

When making ground based observations, or referring to phenomena closer to Earth's surface we instead use different coordinate systems than GSE and GSM, where we have to specify coordinates respective to Earth's geographic or magnetic poles:

- Geographic (GEO) - z is parallel to Earth's rotation axis, the x-axis points towards the intersection of the equator and the Greenwich Meridian. The y-axis is perpendicular to both x and z.

- Magnetic (MAG) - There are various magnetic coordinate systems available, unless explicitly mentioned as otherwise, we refer to the adjusted corrected geomagnetic coordinates (AACGM) system Shepherd (2014). AACGM coordinates are determined by following a magnetic field line from a geographic starting point to the magnetic dipole equator. The AACGM coordinates are then given by the x, y, and z of the dipole field line on Earth's surface that intersects with the point on the dipole equator. Close to Earth's magnetic dipole equator, where the field lines are approximately parallel to Earth's surface, its field lines do not cross the dipole equator, therefore there is a region where no AACGM coordinates exist. The maximum latitude where this region occurs is at approximately 25°, for the purposes of this work, we are interested in the region at around 40° geographic north, we therefore do not need to consider this effect in this thesis. An example of how AACGM coordinates are determined is given in Figure **??**.

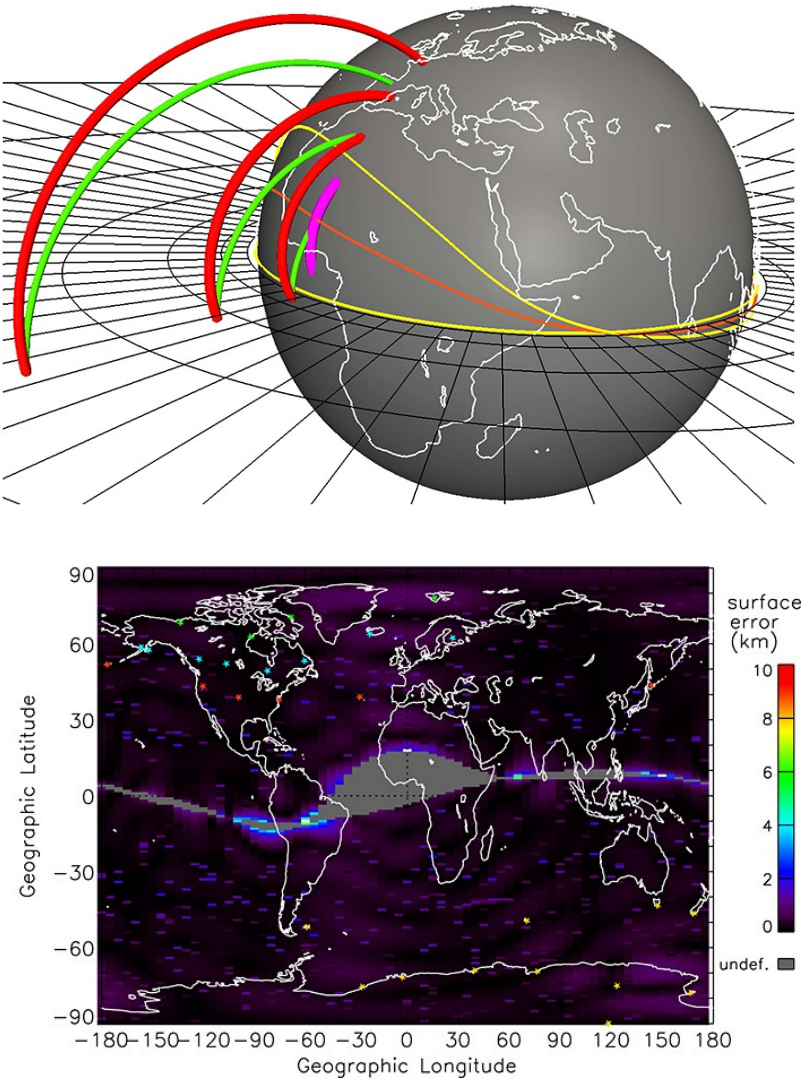

Figure 1.4: (top) Example of determining AACGM coordinates for four geographic locations at 50°, 40°, 30° and 20° latitude. Bold red lines are Earth's magnetic field lines originating from geographic locations and bold green lines show intersecting dipole field lines. Each line ends at the dipole equator, given by the radial wireframe. The bold green lines at Earth's surface show the AACGM coordinate for the equivalent geographic location. The orange line shows Earth's magnetic dip equator, while the yellow lines show the bounds where no AACGM coordinates exist due to Earth's field lines not crossing the dipole equator, exampled by the bold magenta line. (bottom) Error associated with the AACGM coordinates from the AACGM coefficients (see Shepherd, 2014 for details). Colour indicates the error in great-circle distance at the surface of the Earth. Grey shows regions where the AACGM coordinates are undefined due to being too close to the magnetic dipole equator. Stars show the location of SuperDARN sites (see section 2.1). Adapted From Shepherd (2014).

Coordinates for both geographic and magnetic frames are referred to by spherical harmonics (r, θ, ϕ), where r is the radius from the centre, θ is the latitude and ϕ the longitude. Positive latitudes refer to the northern hemisphere while negative the southern. The poles are located at $\pm 90^\circ$ and the equator at 0°. Longitudes range from 0° to 360°.

Magnetic longitude can be expressed as magnetic local time (MLT), defined in hours from 0 to 24, where 1hour = 15° magnetic longitude. MLT is defined such that 12 MLT (noon) is always sunward (dayside) and 00 MLT (midnight) is antisunward (nightside).

Although the magnetic field that Earth produces is approximately dipolar, the presence of the solar wind and IMF distorts the magnetic field. When the solar wind, carrying the IMF, reaches Earth's magnetic field, a bow shock is produced due to the solar wind travelling at supersonic speeds relative to the Earth's regime. Due to frozen-in flow, the solar wind cannot penetrate Earth's magnetic field, so flows around it instead, forming a cavity known as Earth's magnetosphere (Gold, 1959). The dayside of Earth's magnetosphere is compressed towards the Earth by the solar wind, forming the magnetopause. On the night side, the solar wind compresses Earth's magnetic field towards the equator, while simultaneously dragging on the magnetic field, stretching it away from Earth, forming a long magnetic tail known as the magnetotail (Dungey, 1965). The magnetic field lines on the nightside are essentially open, connected to Earth by one end while the other is dragged out into free space. On the dayside, the field lines are instead closed, as both ends connect to Earth's surface. A schematic of Earth's magnetosphere structure is shown in figure 1.5.

1.3.3 Magnetic Reconnection and The Dungey Cycle

Although field lines from two magnetic sources cannot cross, oppositely directed field lines can merge together, known as magnetic reconnection. When antiparrallel field lines lie on either side of a current sheet, the field lines can diffuse, reconnect

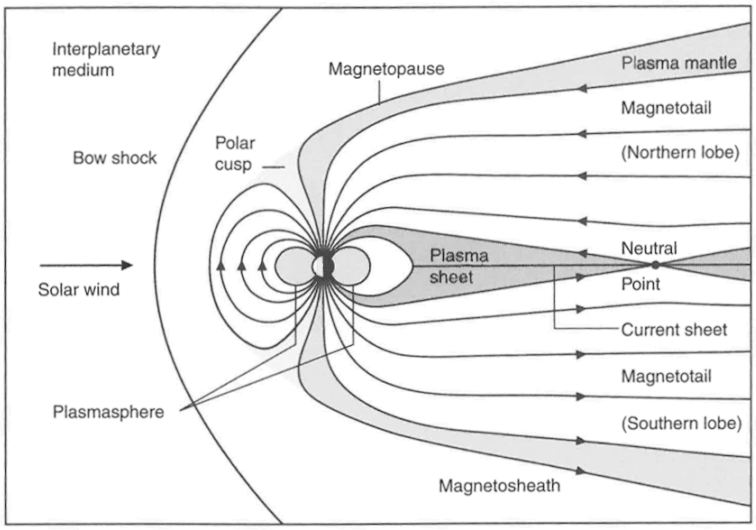

Figure 1.5: Diagram of Earth's magnetosphere structure, sliced across the day-night meridian. Featured are the bow shock from the supersonic IMF approaching Earth's magnetic field, the magnetopause and magnetotail. From Russell et al. (2016)

and the magnetic energy is released as heat, energising the coupled plasma. An example of a magnetic reconnection in a 2D scenario is presented in Figure 1.6.

Magnetic reconnection occurs between the IMF and Earth's magnetosphere. On the dayside, Earth's magnetic field is oriented so that it is directed to Earth's north pole, if the IMF is oriented so that it points towards Earth's south pole, then reconnection occurs between Earth's magnetosphere and the IMF, coupling Earth's magnetic field to the expanding IMF in a process known as the Dungey cycle (Dungey, 1961).

Figure 1.7, shows how reconnection at Earth with a purely southward directed IMF results in convection of the magnetosphere. At time (a), reconnection occurs between Earth's magnetic field and the IMF. The field lines unbend towards the nightside due to magnetic tension (b). Pressure from the solar wind continues to force the field line across the pole (c) and towards the nightside where it is stretched out into the magnetotail (d). Opposing field lines in the southern and northern magnetotail lobes forms a current sheet, where pressure eventually causes them to

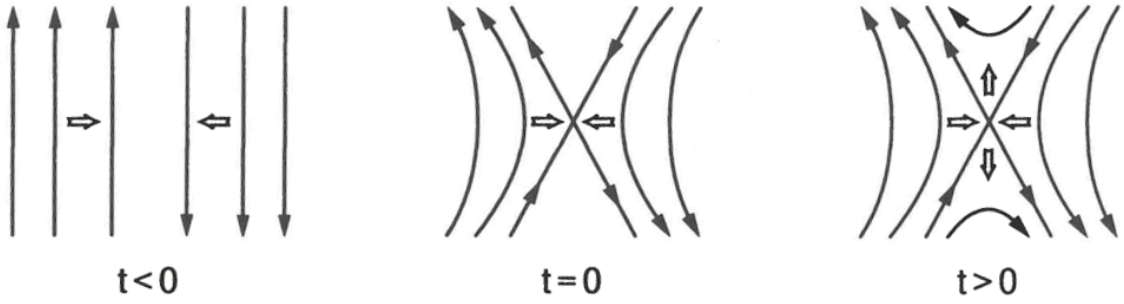

Figure 1.6: Diagram showing the process of magnetic reconnection between anti-parallel magnetic field lines Baumjohann and Treumann (1996)

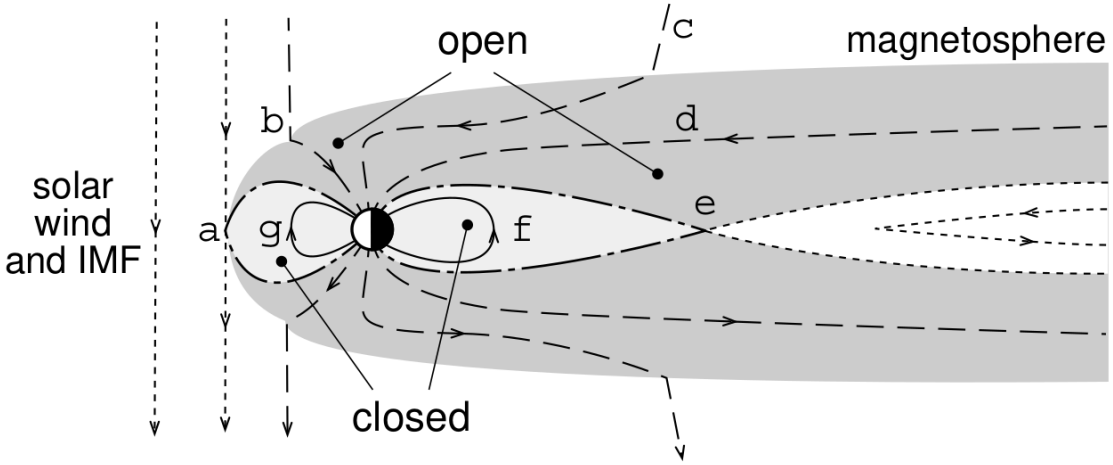

Figure 1.7: Diagram of the Dungey cycle at Earth showing reconnection between the IMF and Earth's magnetic field (a), unbending of the field lines (b), pressure dragging the field lines to the nightside (c) forming a magnetotail (d), reconnection in the magnetotail (e) compressing field lines connected to Earth (f) which convect back towards the dayside (g). From Milan et al. (2003).

reconnect (e), compressing the field lines connected to Earth (f). The closed field line convects back across the poles towards the dayside (g). Although the diagram is for the IMF with magnitude only in the B_z (GSM) direction, any combination of directions is possible. In GSM coordinates, if B_y is non-zero, or a non 90° angle is made between B_x and B_y, then the the location of the reconnection site would differ, and a tilted morphology between dawn and dusk would occur.

1.3.4 Magnetic Field Aligned Currents

During the Dungey cycle, in the high-latitude ionosphere, a "twin-cell" plasma convection pattern develops (Cowley & Lockwood, 1992; Dungey, 1961; Lockwood et al., 1990). Earths magnetic field line footprints are convected anti-sunwards across the centre of the polar cap. They then return to the dayside at a lower latitude through dawn and dusk.

At high altitudes, collisions between charged particles and atmospheric neutrals are rare, so the plasma can be approximated by $\mathbf{E} \times \mathbf{B}$ drift. At lower altitudes ions can collide with neutral atoms while electrons continue to drift. The collisions exchange energy and momentum, affecting the ions $\mathbf{E} \times \mathbf{B}$ drift. Equation 1.56 shows that any difference in the ion and electron flow velocities causes a current to flow. Hall currents flow antiparallel ($-\mathbf{E} \times \mathbf{B}$) to the plasma flow, while Pedersen currents flow in the direction of the electric field, $\mathbf{E}$. Shears in the plasma convection between the open and closed field lines result in currents flowing along the magnetic field lines to connect the Pedersen currents to the magnetosphere. These are known as Region 1 field aligned currents (FACs). At the equatorward edge of the return-flow convection, Region 2 FACs flow out of the ionosphere to connect the Pedersen currents to the partial ring current (Anderson & Vondrak, 1975; Milan et al., 2017). These currents flow along the magnetic field lines so that current continuity is conserved ($\nabla \cdot \mathbf{J} = 0$). Figure 1.8, shows the morphology of the current system alongside the associated twin-cell plasma convection.

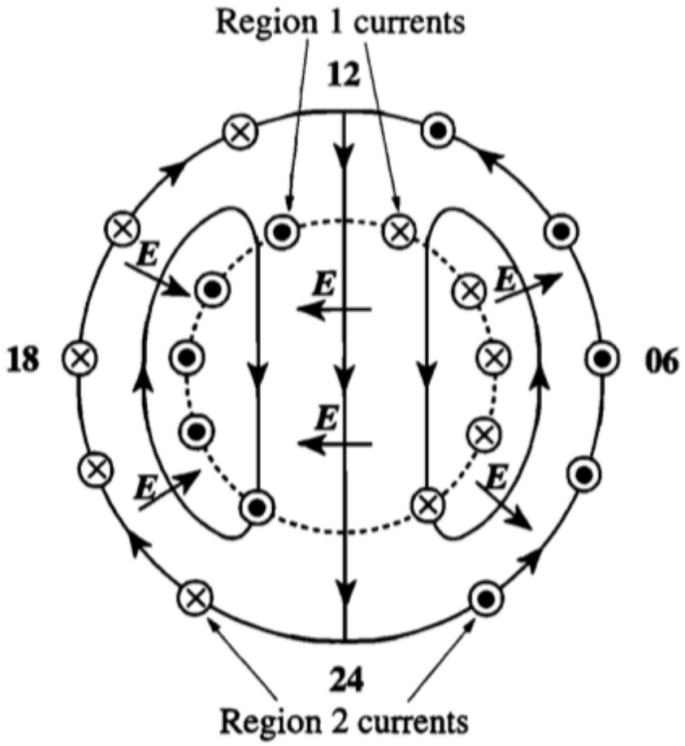

Figure 1.8: Schematic of the high-latitude twin-cell plasma convection pattern and associated currents. Plasma streamlines are shown by the solid lines. The dotted line is the open-closed field line boundary. Magnetic local times are labelled around the circumference of the pattern. From Cowley (2000).

1.3.5 Expansion of the twin-cell convection pattern

The high latitude twin cell convection pattern is driven by the coupling between the IMF and Earth's magnetic field through the Dungey cycle (section 1.3.3). The equatorward extent of this pattern is determined by the flux content of the open polar cap i.e. if dayside field lines are consistently being opened by reconnection with the IMF without being closed on the nightside, the pattern will expand to lower latitudes due to dragging of the field lines by the IMF. The twin-cell pattern is predominately observed at the high-latitudes, and particle precipitation between the open/closed field line boundary results in the production of the aurorae, which can be used as a visual indicator for the size of the twin-cell convection pattern. Under strong IMF

$-Bz$ conditions, the aurorae and twin-cell convection pattern can expand towards the mid-latitudes, bringing the convecting $\mathbf{E} \times \mathbf{B}$ drift plasma with it. Under quiet time conditions, the equatorward extent of the twin-cell pattern typically stays poleward of $> 70°$ geomagnetic latitude. Under geomagnetically intense periods, the pattern can expand to $< 40°$ (Thomas & Shepherd, 2018; Walach & Grocott, 2019; Walach et al., 2021). Thomas and Shepherd (2018) used ionospheric radar observations to derive climatological patterns of the twin cell convection pattern for varying geomagnetic activities.

Figure 1.9 shows the statistical equatorward extent of the twin cell convection pattern as derived by Thomas and Shepherd (2018), where the strongest geomagnetic activity results in the pattern expanding below 50° magnetic latitude. Thomas and Shepherd (2018) also note that the radars used to construct the model have a low latitude limit to their observations and that there may be more equatorward flows that cannot be observed. As such the generated statistical model may under-represent the true expansion of the pattern.

The equatorward expansion of the twin cell convection pattern is important to understand the mid-latitude ionospheric dynamics. At high-latitudes, plasma motion can nearly always be attributed to the twin-cell pattern due to its permanent presence (Grocott & Milan, 2014). At the mid-latitudes, plasma drivers vary and it is necessary to determine if observed plasma motion is due to the twin cell pattern, or drivers equatorward of it. Joshi et al. (2015) observed excited plasma of several hundred meters per second from the expanded twin-cell convection pattern at 50° geomagnetic latitude during the main phase of a geomagnetic storm. During the recovery period of the storm, after the twin cell pattern retracted polewards, they continued to observe plasma drifts due to the neutral wind "flywheel" effect (Deng et al., 1993; Lyons et al., 1985). This flywheel occurs when momentum exchanges from the convective ions drive the atmospheric neutrals into the same pattern. After the convective plasma driver dissappears, the role of the neutrals and plasma reverses, where the neutrals retain their momentum and continue to flow in the convective

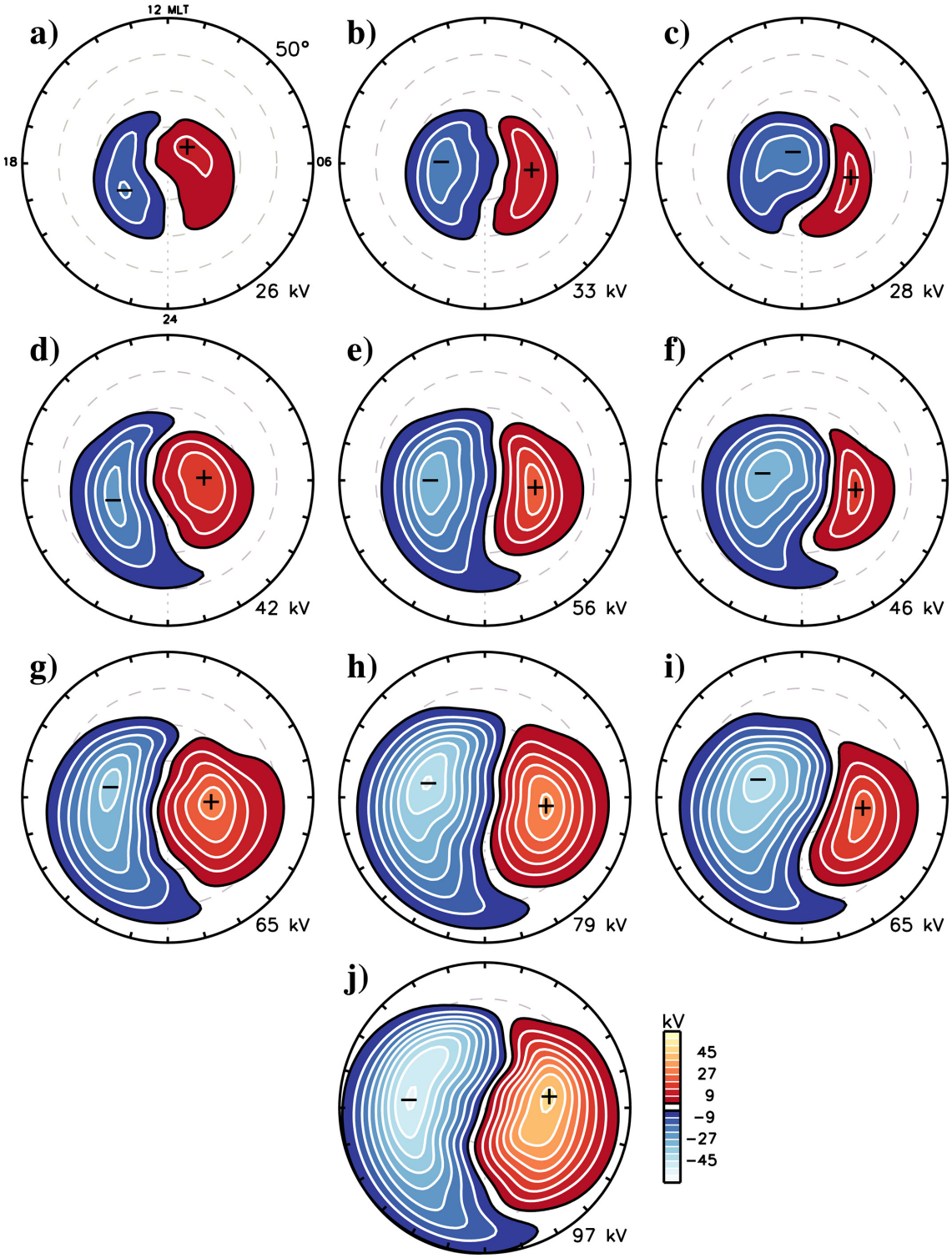

Figure 1.9: Statistical twin cell convection patterns for different goemagnetic activity levels. Dashed lines are every 10° geomagnetic latitude. The left columns are for IMF $B_y < 0$, centre columns IMF $B_y \approx 0$ and the right column IMF $B_y > 0$. The rows are for different levels of geomagnetic activity (a-c) $0 \leq Kp < 1$, (d-f) $2 \leq Kp < 3$ (g-i) $4 \leq Kp < 6$ and (j) $6 \leq Kp$. From Thomas and Shepherd (2018).

pattern exchanging momentum and driving the (remaining) plasma. The plasma continues to convect following the twin-cell pattern long after the field lines retreat polewards (Fuller-Rowell et al., 1997; Wang et al., 2008). Both Zou and Nishitani (2014) and Joshi et al. (2015) observed neutral wind motion driven by the expanded high latitude twin cell convection pattern to persist up to 20 hours after the recovery phase of a geomagnetic storm, resulting in neutral wind driving mid-latitude ion motion.

1.4 The Mid-Latitude Ionosphere

Earth's ionosphere lies between 75 and 1000km altitude. As discussed in the previous sections, Earth's ionosphere is a partially ionised plasma embedded within the neutral thermosphere. Ionospheric dynamics differ significantly between the high ($> 60°$), mid ($40-60°$), low ($40-20°$) and equatorial ($< 20°$) geomagnetic latitudes. The work in this text is focused on the mid-latitudes, as such, this section will discuss the formation of Earth's ionosphere and the dynamics that drive much of the phenomena observed at the mid-latitudes.

1.4.1 Formation and Structure

The main source of ionisation in the dayside ionosphere is the absorption of ultra-violet (UV) and extreme ultra-violet (EUV) radiation from the Sun. Particle precipitation sourced from the magnetosphere is another form of ionisation that mostly occurs at the high-latitudes, which also results in radiation in the visible wavelengths being emitted, producing the aurorae.

1.4.1.1 Solar UV ionisation

Solar EUV ionisation is a form of photoionisation. The two contributors to photoionisation rates are the solar radiation intensity, and neutral density, n_n. As radiation intensity and neutral densities in Earth's thermosphere are anti-correlated

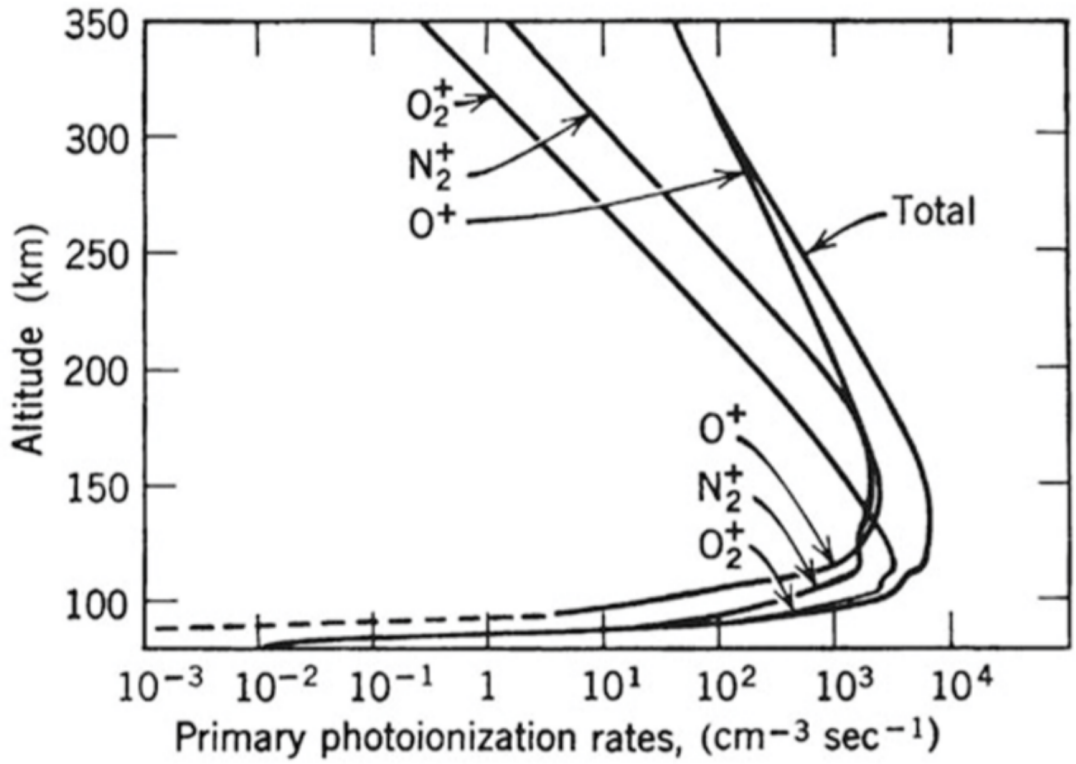

Figure 1.10: Photoionisation rates of different species in the ionosphere. From Hinteregger et al. (1965)

with altitude, there will be an altitude where the photoionisation rate peaks. Figure 1.10 shows an example vertical photoionisation profile for different atmospheric species. Total photoionisation peaks at around 130km. Above 200km O^+ is dominant, while below 130km O_2^+ dominates. The profile shown is for a generic case, factors such as light intensity, seasonal and diurnal variations, geographic locations all affect the photo-ionisation rates.

1.4.1.2 Particle precipitation ionisation

Although lesser at mid-latitudes, particle precipitation still plays an important role in ionising the ionosphere. Particle precipitation is a feature of charged particles gyrating along a magnetic field line and colliding with neutral atoms. If the energy of the charged particle is great enough, then it can knock off electrons, ionising the

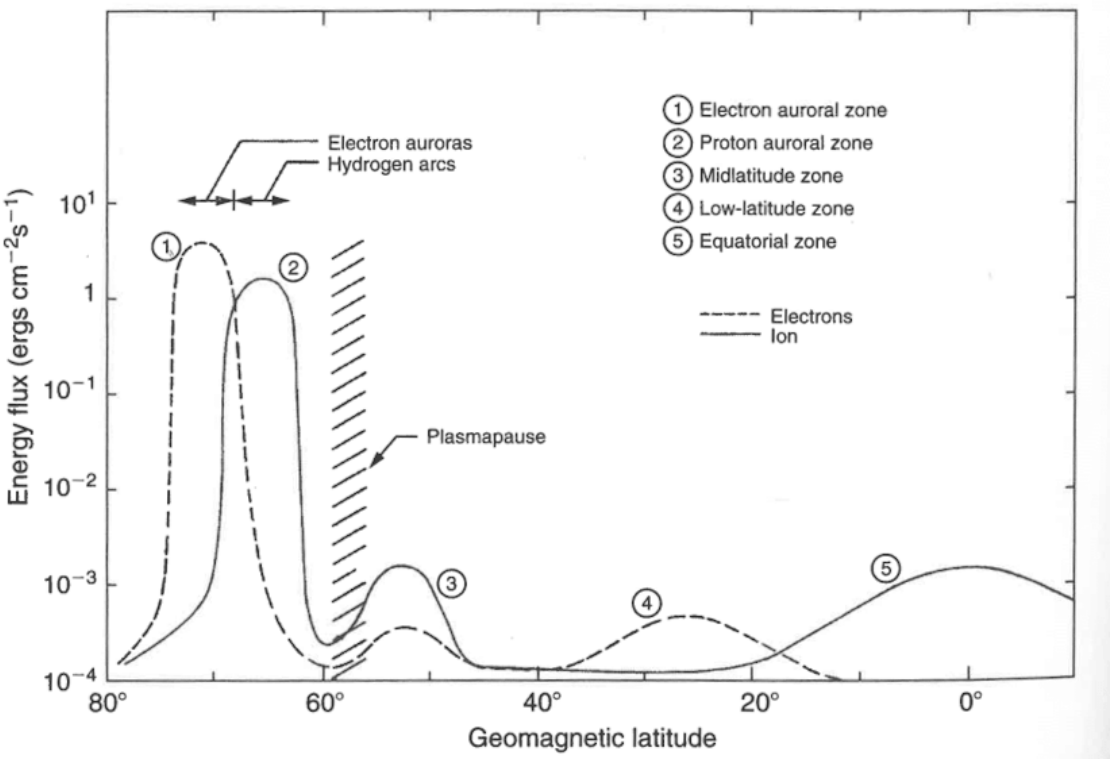

Figure 1.11: Particle precipitation as a function of geomagnetic latitude. From Kelley (2009)

neutral. The energetic ions lose energy as they collide, therefore more energised particles reach lower altitudes. Night time photoionisation sources such as from the cosmic rays and Lyman-α scatter (from the geocorona) generally ionize below 105km altitude (Kelley, 2009; Voss & Smith, 1979, 1980), therefore particle precipitation is primarily responsible for nighttime ion production above this altitude. In the auroral zones and between 20° and 30° geomagnetic latitude electrons dominate particle precipitation. At equatorial, mid and sub-auroral latitudes, positive ions dominate precipitation ionisation (Kelley, 2009).

Figure 1.11 shows particle precipitation as a function of latitude. Although precipitation is lower than in the auroral zone, neutral atmospheric waves gather the ions in the mid-latitudes, producing observable plasma features.

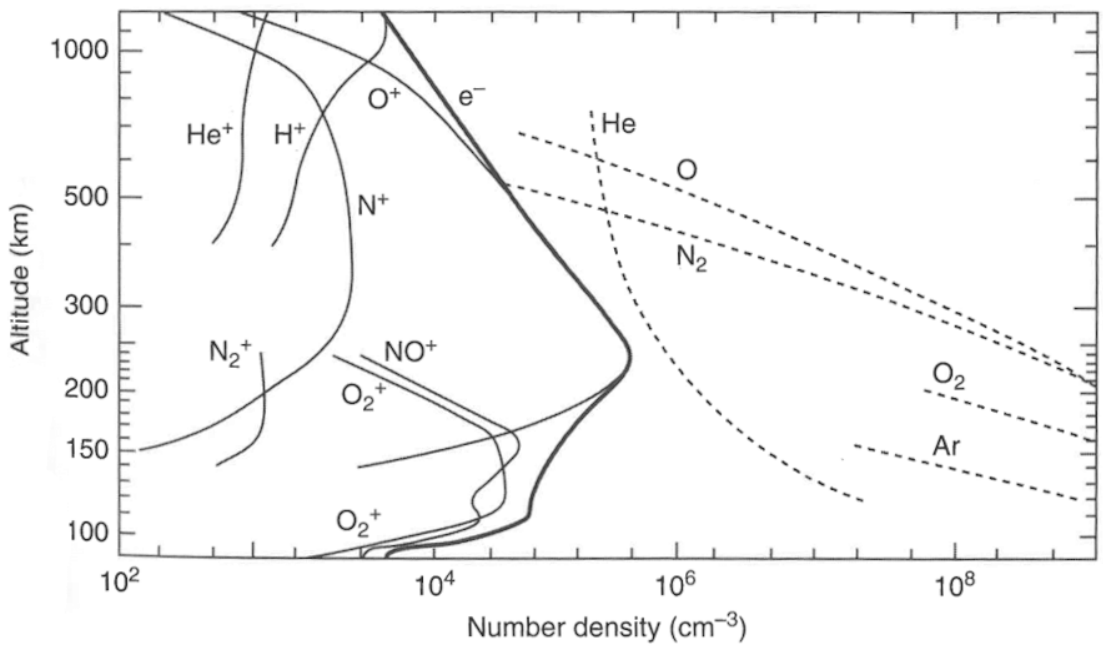

Figure 1.12: International quiet solar year daytime ionospheric and thermospheric composition based on mass spectroscopy measurements. From Russell et al. (2016)

1.4.2 Recombination and Layers

Newly ionised particles may react with free electrons in a process call recombination, where collisional interactions between ions and electrons can turn ions into neutrals. Local rates of ion production and loss vary substantially due to differences in universal time (UT), season and geographic location, therefore "layers" of the ionosphere are produced.

An example of the dayside structure of Earth's ionosphere during an international quiet solar year is given in figure 1.12. Figure 1.12 shows how the neutral density dominates the ion density. The electron density peaks at 250 km, however there is considerable substructure, with varying electron and ion densities across the full altitude range of the ionosphere. Due to this substructure, different layers are designated to the ionosphere. The D region is located below 90 km and appears only in the dayside due to the most energetic ionisation sources, such as 0.1-1 nm

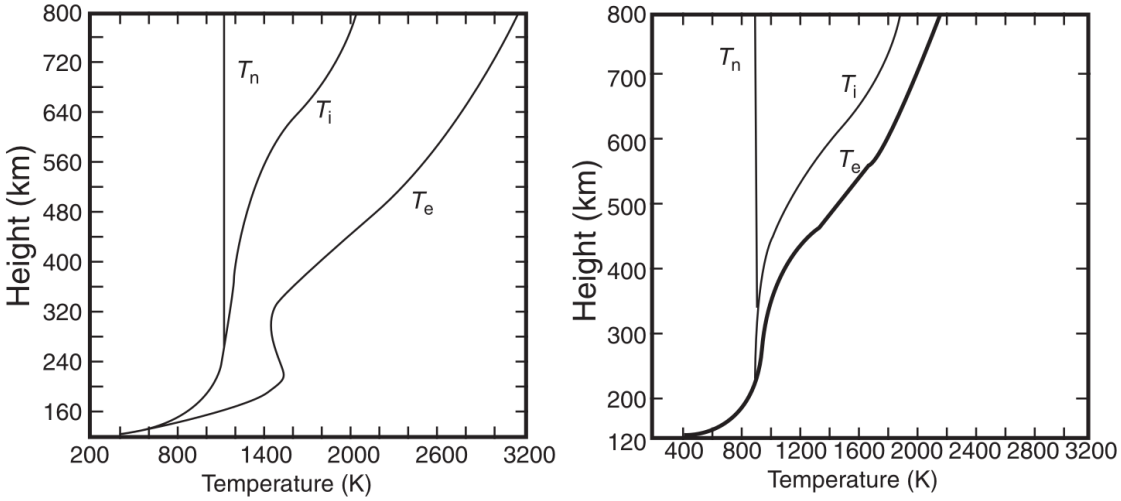

Figure 1.13: Electron, ion and neutral temperature profiles for the ionosphere over mid-latitude North America. The left panel is at 1422 local time and the right for 0222 local time. From Schunk and Nagy (2009).

wavelength solar X-rays. The E region is located between 90-130 km and is primarily produced by UV radiation in the 100-150 nm range and solar X-rays in the 1-10 nm range. The F layer is located above 130 km, however is often split into two separate regions, the F1 layer and F2 layer as sometimes a second ledge appears below the main (F2) peak at 250 km altitude. The F layer occurs due to ion production from photons in the 17-91 nm range, with the F1 layer peaking at around 170km altitude. The F2 layer is highly affected by vertical atmospheric drifts and dynamo electric fields (see section 1.4.3.1), such that the chemistry that occurs is highly complex.

Figure 1.13 indicates the height profile of ion and electron temperatures in Earth's ionosphere. The velocities of the particles can be calculated through the relation,

$$\mathbf{v} = \sqrt{\frac{2\kappa_B T}{m}} \tag{1.75}$$

where $\mathbf{v}$ is the velocity of the particle, κ_B is Boltzmann's constant, T is the temperature and m is the mass. Substituting this into equation 1.13 we can

rearrange for the gyroradius:

$$r_g = \frac{\sqrt{2m\kappa_B T}}{qB} \tag{1.76}$$

At an altitude of 120 km the magnetic field strength is approximately 30,000 nT, while at 800km the field strength is approximately 20,000 nT. Depending on the mass and temperature of the ions and electrons, their gyroradii can typically vary from a few cm to several m, over such scales the strength of Earth's magnetic field varies by orders of nT. As the gyroradii is significantly larger than the magnetic field gradient the effects of the magnetic gradient drift are minimised and can be ignored within Earth's ionosphere.

1.4.3 Sub-Auroral Magnetospheric Drivers

The mid-latitudes are a complicated region. Unlike at the high-latitudes where a single mechanism is dominant, there are often complex interchanges and mechanisms at the mid-latitudes that drive plasma motion which feed into one another so that at any one time, a combination of drivers are responsible for many of the flows that take place equatorward of the twin-cell convection pattern. This section will explore some of the major drivers that contribute to plasma motion at the mid latitudes.

1.4.3.1 Electric Field Dynamo

Pressure inequalities due to solar EUV radiation drives neutral winds in the the F region. Similarly to the flywheel effect, the neutral winds collide with the plasma, exchanging momentum and generating an electric field. The conductivity of the field lines ($\sigma_{\parallel}$) in the E and F regions are larger than the transverse conductivities (σ_P, σ_H), therefore the electric fields generated by this dynamo motion are vertically propogated upwards/downards by the magnetic field (Hargreaves, 1992; Rishbeth, 1971). If the conductivities of the E and F layers are approximately equal, then currents can flow between the layers and the E layer short circuits the currents generated by this dynamo. If, however the E layer conductivity is much lower, the

current cannot pass from the F layer and a polarisation field builds up. According to Rishbeth (1971), the E layer conductivity is sufficient to short circuit the F layer if,

$$\frac{n_F H_F}{n_E H_E} \leq \frac{1}{2}\frac{\Omega_i}{\kappa_{in}} \simeq 150 \tag{1.77}$$

where H is the scale height, n_E and n_F the ion densities in the E and F regions respectively, and Ω_i and κ_{in} the ion gyrofrequency and ion-neutral collision frequency. The electron collision frequency/gyrofrequency ratio is much less than for the ions so the electrons do not move across the magnetic field. Typically the E layer decreases in the nighttime, such that a polarisation field is produced in the F region that drives the F region plasma. The effect can also occur in reverse, where tidal winds originating from the lower atmosphere drives plasma and creates an electric field in the E region. Both sources contribute to setting up a distribution of polarisation fields so that the current is non-divergent globally.

1.4.3.2 Penetrating Electric fields

The Region 1 FACs react to changes in the solar-wind-magnetosphere inputs almost instantaneously, while the R2 FACs take time for charges to gradually respond. As such imbalances are often introduced between the two FAC systems. Under a steady state, the R2 FACs minimise the electric field at low latitudes, producing a "shielding" electric field. Undershielding, or overshielding occurs when the convective electric field is larger or smaller than the shielding electric field respectively. Undershielding occurs if the IMF B_z component undergoes a rapid shift southwards. The R1 FACs suddenly increase while the R2 currents has to spend time for the gradual charge accumulation to balance the enhanced R1 FAC. The dawn-dusk electric field has time to penetrate to low latitudes before the R2 FAC is able to modulate it. Overshielding occurs upon sudden northward turning of the IMF B_z, where the R2 FACs are much greater than the R1 FACs (Kelley et al., 1979).

Penetrating electric fields from undershielding can drive sub-auroral ion flows

during storm times (Blanc et al., 1977; Buonsanto et al., 1992), but at quiet times a combination of high-latitude penetrating electric fields and neutral wind dynamos drive sub-auroral flows, with the conductivity modulating the dominance of either mechanism, although predominantly stronger forcing from penetration occurs in the pre-midnight sector (Carpenter & Kirchhoff, 1975; Maimaiti et al., 2018, 2019; Wand & Evans, 1981) while post-midnight flows are primarily attributed to the neutral wind dynamo (Lejosne & Mozer, 2016; Maimaiti et al., 2019). The flows can be substantial relative to mid-latitude plasma velocities, Maimaiti et al. (2018) reported statistical ion flows of $20 - 50\text{ms}^{-1}$ during quiet times, while under more intense geomagnetic periods, the flows can reach up to 90ms^{-1} (Maimaiti et al., 2019)

1.4.4 The Mid-Latitude Trough

A depletion of plasma occurs in the nightime F region just equatorward of the auroral equatorward boundary known as the mid-latitude ionospheric trough (MIT). The MIT is produced by a stagnation between the westward drift of the high latitude convection and the eastward plasma drift from corotation at lower latitudes (Knudsen, 1974; Spiro et al., 1978). Large scale gradients in the electron density occurs across the trough, with a poleward and equatorward wall of relatively higher plasma densities either side of the lower density trough minimum.

The trough typically occurs between 50° to 70° geomagnetic latitude and its precise location depends on geomagnetic activity (Werner & Prelss, 1997), magnetic local time, longitude (He et al., 2011) and solar activity (Ishida et al., 2014). The trough forms in the nightside close to midnight (MLT) and extends past the terminator to the high-latitude dusk region. Pressure gradients (Eq 1.26) form at the walls of the trough. The pressure forces and magnetic forces in a system must balance:

$$\mathbf{J} \times \mathbf{B} = \nabla \mathbf{P} = \nabla(\mathbf{P_i} + \mathbf{P_e}) \tag{1.78}$$

where $\mathbf{P_i}$ and $\mathbf{P_e}$ are pressure forces due to ion and electron motion respectively.

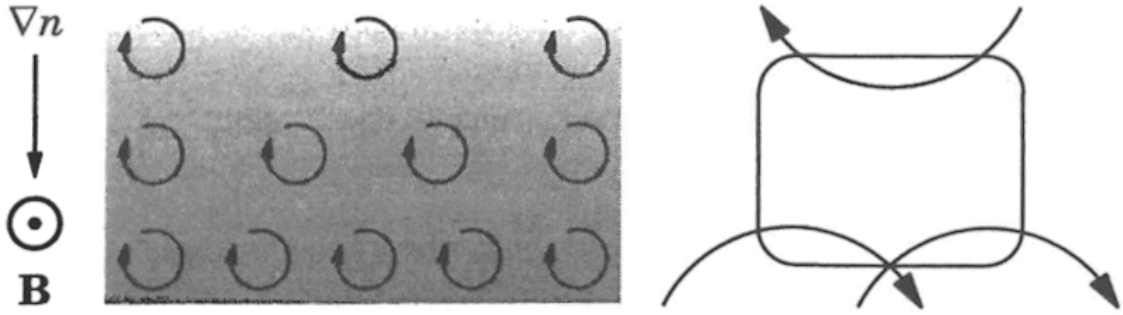

Figure 1.14: Origin of the diamagnetic drift. Density gradients result in non-equal bulk velocity motions. From Baumjohann and Treumann (1996)

Applying the cross product of Ohm's general law (Eq.1.71) with **B**, and assuming that variations in **J** are small, we can substitute in the above and rearrange for **v**:

$$\mathbf{v}_\perp = \frac{R\mathbf{J}}{B^2} - \frac{\mathbf{E}\times\mathbf{B}}{B^2} - \frac{\nabla\mathbf{P_i}\times\mathbf{B}}{nqB^2} \tag{1.79}$$

We can clearly see the $\mathbf{E}\times\mathbf{B}$ drift. We also have a term that affects the transverse velocity of a particle according to pressure. In a velocity field with constant pressure, the number density of gyrating particles in a homogenous plasma is constant, between any two points the number of particles gyrating are equal, the average fluid velocity is then zero. If there is a density gradient, then there are regions where there are more particles gyrating than in the less dense regions. The fluid velocity is then not balanced across the field. This known as the diamagnetic drift, which is given by the third term in the above equation,

$$\mathbf{v_{dia}} = \frac{\nabla\mathbf{P_i}\times\mathbf{B}}{nqB^2} \tag{1.80}$$

and is illustrated in figure 1.14 The pressure gradient caused by the mid-latitude trough induces a diamagnetic drift in plasma species. Because the drift is affected by the charge of the particles, oppositely charged particles drift in opposite directions, creating a polarised electric field that induces an "$\mathbf{E}\times\mathbf{B}$" drift, leading to further perturbations in the density gradient at the boundary, inducing a feedback mechanism that drives plasma motion (Greenwald et al., 2006; Hudson & Kelley,

1976). Hudson and Kelley (1976) predicted the presence of plasma drifts at the walls of the mid-latitude trough and Greenwald et al. (2006) observed persistent nighttime mid-latitude plasma drifts of up to 50ms^{-1} that they associated with pressure gradient forces due to being at the equatorward wall of the trough. Clausen et al. (2012) also observed plasma drifts of up to 100ms^{-1} associated with pressure gradients at the equatorward wall of the trough, while Liu et al. (2021) observed pressure gradient drifts at both the equatorward and poleward wall of the trough.

1.4.5 Sub Auroral Polarisation Streams

A prominent feature in the mid-latitude F region ionosphere are sub auroral polarisation streams (SAPS) (Foster & Vo, 2002), which are latitudinally narrow channels ($< 5°$) of enhanced westward flows, located just equatorward of the lower auroral electron precipitation boundary at the nightside region. Although separate to the high-latitude twin cell convection pattern, they are similarly dependent on geomagnetic activity (Huang & Foster, 2007), however recent studies have shown that SAPS can still occur at minor levels of geomagnetic activity (Kunduri et al., 2017, 2018). SAPS are formed when the equatorward edge of the ion precipitation boundary moves equatorward of the electron precipitation boundary (Gussenhoven et al., 1987; Heinemann et al., 1989). The misalignment produces a poleward directed electric field which induces a westwards directed $\mathbf{E} \times \mathbf{B}$ drift. Furthermore Anderson et al. (1993) suggested that the misalignment between the precipitation boundaries causes a portion of the Region 2 FACs to flow towards equatorward regions of low conductivity (such as the MIT) which hinders current closure, resulting in further poleward directed electric fields to form. Under weak conditions SAPS move in a stream of a few hundred ms^{-1} (Billett et al., 2022; Kunduri et al., 2018) while under strong conditions velocities can be over 1000ms^{-1} (Clausen et al., 2012; Huang & Foster, 2007). SAPS affect the chemistry of the mid-latitude ionosphere, the fast plasma increases the ion recombination rates in the stream of the flow, which decreases the conductivity of the region, allowing the electric field to

grow, which in turn decreases the conductivity further, producing a feedback effect that enhances the flow stream.

The suggestion by Anderson et al. (1993) that SAPS electric fields form in regions of low conductivity suggests that there may be a correlation between SAPS location and the MIT. Kunduri et al. (2021) observed SAPS to form just equatorward of the Region 2 FACs and inside the MIT during the recovery period of a minor geomagnetic storm, however after the FACs retreated poleward, the locations of the MIT and SAPS remained firmly embedded within another, likely due to the recombination-conductivity feedback mechanism, which sustained the SAPS flow long after the magnetospheric driver subsided.

The entire mid latitude system is highly interconnected. The equatorward boundary of the twin cell convection pattern affects the location of the MIT. In turn the MIT affects both the location of pressure gradient driven plasma and SAPS. SAPS embedd themselves within the trough due to its low conductivity, and through recombination-conductivity feedback, maintain's the MIT. Clausen et al. (2012) observed all these interconnected affects alongside patterns relating to the high latitude twin cell convection pattern simultaneously using a pair of coherent scatter radars, as shown by figure 1.15, which labels different types of ionospheric scatter. Meteor trails that drift with neutral wind velocities in the D-region are labelled as type I scatter in figure 1.15. Type II Scatter with line of sight velocities of approximately -100ms^{-1} is identified as forming from pressure gradient drifts at the equatorward boundary of the MIT. The type III scatter is approximately 3° in latitude wide with line of sight velocities over 1000ms^{-1} due to a strong SAPS flow. The type IV scatter with line of sight velocities $> 100\text{ms}^{-1}$ is directed towards the radar and is likely part of the anti-sunward component of the high-latitude twin cell convection pattern.

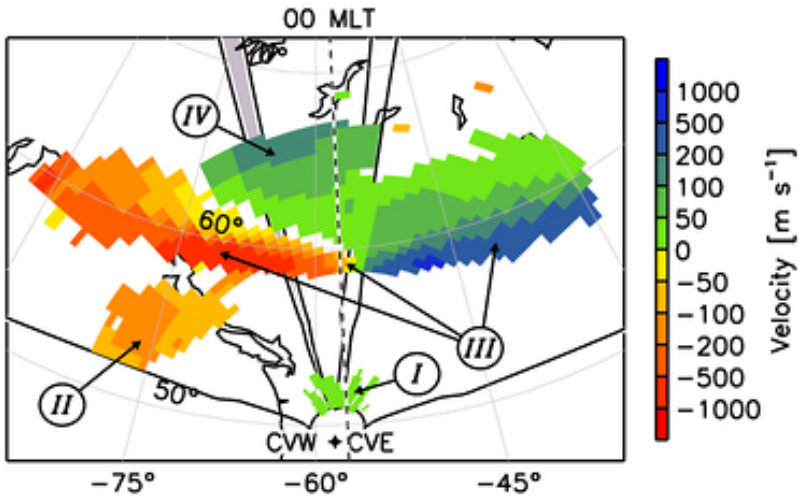

Figure 1.15: Mid-latitude night-time line of sight ion scatter observed by two coherent scatter radars. Positive values indicate motion towards each radar. Labelled are scatter from D region meteor trails (I), pressure gradient forces (II), SAPS (III) and high latitude twin cell convection (IV). From Clausen et al. (2012)

1.5 Joule Heating

Joule heating, otherwise known as resistive, Ohmic, or frictional heating is the energy that is dissipated when current driven particles collide with a conductive medium. Upon collisions, charged particles exchange momentum with a neutral, which becomes randomly scattered and converts kinetic energy into thermal energy. In Earth's ionosphere, driven plasma collides with neutrals in the thermosphere which acts as the conductor. The simplest way to formulate Joule heating is through the relationship

$$P = I\Delta V \tag{1.81}$$

where I is the electric current, ΔV is some potential difference and P is the power dissipated. The differential form of equation (1.81) takes the form:

$$Q = \frac{dP}{dV} = \mathbf{j} \cdot \mathbf{E} \tag{1.82}$$

Where Q is the Joule heating rate and dV is unit volume. This expression includes both the Joule heating and the amount of work done by $\mathbf{j} \times \mathbf{B}$ forces on the

thermosphere. In the ionosphere the Hall current (perpendicular to **E**) does not dissipate and the electric field aligned with the magnetic field is small (Lu et al., 1995) so we can approximate **j** with the component that is perpendicular to the **B**, $\mathbf{j}_\perp$, which is parallel to **E** and in the direction of the Pedersen current. In the reference frame of the neutral atmosphere that corotates with Earth, the total ionospheric electric field is the sum of ionospheric drivers ($\mathbf{E_v}$) and the neutral wind dynamo electric field ($\mathbf{u} \times \mathbf{B}$), therefore using equation (1.59), equation (1.82) becomes,

$$Q = (\sigma_p \cdot \mathbf{E}) \cdot \mathbf{E} = \sigma_p(\mathbf{E_c} + \mathbf{u} \times \mathbf{B})^2 \tag{1.83}$$

where $\mathbf{E} = \mathbf{E_c} + \mathbf{u} \times \mathbf{B}$, **B** is the terrestrial magnetic field and σ_p the Pedersen conductivity. The expanded form of the above equation is quite handy for describing each process that contributes to the total Joule heating rate,

$$Q = \underbrace{\sigma_p \mathbf{E_c}^2}_{Q_c} + \underbrace{2\sigma_p \mathbf{E_c} \cdot (\mathbf{u} \times \mathbf{B})}_{Q_{w1}} + \underbrace{\sigma_p(\mathbf{u} \times \mathbf{B})^2}_{Q_{w2}} \tag{1.84}$$

The term Q_c is the ion heating and is the amount of Joule heating generated by plasma motion via friction against a stationary neutral background. Under geomagnetically active periods, **E** is generally stronger, or when solar EUV irradiance is increased, σ_p is higher and so Q_c is enhanced. The two remaining terms Q_{w1} and Q_{w2} are modifications made to Q_c to account for a non-stationary neutral wind. Q_{w1} accounts for the difference between the plasma and neutral velocities, such that it is negative if they flow in the same direction and positive if they oppose. Q_{w1} effectively acts as a measure of the momentum exchanged between the two when they collide. Q_{w2} is essentially the opposite of Q_c and is the amount of Joule heating generated by neutral motion against a stationary neutral background. It can be seen then that the complex interactions between plasma and neutrals in the thermosphere/ionosphere system are significant factors in the amount of Joule heating deposited in the ionosphere.

Joule heating has been extensively studied at the high-latitudes. In the magnetosphere-ionosphere system Joule heating is the dominant energy input source

(Knipp et al., 2004; Lu et al., 1996, 1998, 2016) and during geomagnetic storms, Joule heating is responsible for up to 70% of the total ionospheric power input (Knipp et al., 2004). In the high-latitudes neutral wind motion is typically small compared to plasma convection. High-latitude Joule heating calculations have often discounted the effects of the neutrals, simply only calculating the ion heating term, Q_c (Baloukidis et al., 2023). However during non-storm times and at lower latitudes, the velocities of the neutrals relative to the ions can be significant, where it should be obvious through equation (1.84) that they can have a strong effect on the overall Joule heating. Using model simulations, Lu et al. (1995) calculated the neutrals to have decrease the high-latitude Joule heating by approximately 28% while Kiene et al. (2019) observed the motion of neutrals to reduce the total high-latitude Joule heating by a factor of 3.

Due to being a form of frictional heating, Joule heating calculations must ensure that parameters used from equation (1.84) are colocated, otherwise a misrepresentation of the heating will occur. Billett et al. (2022) observed significantly different neutral responses to a SAPS event from two locations, one immediately at the equatorward boundary of the SAPS and driven by the SAPS channel itself, while a second location reacted due to pressure gradient forces approximately 2 hours after responses were found at the first location. Kiene et al. (2019) used two high-latitude instruments to observe neutral and plasma motion and estimated the Joule heating occurring in the high-latitude auroral regions. Using high-resolution velocity estimations (Bristow et al., 2016), they found that Joule heating rates varied as much as a factor of 10 due to local variations in the observed ion-neutral structure. Figure 1.16 shows some of the maps produced in that study, displaying the local variations in the Joule heating rate.

Most studies that investigate Joule heating do so over large-scales using a combination of globally averaged/fitted datasets and models of the necessary parameters (Baloukidis et al., 2023; Billett et al., 2018; Lu et al., 1995, 2016). Studies using globally averaged data are useful for determining the average global

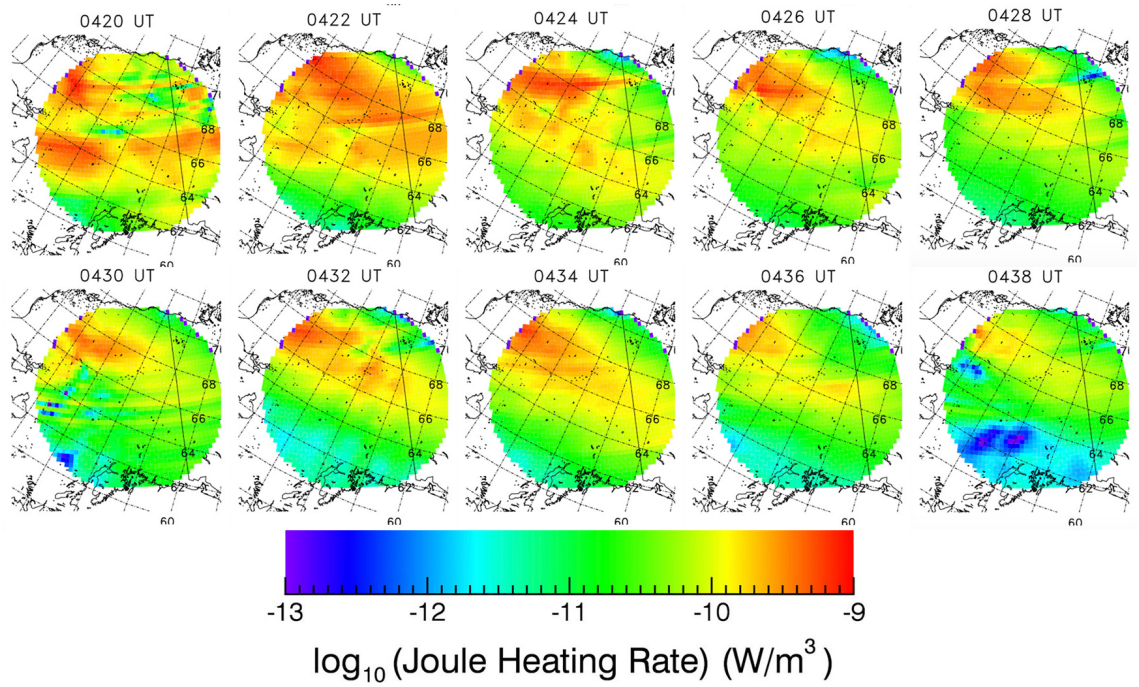

Figure 1.16: Maps of high latitude Joule heating magnitudes at 250km altitude estimated using ground based instrument observations. Adapted from Kiene et al. (2019)

Joule heating patterns and can be used to validate the large-scale performance of upper atmospheric models, which are all useful tools for predicting and/or analysing the impact of space weather on Earth's upper atmosphere. However, there are considerations such as ion-neutral collisional drag time-lags that can occur when using separate models for individual parameters and small scale dynamics that may not be captured by such global scale models. Any datasets that use large-scale averaging and fitting techniques to derive global Joule heating patterns are vulnerable to removing high/low magnitude features, resulting in an overly smoothed Joule heating representation. Studies that use observations to estimate local Joule heating rates can provide a better representation of the small-scale Joule heating and are useful for gaining a perspective into the small-scale performance of upper atmospheric models. However, these studies are often limited in their geographic locations due to requiring co-located observation. For example, Baloukidis et al.

(2023) was not able to account for the neutral wind in their Joule heating calculations due to no co-located neutral wind measurement availability. Both Anderson et al. (2013) and Kiene et al. (2019) were able to account for the neutral wind in their studies, however they used the same pair of instruments to estimate the high-latitude Joule heating, so no information was obtained in the geographic variability of Joule heating. Expansion of observation networks towards the mid-latitudes in the last decade opens up the possibility to extend the geographic range of Joule heating research, not just globally but also locally. This body of work is, for the first time, focused on investigating the local Joule heating rates in the mid-latitude ionosphere and includes the following chapters:

2 : Details the instrumentation, models and datasets used in the proceeding works.

3 : Identifies a quiet time mid-latitude event that displays remarkable levels of plasma and neutral activity, investigates the drivers behind them and compares them to modelled plasma and neutral velocities from a global upper atmospheric model.

4 : Uses the same event as investigated in chapter 3 and analyses appropriate methods for parametrising the plasma and neutral motion observations to estimate the local Joule heating rates. Comparisons are made between the observed Joule heating estimates and that modelled by the atmospheric model.

5 : Instigated from findings in chapter 4, we perform a statistical analysis on observations of mid-latitude plasma velocity distributions and compare them to statistical patterns from the atmospheric model. We show how the estimated Joule heating patterns are sensitive to differences between the observed and modelled statistical plasma distributions.

Chapter 2

Data & Instrumentation

The following chapter discusses the instrumentation used within this thesis and their general operation. Descriptions of any models used will also be discussed.

2.1 SuperDARN

The Super Dual Auroral Radar Network (SuperDARN) (Chisham et al., 2007; Greenwald et al., 1995; Nishitani et al., 2019) is a series of high frequency (HF) radars in the northern and southern hemispheres that observe ionospheric dynamics across both high and mid-latitudes in the E and F regions of the ionosphere, achieving near total high-latitude hemispheric coverage. Figure 2.1 shows the fields of view's (FOV) of each radar as of 2019.

2.1.1 Coherant Scatter

All SuperDARN radars work on the principles of coherent scatter, which is essentially a form of Bragg scatter. A high frequency beam (HF) is projected into the ionosphere from the radar, which scatters against magnetic field aligned plasma irregularities. Under certain conditions, the "backscatter" can return and be received by the radar. For a wave with wavelength λ, scattering on an incident volume at an angle θ, Bragg's condition states that constructive interference occurs

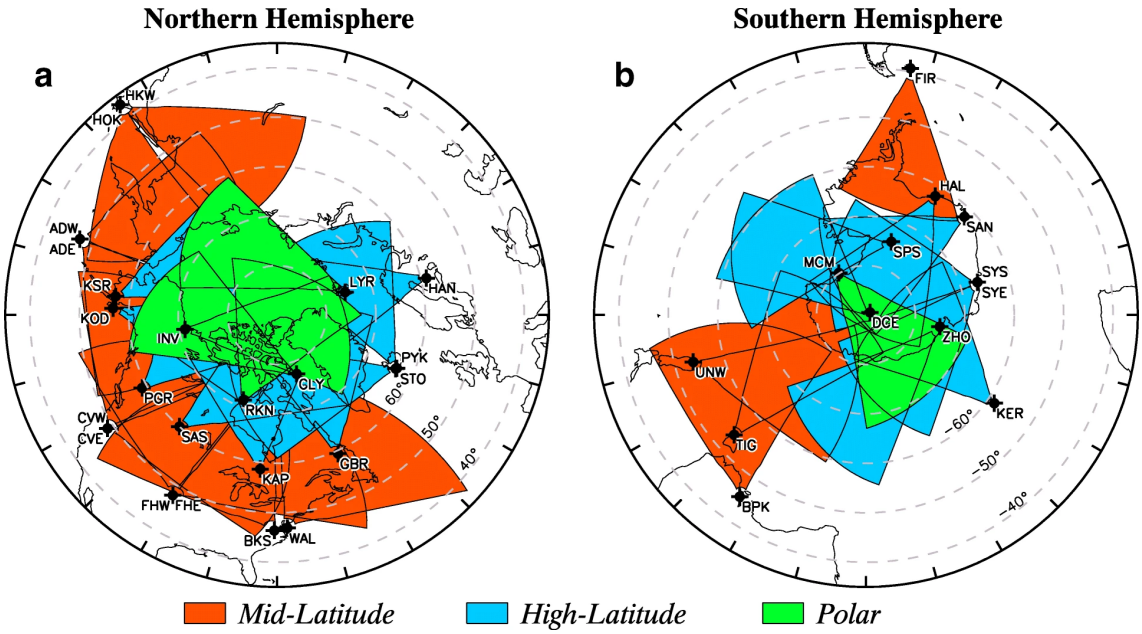

Figure 2.1: Fields of view of the SuperDARN network in 2019. The base of each field of view lists the three letter site code of the radar. From Nishitani et al. (2019).

when,

$$2d \sin\theta = n\lambda \tag{2.1}$$

where d is the interplanar distance and n is the number of planes separating the waves. For a wave to return to the same location as transmitted, the ionospheric irregularity and the wave must be orthogonal, $\theta = 90°$. If d is the irregularity width ($n = 1$) then,

$$2d = \lambda \tag{2.2}$$

indicating that the wavelength of the transmitted wave must be twice the irregularity width in order to receive strong backscatter such that the scattered wave can be received. Parameters can be obtained from the received signal such as the line of sight (LOS) Doppler velocity of the plasma, backscattered power and spectral width of the signal. Varied frequencies allow the observation of varying irregularity sizes.

Achieving orthogonality from a ground-based radar against magnetic field aligned plasma is difficult due to the inclination of the magnetic field. At high-latitudes the field is quasi-vertical, while at the mid-latitudes the field is inclined off

of the vertical ($\sim 20°$ at $50°$ geomagnetic latitude.) In order to achieve orthogonality, a SuperDARN radar sends out multiple beams at various elevation angles which are gradually refracted by the ionosphere. The amount of refraction is determined by the transmitted frequency (f) and electron density of the ionosphere (n_e) and is described by the Appleton-Hartree equation for the ionospheric refractive index (μ). The entire Appleton-Hartree equation is complex, however because Earth's magnetic field strength is several orders of magnitude smaller than electron densities we can refer to the simplified form of the Appleton-Hartree equation in the absence of a magnetic field (Barclay et al., 2003):

$$\mu^2 = 1 - \left(\frac{2\pi e \sqrt{\frac{n_e}{m_e \epsilon_0}}}{f^2} \right) \tag{2.3}$$

The SuperDARN radars typically operate in a frequency range of 8-20 MHz, where the precise frequency is altered according to its site location and variations in ionospheric composition (such as during day/night) in order to allow the transmitted waves to achieve orthogonality with the magnetic field. Due to refraction the elevation angle has a significant impact on the availability of returned backscatter. Too steep of an elevation angle can cause the transmitted wave to penetrate through the entire ionosphere, while too low an elevation angle can cause the wave to lose too much power before scattering off the ionosphere. An example of the transmitted paths with elevation angle is given in Figure 2.2, which ray traces a beam from the Blackstone (BKS) SuperDARN radar, which is used later in Chapters 3 and 4. The thick brown line located 759 km away from the radar is the approximate location where ionospheric data in Chapters 3 and 4 returns from, generally at altitudes of 100 - 150 km but occasionally up to 200 km. Ideally, rays scatter off of the ionosphere before a range of around 750km, although this can change depending on the state of the ionosphere. Rays that immediately scatter off the ionosphere are known as "$\frac{1}{2}$-hop" scatter. Rays that do not scatter instead continue and are refracted back towards the ground (effectively reflecting off the ionosphere), known as 1-hop scatter. Rays that reach the ground can either reflect back towards the

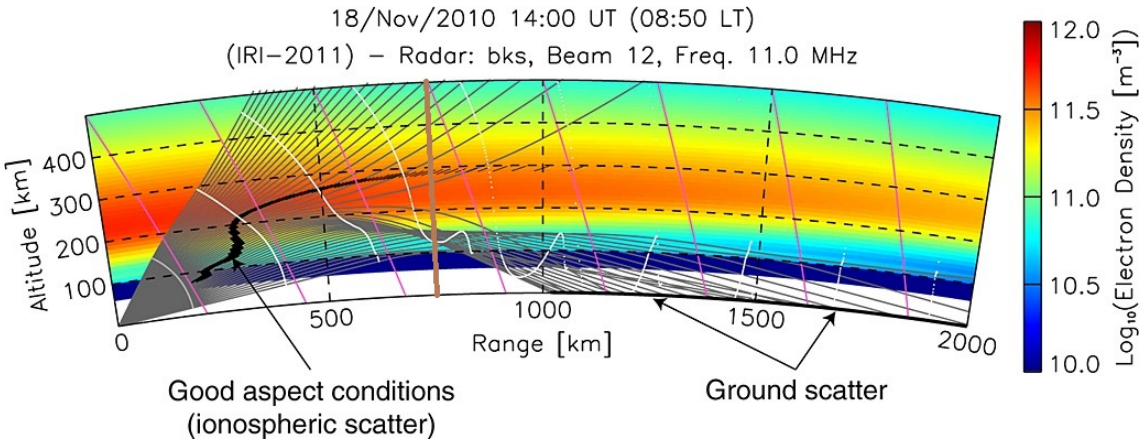

Figure 2.2: Ray tracing of beam 12 of the Blackstone SuperDARN radar at 11MHz. The black lines indicate regions where the rays are within 1° of orthogonality to the magnetic field (pink lines). The thick brown line indicates the approximate location where backscatter is located in chapters 3 and 4, 759 km away from the radar. Adapted From Larquier et al. (2013).

receiver, known as groundscatter, or they can reflect back up to the ionosphere and so on... Ionospheric scatter is generally referred to as "n$\frac{1}{2}$-hop" scatter and groundscatter as "n-hop scatter", where n is a positive integer.

2.1.2 Radar Operation

For the period of study discussed in this theses, each radar in the SuperDARN network typically operates between 16-24 electronically steerable longitudinally spaced beams, each approximately 3° wide, resulting in a fan $\sim$ 50° wide that extends up to 75 range gates (from 200 to 3000km (Chisham et al., 2007)). Each radar site is typically equipped with a main array of 16 transmit and receive antennas alongside a secondary interferometer array of 4 receive only antennas. The phase difference of the backscattered signal between the main and interferometer arrays determines the angle of arrival of the backscattered signal, which is then used to determine the range and altitude of the reflected signal. A virtual height model (Chisham et al., 2008) is alternatively used if no interferometry data is available. The duration of the

radar pulse determines the range resolution of the radar measurements which, for a standard 300 us pulse, is 45km in length. Each beam has a typical integration period of 7 seconds, resulting in a full scan across the FOV of the radar of approximately 2 minutes (Ruohoniemi & Baker, 1998).

Signals are transmitted as a multi-pulse sequence with uneven time spacing so that several "lags" are formed between pairs of pulses. An autocorrelation function (ACF) is then fitted to the pulses producing a real (R) and imaginary (I, 90° out of phase) waveform. To determine the Doppler velocity, backscattered power and spectral width of the signal, a fit is performed to the ACF data where the product is known as FITACF. Doppler velocity is calculated as a linear fit to the ACF phase angle ($\arctan(I/R)$). The spectral width and backscattered power are estimated by a Lorentzian fit to the ACF amplitudes which effectively models the de-correlation of amplitude with increasing lag.

2.1.3 Post-processing for mid-latitude studies

2.1.3.1 Median Filtering

The FITACF data often contains high amounts of "salt and pepper" noise, which appears as speckles of extreme velocities (often $> 1000\text{ms}^{-1}$) that can contaminate LOS observations. This noise is typically unphysical i.e. due to instrumentation/sampling errors and so techniques are used to remove it from the FITACF dataset.

The FITACF data can be median filtered using a $3 \times 3 \times 3$ beam by range gate by time scanning boxcar filter (Ruohoniemi & Baker, 1998). Smoothing the data spatio-temporally and removing extreme values. For a target beam, b, range gate, g, cell at time t, the filter encompasses all samples between $b-1$ to $b+1$, $g-1$ to $g+1$ and $t-1$ to $t+1$ inclusively. Weights are assigned to each value so that the target cell is favoured while samples from cells from a different beam, gate and time are less favoured. An example of the boxcar filter and the magnitude of the weights assigned to a given boxcar is shown by Figure 2.3. A distribution of all samples in

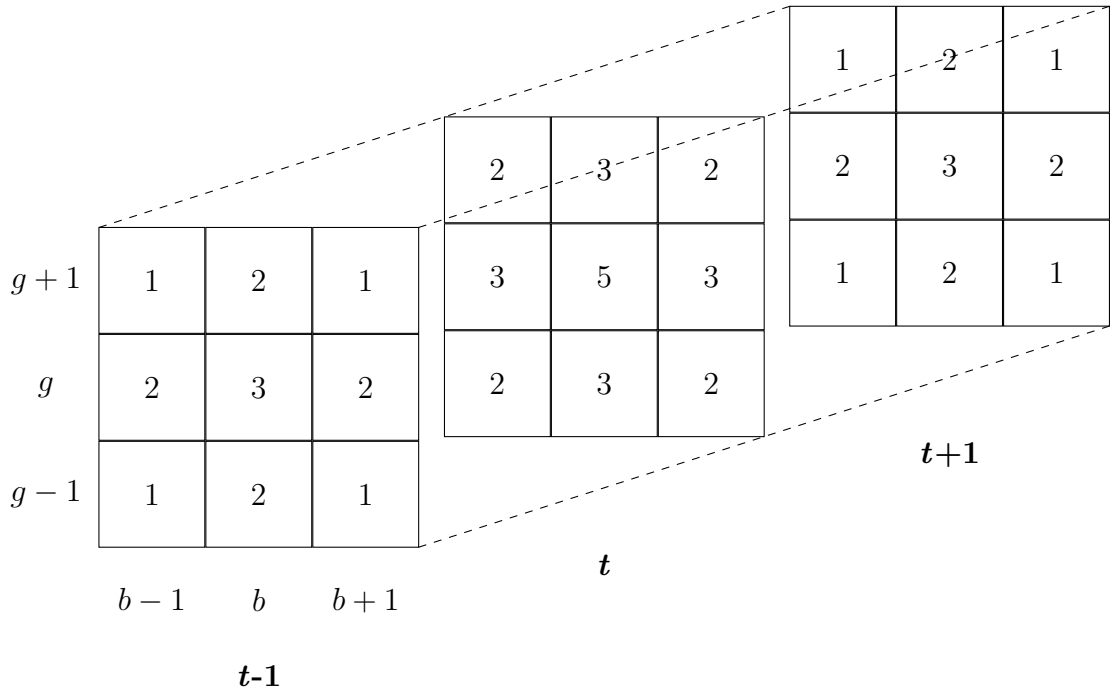

Figure 2.3: Matrix of weights assigned to $3 \times 3 \times 3$ boxcar filter used for median filtering.

the boxcar is then taken, where each sample is populated a number of times equal to its weight. Outliers are then removed from the deviation. Normally this is done by removing values more than two standard deviations away from the mean of the weighted distribution (Ruohoniemi & Baker, 1998). For high-latitudes and high velocity scatter this normally removes unphysical values, however the work in this thesis concerns mid-latitude scatter, often with much lower ($< 50\,\mathrm{ms}^{-1}$ (Maimaiti et al., 2018)). For this low velocity scatter the standard deviations between the real and unphysical noise are so large (especially as the distances between the mean and large values are squared, resulting in large deviations being weighted more heavily) that the noise is not removed. It is necessary to use an alternative method that is more robust to these outliers. We use the median absolute deviation (MAD) (Howell, 2005), which is defined as

$$\mathrm{Median}(|\tilde{x} - x|) \tag{2.4}$$

where x is each sample in the distribution while $\tilde{x}$ is the median of the distribution. We then remove any values from the boxcar filter that are two median absolute deviations from the median value of the weighted distribution. Finally, the median of the remaining values in the boxcar filter is set to the target cell. Deviations in the MAD are much smaller than in the standard distribution. Because the MAD is generally smaller than the standard deviation, there are some cases where real scatter, or at least more real scatter, is removed compared to the normal technique using the standard deviation. However, because any remaining values are median filtered, and that scatter which would get removed would be at the edge of the weighted distribution, we have found that it has no discernable impact on the final filtered velocity. Errors of the final median filtered velocities are calculated as the standard deviation of the sampled boxcar velocities after removing outliers.

2.1.3.2 Groundscatter determination

In order to accurately assess ionospheric phenomena, groundscatter needs to be excluded from observations. At high-latitudes, ionospheric plasma moves at great enough velocities while returning strong spectral widths that simply assessing the magnitude of the returned values is an appropriate method for determining groundscatter. Typically, values are classified as groundscatter if the following relationship is satisified (Burrell et al., 2018):

$$|v| + \frac{1}{3}|w| < 30\text{ms}^{-1} \tag{2.5}$$

where, v is the LOS (FITACF) velocity and w is the spectral width. This criterion, while effective at ensuring clean ionospheric backscatter is returned, also misidentifies a significant amount of slow-moving ionospheric backscatter (Blanchard et al., 2009) which is much more prevalent in the mid-latitude ionosphere. In principle, clusters of ionospheric/ground scatter can be identified by comparing the magnitudes of velocities and spectral widths within a cluster. Clusters can be attributed to n-hop (ground-scatter, lower magnitudes) or $n\frac{1}{2}$-hop (ionospheric-scatter, higher magnitudes) scatter. Slow-moving ionospheric backscatter can still

Hours	Ratio (h/l)
$1 < H \leq 2$	> 0.475
$2 < H \leq 3$	> 0.33
$3 < H \leq 14$	> 0.2

Table 2.1: Ratio of high (h) to low (l) velocity scatter for a cluster of H hours to be classified as ionospheric scatter (Ribeiro et al., 2011).

be difficult to distinguish compared to groundscatter but we can identify them by considering the fraction of fast and slow moving measurements made within spatially and temporally connected groups of backscatter. Ribeiro et al. (2011) developed an algorithm specifically designed to identify low-velocity ionospheric scatter from mid-latitude radars using this method. FITACF velocities are first median filtered as described in section 2.1.3.1. Individual clusters of scatter are then identified. For each cluster the leading and trailing edges in time, at times t_L and t_T respectively, are examined. By default each cluster is classified as groundscatter. For the leading edge, beam-range gate cells at times $t_L - 4 < t_L \leq t_L + 4$ are collected, while at the trailing edge cells at times $t_T - 4 < t_T \leq t_T + 4$ are collected. Each collection of cells are examined for the ratio of "high" to "low" velocity LOS scatter, where scatter is marked as "high" velocity if it is greater than $15\,\mathrm{ms}^{-1}$. If the ratio of "high" to "low" velocity scatter is not sufficient at the leading edge then the time is incremented ($t_L = t_L + 1$) until the ratio of scatter is sufficient, then the cluster of scatter is marked as ionospheric from t_L. If the ratio at the trailing edge is not sufficient, then the time is decreased ($t_T = t_T - 1$), until the ratio is sufficient, at which point the returned scatter is identified as turning from ionospheric to ground scatter at t_T. Clusters must last for at least 1 hour to be classed as ionospheric scatter while the necessary ratio of high-to-low velocity scatter is decreased as cluster length increases according to table 2.1. Clusters must also have a duration of less than 14 hours to be classified as ionospheric scatter to protect against ground scatter contamination that could occur if temporally long patches of ionospheric and groundscatter bleed

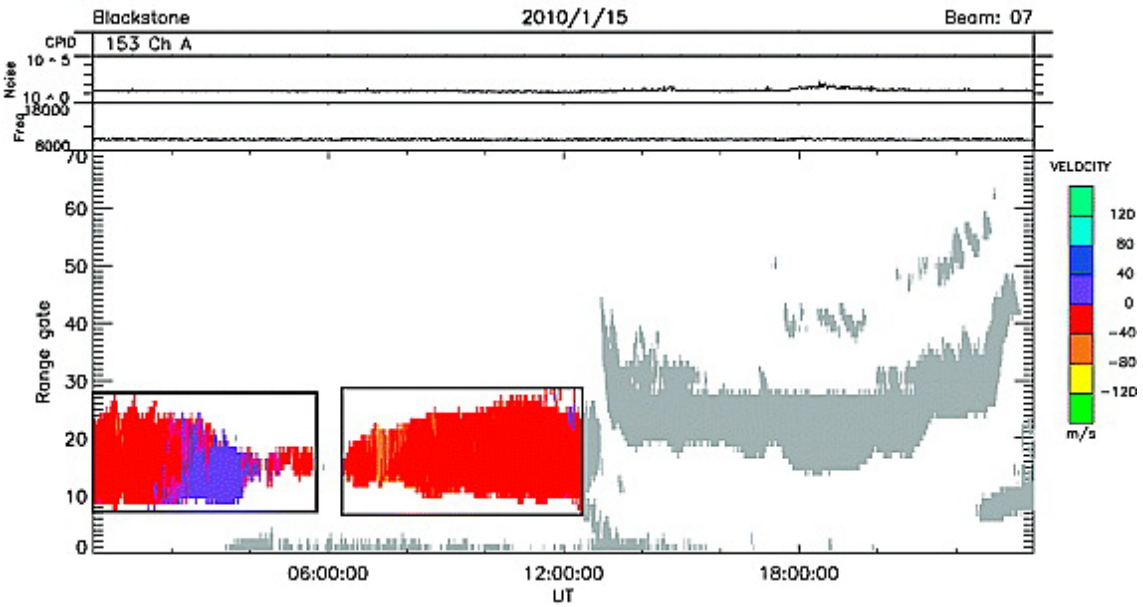

Figure 2.4: Time series of boxcar filtered FITACF velocity from 15 January 2010 of beam 7 of the Blackstone (BKS) SuperDARN radar. Grey points are groundscatter, while ionospheric velocity magnitude is given by the colourbar on the right. Adapted from Ribeiro et al. (2011).

into each other.

Figure 2.4 shows an example of the groundscatter algorithm used on a single beam from the Blackstone (BKS) SuperDARN radar on 15 January 2010. Range gate appears on the Y-axis while time on the X-axis. Three distinct large patches of ionospheric scatter are visible in Figure 2.4, one between 0000 UT and $\sim$ 0530 UT (patch 1). One from approximately 0630 UT to $\sim$ 1200 UT (patch 2) and one from $\sim$ 1300 UT to just before 2400 UT (patch 3). Both patch 1 and patch 2 have been classified as ionospheric scatter with velocities less than 40 ms^{-1} and have a similar spread of range gates, indicating that this is $\frac{1}{2}$-hop ionospheric scatter. Patch 3 has not been classified as ionospheric, indicating that this is 1-hop groundscatter. A small strip at the end of patch 2 has been erroneously identified as groundscatter which is a slight disadvantage to the algorithm, however if patches 2 and 3 had bled into each other (as often occurs) and no trailing edge idenfiticaion was performed,

then the entire combined patch would be erroneously classified as ionospheric or groundscatter. Ranges less tan 315 km from the radar are automatically discounted as ionospheric scatter to eliminate scatter originating from the E-region or from meteor echoes at near ranges (Hall, 1997). Using standard methodology, each beam is analysed separately, meaning that scatter cannot be considered across multiple connecting beams which can cause a disconnect between identifying the start of ionospheric scatter across beams and/or clusters of scatter spanning multiple beams being classified as separate ionospheric/groundscatter patches. We therefore modify the algorithm similar to Burrell et al. (2018), so that clusters are considered to be connected across beams.

2.2 Faby-Pérot Interferometer

Neutral wind observations are made by using a Fabry-Pérot interferometer (FPI), specifically from the North American thermosphere ionosphere observing network (NATION) which was a network that consisted of five FPIs across mainland United States of America. The five FPI sites are given by Table 2.2. The FPIs operate by observing the Doppler shift of airglow that moves with the neutral atmosphere.

2.2.1 Airglow

Airglow is a phenomena that lights Earth's high altitude atmosphere. Whereas aurorae, which are highly structured are generated by charged particles entering Earth's atmosphere from the magnetosphere, airglow is produced by ion recombination and is always present, covers all latitudes and is completely unstructured. On a moonless night, airglow contributes the major part of light arriving from the sky, exceeding starlight in its total intensity. The production mechanisms of airglow include:

- Radiative recombination reactions which emit a photon;
- Relaxation of excited products, releasing excess energy as radiation;

[] at (-3, 8.24) Excitation energy 4.17 eV

Site	Latitude (GEO °N)	Longitude (GEO °E)
Millstone Hill, Massachusets (MH)	42.61	288.52
Peach Mountain, Michigan (ANN)	42.27	276.24
Urbana Atmospheric Observatory, Illinois (UAO)	40.13	271.80
Eastern Kentucky University, (EKU)	27.75	275.71
Virginia Tech, Virginia (VTI)	37.21	279.58
Pisgah Astronomical Research Institute, North Carolina (PAR)	35.20	277.15

Table 2.2: Site details for locations of the FPIs within the NATION network.

- Excitation by hot electrons (after ionisation) and electric fields;
- Excitation by solar radiation, generating resonance emissions at the same wavelength;

The velocity of an emitting species can be identified by observing the Doppler shift of a known airglow emission line. One of the most prominent set of emissions from airglow are two lines from atomic oxygen, the green line at 557.7 nm and the triplet red line at 630/636.4 nm, however the third line is typically so weak that the emission lines appear as a doublet. In the F-region, excited oxygen atoms come from dissociative recombination of diatomic charged Oxygen (Hargreaves, 1992):

$$O_2^+ + e \rightarrow O + O^* \tag{2.6}$$

and charged Nitric Oxide (Makela et al., 2012),

$$NO^+ + e \rightarrow N + O^* \tag{2.7}$$

where $*$ represents an electronically excited species. The green line emission, with a lifetime of 0.74 s, is created when oxygen in the ^{1}S state reverts to the ^{1}D state.

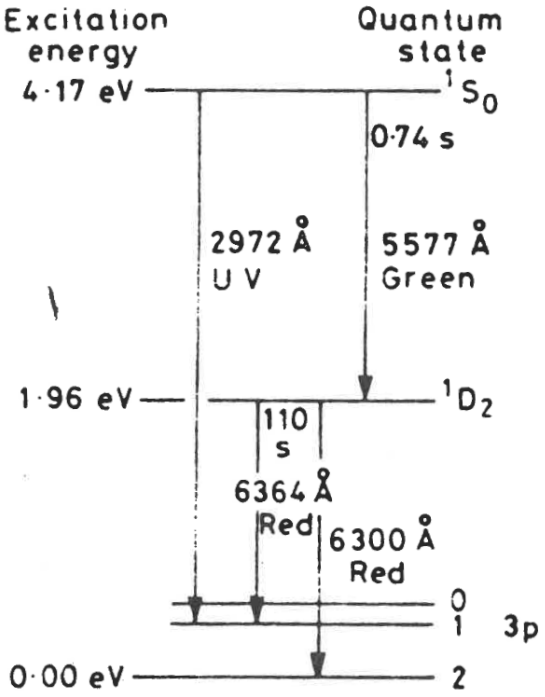

Figure 2.5: Energy levels and transitions of atomic oxygen that produce the 557.7 nm green and 630/636.4 nm red emission lines. Units are given in ångströms. From Bauer (1973).

Further relaxation to the ^{3}P state produces the red line emissions with a lifetime of 110 s, as shown by Figure 2.5.

A third UV line at 297.2 nm is also produced from direct transitions to the ground state, however this emission is too weak to produce and contribute to airglow.

At E-region altitudes the main source of excited oxygen is the reaction,

$$O + O + O \rightarrow O_2 + O^* \tag{2.8}$$

and O^* is in the ^{1}S state. At E-region altitudes, the lifetime of the intermediate ^{1}D state is long enough that the energy held by the Oxygen ion is removed by collisions with other molecules before the red-line emission can be emitted, this process is known as quenching. Observation of the Doppler shift of the emission lines can be interpreted as the velocity of the neutral air. The green line Doppler shift allows for dynamical studies of the neutral atmosphere, whilst observation of the red line

Doppler shift can tell us about the motion of neutrals at F-region altitudes because of quenching that occurs in the E-region.

2.2.2 Instrument Operation

The NATION FPIs observe the spectral line shape of the 630nm oxygen red emission line, with a typical spectral resolution of $\lambda/\delta\lambda \sim 310,000$ (Makela et al., 2012). The high resolution is necessary to overcome the instrumental Challenge of measuring small magnitudes of the Doppler shift and Doppler width. A $100\,\mathrm{ms}^{-1}$ Doppler shift correspondes to a wavelength of 0.0002 nm.

The NATION FPIs use imaging technology, with an etalon aperture of 7 cm and a short focal length lens that generates a ring pattern with N=12 rings. Typically 5 minutes of imaging FPI observations will produce a result with $5\,\mathrm{ms}^{-1}$ accuracy in the wind velocities.

The observation of the night sky 630 nm spectral emission by the FPI produces a circular interference pattern in which the Doppler red shift produces a ring pattern which decreases in diameter for each ring. By annularly summing the pixels of the ring pattern, a one dimensional set of fringes is extracted and a weighted average is performed to determine the overall Doppler velocity (Makela et al., 2011). Figure 2.6 shows an example of the interference patterns of 630nm night sky observations (c) and a HeNe laser used to calibrate the FPI. The broader width of the observational lines compared to the laser is a product of thermal broadening introduced by the moving atoms to and away from the FPI line of sight. The interference patterns calculated by annularly integrating around the centre of the rings in each image are also shown to the right.

The 630 nm Oxygen emission line characteristically peaks at $\sim$ 250 km altitude. The NATION FPI's measure the line of sight 630 nm Doppler shift in the cardinal directions (geographic North, East, South, West) at the station with an elevation angle of 45°. The FPI's also measure the line of sight direction vertically above each station, which alongside the measurements from opposing cardinal line of

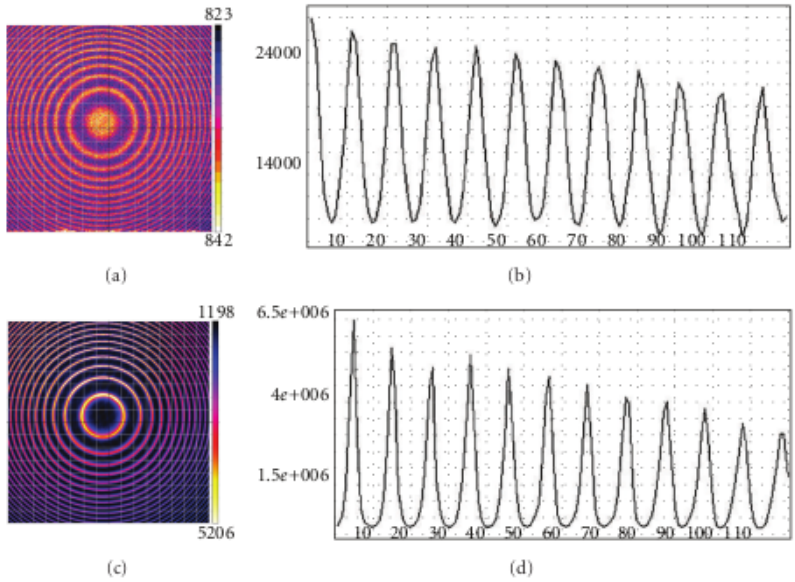

Figure 2.6: Interference patterns (a) of the 630nm sky and HeNe laser observations (c) by an imaging FPI. The interferograms of the observed (b) and laser patterns (d) are shown to the right. From Makela et al. (2012).

sight observations, are used to determine the two dimensional horizontal neutral wind vector. For more information see section 4.1.3: Each site is equipped with a second instrument, which monitors the 8-14 μm infrared radiation to deduce the sky temperature. The sky temperature is compared to the ambient ground-level temperature where large differences between them represent clear observing conditions. As the temperature difference decreases, the observation quality also decreases so that sky temperatures $< -20°$C typically indicate clear skies, temperatures $> -10°$C represent cloudy skies, while in between are borderline cases. Because the 630nm red line emission is faint, observations can only be made during local nighttime. Brightening of the sky, such as the presence of a full moon in a look direction also reduces the airglow visibility, preventing measurements from being recorded.

2.3 Magnetic Field Modelling

The 13th generation international geomagnetic reference field (IGRF) model (Alken et al., 2021) profiles Earth's main geomagnetic field in spherical coordinates, $\mathbf{B}(r, \theta, \phi, t)$, where r, θ, ϕ are radial distance from the center of Earth, geocentric co-latitude and longitude respectively. A fourth term, time (t) is profiled due to the moving nature of Earth's magnetic dipoles. Earth's geomagnetic field near the surface can be described as the gradient of a scalar potential, $\mathbf{B} = -\nabla V$, and the potential function $V(r, \theta, \phi, t)$ is represented as a finite series expansion in terms of spherical harmonic coefficients, g_n^m and h_n^m, known as the Gauss coefficients:

$$V(r, \theta, \phi, t) = a \sum_{n=1}^{N} \sum_{m=0}^{n} \left(\frac{a}{r}\right)^{n+1} \left[g_n^m(t) \cos m\phi + h_n^m(t) \sin m\phi\right] P_n^m \cos\theta \tag{2.9}$$

A reference radius of $r = 6371.2$ km is chosen as the mean Earth radius. The $P_n^m \cos\theta$ term are schmidt semi-normalised associated Legendre functions of degree n and order m (Winch et al., 2005). N specifies the maximum spherical harmonic degree of expansion, which is 10 for 5-year epochs up to and including epoch 1995. Five-year Epochs after 1995 use N=13 to account for the smaller scale internal signals which could be captured by higher-resolution satellite missions. The Gauss coefficients, $g_n^m(t)$, $h_n^m(t)$ are time-dependent and are changed for each 5-year epoch interval, such that a new generation of the IGRF model is produced. For a more detailed analysis on how these coefficients are calculated and for their values, see Alken et al. (2021). The 13th generation model is valid from the years 1900 to 2025.

The tilt in the angle of the magnetic field at mid-latitudes needs to be accounted for when comparing the electric field generated by the neutral wind dynamo ($\mathbf{u} \times \mathbf{B}$) with the electric field that is calculated from $\mathbf{E} \times \mathbf{B}$ drift, due to the difference in angle between the ion velocity vectors (which move relative to the magnetic field) and the neutral velocity vectors (which move relative to Earth's surface). The IGRF13 model provides the declination and inclination of the magnetic field at necessary observation locations. Figure 2.7 shows maps of the inclination and declination of

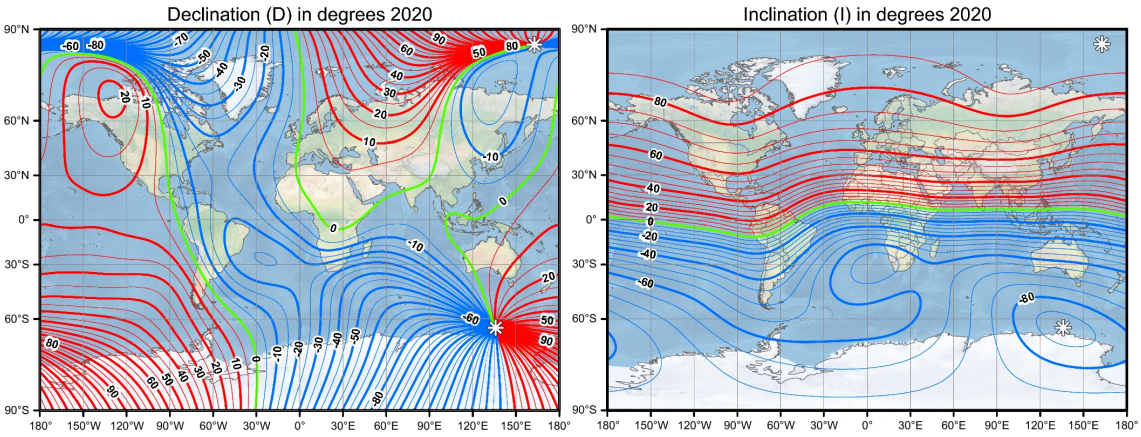

Figure 2.7: Declination and Inclination of the IGRF13 magnetic field. Adapted from Alken et al. (2021).

the IGRF13 magnetic field.

2.4 Auroral Boundary

The location of the equatorward boundary of the auroral oval is important for determining the drivers of plasma motion at the mid-latitudes. If the equatorward boundary of the auroral oval is equatorward of observation locations, then the primary driver for the ion motion can be attributed to the high-latitude two-cell convection pattern. If, however, the boundary is poleward, then one of, or a combination of sub-auroral drivers would instead be responsible.

Both the equatorward and poleward boundaries of the auroral oval are typically be determined by satellites in polar orbits that monitor the proton and electron fluxes along their orbit tracks (Andersson et al., 2004; Clausen et al., 2012; Grocott et al., 2011; Kilcommons et al., 2017; Kunduri et al., 2017, 2018; Peterson et al., 2008; Redmon et al., 2010). The defence meteorological satellite program (DMSP) and polar orbiting environmental satellite (POES) provide measurements of the particle precipitation along their orbital paths. The total energy detector (TED) on POES monitors the energy flux of precipitating particles with energies between 50 eV and 20 keV at a resolution of 16 s. The DMSP satellites are equipped with the SSJ/4

precipitating electron and ion detectors which make observations of the precipitating particle flux between 30 eV and 30 keV. Both DMSP and POES are comprised of several independent orbiting satellites and complete orbits approximately 14.25 and 10.1 times per day respectively. For determining the equatorward auroral boundary for a given time, t, flux measurements from each satellite are tracked for $t \pm 30 - 40$ minutes. The locations of the equatorward precipitation boundaries are then identified. Several studies have shown the the shape of the nightside equatorward auroral oval can be approximated by a circle (Gussenhoven et al., 1983; Hardy et al., 1989; Holzworth & Meng, 1975), therefore a circular fitting function is applied to the precipitation boundary points to obtain the equatorward auroral boundary at all local times. Figure 2.8 shows an example of the nightside equatorward auroral boundary being determined by fitting to particle precipitation data from both DMSP and POES satellites.

To reduce the uncertainty in the estimation of the equatorward auroral boundary, satellite passes used to identify the points for the circular fit should be (ideally) overhead of any local observation positions. This is often difficult to achieve, however especially in the context of ion-neutral coupling, where there are already limitations requiring coincident measurements from two other instruments. We investigate an additional technique to determine the auroral boundary.

The Active Magnetosphere and Planetary Electrodynamics Response Experiment (AMPERE) (Anderson et al., 2002, 2014; Anderson et al., 2021) uses magnetometers on the Iridium constellation of telecommunication satellites to provide field aligned current measurements across both hemispheres. The Iridium constellation consists of > 60 satellites in low altitude, 780 km polar orbits in six equally spaced planes with at least eleven satellites in each plane. Magnetometors on each satellite record magnetic field data at a resolution of 48 nT, enough to detect FAC signatures. The magnetometers are sampled 11 times per second on board, however data are only saved for telemetry to the ground every 200 seconds. Multiple satellites in each orbit plane helps to compensate for the coarse

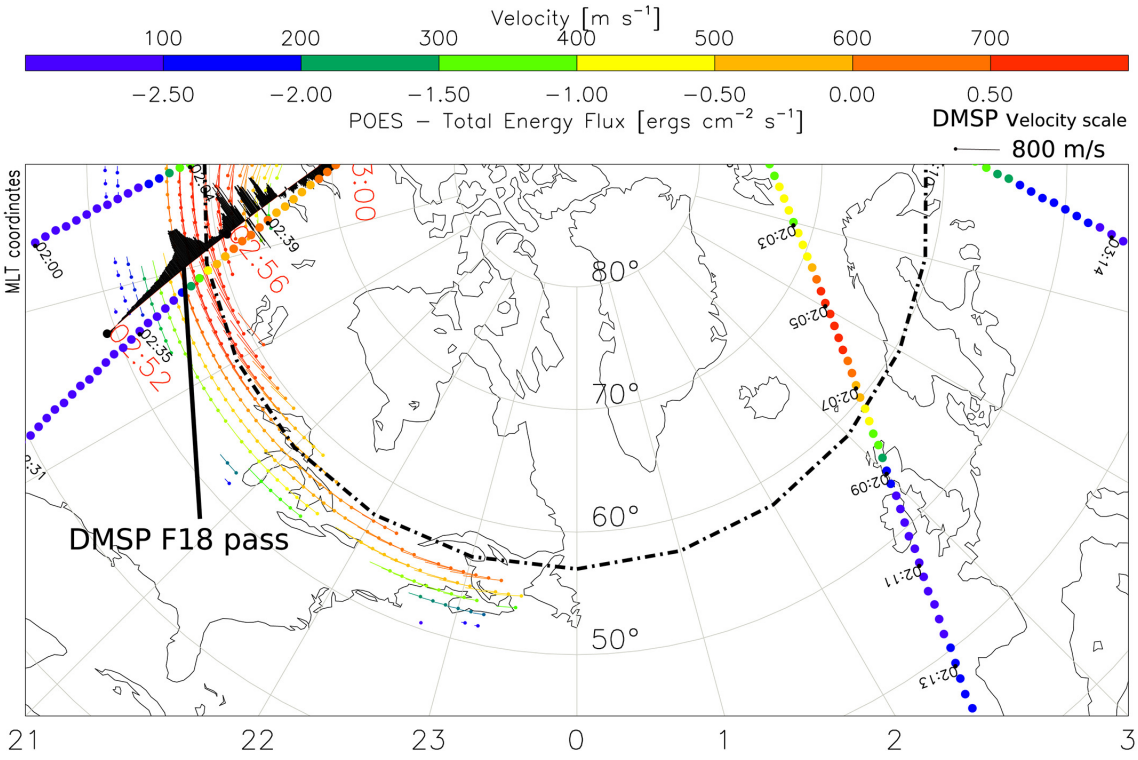

Figure 2.8: Dashed black lines show the equatorward boundary of the auroral oval determined by a circular fit to the precipitation boundary measured by the POES energy fluxes (coloured dots according to the colourbar). The cross-track ion driftmeter from a DMSP pass is in black, which correlates well to the POES observations. Also shown are ion velocity vectors of the twin cell convectionFrom Kunduri et al. (2017).

sampling frequency on individual satellites. Satellite locations are calculated in AACGM coordinates. Earth's main magnetic field is subtracted from the horizontal magnetometer measurements to leave only the field due to external currents. The remaining data is then temporally de-trended. A spherical harmonic fit is performed over Earth's entire sphere from pole to pole. A latitude order of 60 (corresponding to a resolution of 3°) and a longitude order of 5, which is consistent with the spacing between orbital planes is used. For a more detailed description of the analysis, see Anderson et al. (2021). Current density is calculated from Amperès law (Equation

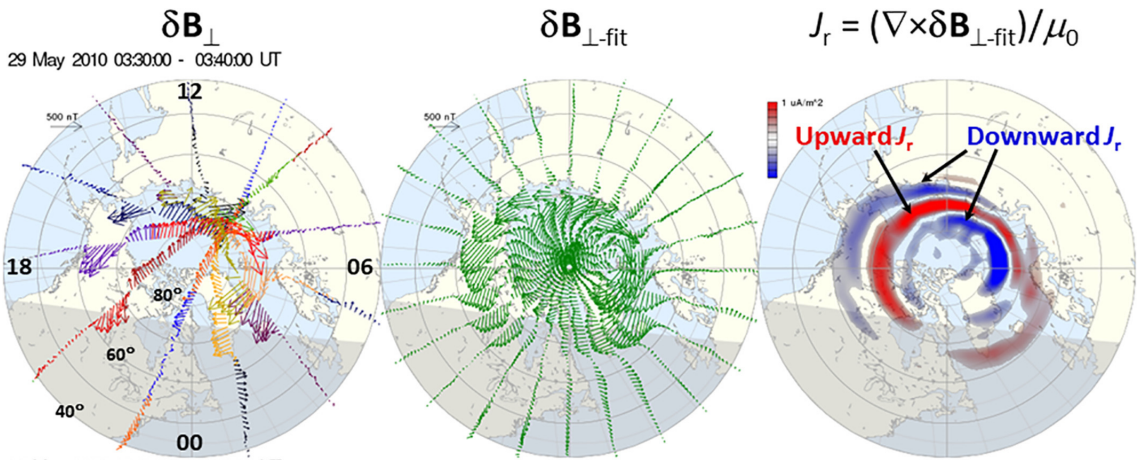

Figure 2.9: (left) Horizontal magnetic field perturbations recorded by IRIDIUM satellite magnetometers. (centre) Horizontal magnetic field perturbations after spherical harmonic fitting and (right) radial current density. Adapted from Anderson et al. (2021).

1.2), assuming a constant electric field, to the fitted perturbations:

$$\mathbf{J} = \frac{(\nabla \times \delta \mathbf{B}_{\perp})}{\mu_0} \tag{2.10}$$

radial current density is calculated by separately integrating the upward (positive) and downward (negative) current densities. Figure 2.9 shows an example of the data fitting process. The horizontal magnetic field perturbations are given at the left, different colours represent measurements taken by different satellites. The central panel shows horizontal perturbations after performing the spherical harmonic fitting and right, is the radial current density.

The R1/R2 FAC current patterns can be determined by examining the upward and downward FAC patterns produced by AMPERE and employing a circular fit between the boundary (Kilcommons et al., 2017; Milan et al., 2015, 2017).

Figure 2.10 shows a figure adapted from Kilcommons et al. (2017) of statistical distributions of the (a) northern and (b) southern hemisphere FACs ±45 days around June solstice for $2010 - 2012$ determined using DMSP data. Bold black circles show the statistically derived patterns of the auroral boundary for the same period. (a) Shows that the equatorward auroral boundary exhibits good correlation

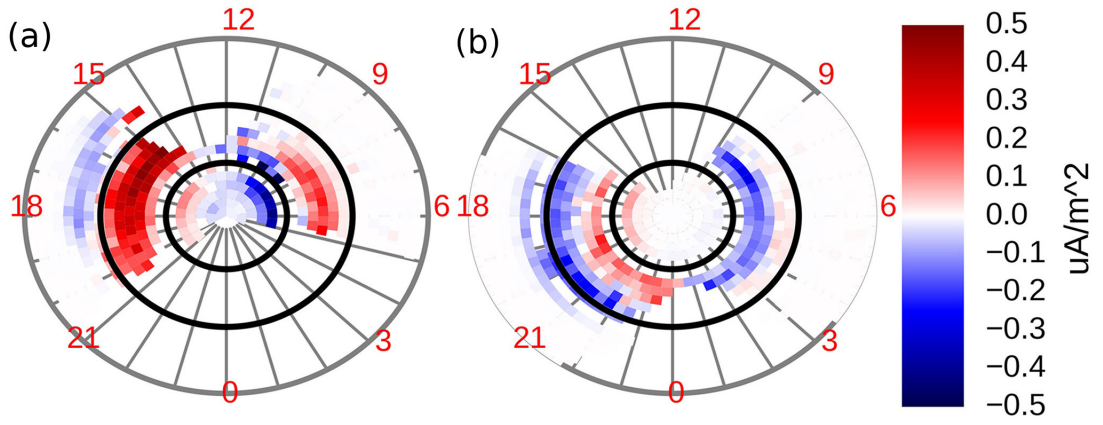

Figure 2.10: Statistical distributions of FAC currents ± days around June solstice for 2010-2012 derived from DMSP Data given by the colourbar on the right. Bold black circles are statistical patterns of the determined statistical patterns of the auroral boundary. Adapted from Kilcommons et al. (2017).

with the R1/R2 boundary on the northern hemisphere duskside, while it is slighty equatorward of the R2 currents on the dawnside. These maps show that the distribution of FAC current density maps can be used as a proxy for the equatorward boundary of the auroral oval during summer months.

2.5 The Mid-Latitude Ionospheric Trough

The location of the mid-latitude ionospheric trough is important for identifying mid-latitude dynamics. The trough plays a significant factor in the latitudinal distribution of SAPS and its equatorward and poleward boundaries induce ion motion through pressure gradient drifts. The mid-latitude ionospheric trough can be identified using total electron content (TEC) measurements from global positioning system (GPS) data from the international global navigation satellite system (GNSS) service. The TEC measurements of the ionosphere describe the total number of electrons contained in a cylinder of cross-sectional area 1 m^2 that extends vertically above a given point on the Earth all the way through the ionosphere. One TEC unit (TECU) is given as 1×10^{16} electrons/m^2. Typical peak dayside values can range

from less than 10 TECU during quiet times to hundreds of TECU during strong geomagnetic storms (Thomas et al., 2013). Although values vary due to geomagnetic activity, the mid-latitude trough can be identified as by TEC values of < 8 TECU (Kunduri et al., 2021). The TEC data are processed using the algorithms described in Rideout and Coster (2006) and Vierinen et al. (2016) to produce global TEC maps binned into $1^\circ \times 1^\circ$ degree, geographic latitude by longitude cells, assuming a slab ionosphere at 350 km altitude. TEC maps are produced every 5 minutes and we median filter the TEC data using the same process as described in section 2.1.3.1 to reduce the geospatial noise among the dataset.

2.6 Solar wind and Geomagnetic Indices

Solar wind and IMF data products are available from OMNI, which is a dataset of several Earth and near-Earth geomagnetic parameters that are collated and maintained by the Space Physics Data Facility (SPDF) at NASA (https://omniweb.gsfc.nasa.gov). Data for OMNI IMF values are provided by spacecraft between Earth and the Sun. Recorded data products are time shifted so that they are propagated to Earth's bow shock. The ACE spacecraft provides measurements of the IMF B_z, which if negative introduces reconnection between the IMF and Earth's magnetosphere and IMF B_y, which could introduce asymmetries in the twin-cell convection pattern that could be important if it expanded to the mid-latitudes. ACE also provides measurements of the IMF velocity in the x direction (GSM/GSE), which influences the rate of reconnection under IMF $B_z < 0$.

Increased auroral activity often occurs alongside the expansion of the twin-cell convection pattern. Variabilities in high-latitude magnetospheric or ionospheric currents produce magnetic perturbations to the magnetic field which can be monitored using ground-based magnetometers. North-South perturbations at auroral latitudes are monitored, where the intensity of the perturbations for the eastwards Hall currents produces the auroral upper (AU) index while the westwards

Hall currents produce the auroral lower index. The envelopes of the upper and lower perturbations produce the AU and AL index respectively. Measurements are performed by a network of 12 auroral latitude magnetometers (Weygand et al., 2014). Increased intensity in the AL index (such that $|\mathrm{AL}| > |\mathrm{AU}|$) typically indicates increased magnetotail reconnection activity. A third index is derived, the Auroral electroject (AE) index:

$$\mathrm{AE} = \mathrm{AU} - \mathrm{AL} \tag{2.11}$$

which details the difference between the eastward and westward components of the Hall currents. The auroral indices are provided by the World Data Center for Geomagnetism in Kyoto and are accessible through the OMNI database. AE index values of > 100 nT typically indicate strong geomagnetic activity.

The disturbance storm-time index (Dst) is a measure of the strength of Earth's ring current and is generally used as a measure of overall global geomagnetic activity. The ring current, which is centred in Earth's equatorial plane and circulates westwards due to longitudinally drifting particles around Earth's magnetosphere. The ring current generates a magnetic field that opposes Earth's dynamo generated field, effectively decreasing the magnetic field strength inside of the ring current L-shells. The Dst index is derived by a network of near-equatorial magnetometers and monitors the hourly horizontal magnetic field. The Dst index is calculated by subtracting the combined main geomagnetic field from Earth's combined internal dynamo and tidally induced magnetic field variations from the observations, then averaging the residuals over all stations. The Dst index serves as a good proxy for the longitudinally symmetric component of the ring current. The SYM-H index is effectively the same as the Dst index, however unlike the Dst index which is derived hourly, the SYM-H index is calculated at a minutely resolution. Subtracting the globally symmetric component of the magnetic field variation from the variations recorded at each station provides the longitudinally asymmetric geomagnetic field variations. The range between the maximum and minimum of these variations are compiled as the ASYM-H index. Penetrating electric fields, partial ring currents

Level	Kp
Minor	< 5
Moderate	6
Strong	7
Severe	8
Extreme	9

Table 2.3: Table of geomagnetic storm levels and associated Kp level as used by the National Oceanographic and Atmospheric Association (NOAA) (Oceanographic & Administration, n.d.).

and field-aligned currents often result in asymmetries in the ring current which become enhanced during geomagnetic storms and the ASYM-H index can be useful for monitoring the effects of such phenomena.

The K-scale is a quasi-logarithmic scale derived from the maximum fluctuation in the horizontal component of Earth's magnetic field observed by a magnetometer relative to a quiet day during a three hour interval. The conversion from maximum fluctuation to K-index varies by observatory so that the historical rate of occurrence of K levels are approximately equal between all observatories. The K-index is calculated at intervals of 3 hours starting at 0000UT. The maximum positive and negative fluctuations during each 3 hour period are added together to determine the maximum fluctuation. The Kp index is calculated as a weighted average of K-indices from a network of magnetometers at mid-latitude locations. The National Oceanographic and Atmospheric Association (NOAA) runs a G-scale, which prescribes the level of a geomagnetic storm according to Kp value and is given by table 2.3 Alongside the A/SYM-H and Dst indices the Kp index is often used to describe overall levels of global geogmagnetic activity.

2.7 TIEGCM

The Thermosphere Ionosphere Electrodynamic General Circulation Model (TIEGCM) is a fully three-dimensional time dependent model of Earth's ionosphere and thermosphere developed by the National Center for Atmospheric Research (NCAR) (Qian et al., 2014; Richmond & Roble, 1997; Richmond et al., 1992). TIEGCM is widely used to study global ionosphere-thermosphere coupling for locations and periods of difficult data availability. TIEGCM is also well used within the upper atmospheric modeling community for space weather prediction (Elvidge & Angling, 2019). The TIEGCM model solves the equations fo continuity, energy and momentum for the major ion and neutral species (O_2, O_2^+, O, O^+ NO, He, AR). For our purposes it provides the three dimensional ion and neutral wind velocities which we compare to those measured by the BKS SuperDARN radar and the ANN FPI, respectively.

The high latitude electric potential pattern, driven by the high-latitude twin-cell convection pattern, is provided by a separate background model, the Heelis (Heelis et al., 1982) or Weimer (Weimer, 2005) models and drives the high-latitude $\mathbf{E}\times\mathbf{B}$ ion motion. Wu et al. (2017) compared TIEGCM's high-latitude thermospheric winds and ion drifts using each electric field model and compared them to observational data. They found that the Weimer model produced simulations which were more representative of the observed patterns. Therefore in this work, we use the Weimer pattern to drive the high-latitude potential in TIEGCM. Inputs for the Weimer driven TIEGCM are the f10.7 solar radio flux, which is the intensity of 10.7cm wavelength radiation from the sun and a good indicator of solar activity, IMF B_x, IMF B_y, IMF B_z (GSM), IMF velocity in the x direction and the solar wind density. Other ion drivers in TIEGCM include auroral precipitation (Roble & Ridley, 1987) with hemispheric power estimations (Zhang & Paxton, 2008), tidal climatology for the lower atmosphere boundary (Hagan & Forbes, 2002, 2003) and solar EUV irradiance (Solomon & Qian, 2005).

The equatorward boundary of the high-latitude convection pattern in TIEGCM

does not follow a 1:1 ratio with the latitude where the electric potential of the background model (Weimer) goes to zero, instead two boundaries are set. The first is the high-latitude convection boundary, b_1, which is calculated as:

$$b_1 = 0.5 \times \phi_0^\circ \tag{2.12}$$

where ϕ_0° is the colatitude where the background electric potential pattern goes to zero. Additionally, b_1 has a minimum latitude of 60° and a maximum of 75°. A second boundary is then created, b_2 which is 15° degrees equatorward of b_1. Equatorward of b_2, a self-consistent solution for the mid and low-latitude dynamo electric field is calculated and used to drive ion motion. Poleward of b_1 the high-latitude electric potential pattern drives the ion motion and between b_1 and b_2, there is a linear variation of the combined dynamo and imposed high latitude solution (TIEGCM draft model description, HAO, 2018).

TIEGCM produces the geographic meridional, zonal and vertical ion and neutral velocities at the specified run resolution, which is nominally 20 minutes. The Pedersen conductivity, which is also required to calculate Joule heating, is also modelled by TIEGCM. Outputs from TIEGCM are in geographic coordinates with a spatial resolution of $2.5^\circ \times 2.5^\circ$ or $5^\circ \times 5^\circ$ degrees. Altitude cells in TIEGCM are given by scale height, with a resolution of 0.25, however estimations of the altitude (km) of each cell are calculated, such that we can model the necessary parameters at $\sim$ 250 km altitude, which corresponds to observations from the SuperDARN and FPI instruments.

Chapter 3

Mid-Latitude Ion-Neutral Observations During a Quiet Time Interval

This Chapter contains work from the published article:

Day, E. K., Grocott, A., Walach, M.-T., Wild, J. A., Lu, G., Ruohoniemi, J. M., & Coster, A. J. (2024). Observation of quiet-time mid-latitude joule heating and comparisons with the tiegcm simulation. *Journal of Geophysical Research: Space Physics*, *129*. https://doi.org/10.1029/2024JA032578

3.1 Introduction

Most studies investigating Joule heating pertain to the high-latitudes and multiple studies exist both analysing the high-latitude Joule heating rates using observations (Anderson et al., 2013; Baloukidis et al., 2023; Billett et al., 2018; Kiene et al., 2019) and global scale models (Lu et al., 1995, 2016; Wang et al., 2020). Studies focusing on the mid-latitudes typically investigate ion-neutral coupling parameters over large-scales (Billett et al., 2022; Joshi et al., 2015) rather than localised Joule heating rates due to the difficulty in monitoring those processes over persistent co-located

periods. As discussed in section 1.5, because Joule heating is a frictional heating between the ions and the neutrals, the ion and neutral measurements need to be from the same point to accurately capture the coupling between the two. Measurements taken from points that are not co-located may result in inaccurate representations of the overall Joule heating rates. Global scale models, such as TIEGCM are, in principle, perfectly capable of estimating localised Joule heating rates at the mid-latitudes, with the only limit being the spatio-temporal resolution of the model. The combination of observational and modelling studies at the high-latitudes, alongside studies which focus on evaluating model performances compared to observations (Wu et al., 2017), show that models such as TIEGCM can perform well at high-latitudes, both in terms of the ion-neutral coupling and resulting Joule heating estimations. There are however, limited studies confirming the performance at the mid-latitudes. This Chapter focuses on identifying an interval of local high-quality co-located persistent observations of both the ions and neutrals and comparing to outputs from TIEGCM to assess its modelled performance.

The first step for performing Joule heating estimations is obtaining known ion and neutral velocities. The SuperDARN and NATION observational network each consist of multiple instruments that have at least some portion of their FOVs overlapping each other. Joshi et al. (2015) used the Blackstone (BKS) and Fort Hays East (FHE) SuperDARN radars alongside the ANN Arbor (ANN) and Michigan (UAO) NATION FPIs to calculate the ion-neutral coupling timescale at mid-latitudes. Their FOVs are shown in Figure 3.1. We use the same instruments as a basis for our investigations. Joshi et al. (2015) investigated the coupling on large spatial scales, therefore fully co-located measurements were not necessary. The UAO FPI has its West facing observation direction excluded from the FOV of any SuperDARN radar. Furthermore, the BKS SuperDARN radar comprises of 24 possible beams but typically operates with only 20. Often-most, the beams which are not used are the four west-most facing beams, which overlap the UAO North, South and Zenith observation directions, leaving only the Eastward direction in the

FHE field of view. Assumptions often need to be made that the neutral wind flow is consistent across the FOV of the FPI (approximately 500 km from opposing look direction peak emission locations). By considering small spatial scales, fluctuations become much more important, therefore we discount using the UAO FPI.

While the FHE radar does overlap all but the westward observation direction of the ANN FPI, the ANN FPI lies at a range from the FHE radar that often returns groundscatter. The ANN FPI is also within the FOV of the Christmas valley east (CVE) SuperDARN radar. While ionospheric scatter close to the ANN FPI from the CVE radar is often ionospheric, the quantity of observations are limited due to the ANN FPI being located at the far end of the CVE radar FOV ($\geq 1\frac{1}{2}$-hop scatter). The BKS Radar consistently, but not always, returns ionospheric scatter overhead of the ANN FPI. Although observations from multiple radars (BKS & CVE) would be ideal, requiring observations from both radars severely limits possible intervals to an extent that feasible studies are not possible. We therefore choose to only rely on the combination of the ANN FPI and BKS Radar for investigating the mid-latitude ion-neutral observations.

3.1.1 Interval Determination

While the BKS radar consistently returns ionospheric scatter, the ANN FPI observations are susceptible to being interrupted by terrestrial weather (cloud cover) and light from the moon. Geomagnetic storms are known drivers of strong ion motion, especially if the high-latitude twin-cell convection pattern expands equatorward. While coupling exists between the ionosphere/thermosphere and lower altitude atmosphere, geomagnetic activity does not always correlate with terrestrial weather effects. Intervals of known geomagnetic storm dates (Walach & Grocott, 2019) do not return quality ion/neutral observations from both the BKS radar and ANN FPI. We therefore undertook a manual search for co-incident high-quality ion-neutral observations from January 2012 to July 2015 (dates that both instruments were operational). Only a single interval of quality consistent measurements from

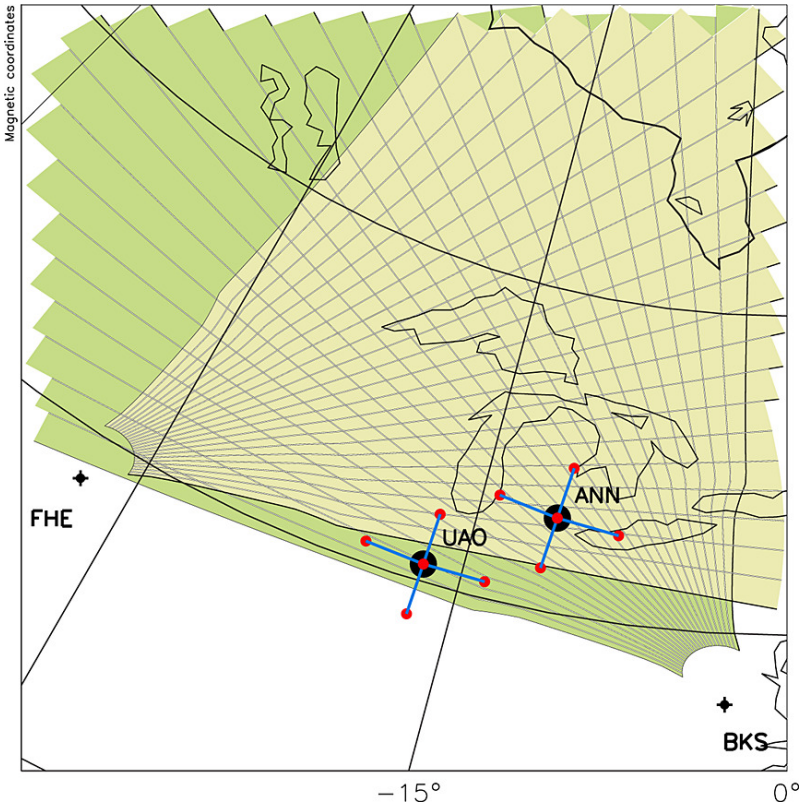

Figure 3.1: Field of views of the FHE (yellow area) and BKS (green area) SuperDARN radars and the ANN and UAO NATION FPIs. Black dots are the FPI locations, the red dots are the assumed peak emission locations of each look direction for the FPIs. From Joshi et al. (2015).

both instruments was identified; The night-time of 16 July 2014, which is therefore the focus of this study.

3.2 TIEGCM

TIEGCM was ran using the Weimer background electric potential model at the higher resolution of 2.5° × 2.5°. The inputs used were the historical geomagnetic conditions during the night of 16 July 2015 and are shown in Figure 3.2. Outputs were obtained every 20 minutes. Data from TIEGCM was taken at an altitude of 250km to match the altitudinal profile of the instrument observations.

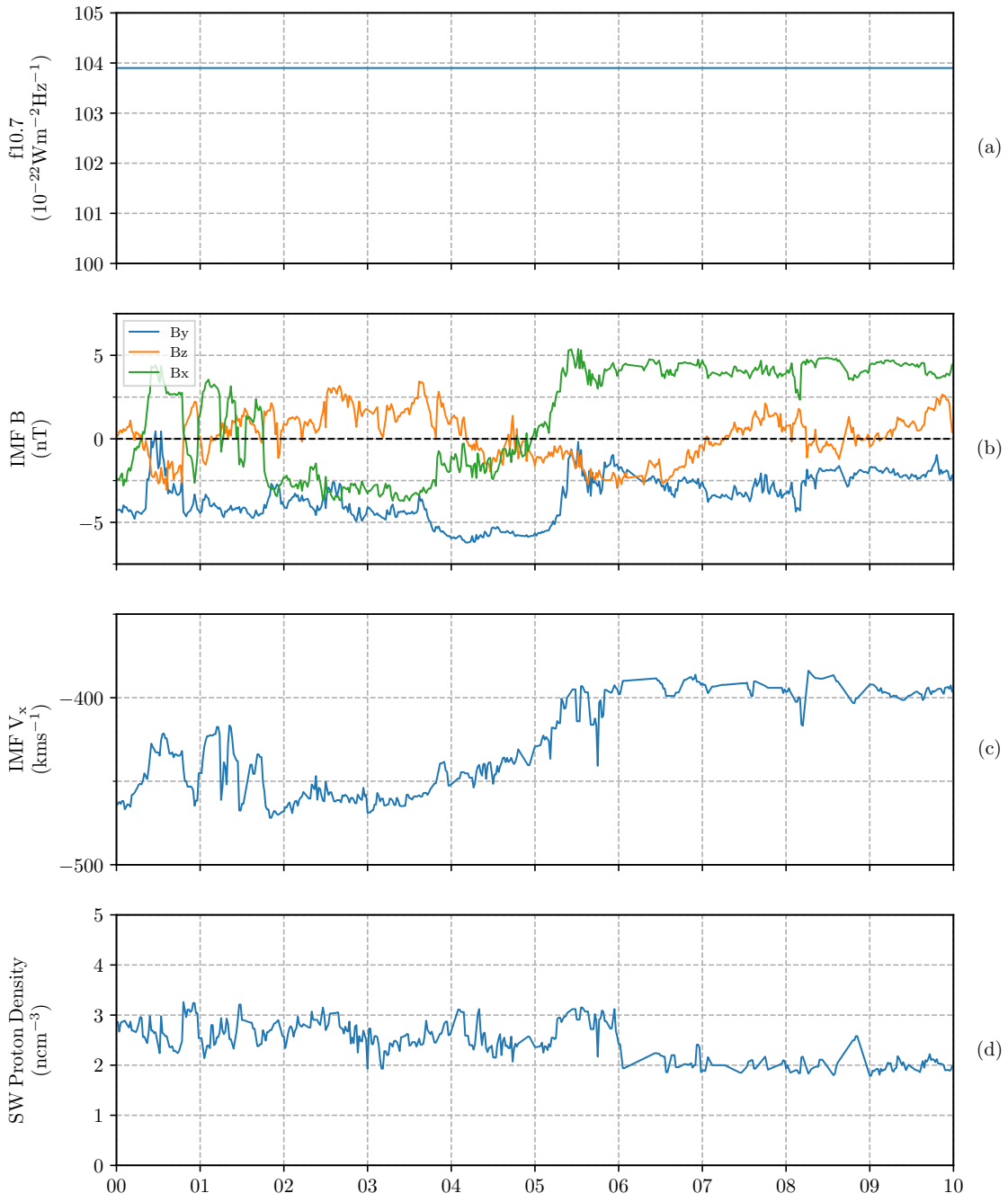

Figure 3.2: Geomagnetic inputs used to drive the TIEGCM model for the 16 July 2014 interval between 0000 and 1000 UT. (a) Shows the f10.7 solar index, (b) the IMF magnetic field strength in x, y, and z, (c) the solar wind speed in the x direction and (d) the solar wind proton density.

3.3 Geomagnetic Conditions

Figure 3.3 show the geomagnetic and solar wind conditions during the local night time (0 - 10 UT) of 16 July 2014. Panel 3.3a shows the solar wind speed while 3.3b presents the y and z components of the IMF. Of particular note is the slight negative IMF Bz between 0400 and 0700 UT indicating a southwards directed IMF, allowing low latitude magnetic reconnection to occur between the IMF and Earth's magnetic field. Panel 3.3c shows the auroral indices, signifying enhancements to the AL, AU and derived AE index coincident with the period of southwards IMF, indicating an increased intensity of the auroral Hall currents. The magnitude of the AL index is not particularly stronger than the AU index, indicating that no discernable substorm activity occured during this interval. The SYM-H index (3.3d) shows an increase in ring current intensity from 0500 UT while the ASYM-H index (3.3e) shows an increase in asymmetries in the ring current. Figure 3.3f shows the Kp index of between 1.7 and 2.3, which indicates minor geomagnetic activity throughout this period.

3.4 Ionospheric Plasma Observations

Figure 3.4a reproduces the IMF Bz data from Figure 3.3 followed by panels presenting measurements of ionospheric ion velocities for selected beams of the BKS SuperDARN radar between 0000-1000 UT, specifically beams 15 (b), 17 (c), 7 (d), 9 (e) and 17 (f) which are the beams that intersect through the FPI North, East, South, West and zenith assumed peak emission locations respectively. Negative velocities indicate line of sight ion motion away from the radar and positive velocities towards the radar. The velocity magnitude is given by the colour bar on the right. Portions of the observations that have been determined to be groundscatter according the Ribeiro et al. (2011) groundscatter algorithm have been marked in grey. The horizontal dashed lines across each beam range gate panel show the range gate where the assumed peak FPI emission point is located, calculated using the

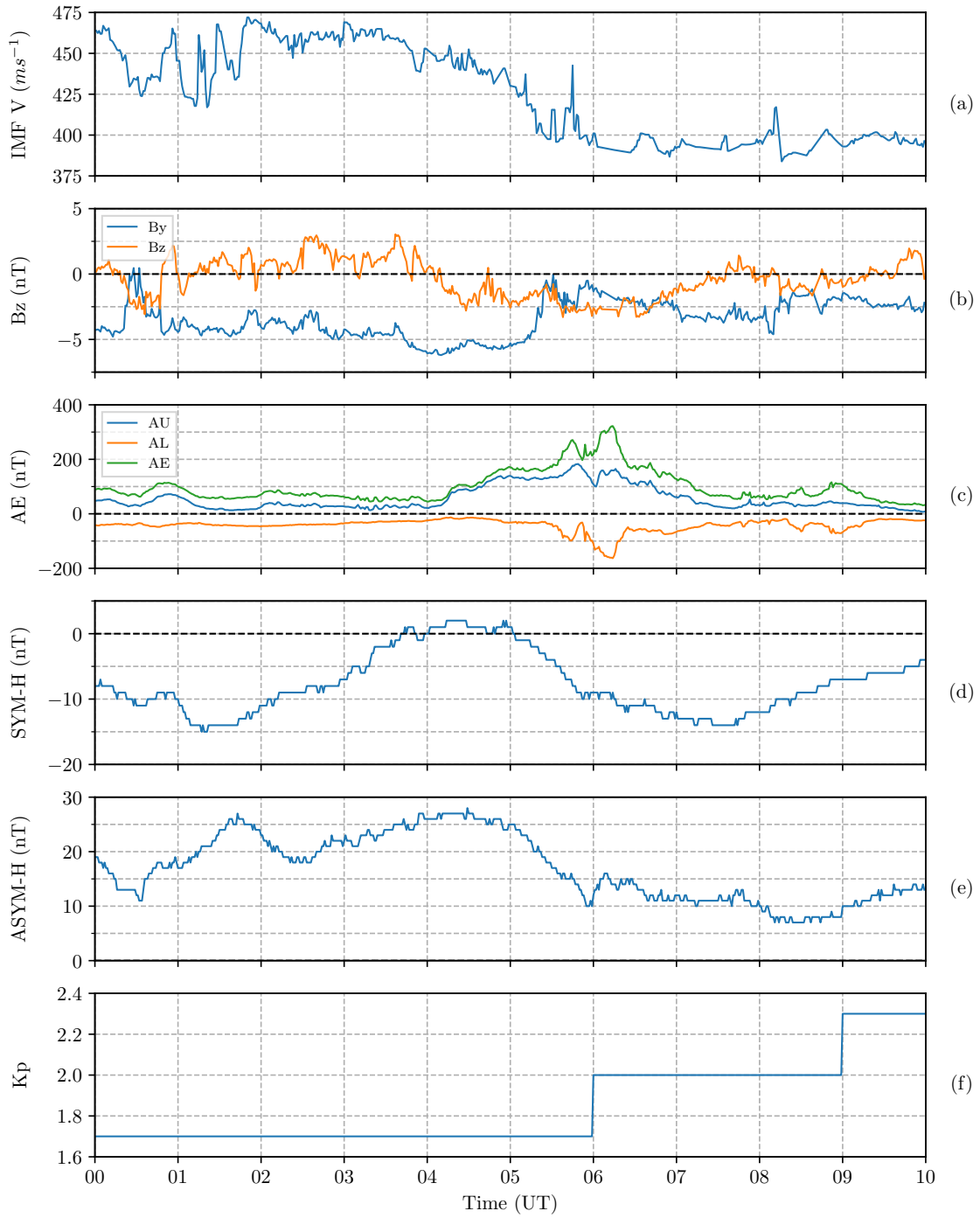

Figure 3.3: Geomagnetic conditions recorded during the nighttime interval (0000-1000 UT) of 16 July 2014. (a) Shows the IMF solar wind speed, v, (b) the IMF magnetic field strength in the y and z directions (c) the AU, AL and AE indices, (d) the SYM-H index, (e) the ASYM-H index and (f) the three hourly Kp index.

standard SuperDARN virtual height model, which uses ray tracing to estimate the altitude and location of returned radar beams.

Across all beam range gate panels we observe enhancements of the ion velocities during the southwards IMF Bz interval between 0400 and 0700 UT, with the most persistent flows traversing the southern and western part of the FPI region (panels d and e). The observed flows exceed -100ms^{-1}. At high-latitudes, these flows may not be considered to be particularly strong, but at mid-latitudes and especially during periods of low geomagnetic activity such as this, these magnitudes particularly stand out from the background quiet time velocities of typically less than 20 ms^{-1} magnitude. Beams 15 and 17 show positive flows $> 40\text{ms}^{-1}$ between 0500 and 0600 UT close to the FPI (panels b and c) emission locations, indicating a change in flow direction during these periods, whereas beams 7 and 9 (panels d and e) show the line of sight ion velocities remaining strongly negative. The flow direction switch only in two adjacent beams indicates that multiple flow channels exist during this interval.

To illustrate the spatial morphology and geographical mapping of the excited ion flows, Figure 3.5 presents a snapshot of SuperDARN flow data from all the north American mid-latitude SuperDARN radars at 0600 UT, superimposed with the Total Electron Content (TEC), field-aligned currents (from AMPERE) and particle precipitation flux (from DMSP).

The background of Figure 3.5 shows the $1^\circ \times 1^\circ$ geographic latitude by longitude height integrated TEC map, colored according to the white-black greyscale colour bar on the bottom. Dashed grey circles represent each 10° of geographic latitude. The AMPERE dataset shows the field aligned current densities, given by the blue-red colourscale; upward field aligned currents are in blue and downwards in red. Line of sight ion velocities from all the North American mid-latitude SuperDARN radars are plotted according to the purple-green colour bar, velocities $< |15|\text{ms}^{-1}$, which is the boundary for low/high velocity scatter in the Ribeiro et al. (2011) groundscatter algorithm, have been removed to improve visual clarity. Total particle precipitation

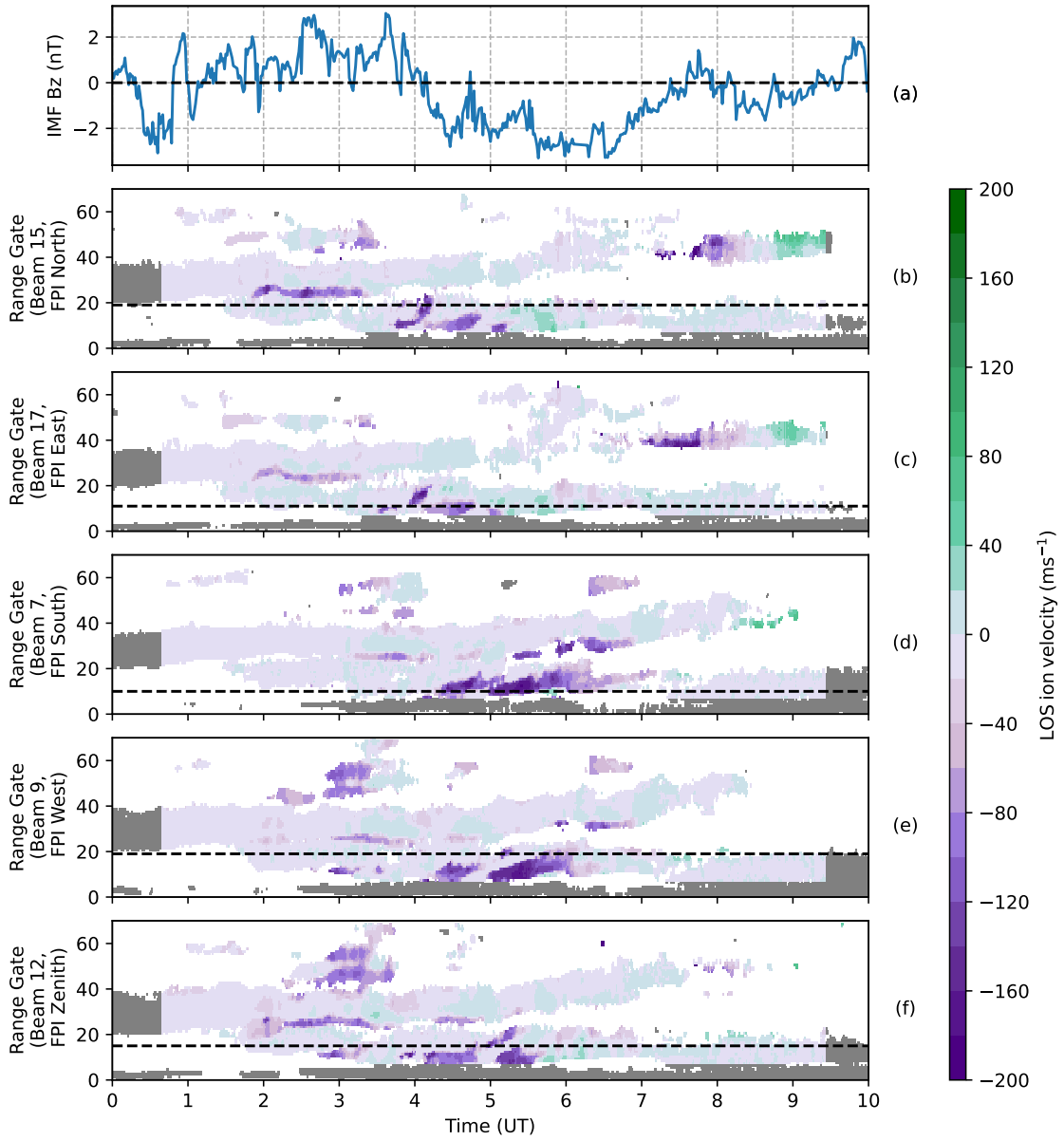

Figure 3.4: (a) shows the IMF Bz, followed by range gate, time plots for the BKS radar on 16 July 2014, with beams slicing through the assumed peak emission observation locations of the ANN FPI where beam 15 slices through north (b), 17 east (c), 7 south (d), 9 west (e) and 12 the zenith (e). Line of sight ion velocities follow the colour bar on the right, where positive values indicates motion towards the radar and negative away. Grey values are groundscatter. The dashed horizontal lines represent the range gate where the beam slices through the assumed cardinal peak emission of the ANN FPI.

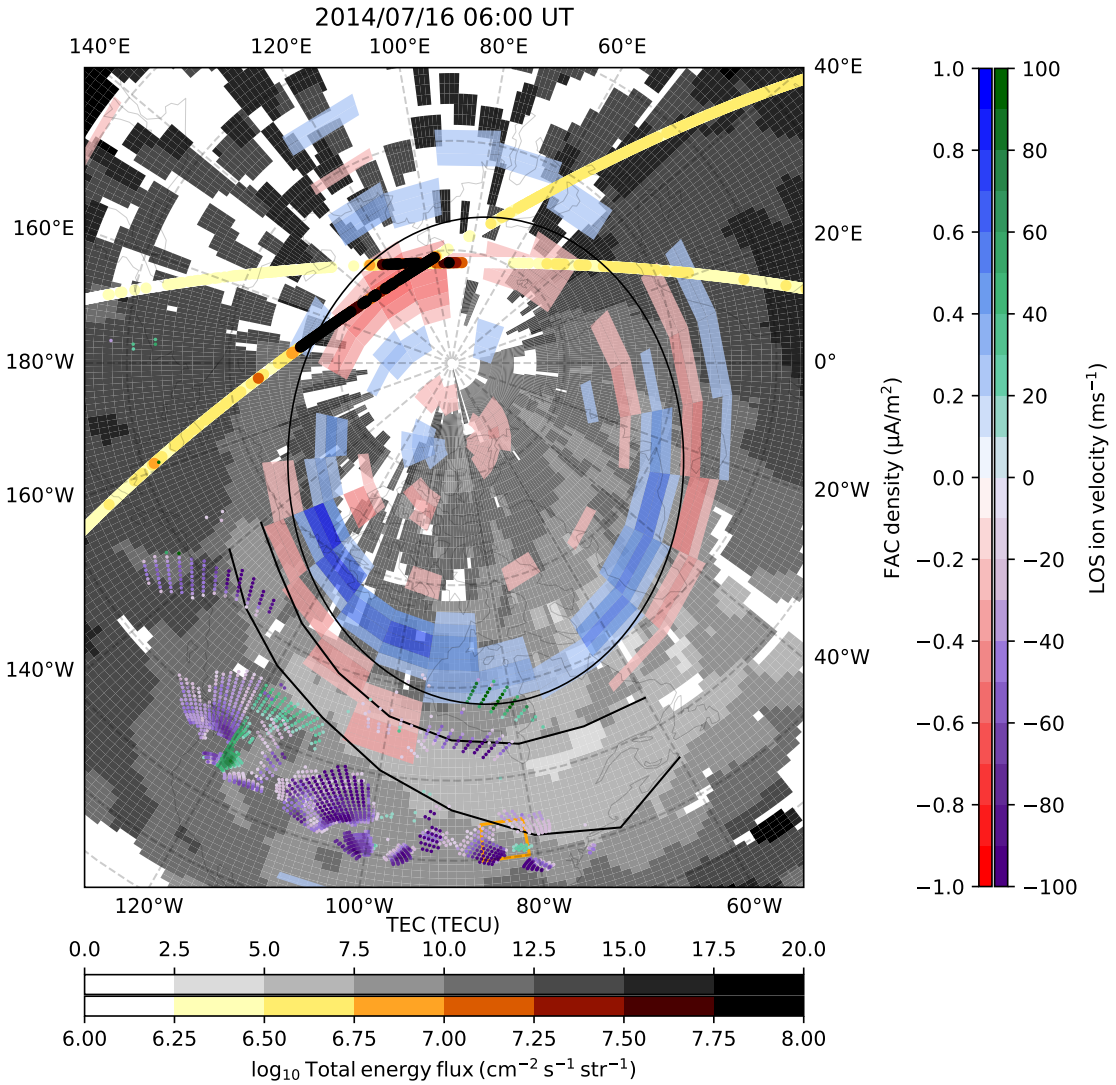

Figure 3.5: Geographic plot at 0600 UT 16 July 2016, showing the 1° × 1° latitude × longitude height integrated global total electron content according to the colorscale on the bottom. Dashed lines represent every 10° line of geographic latitude. Also shown is the AMPERE field aligned current density data, binned into 1° magnetic latitude by 1 hour MLT. Upward field aligned currents are given in blue and downwards in red with magnitude according to the red-blue colour bar. Further plotted are line of sight ion velocities from all the north American mid-latitude SuperDARN radars according to the purple-green colour bar, where absolute velocities $< 15\text{ms}^{-1}$ have been removed. Note that the line of sight SuperDARN ion velocities are colored so that positive values indicate an eastwards motion and negative a westwards directed flow.

fluxes ±40 minutes of 0600 UT from two DMSP satellites are plotted according to the white-yellow-black colour bar. Multiple radars are used in order to identify the spatial extent of the ionospheric scatter over the FPI, given as an orange box at around 85° west, 42° north, which traces the boundaries of the assumed peak neutral wind emission locations. The sign of the SuperDARN ion velocities have been altered from the presentation in Figure 3.4 such that here positive velocities indicates eastwards directed ion flows and negative westwards, which is determined based on the LOS measurements moving towards or away from a westwards or eastwards facing beam.

Figure 3.5 corresponds to 0600 UT (0100 local time at the ANN FPI), chosen due to a strong westwards flow in the south-west region of the FPI area. By tracing a westwards line that starts at 40°N ∼ 85°W and finishes at 45°N 105°W, we can see that the strong ion velocities close to the FPI persist through multiple ionospheric scatter ranges and into the FOV of more westwards located radars. No polar orbiting satellites crossed over the nightside region during this interval, which leaves some uncertainty in propogating a fitted equatorward auroral boundary to the nightside, necessitating the use of FAC data. The black circle indicates the boundary between the R1/R2 currents from the AMPERE dataset and at midnight is at approximately 63° geographic latitude, roughly 20° poleward of the FPI, we thus conclude that the observed flows are sub-auroral. From the TEC data we can see the formation of the ionospheric trough equatorward of the Region 2 currents and poleward of the FPI. The centre of the trough appears to start at ∼ 50° geographic latitude at local midnight and wraps around to ∼ 65° geographic latitude at the duskside. Black lines are used to mark the approximate poleward and equatorward boundaries of the trough, which at midnight are ∼ 5° equatorward of the R1/R2 boundary and latitudinally co-located with the location of the ANN FPI.

A more detailed presentation of the ion flow data from the BKS radar overlooking the ANN FPI is provided by Figure 3.6 which shows the line of sight velocities for the BKS radar beam range gates that contain the assumed cardinal peak emission

locations of the FPI. Panels, a, b, c, and d are for the beams that slice through the North, South, East and West locations respectively, at the range gate that contains the assumed peak emission location. The median filtered line of sight ion velocities are indicated in blue. Shaded regions indicate the errors in the filtered velocities. Compared in orange are the line of sight velocities from TIEGCM at the same geographic latitude and longitude as the beam range gates and projected into the same LOS direction as the radar beams.

The line of sight velocities show high activity between 0400 UT and 0700 UT across all beams. The northern and eastward observations show an early spike at 0400 UT with line of sight velocities of approximately 160 ms^{-1}. The southern observations show several spikes of high velocities from 0400 to 0630 UT peaking at $-180\,\mathrm{ms}^{-1}$ slightly after 0530 UT. The westward observations show high velocity spikes occurring between 0500 and 0600 UT, peaking at slightly less than $-150\mathrm{ms}^{-1}$. An interesting observation is that IMF Bz was directed northwards until after 0400 UT, however the north and southward BKS radar line of sight measurements show strong flows from as early as 0330 UT, and the eastwards observation starts to spike just before 0400 UT, indicating some driver other than the IMF Bz contributed to the fast ion motion. Furthermore, we can see that the westwards spikes begin ($\sim$ 0510 UT) shortly after the strong eastwards observations end ($\sim$ 0445 UT), which could indicate that it is the same patch of scatter that traverses across the FOV of the radar.

The TIEGCM line of sight resolved ion velocities follow the same general trend over each observation point. Differences between each region can be identified most notably at 0500 UT, where the east location is around 0 ms^{-1} while the southern point has model velocities of $\sim -40\,\mathrm{ms}^{-1}$. There are also slight variations in the magnitudes of the velocities due to the difference in the beam azimuth relative to TIEGCM's modelled three-dimensional ion flows. The TIEGCM line of sight ion velocities hover around their peak value of between $40 - 60\mathrm{ms}^{-1}$ in all cells from roughly 0100 to 0300 UT, well before the first observed ion velocity spikes

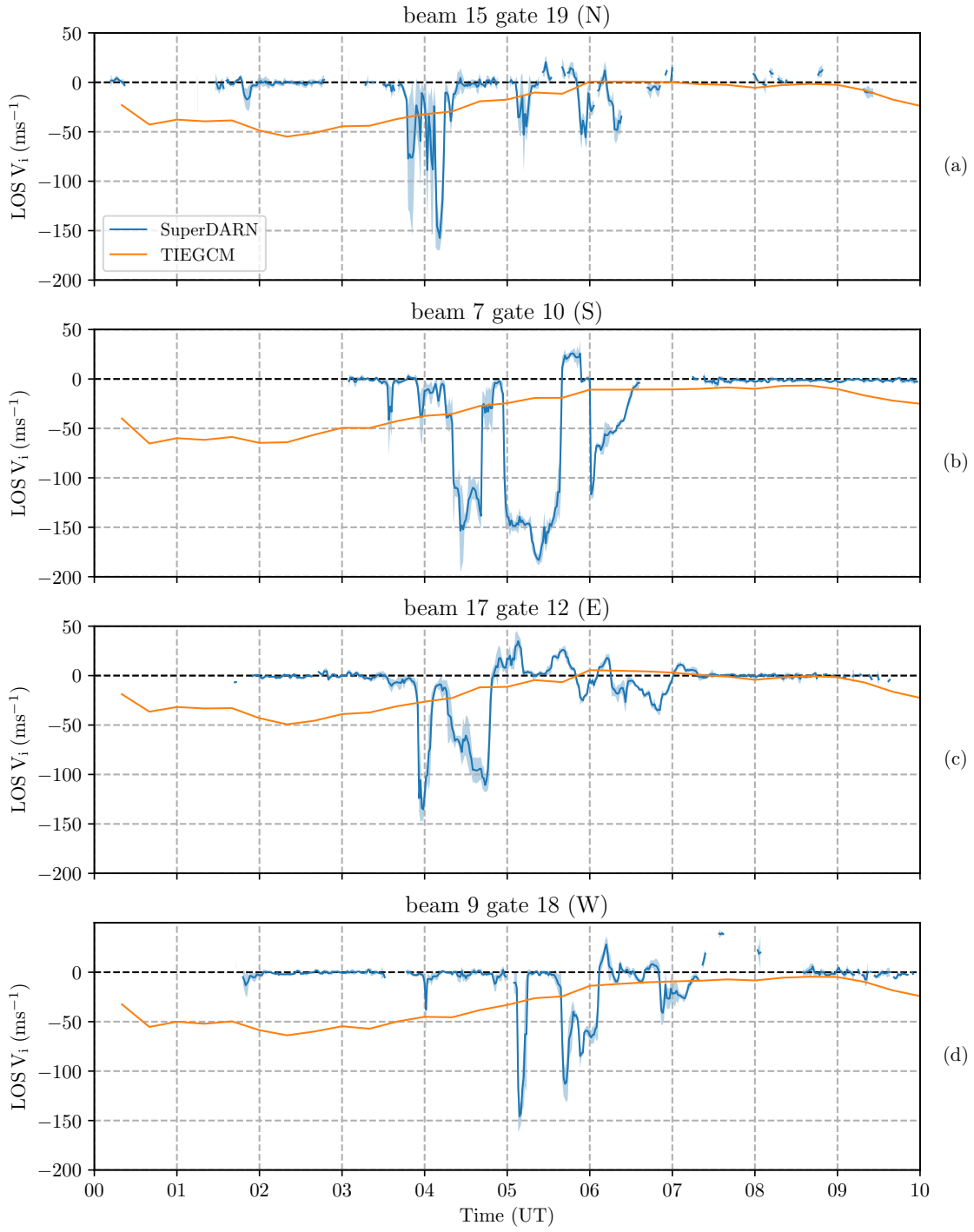

Figure 3.6: Line of sight ion velocities (blue) recorded from the BKS radar through 0000-1000 UT where the the velocities slice through the ANN FPI assumed peak emission locations, north (a), south (b), east (c) and west (d). Positive values indicate motion towards the radar and negative away. Errors are indicated by shaded regions. Also plotted are the equivalent line of sight ion velocities modelled by TIEGCM (orange).

and southwards directed IMF Bz and is much larger than the quasi zero-magnitude velocities recorded by the BKS radar. The TIEGCM velocities then decrease in magnitude, without any equivalent enhancements seen in the observations, until they are then close to $0\,\mathrm{ms}^{-1}$ at 0500 UT (for the east observation point) and 0700 UT (for the south observation point). At this time both the TIEGCM modelled velocities, and the BKS radar observed velocities are near zero, suggesting that no strong ion motion occurs between 0700 UT (or from 0500 UT at the eastwards point) and 1000 UT.

3.5 Neutral Observations

Figure 3.7 compares the FPI line of sight velocities (blue) with the neutral velocities modelled by TIEGCM at the assumed peak emission locations (orange). Panel a, shows the recorded ambient cloud temperature. Before 0300 UT the overhead skies are cloudy. Between 0300 UT and 0400 UT the temperature drops to below 20°C, indicating predominatly clear skies past 0400 UT, making this a suitable interval for using the FPI observations. Panels b, c, d and e show the North, South, East and West observation directions respectively. Since TIEGCM's output velocities are given as geographic meridional and zonal magnitudes, we take TIEGCM's meridional flow for the North and South observations and the zonal flow for the East and West observations at each assumed peak emission location. Using TIEGCM's vertical velocities, we then project them into the same elevation angle as observed by the FPI. Positive velocities indicate motion to the North (meridionally) and East (zonally). The zonal directions (East, West) show generally low velocities throughout the night-time period, the meridional velocities however, show a gradual increase, particularly after the IMF Bz turns southward after 0500 UT. The North facing observations especially, show a large increase in magnitude up to a peak value of $-150\,\mathrm{ms}^{-1}$ whereas the south facing observations peak at roughly $-80\mathrm{ms}^{-1}$. The zonal velocities show similar magnitudes with the East look direction peaking at $-30\,\mathrm{ms}^{-1}$ and the

west look direction at $-40\,\mathrm{ms}^{-1}$. Although in our ANN data, the south observations stop after 0630 UT and a 3 hour data gap occurs in the east observations between 0400 and 0700 UT due to the presence of the moon in that direction, the trend in the data between the opposing observation points are similar enough that we assume that there are no significant changes in the spatial distribution of the neutral wind flows over the ANN FPI. The vertical velocities are shown to fluctuate highly relative to their greatest magnitude, ranging from values of $5\,\mathrm{ms}^{-1}$ to $-20\,\mathrm{ms}^{-1}$.

When comparing TIEGCM's output, we find that the modelled meridional velocities are similar in magnitude to the observations. At the North location, TIEGCM's neutral velocities are closely aligned with these observations. TIEGCM's velocities at the southern location follow a similar pattern and although the observations stop after 0600 UT, the trend of increasing magnitude from 0200 UT is apparent in both the observed and modelled data. The meridional velocities then match well with our observations. Both TIEGCM's velocities at the East and West locations are shown to have a large difference to the observations. Although the trend of a somewhat sinusoidal variation in both the observed and modelled neutral velocities between 0000 UT and 0900 UT, peaking at 0500 UT, are somewhat similar, TIEGCM's velocities are significantly faster, especially at the peak. TIEGCM is more accurate when estimating the mid-latitude meridional neutral flows than in the zonal direction in this case.

3.6 Analysis and Discussion

In the previous section, we presented observations of the line of sight ion and neutral measurements and the equivalent modelled values from TIEGCM, here we will discuss the differences between them, and with reference to the geographical mapping of the field aligned current observations from AMPERE and identification of the mid-latitude ionospheric trough from the TEC data (Figure 3.5), we will consider the possible drivers behind the observations, which we shall now discuss.

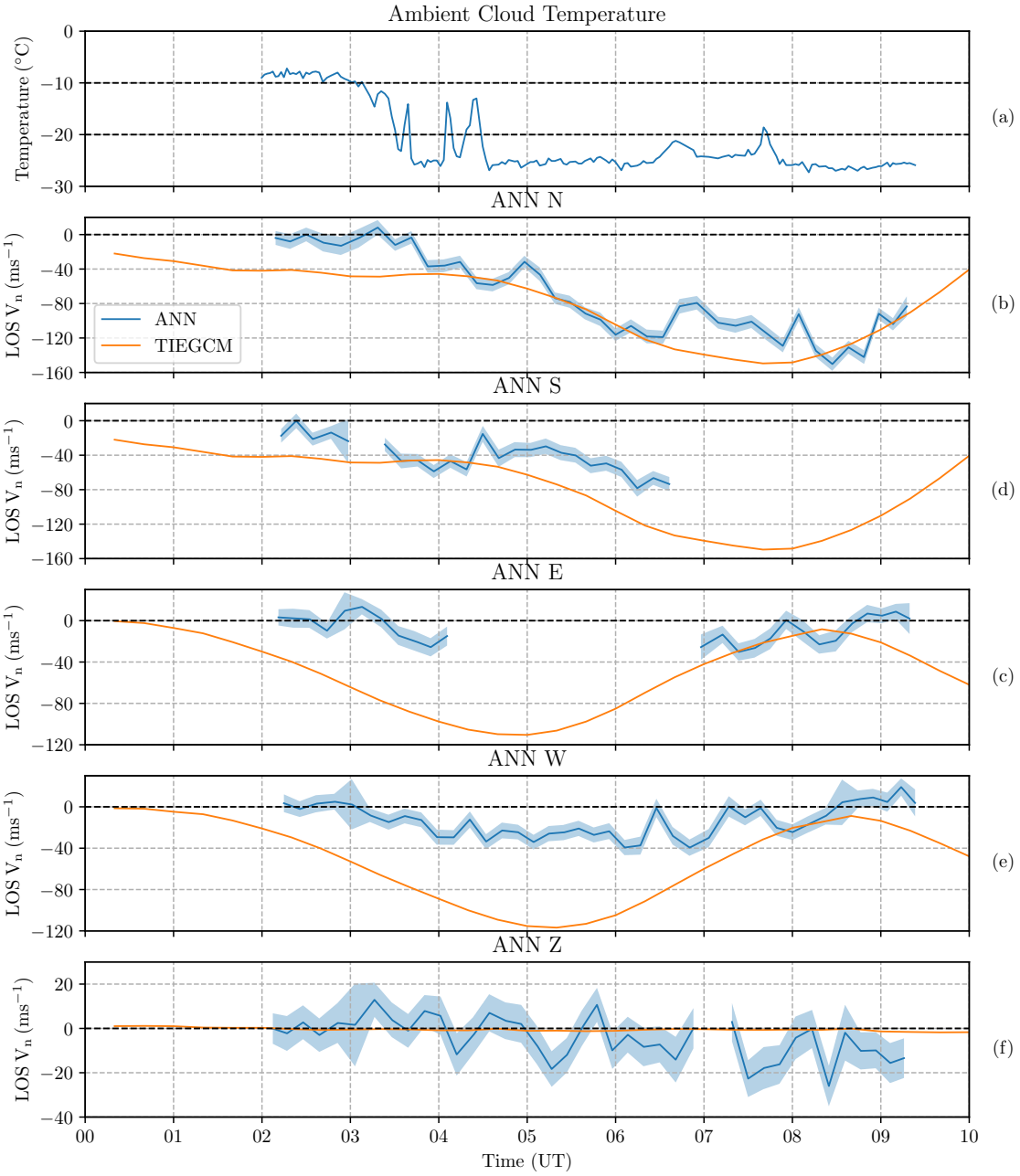

Figure 3.7: Ambient cloud temperature records (f) and the boundaries indicating cloudy ($> 10°$C), borderline ($10 - 20°$C), and clear ($< 20°$C) skies. Line of sight neutral velocities recorded by the ANN FPI (blue) through 0000-1000 UT are plotted for each cardinal observation direction, north (b), south (c), east (d), west (e) and the vertical velocity measured by the zenith (f). Shaded regions show the error in the ANN observations. Positive velocities indicate motion north/east/upwards. Gaps are left where sequential measurements are made more than 20 minutes apart. The neutral velocities from TIEGCM for the equivalent line of sight locations and directions are plotted in orange.

The strong westwards driven ion flows that are observed in Figure 3.5, which persist through a longitude range of approximately 30° from 80°W to 110°W, could indicate that the flows captured in the FPI region are part of a SAPS. Although this is a low geomagnetic activity event, Kunduri et al. (2017) found SAPS to occur 15% of the time in the nightside during relatively quiet conditions with velocities $\sim 100\text{ms}^{-1}$ (Kunduri et al., 2018). Confirmation of the ion flows (not) being part of SAPS would require ion flux measurements from satellites (Clausen et al., 2012; Grocott et al., 2011; Kunduri et al., 2017, 2018), however reliable POES data was not available during this interval and the DMSP satellites did not cross over the trough during the times of interest. Instead we compare with findings from Kunduri et al. (2017), which studied the latitudinal distribution of SAPS with correlation to the DST index. At 0600 UT (0030 MLT at the FPI location) the DST index was -1, which according to Kunduri et al. (2017), would place the mean SAPS position at 61° magnetic latitude ($\sim$ 51° geographic) with a minimum of 59° magnetic latitude ($\sim$ 49° geographic), which would still be at least 7° poleward of the FPI location. Furthermore Nagano et al. (2015) calculated a quantitative estimation of the lower latitudinal boundary for SAPS keyed by SYM-H, which during this interval reached a minimum of -20nT. According to Nagano et al. (2015) this would result in a lower latitude boundary for SAPS of $\sim$ 58° magnetic latitude ($\sim$ 48° geographic), still poleward of the FPI. Furthermore, Kunduri et al. (2021) also found SAPS latitudinal distribution to correlate strongly with the ionospheric trough, which during this interval lies poleward of the FPI. We therefore suggest that the observations during this interval are not likely due to SAPS. If the ion enhancements are not due to high-latitude convection or to a SAPS, they may instead be part of a persistent quiet-time mid-latitude nighttime feature (Clausen et al., 2012; Greenwald et al., 2006) that appears due to pressure gradient instabilities often found at the equatorward boundary of the ionospheric trough (Greenwald et al., 2006; Hudson & Kelley, 1976; Liu et al., 2021), which would align spatially with our observations.

Kilcommons et al. (2017) showed that the duskside and dawnside FAC systems

observed by AMPERE showed good correlation with the location of the auroral particle precipitation boundaries determined by DMSP. While the precipitating particle flux tracks from DMSP in Figure 3.5 do not cross over the nightside during the peak activity of this event, we can still observe if they map to FAC features. The midnight/duskside FAC boundary can be easily traced from 60° geographic North, 100° geographic West up to ∼ 75° geographic North, 140° geographic West. If we were to continue tracing that line then we can see that it corresponds very closely the point where the particle precipitation boundary is clearly observable at ∼ 85° geographic North, ∼ 180° geographic West. Furthermore, by looking at the dayside, we can clearly make out the three remaining particle precipitation boundaries, all at ∼ 80° geographic North and ∼ 125°, 100° and 80° geographic East. These three boundaries all correspond well to edge of the R1 current sheets. The equatorward boundaries of the particle precipitation data corresponds well to features of the R1/R2 FAC systems observed by Ampere during this interval. Using features of the AMPERE data is then highly suitable for determining the equatorward boundary of the auroral oval on the nightside.

In all directions the TIEGCM ion velocities are unable to model the enhancements observed by the BKS radar. As a global scale model, TIEGCM focuses on large-scale electrodynamics; microscale pressure gradient forces, such as those present at the boundaries of the ionospheric trough, and which we have determined to be the likely driver of the ion enhancements are not accounted for within TIEGCM. Expecting TIEGCM to be able to model these dynamics may then be unreasonable, as TIEGCM also lacks any large-scale sub-auroral dynamic drivers, such as the SAPS. Although we have determined SAPS to not be the responsible driver of the observations, if TIEGCM were capable of modelling SAPS, then secondary drivers such as large-scale pressure forces to the neutrals, depletion of electron content at the SAPS latitude and momentum exchanges to the neutrals could "force" TIEGCM into producing a more dynamical mid-latitude ionosphere. Studies by Wang et al. (2012) and Zhang et al. (2021) imposed SAPS ion velocities

to the sub-auroral region at all altitudes in TIEGCM, where the locations and magnitudes were determined by the Kp index. The background $\mathbf{E} \times \mathbf{B}$ drift at sub-auroral regions corresponding to SAPS latitudes were replaced by the imposed SAPS ion velocities without any other changes, thus the global ionosphere-thermosphere system in their (SAPS-TIEGCM) studies remained self-consistent. We ran the SAPS-TIEGCM model from Zhang et al. (2021) and noted the differences in the ion velocities at the location of the FPI, plotted in Figure 3.8.

The top row of Figure 3.8 shows large scale maps of the zonally directed ion velocities modelled by the standard version of TIEGCM (a) with the modified SAPS-TIEGCM version (b) at 0600 UT according to the purple green colour bar. The red vertical line shows the geographic longitude of MLT midnight, which should be close to the minimum SAPS latitude. The orange dot shows the location of the ANN FPI. Positive values indicates ion motion towards the east and negative west. The high-latitude twin-cell convection pattern can be seen above 60° geographic latitude. The imposed SAPS velocities can be observed just equatorward of the high-latitude pattern in the SAPS-TIEGCM run. Each pixel corresponds to a single $2.5° \times 2.5°$ latitude longitude cell, giving the SAPS channel an approximate 12.5° latitudinal width. Despite this extraordinarily large width, the channel lies at least one full cell poleward of the ANN FPI where the cells immediately surrounding the FPI do not appear to have much difference in their velocities between TIEGCM versions. The bottom row investigates this further. The meridional and zonal velocities at the ANN FPI are plotted between 0430 and 0830 UT, which are the inclusive times where TIEGCM's geomagnetic drivers were sufficient to turn on the SAPS model within SAPS-TIEGCM. The standard version of TIEGCM is plotted in panel c, while the SAPS version in panel d. Positive values indicate motion northwards (meridionally) and eastwards (zonally). The variations in the velocities at the FPI between the standard and SAPS-TIEGCM version are so slight that they are essentially negligible. The SAPS-TIEGCM version has a large impact on the mid-latitude sub-auroral ion motion over a large latitudinal range. But, despite the

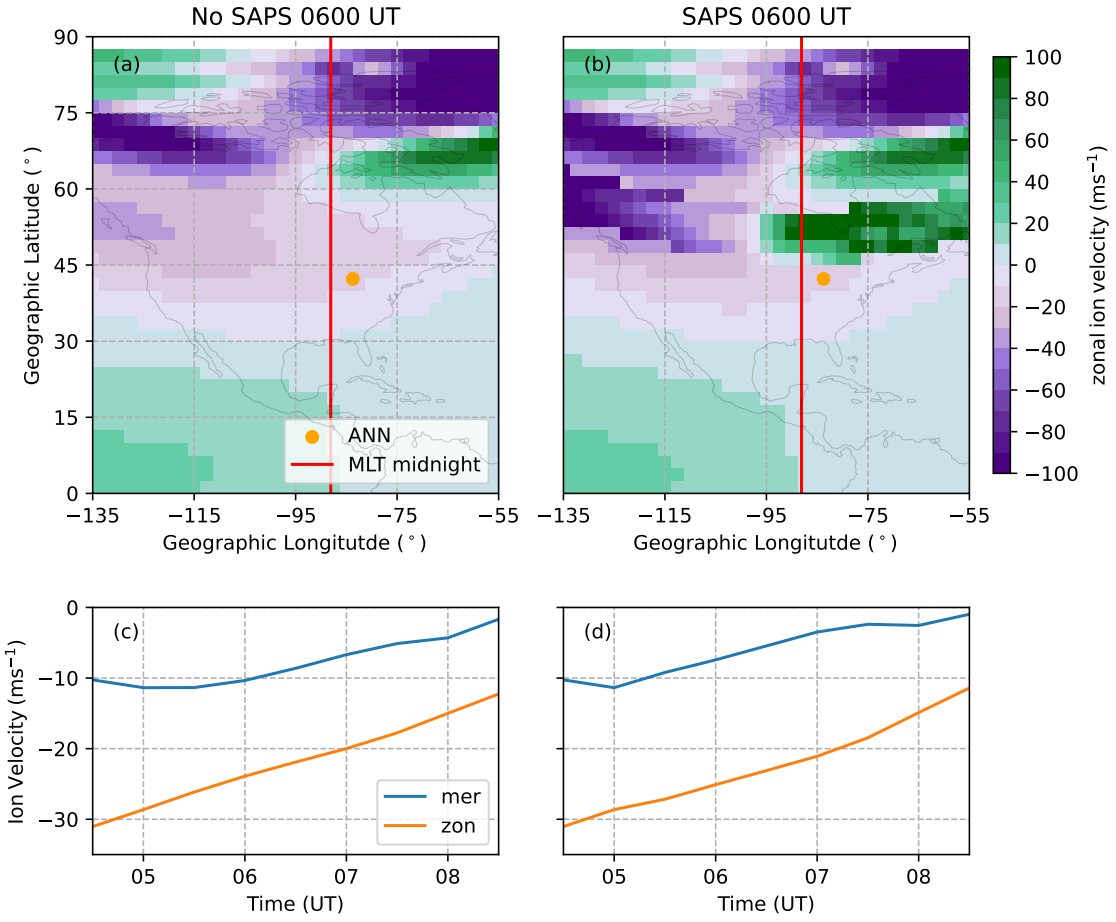

Figure 3.8: The top row shows large scale maps of the TIEGCM zonal ion velocities for the standard model (a) and the SAPS-TIEGCM version (b) according to the colour bar on the right. Positive values indicate motion to the East. The orange dot shows the location of the ANN FPI and the vertical red line is the longitude that corresponds to MLT midnight. The bottom row shows the meridional and zonal ion velocities at the location of the ANN FPI for the standard model (c) and SAPS-TIEGCM version (d) from 0430 to 0830 UT. Positive values indicates motion eastward (zonally) and northward (meridionally).

ANN FPI being only 2 cells equatorward of the SAPS channel, there is no meaningful impact to the velocities at the FPI. It appears then, that large-scale dynamics within TIEGCM has little ability to propagate any affects or feedback mechanisms across the ionosphere. The addition of more large-scale drivers within TIEGCM may not be enough to improve its modelling performance to regions implicitly affected by those dynamics. Although TIEGCM's maximum resolution of $2.5° \times 2.5°$ is rather coarse and potentially a limiting factor, it is clear that to better represent the highly dynamic nature of the mid-latitude ionosphere, a better representation of the micro-scale electrodynamics and feedback mechanisms are required within the model.

3.7 Summary

The night-time of 16 July 2014 was identified as a single interval where high-quality persistent co-incident F-region ion and neutral velocity observations were made by the mid-latitude BKS SuperDARN radar and ANN FPI. Despite low levels of geomagnetic activity, high ion velocities $> 100\,\mathrm{ms}^{-1}$ were observed from the whole chain of mid-latitude North-American SuperDARN radars. Specifically, the BKS radar observed multiple spikes of ion velocities $> 150\,\mathrm{ms}^{-1}$ between 0400 UT and 0700 UT. Although the neutral velocities recorded by the ANN FPI did not spike in the same manner as the ion velocities the meridional neutral velocities recorded gradual increases from $0\,\mathrm{ms}^{-1}$ at 0200 UT to approximately $-150\,\mathrm{ms}^{-1}$ 0830 UT.

Nightside FAC measurements from AMPERE indicate the observed ion enhancements by the BKS radar to be equatorward of the R1/R2 FAC boundary. Furthermore, precipitating particle flux measurements from DMSP satellites show strong correlation between the particle precipitation boundaries of the auroral oval with the R1/R2 FAC boundaries recorded by AMPERE, we therefore conclude the observed flows to be sub-auroral. TEC data from GNSS indicates the mid-latitude ionospheric trough to be poleward of the FPI. Placement of the trough, alongside statistical patterns of latitudinal distributions of SAPS eliminate the possibility of

the ion flows to be due to a SAPS. We suggest that the ion flows are driven by pressure gradient forces often found at the equatorward edge of the ionospheric trough, which aligns spatially with our observations.

Modelled ion velocities, resolved into the same LOS directions as observed by the BKS radar from TIEGCM followed a uniform pattern throughout the interval. TIEGCM's ion velocities started at approximately -50 ms^{-1} at 0000 UT and decreased to near zero at 0800 UT with no fluctuations or spikes to the their magnitudes. Adding a large scale mid-latitude driver by imposing a SAPS model into TIEGCM had a negligible impact on the ion velocities at the FPI despite its spatial proximity. We suggest that a better representation of the ionospheric forces at the mid-latitudes is needed, especially for small-scale forces. TIEGCM's modelled neutral velocities performed well compared to the meridional neutral observations, matching both the magnitude and trend closely, it does however significantly overestimate the velocities in the zonal directions, reporting velocities approximately 3 times large than observed at 0500 UT.

The following Chapter uses the observations in this study to estimate and compare the Joule heating rates from both the observational and modelled data. We estimate the overall two-dimensional flows of the observed ion and neutral winds and the contribution and impact each parameter has on both the observed and modelled Joule heating rates.

Chapter 4

Estimation of the Quiet Time Sub-Auroral Joule Heating

This chapter contains work from the published article:

Day, E. K., Grocott, A., Walach, M.-T., Wild, J. A., Lu, G., Ruohoniemi, J. M., & Coster, A. J. (2024). Observation of quiet-time mid-latitude joule heating and comparisons with the tiegcm simulation. *Journal of Geophysical Research: Space Physics*, *129*. https://doi.org/10.1029/2024JA032578

Works from this chapter resulted in contributions to the open-source software package PyDARN:

Martin, C. J., Shi, X., Schmidt, M. T., Day, E. K., Bland, E. C., Khanal, K., Billett, D. D., Kunduri, B. S. R., Tholley, F., Frissell, N., Coyle, S., R, A. R., T, J. K., & K, J. K. (2023). Pydarn. https://doi.org/10.5281/zenodo.7767590

4.1 Introduction

The previous study provides a good insight into the magnitudes of ion and neutral velocities modelled by TIEGCM compared to ion and neutral observations during a quiet-time night-time period at the mid-latitudes. The LOS observations from

that study provided a good analysis opportunity to compare the co-located plasma and neutral flows, however it did not allow for a calculation of the Joule heating. The second term in the Joule heating equation (1.84), Q_{w1}, requires knowledge of the ion/neutral direction relative to each other to properly account for collisional exchanges between them. The LOS observations are but a component of a full flow viewed in a particular direction. Several techniques exist to estimate the two-dimensional ion flow velocity from LOS SuperDARN observations. We consider using two main techniques, high-latitude spherical harmonic mapping, and L-shell fitting, for resolving the LOS ion velocities from chapter 3 into two-dimensions, obtaining both their magnitude and direction. We also describe the method used to obtain the full velocities of the neutral velocities from chapter 3. We shall then use the fitted velocities to calculate the Joule heating rates during the night-time interval of 16 July 2014 and compare them to the modelled outputs from TIEGCM.

4.1.1 High-Latitude Spherical Harmonic Mapping

Two-dimensional ion velocity estimates from SuperDARN data are typically derived by using a spherical harmonic fitting technique (Ruohoniemi & Baker, 1998) to derive a global electric potential map. A solution is employed that finds the form of the electric potential, Φ, which best fits LOS velocities measured by all SuperDARN radars to a representative high-latitude convection pattern, assuming that Φ is related to the $\mathbf{E} \times \mathbf{B}$ drift through the relations

$$\mathbf{E} = \nabla\Phi \tag{4.1}$$

and,

$$\mathbf{v} = \frac{\mathbf{E} \times \mathbf{B}}{B^2} \tag{4.2}$$

All LOS velocities are mapped into equispatial 111 km $\times$ 111 km AACGM latitude by longitude cells. The velocities are then transformed into a MLAT-MLT grid and overlapping vectors are merged using a least-squares linear regression, producing "gridded" velocities. A low latitude boundary for the high-latitude

potential, the Heppner-Maynard boundary (HMB) (Heppner & Maynard, 1987), is determined by the lowest magnetic latitude where 3 LOS velocities from all SuperDARN radars exceed 100 ms^{-1}. The electric potential below this point is assumed to be zero and vectors below this latitude are discarded. A spherical harmonic fitting technique is then performed in order to conform the gridded velocities to the high-latitude potential pattern (Ruohoniemi & Baker, 1998), following the equation,

$$\Phi(\theta,\phi) = \sum_{l=0}^{L} \sum_{m=0}^{min(l,M)} \left[A_{lm}(t)\cos m\phi + B_{lm}\sin m\phi\right] P_l^m \cos\theta \tag{4.3}$$

where P_l^m are legendre polynomials and l and m are the order and degree of the expansions respectively (L and M are the maximum values). A_l^m and B_l^m are complex coefficients. The values of l and m set the global scale characteristics of the fit, where higher orders are able to resolve smaller scale structures. In this study we use a value of 8 for the order, which is suitable for studying global scale data with a spatially higher structural resolution.

Statistical patterns of the high-latitude potential (Cousins & Shepherd, 2010; Ruohoniemi & Greenwald, 1996; Thomas & Shepherd, 2018) are used (with lower weightings than observed gridded velocities) to constrain the fit in regions of poor coverage. The aim of the spherical harmonic fitting method is to conform the LOS velocities to the high-latitude twin-cell convection pattern. Although we have determined the ion observations in chapter 3 to be sub-auroral and therefore not part of the high-latitude twin cell convection pattern, the nature of determining the HMB often results in sub-auroral ion motion being included within the fits, and the statistical patterns that are used to constrain them. There is some argument then, that this method has some ability to constrain sub-auroral ion motion towards representative sub-auroral ion flows. We therefore consider using this method for determining the two-dimension ion flows co-incident over the FPI.

Running the spherical harmonic fitting method is fairly simple. The SuperDARN radio software toolkit (Thomas et al., 2022) and PyDARN (Martin et al., 2023) are

specialist software packages that easily allows the conversion of fitacf LOS data into the "gridded" format and running of the spherical harmonic fitting method. The fitted velocity over the ANN FPI can be readily obtained after running the processes. As discussed below, we ultimately reject the spherical harmonic fitting method for our interval in favour of a variant of the L-shell fitting method.

4.1.2 L-Shell Fitting

In L-shell fitting (Ruohoniemi et al., 1989; Villain et al., 1987), observed ion flows are assumed to be constant across a given L-shell. If such a flow is observed by a SuperDARN radar then the line of sight velocities vary azimuthally across the beams such that if a beam crosses the flow perpendicular to the flow direction it will return with a zero velocity. Conversely, if the beam is sounding in the direction parallel/anti-parallel to the full flow then it will return its full velocity. A cosine curve can be fitted to the line of sight velocities against their beam azimuths, where the magnitude of the fit provides the full 2D ion flow perpendicular to the magnetic field. Positive velocities indicate motion towards the radar and negative away. The flow direction can thus be determined according to the look directions of the (theoretical) beams which are parallel/anti-parallel to the flow.

L-shell fitting techniques have often been used to estimate mid-latitude ion velocities (Clausen et al., 2012; Kunduri et al., 2018; Maimaiti et al., 2018). It does however, require tailoring to define the area to select the LOS velocities to perform the cosine fit, which we shall refer to as the "fitting area", to the needs of each study. Maimaiti et al. (2018) used L-shell fitting within areas of 1° magnetic latitude × 7 min MLT to accrue statistical patterns of mid-latitude ionospheric scatter. Kunduri et al. (2018) instead used fitting areas of 0.5° magnetic latitude and 1 hour MLT (but could expand up to 3 hours in MLT if data availability within 1 hour was poor) to capture the latitudinally narrow but longitudinally wide flows of SAPS in a statistical study. Figure 4.1 shows an example of the fits performed on LOS data in their study, which displays the excellent nature of the sinusoidal

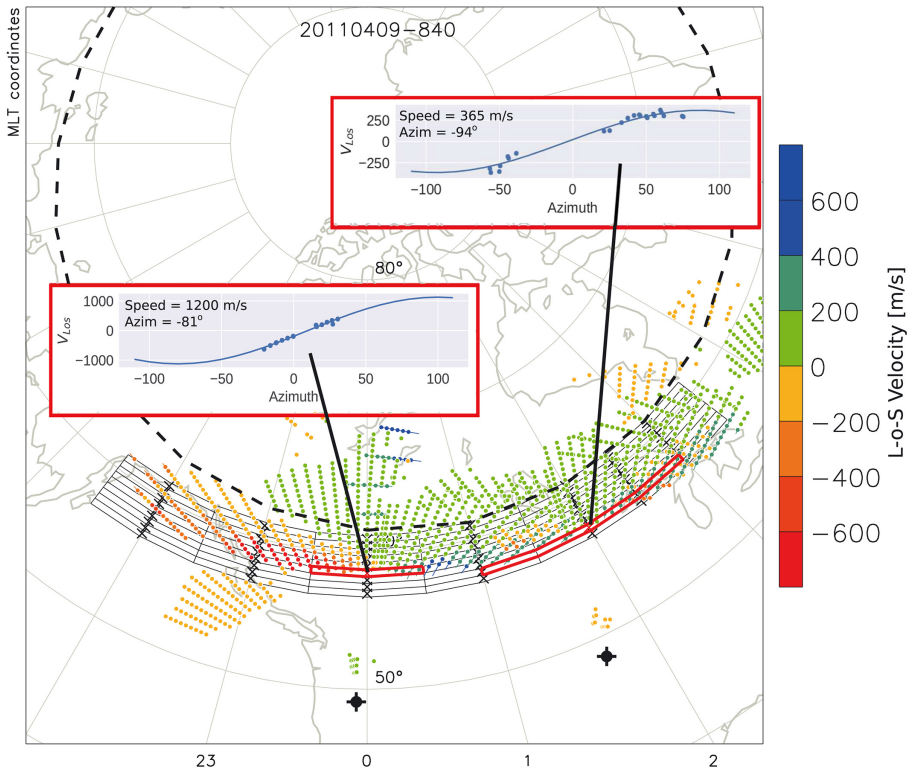

Figure 4.1: LOS ion velocities recorded by all the North America mid-latitude SuperDARN radars during a SAPS event on 9 April 2011 at 0840 UT according to the colour bar on the right. Black boxes show MLAT-MLT cells defining individual L-shell fitting areas. Insets show example cosine fits to LOS ion velocities against their beam azimuths for two cells, highlighted by the red boxes. From Kunduri et al. (2018).

dependence on LOS velocity with beam azimuth for a constant flow.

Clausen et al. (2012) used L-shell fitting to study a SAPS event and obtained the velocities for the fit by using the highest velocity magnitude in each beam of paired SuperDARN radar FOV's. The direction perpendicular to the ion flow returns a LOS velocity of 0 ms^{-1} while either side of this point, velocities will have opposing signs. As the study by Clausen et al. (2012) used observational data around this point, they fit their LOS velocities against beam azimuth to a straight line, due to being approximate to the line through the nodes of a sinusoid. These three studies each show that slightly different methods are required depending on the needs of

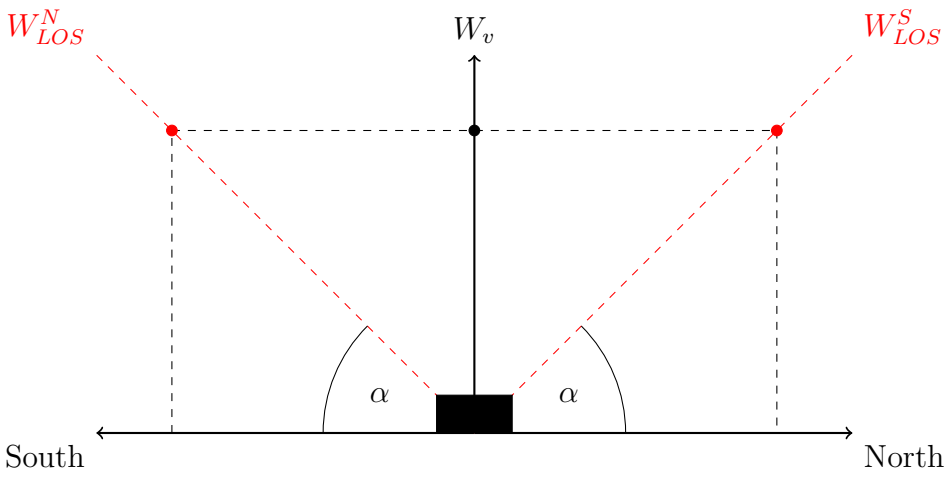

Figure 4.2: Schematic of the FPI geometry in the North-South plane. The black box depicts the FPI site, the angled red-dashed lines show the line of sight observations made in the North (W^N_{LOS}), South (W^S_{LOS}) directions while the black solid line indicates the line of sight observations in the vertical (W_v) direction. The dots mark the assumed location of the observations based on peak emission altitudes of 250 km. The angles of the line of sight observations are given by α.

the individual study. Section 4.2 will detail the approach that we take to tailor the L-shell fitting technique to be suitable for fitting the LOS ion velocity data captured in chapter 3.

4.1.3 Neutral Winds

Figure 4.2 gives an overview of the direction of the observations made by the FPI, given by the black box, in the North-South plane. Line of sight observations are made to the North (W^N_{LOS}) and South (W^S_{LOS}), given by the red-dashed lines. The vertical line of sight velocity (W_v) is also obtained. We assume the observations are made at the peak emission height, 250 km, and by using the inclination angle of the observations (given by α in Figure 4.2), we calculate the horizontal components of each cardinal observation, W^X_h, where X is either North, South, East or West by using equation 4.4 (Makela et al., 2012),

$$W_h^X = \frac{W_{LOS}^X - W_v \sin(\alpha)}{\cos(\alpha)} \tag{4.4}$$

where W_{LOS}^X is the line-of-sight Doppler velocity for the X cardinal direction. W_v is the vertical neutral velocity which we assume is constant across all cardinal locations. α is the elevation angle of the line of sight measurements, which during this interval was 45°. W_h^X is obtained for each cardinal direction. The signs of the velocities are then changed such that positive velocities are directed either northwards (meridionally) or eastwards (zonally). Because the FPI observations are made at different times with irregular cadences for each cardinal location, we linearly interpolate the observations so that the cadence of opposing North/South and East/West observations match. If only one opposing cardinal measurement is available at a given time, such as after 0600 UT, where no southwards observations were taken, we use the measurement we do have as the full meridional/zonal flow.

Due to the magnetic field inclination, it is important that calculations of the coupling between the ions and neutrals are made in the same plane relative to each other. As there is no estimate of the ion velocity in the direction parallel to the magnetic field, it is not possible to calculate the ion velocity in the plane parallel to the Earth's surface. Since the FPI observes the geographic horizontal and vertical directions, the neutral wind velocity is obtainable fully in three-dimensions. By applying the three-dimensional rotation matrix transformation given by equation 4.5,

$$\begin{bmatrix} N_{Bz} \\ N_{Bx} \\ N_{By} \end{bmatrix} = \begin{bmatrix} N_{mer} \\ N_{zon} \\ N_{ver} \end{bmatrix} \begin{bmatrix} \cos(\theta) & -\sin(\theta) & 0 \\ \sin(\theta) & \cos(\theta) & 0 \\ 0 & 0 & 1 \end{bmatrix} \begin{bmatrix} \cos(\phi) & 0 & \sin(\phi) \\ 0 & 1 & 0 \\ -\sin(\phi) & 0 & \cos(\phi) \end{bmatrix} \tag{4.5}$$

where N_{Bz}, N_{Bx} and N_{By} are the neutral wind components in the z, x, and y directions in magnetic field aligned coordinates respectively, and defining the magnetic field to be in the z direction, we can deduce the neutral wind flow in the plane of the plasma flows (the $\mathbf{E} \times \mathbf{B}$ direction). N_{mer}, N_{zon} & N_{ver} are the geographic meridional, zonal and vertical neutral wind components, θ is the angle

subtended by the great circle lines connecting the FPI location to the geographic and magnetic north pole, while ϕ is the angle subtended between the magnetic field and the plane horizontal to Earth's surface at the location of the FPI.

4.2 Tailoring the L-shell Fitting Method

We start by defining a fixed rectangle around the FPI where the centre of each side intersects the assumed peak cardinal emission locations (the same area which is shown by the orange box in Figure 3.5). As plasma motion is driven relative to the magnetic field orientation, the fitting area should be bound by lines drawn in magnetic coordinates. At the location of the ANN FPI the latitudinal line connecting the geographic poles is approximately parallel to the line that connects the magnetic poles (see central USA in Figure 2.7). At the ANN FPI then, the lines parallel to the magnetic field can be drawn in the geographic frame. LOS ion velocities are time-integrated over 10 minutes to reduce temporal variability. Since we aim to capture the motion of active scatter we only select the maximum velocity from each beam within the area. We then fit a cosine curve to the magnitude of the selected ion velocities against their beam azimuths. A radar beam pointing with a beam azimuth of 0° points to magnetic North while theoretical beams pointing at +90° or −90∘ will point directly East or West respectively. In the scenario where an observed ion flow is travelling along an East/West line the beam pointing at 0°, perpendicular to the flow will return a zero velocity in the line of sight direction of the beam. The theoretical beams at ±90° will observe the maximum flow (either with a positive or negative magnitude depending on its direction). The full phase width of the sinusoidal fit is therefore fixed to 360° so that the maximum and minimum velocities return with an azimuth separation of 90° as per the geometry of the radar. Figure 4.3 (top) shows a snapshot of the fitacf LOS velocities from 0521 UT to 0531 UT with the fit from the selected LOS ion velocities (below).

Non-F-region ionospheric scatter or groundscatter identified by the Ribeiro et

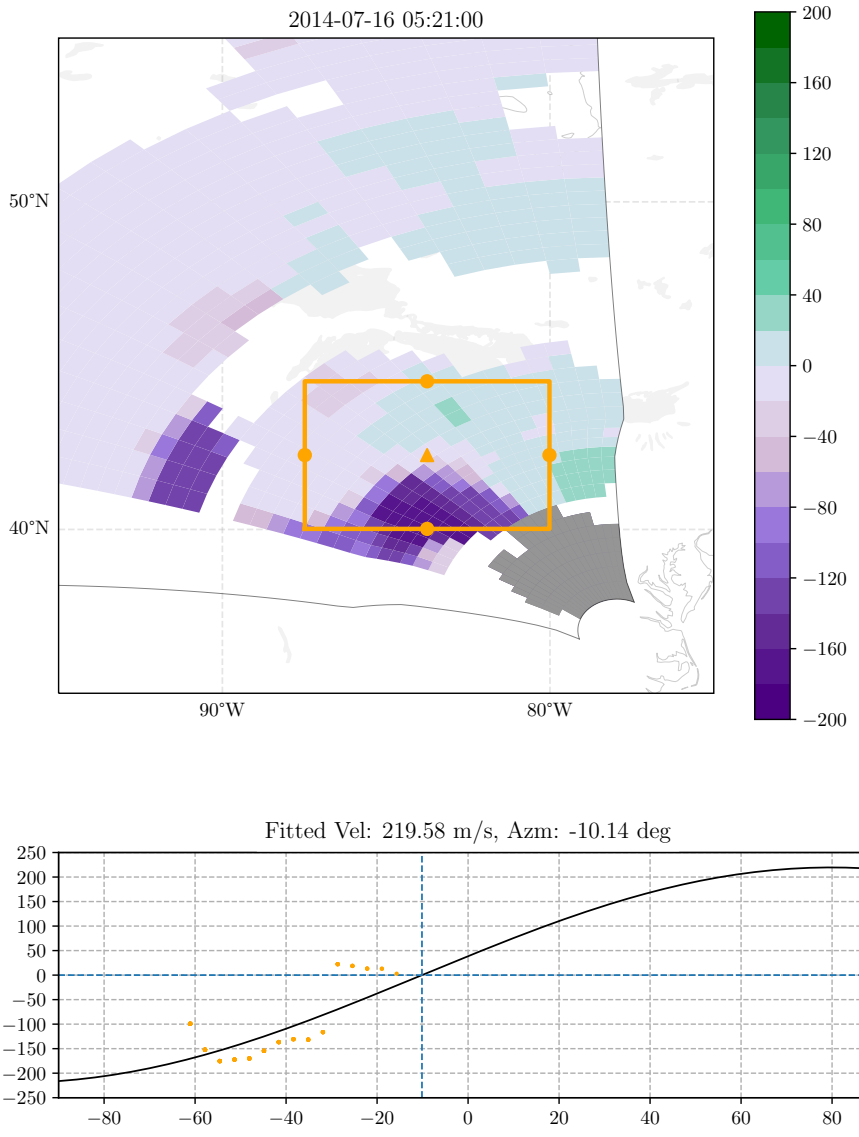

Figure 4.3: 10-minutely integrated scan starting from 0521 UT of the BKS radar plotted on a geographic map in the top panel. Ion velocities are colour coded according to the colour bar on the right, where positive velocities indicate motion towards the radar and negative away. Non-ionospheric scatter as marked by the Ribeiro algorithm is coloured grey. The orange triangle represents the location of the ANN FPI, and the orange dots mark the assumed peak neutral wind emission locations. The fitting area is outlined as an orange box around the FPI. Below shows the line of sight ion velocities plotted as orange dots against their beam azimuth. The black line represents the least-squares sinusoidal fit where the magnitude of the fit, and azimuth where the fit returns zero is given above the box.

al. (2011) algorithm has been coloured grey. The location of the FPI is plotted at approximately 42° north, 84° west by the orange triangle. The assumed locations of the peak neutral wind measurements are shown by the orange dots. The orange box indicates the selected fitting area, where only points contained within the area are considered. Positive velocities indicate motion towards the radar and negative away according to the colour bar on the right. We can see a patch of fast moving scatter away from the radar (deep purple) to the South of the fitting area below the FPI. Above the FPI the magnitudes of the velocities are much smaller. The panel below shows the magnitude of the maximum velocities in each beam as orange dots. Beams facing directly westwards would be at an azimuth of $-90°$ and beams pointing directly to magnetic north are at 0°. The sinusoidal least squares fit to these velocities is given by the black line. A quick examination of the fit tells us that the points from the five eastwards-most facing beams and the single westwards-most facing beam do not conform to the fit, which is in fact poor compared to all of the data points. Examination of fits at other timesteps show a general trend of poor fits to the data points. The latitudinal difference between the South and North assumed peak emission locations is approximately 4.5° in latitude, which is rather wide compared to fitting areas used in other studies. Spatial regions of fast and slow moving scatter display a latitudinal difference across multiple timesteps. In Figure 4.3 especially, the fast moving scatter is in a block in the southern half of the fitting area. In the North-East of the fitting area, there are two cells in the fifth-most eastward facing beam that are faster than other velocities in the same beam, however it appears to be part of a different patch of scatter than the fast moving patch to the South. Because of the large fitting area this has still been included in the fit. Instead of fitting over one single latitudinally wide area, it may make sense to split the overall area in multiple, latitudinally narrower ones. While this was tested (see Figures B.1 and B.2 in Appendix B), splitting the fitting area into latitudinally narrower areas did not improve the quality of the fits. The strong moving patch at the South of the area is not uniform across a single line of

latitude. We know from Figure 3.5 that the Ionospheric trough during this interval does not stick to a single line of latitude, but instead curves to a higher latitude at the duskside. If the ion patches are driven by pressure-gradient drifts due to the equatorward boundary of the trough, then the patches would also not be aligned with latitude and simply defining the areas by latitude is not sufficient to produce good quality fits. There are cases where multiple patches of fast moving scatter exist, in fact there are three patches of fast moving scatter in the period of Figure 4.3, 0521 UT to 0531 UT, (although the colour bar does saturate their visibility somewhat at this time) each over a different latitude range. It is necessary then to devise a technique that allows us to simultaneously track multiple patches of scatter that are not necessarily aligned along lines of latitude, or to each other.

We do this by creating fitting areas with a method that we shall call "patch-tracking". By selecting individual beam range-gate cells of velocities $\geq 20\,\mathrm{ms}^{-1}$, we manually identified individual patches of ionospheric scatter and marked the boundaries of each patch spatially and temporally. We then selected the highest magnitude velocity from each beam within each defined patch and fit to those points. A minimum of five unique beams were used to constrain the fits, which although is less than used in other studies, e.g. (Kunduri et al., 2018; Thomas & Shepherd, 2018), manual (rather than automated) selection and review of the points ensures that they are still constrained to the fit. This further allowed deselecting beams at the sides of patches if by inspecting the fits it became clear that part the flow does not belong to the patch (such as the low velocity scatter from the five eastmost-facing beams next to the strong moving southwards patch at 0521 - 0531 UT), ensuring that motion only belonging to that patch was captured.

Figure 4.4 shows an example of patch fitting for the BKS scan from 0521 UT to 0531 UT, the same as used for Figure 4.3. The top panel shows the scan of line of sight ion velocities plotted onto a geographic grid with the ion velocities corresponding to the colour bar to the right. Positive velocities indicate motion towards the radar, negative velocities away. The orange boxes mark what has been

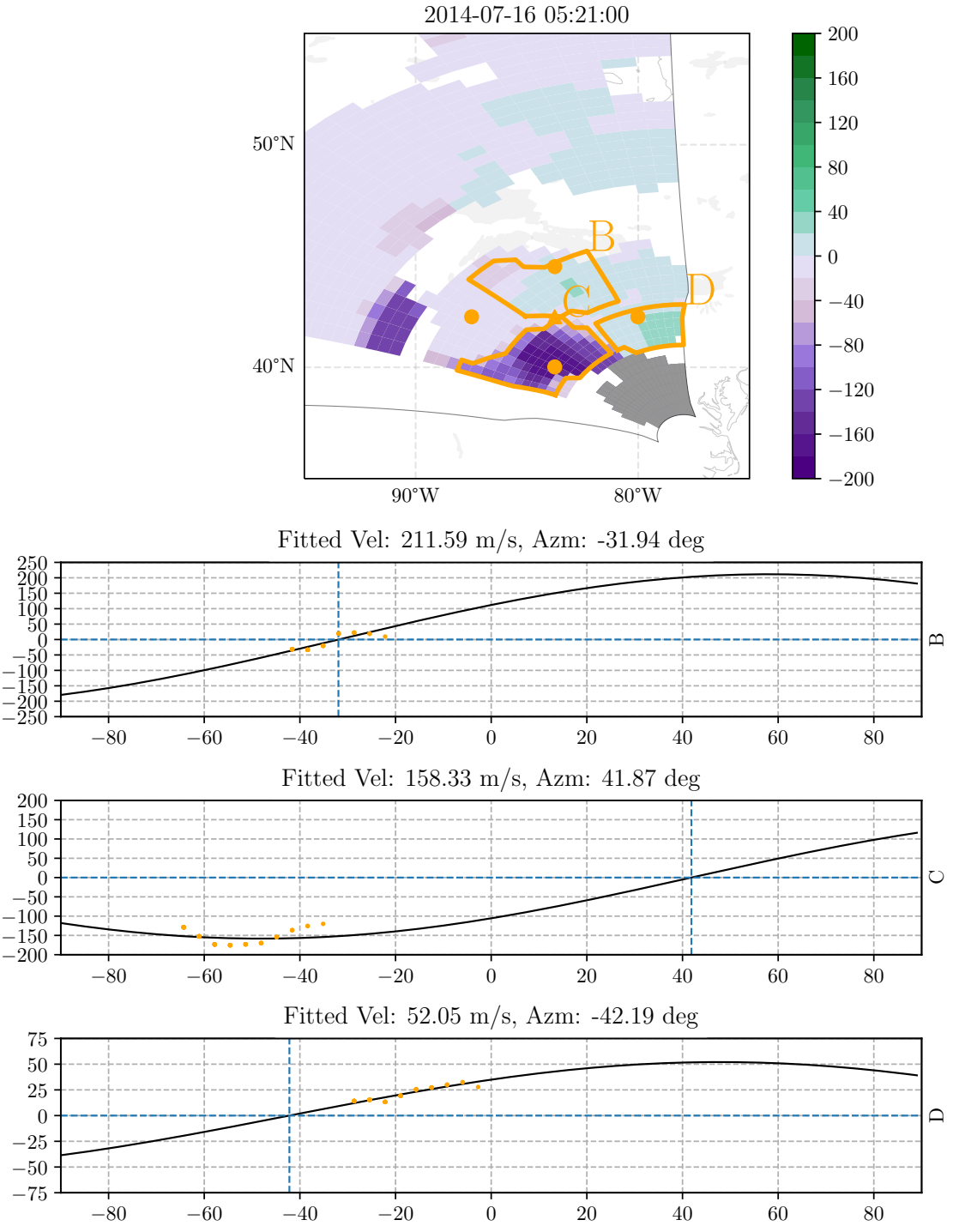

Figure 4.4: The same as Figure 4.3, however fitting areas have been drawn around regions of tracked active patches. Outlined in orange with labels to the top-right are patches identified as B, C and D. Patches A, and E are not present at the time of the plot. Below shows the line of sight ion velocities and the fits for each patch, according to the letter at the right of the axis.

determined to be a patch of fast moving ionospheric scatter. Since we take the maximum velocity of each beam within a patch, it is only necessary to ensure that the highest velocity within a beam is included within the patch boundaries rather than needing to determine the exact spatial structure of the patch across all radar range gates. At the top right corner of each patch outline, a letter identifier (A, B, C, D and E) has been used to track each patch. At the time of the example in Figure 4.4 only patches B, C and D are present. Patch A occurred before 0521 UT and patch E occurred after 0531 UT and so are not shown here. The three panels below show the highest line of sight ion velocities in each beam for all the patches outlined (B, C, D), plotted against their beam azimuths with the resulting cosine fits for each of those cells. If we investigate the points used for fitting, patches B and D shows velocities that trend to positive at +90° azimuth, while patch C shows velocities that trend to a negative at +90° azimuth, indicating two patches moving in separate directions at the same latitude. With patch tracking, The low velocity scatter (patch D) to the East of the fast southern patch (patch C) is now tracked separately so instead of one poor fit that tries to conform to all of the velocities, two separate fits are produced which each look more convincing.

By taking the patch-fitted magnitudes throughout the interval we are able to estimate the two dimensional ion flow during this period. Then by applying Equation 1.72 with the IGRF magnetic field strength we can calculate the total local electric field strength across this interval.

4.3 Fitted Velocity Analysis

Figure 4.5 shows the IMF Bz (a) followed by the estimated observed (blue) and modelled by TIEGCM (orange) magnitude of the full neutral wind vector (b). The modelled data come from the same TIEGCM runs as performed in chapter 3. Figure 4.5c shows the patch-fitted two dimensional ion velocities for each identified patch compared with those modelled by TIEGCM, while (d) shows the

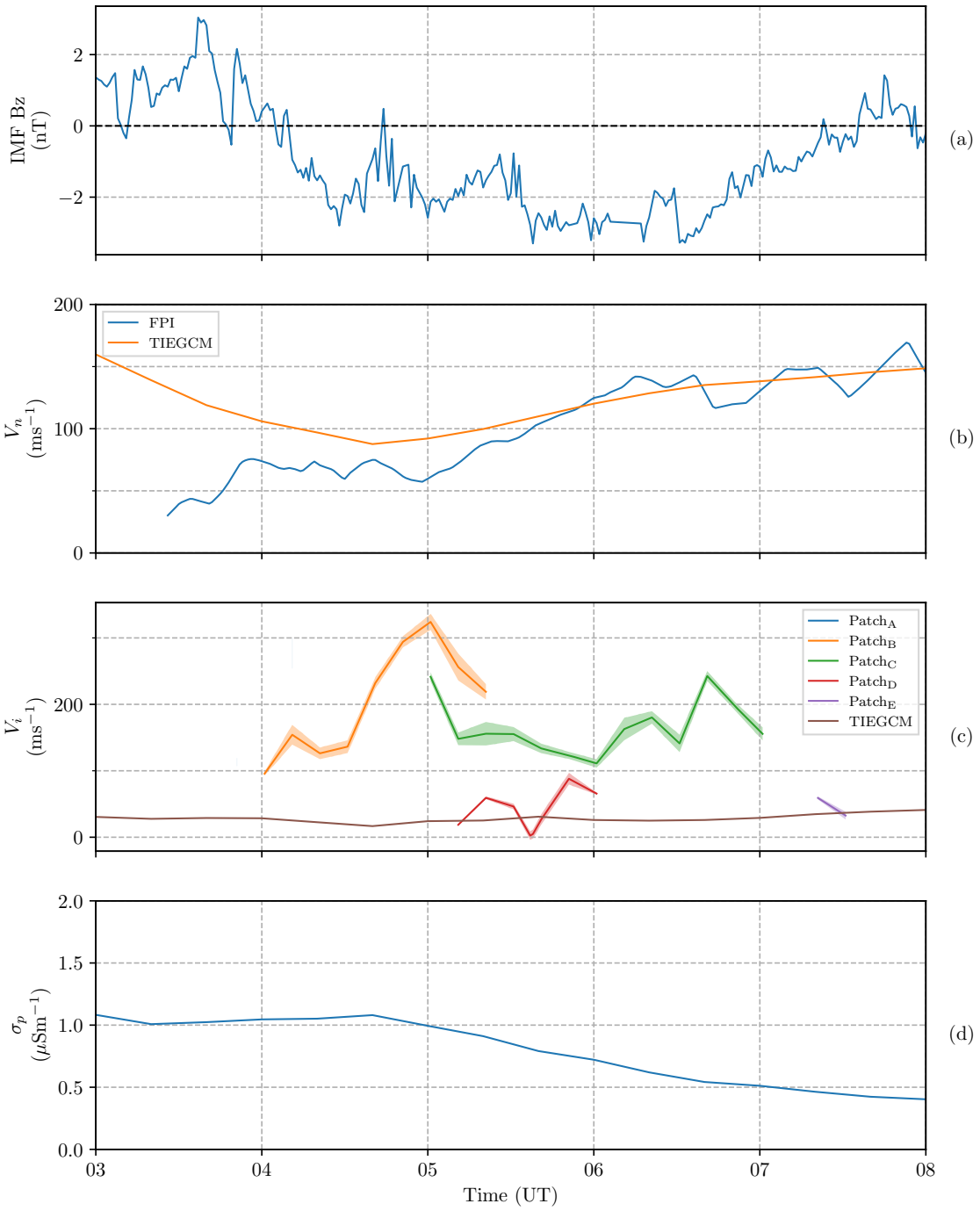

Figure 4.5: (a) IMF Bz followed by, (b) the magnitude of the full neutral wind vector in blue with TIEGCM's neutral velocities in orange, (c) the magnitude of the full ion velocities for each identified patch. The dark lines represent the fitted values, the shaded region either side of the line shows the root mean squared error (RMSE) of the fit used to estimate the velocity. The TIEGCM ion velocities are plotted as the burgundy line without a RMSE shaded region. (d) Shows the Pedersen conductivity at the FPI location, as modelled by TIEGCM.

Pedersen conductivity, σ_p at the FPI location as modelled by TIEGCM and used for calculating the Joule heating. The solid lines represent the magnitude of the fitted velocity while the shaded region is the RMSE error of the fits. The largest RMSE is less than 20ms^{-1}, which given that the two major patches (B and C) are always at least 100ms^{-1} indicates that the fits to determine the two dimensional ion velocities conform to the data. The time boundaries for the plot have been restricted to between 0300 UT and 0800 UT since no significant ion patches were identified either side of these times. The observed neutral's speed is seen to steadily increase from ~ 40 to $\sim 200\text{ms}^{-1}$ over the course of the night. TIEGCM overestimates the neutral velocities prior to 0600 UT, however afterwards, the total velocity magnitude is in line with the observations. Of the identified ion patches, two take precedence, patches B and C. Patch B appears at 0400 UT with velocities of 100ms^{-1}, increasing to in excess of 250ms^{-1} at 0500 UT before dissipating. Patch C starts at 0500 UT, hovering at between 100 and 200ms^{-1} until it also dissipates at 0700 UT. It is worth noting that the patches were only marked if they were at least covering part of the region within the FPI measurement locations. It is likely that the patches originated or dissipated outside of this area and merely traversed through the region over the FPI; we have only noted the times where the patch is contained within the FPI region. Furthermore, patch A was identified to occur between 0350 and 0420 UT, however the azimuthal span of the patch was not enough to satisfy the conditions we set in section 4.2 to fit a two-dimensional velocity, hence it is missing in this and further presentations of the patch ion velocities and Joule heating. TIEGCM's ion velocities remain a fairly steady $20-40\text{ms}^{-1}$ throughout the interval due to it lacking the micro/mesoscale physics to capture the ion irregularities that produce the ion drift patches observed by the BKS radar. The Pedersen conductivity is modelled to be relatively constant, although decreasing throughout the nighttime period.

4.3.1 Comparison of fitting techniques

Figure 4.6 compares the different velocity fitting techniques. Panel a shows the latitude of the ANN FPI in blue, while the latitude of the Heppner-Maynard boundary is in orange. Panel b shows the magnitude of the ion velocities at the location of the ANN FPI for the "Gridded" LOS velocities (blue), the spherically harmonic fitted velocities (orange) and the patch-fitted velocities of each patch in green.

Processing the fitacf LOS velocities into the gridded format, which is a necessary step to obtain the spherical harmonic fitted velocities, has reduced the magnitude of the LOS ion velocities reported in chapter 3. Features of the overall spiking in ion velocities at 0500 UT to $100\,\mathrm{ms}^{-1}$ remain, however the magnitude is much less than the observations that exceed $150\,\mathrm{ms}^{-1}$ in figure 3.6. Secondary spikes which appear in many of the beams have effectively been eliminated. The spherical harmonic fitted velocities are generally larger than the gridded velocities, however smoothing from the global fit has entirely removed the strong ion velocity spikes at 0500 UT, with the magnitudes fluctuating at around $20\,\mathrm{ms}^{-1}$ to $30\,\mathrm{ms}^{-1}$. The patch-fitted velocities at 0500 UT exceed $300\,\mathrm{ms}^{-1}$, over 10 times larger than the spherical harmonic fitted method. Except for a point at 0530 UT, all of the patch-fitted velocities exceed the spherical harmonic fit, with the velocities from the slower moving patch, D, approximately $50-100\,\mathrm{ms}^{-1}$ faster than the spherical fitted velocities, while patches B and C are at least $100\,\mathrm{ms}^{-1}$ faster than the spherical harmonic fit. For a more detailed discussion on the performance of the spherical harmonic fitting compared to the L-shell fitting, see section 4.5.

We should note that at high-latitudes, the quasi-vertical magnetic field results in the ion drift travelling approximately parallel to the Earth's surface in the same plane as the neutrals. However, since the magnetic field is inclined (69.26° to the horizontal) at this latitude, the ions and neutrals reference planes are instead inclined roughly 20° relative to each other. If we assume that the ion motion is due to $\mathbf{E}\times\mathbf{B}$ drift, then there is no ion motion in the direction of the magnetic field and the fitted

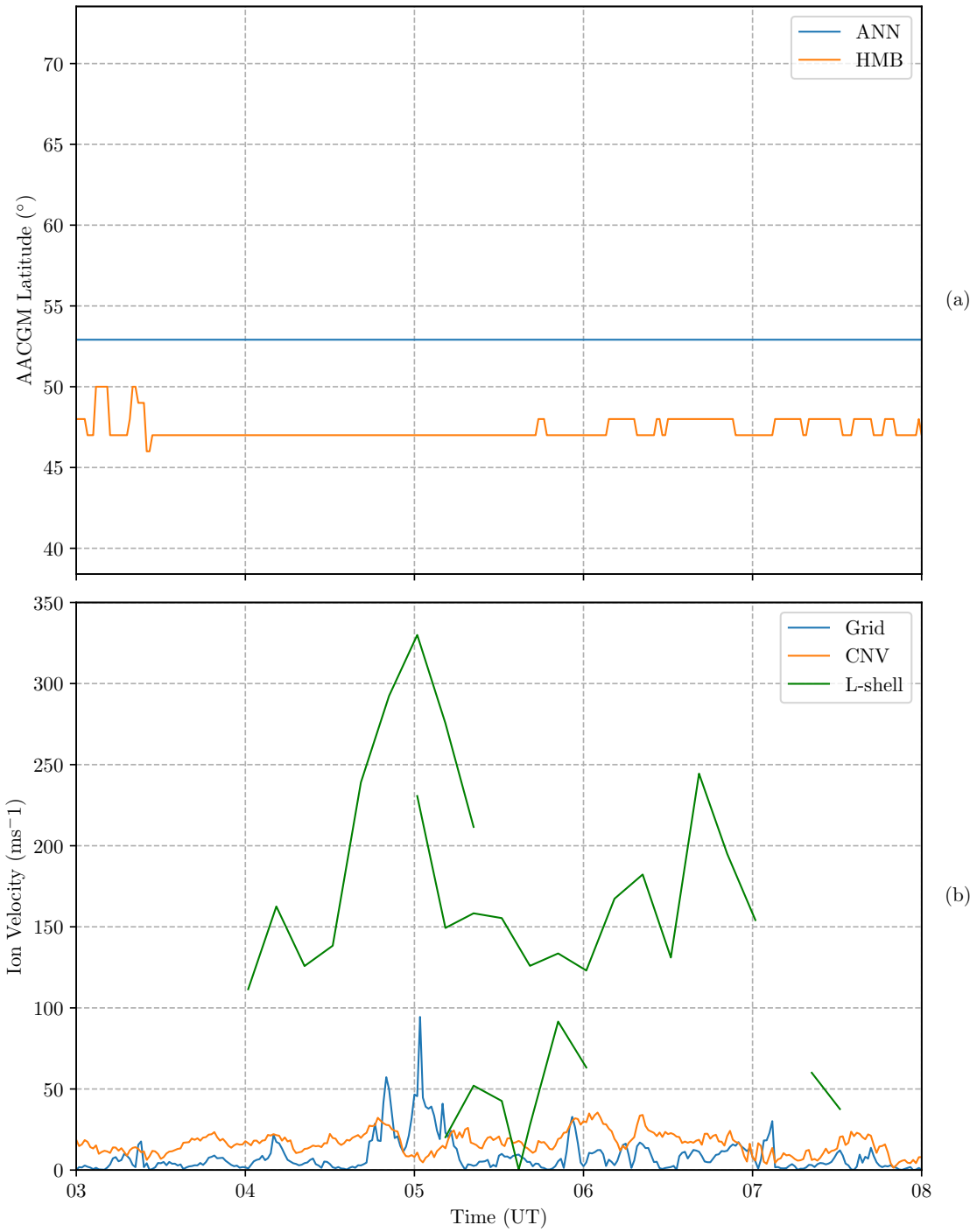

Figure 4.6: Panel a shows the latitude of the ANN FPI (blue) and the latitude of the Heppner-Maynard boundary (orange) between 03 and 08 UT. (b) Shows the magnitude of the ion velocities at the FPI location of "gridded" LOS ion velocities (Grid/blue), the spherically harmonic 2D fitted velocities (CNV/orange) and the patch-fitted 2D fitted velocities of each patch (L-shell/green).

two dimensional ion velocities (both patch and spherical harmonic fitted) would also be the full three dimensional velocities of the ion motion. This does however also assume that there is no coupling to the neutrals. Given that the neutrals are inclined relative to the ions, and that there are non-zero vertical velocities in the neutrals, there is likely to be some momentum exchange that could result in some ion motion in the direction of the magnetic field that would not be captured by the BKS radar. It is therefore necessary to mention that the derived fitted velocities may not be the representative of the full three dimensional ion velocities, but only the two dimensional velocities perpendicular to the magnetic field.

4.4 Joule heating

Using the estimated patch-fitted two dimensional ion and neutral velocities, we have calculated the Joule heating rate by expanding the convection electric field term from equation 1.84 to produce equation 4.6,

$$Q_j = \underbrace{\sigma_p(-\mathbf{v}\times\mathbf{B})^2}_{Q_c} + \underbrace{2\sigma_p(-\mathbf{v}\times\mathbf{B})\cdot(\mathbf{u}\times\mathbf{B})}_{Q_{w1}} + \underbrace{\sigma_p(\mathbf{u}\times\mathbf{B})^2}_{Q_{w2}} \tag{4.6}$$

where $\mathbf{v}$ is the ion velocity, $\mathbf{u}$ is the neutral velocity and $\mathbf{B}$ is the magnetic field strength. Q_c is the convection heating due to ions moving against a stationary neutral background, Q_{w1} accounts for the direction of the ion flow relative to the neutral flow and Q_{w2} is the heating generated by neutrals moving against a stationary ion background. Assuming an altitude of 250km, we use the Pedersen conductivity (σ_p) as shown in Figure 4.5. Figure 4.7 plots the resulting Joule heating Q_j, alongside its components, Q_c, Q_{w1}, and Q_{w2} for each patch. Due to the magnitude of the spherical harmonic fitted velocities being less than the LOS velocities, we do not consider using them for our Joule heating calculations. Panels a, b, c, d and e show the Joule heating rate and components for patches A, B, C, D and E respectively. The blue line represents the ion heating rate, Q_c, the orange and green lines the two wind correction terms, Q_{w1} and Q_{w2} respectively and the

red line the total Joule heating rate of the patch, calculated as the sum of the three components (Equation 1.84). A negative Q_{w1} indicates that the direction of the ion and neutrals were aligned with each other, resulting in fewer collisional interactions and thus dampening the overall heating rate, a positive value indicates the ions and neutrals were opposed. Panel f shows the same components, but as modelled by TIEGCM. The final panel, g, compares the average total Joule heating rate from all the patches over the FPI region, with the total heating rate modelled by TIEGCM. Based on the measurements, the most significant heating rate occurred between 0430 and 0500 UT which was driven by ion motion from patch B, with heating due to ion motion, Q_c, peaking at 236pWm^{-3} out of its total heating, Q_j, of 237pWm^{-3}. Patch C also exhibited some enhanced ion heating at 49.1pWm^{-3}, however this is somewhat lower than the peak heating rates in patch B.

The positive magnitude of Q_{w1} in patch C and D indicates that the ions and neutrals were opposed in direction for most of each patch and so collisional interactions were increased. This increase is greatest in patch D at $\sim$ 0520 UT, where the total heating is increased by 47pWm^{-3} to 109pWm^{-3}, resulting in a 78% increase due to the ion-neutral directions. The impact of this term is further shown in patch D, where at $\sim$ 0550 UT, Q_{w1} is at its most negative value and results in decreasing the total Joule heating by $\sim$ 76%. The heating directly due to the neutrals Q_{w2} is low throughout the entire interval, hovering at around $\sim$ 5pWm^{-3}, therefore despite the large influence of the neutral wind direction on the total heating rate, the overall Joule heating magnitude is only significantly enhanced when driven by ion motion.

The Joule heating enhancement observed in panel g at 0500 UT that peaked with a magnitude of 235pWm^{-3} is nearly 8 times higher than the TIEGCM modelled Joule heating of 30.8pWm^{-3}. Aside from $\pm$ 20 minutes of the 0500 UT peak, the TIEGCM Joule heating rate is significantly higher than the observational estimate. When we investigate the drivers behind the heating we find that the larger magnitudes in the observed ion heating, Q_c, especially in patch C, indicates

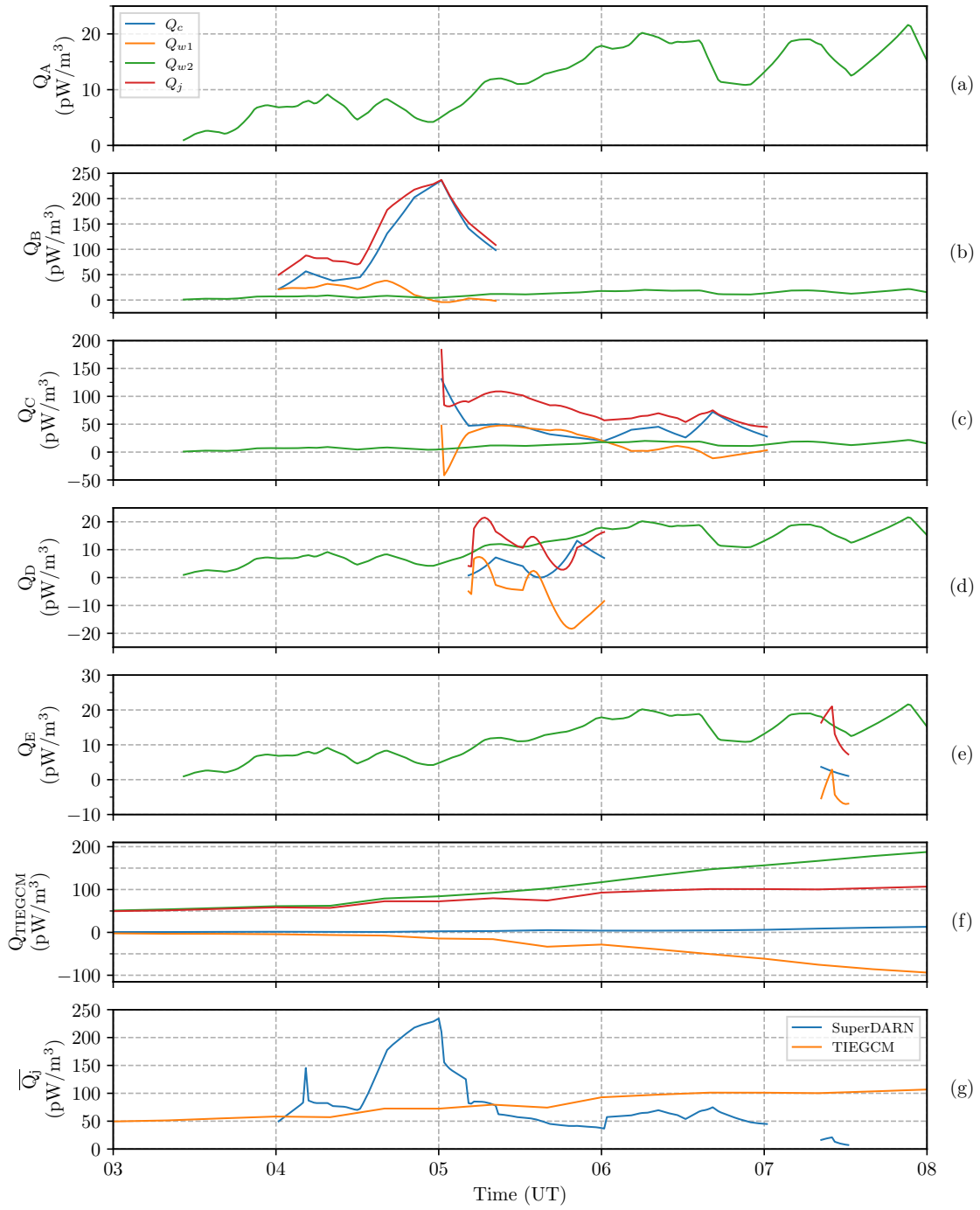

Figure 4.7: Panels a, b, c, d & e shows The estimated Joule heating components and total heating for each identified patch, the panel labels correspond to the patch velocity labels shown in figure 4.5c. Each component is plotted according to the legend in panel a. Panel f shows the Joule heating components and total heating modelled by TIEGCM. g shows the total Joule heating rate calculated as the average heating rate of all patches in the common area, while re-plotting TIEGCM's total Joule heating in orange for comparison.

that the observed heating is primarily driven by ion motion. Panel f shows that the magnitude of the total heating in TIEGCM is driven by the neutral winds, Q_{w2} whose significance increases throughout the interval compared to the ion contribution. During this event, we find that our observations disagree with not just the magnitude of the modelled Joule heating rate at the mid-latitudes, but the modelled Joule heating being driven by the neutral wind disagrees with that calculated from our observations.

4.5 Discussion

Previous studies by Greenwald et al. (2006) and Maimaiti et al. (2018, 2019) investigating mid-latitude night-time ionospheric scatter have found ion velocities typically less than 100ms^{-1}. They are often attributed to penetrating electric fields, driven by the neutral wind dynamo or due to pressure gradient forces. Given the magnitude of Q_{w2} is small compared to the total Joule heating rate, Q_j, in this study, we infer that the ions are responsible for driving the increased Joule heating rate. Maimaiti et al. (2018, 2019) carried out statistical studies of the nightside mid-latitude and sub-auroral ionospheric convection and found persistent westward flows between $20-90$ms^{-1} depending on season and MLT, which is somewhat slower than our results, particularly as they found that the fastest flows occured in winter. Although Maimaiti et al. (2018) used the same groundscatter algorithm (Ribeiro et al., 2011) as in this study to remove low velocity non-ionospheric scatter, they also deployed the additional technique as described in (Ribeiro et al., 2012), where events were only considered if the 3rd and 97th percentile of their ion velocity distributions were greater than -120ms^{-1} and less than 120ms^{-1} respectively. This ensured that they only studied the quiet time mid-latitude nighttime scatter and any fast events may have been lost. By selecting active patches in this study, we have not considered low-velocity ionospheric scatter during this event and this will have skewed our velocities to a higher range than theirs. We believe that the higher ion

velocities estimated in this study are therefore reasonable. Furthermore, despite our ion velocities being greater than other quiet time studies, they are significantly slower than other mid-latitude studies that occur under geomagnetically active periods. When enhanced ion velocities have been observed due to the equatorward expansion of auroral convection (Joshi et al., 2015) or SAPS (Billett et al., 2022; Clausen et al., 2012; Kunduri et al., 2017) velocities are observed in excess of 500ms^{-1} and up to 1000ms^{-1}. Our observed ion velocities therefore fall within a reasonable expectation when considering the geomagnetic activity and methods used in this study.

The LOS ion velocities are one component of the full ion flow, therefore should be a lower magnitude than the full flow. Figure 4.6 shows that the spherical harmonic fitted velocities are lower than the excited LOS ion velocities at 0500 UT. During this interval studied here the spherical harmonic fit is indicative of a fairly typical twin-cell convection pattern. The Heppner-Maynard boundary is a fairly consistent 5° equatorward of the ANN FPI over the interval. If we consider that the southern FPI point is approximately 2° equatorward of the ANN FPI location, then only 3° exists between the HMB and the equatorward-most regions of our fitted area. The spherical harmonic fit works to create a zero-value electric potential at the HMB, which necessitates that the ion velocities at the edge of the HMB tend toward zero, forcing the magnitude of the velocities close to the boundary to a small value. A possible solution could be to manually adjust the definition of the HMB, for example, using a velocity threshold of 50 ms^{-1} instead of 100 ms^{-1}. There is however, a limit to how far the HMB can descend from the poles according to observations, as the SuperDARN network only extends to around 40° magnetic latitude. An alternative could be to force the HMB to a specified latitude, however given that the spherical harmonic fit attempts to conform to the twin-cell convection pattern, it only makes sense to force the HMB to the latitude that we know the twin-cell pattern expands to, which in this interval is at the most 60° geographic latitude (50° geomagnetic). Although there is some merit in the statistical patterns used to constrain the solutions to the spherical harmonic fit containing mid-latitude driven

phenomena, the weighting of these patterns is not enough to prevent the twin-cell pattern from decreasing the magnitude of the velocities close to the HMB. The statistical patterns are also based on geomagnetic activity, which as discussed in the previous paragraph, are typically less than 100 ms^{-1}. It is unlikely then, that the statistical patterns actually *do* contain some representative ion flows of the sub-auroral ion scatter. The patterns from Thomas and Shepherd (2018), which are the statistical models used in this study and are shown in Figure 1.9, for Kp 2-3 only expand to 70° geomagnetic latitude, well poleward of the ANN FPI. The analysis in this study then, confirms that the spherical harmonic fitting technique should be solely reserved for studies where ion scatter is certain to be due to motion from the high-latitude twin-cell convection pattern.

Strong ion motion has been shown to drive the neutral atmosphere into a similar direction as momentum is exchanged through frictional collisions. During both patches C and D the directions of the ions and neutrals are initially opposed, resulting in an increased Joule heating rate, however as both patches persist, the neutrals are slowly driven into the same direction as the ions, given by Q_{w1} decreasing. When the ion driving to the neutrals is at its greatest Q_{w1} would reach its peak negative value, and start to increase once the ion driving recedes and the neutrals retain momentum and start to drive the ions. In our observations Q_{w1} continues to decrease and never reach a negative peak over the tracked lifespan of both patches, with patch B lasting $\sim$ 1.5 hours and patch C $\sim$ 2 hours, suggesting the ions continue to drive the neutral motion throughout the period where we track them. Joshi et al. (2015) calculated the mid-latitude ion neutral coupling timescale during a geomagnetic storm and found a time-lag of $\sim$84 minutes for the neutrals to respond to the ion driving. Billett et al. (2022) found a response time of 2h for mid-latitude neutral wind to respond to pressure gradient forces. In the case of Joshi et al. (2015), ions were driven by expanded auroral convection during a geomagnetic storm, and for Billett et al. (2022) a SAPS event, with ion velocities several 100ms^{-1} faster than this study's quiet time events. Kosch et al. (2001) found an average of

high-latitude response times during geomagnetically quiet periods to be 3.3 hours, which our observations fall in line with despite the latitudinal difference.

Studies by Aruliah et al. (2005) and Anderson et al. (2013) investigated the impact that neutral winds have on Joule heating rate estimations. They calculated the high-latitude neutral wind dynamo to account for 29% (Aruliah et al., 2005) and 36% (Anderson et al., 2013) of the total Joule heating rates. Across patches B, C and D, the average neutral contribution (Q_w) to the total heating rate was 24.7%, 40.4% and 43.1% respectively, which is consistent with the previous studies, albeit at different latitudes. Patch B's lower neutral contribution can be accounted for by the significantly stronger ion enhancements than in the other two patches, while their contributions although higher, still signify the majority of mid-latitude Joule heating response being due to the ions. Billett et al. (2018) indicated that the high-latitude Joule heating rate was nearly entirely eliminated when the neutral wind was pulled into the orientation of the ion flow. Kiene et al. (2019) used a scanning doppler imager with a SuperDARN radar to estimate high-latitude local Joule heating rates. They found that inclusion of the neutral winds in their Joule heating rate calculations dropped the total heating rate by a factor of $\simeq 3$ at high-latitudes. At the minimum value of Q_{w1}, which occurred in patch D, the Joule heating rate was decreased from 24.1pWm^{-3} to 5.61pWm^{-3}, representing a 4.2 times decrease, similar to the observations found in Kiene et al. (2019). However, our observations vary substantially with the winds either contributing positively or negatively to the total heating rate, amounting to either a $> |75\%|$ increase or reduction in the total Joule heating rate depending on the neutral flow direction relative to the ions. When considering the multiplicative reduction, and the percentage decreases, our results show that the neutral winds have a significant reducing action on the overall Joule heating rate in line with the results obtained by the high-latitude studies of Billett et al. (2018) and Kiene et al. (2019). Although these studies did not show cases of the neutrals increasing the heating, Aruliah et al. (2005) and Anderson et al. (2013) did find that high-latitude neutrals were able to enhance or reduce the total Joule

heating rates as similarly shown in this study. The increased heating rate magnitude of $\sim 75\%$ in this study is symmetrical to the heating magnitude when the neutrals were decreasing the heating rate, implying that the neutrals are equally effective at enhancing Joule heating rates as they are at dampening them.

Typically, studies investigating Joule heating rates calculate a height-integrated value using model values (Lu et al., 2016; McHarg et al., 2005; Zhang et al., 2005) or based on assumptions of the height integrated neutral pattern being representative of the neutral pattern at approximately 160km altitude (Billett et al., 2018) as shown by Lu et al. (1995), or by assuming that F-region altitude measurements map down to a range of altitudes (Cai et al., 2014). Direct comparisons of our values to other studies are somewhat limited, however Anderson et al. (2013) and Kiene et al. (2019) calculated high-resolution high-latitude local Joule-heating rates using instruments observing the ions and neutrals at 250km, which provides an excellent comparison to our mid-latitude study. The Joule heating rate in this study peaks at $\sim 235 \mathrm{pWm}^{-3}$. Both Anderson et al. (2013) and Kiene et al. (2019) estimated the local high-latitude Joule heating rates up to the order of nWm^{-3} for geomagnetically active intervals, an order of magnitude higher than our observations. The majority of their observations however were in the tens, or hundreds of pWm^{-3}, which matches our observations, suggesting small patches of ion scatter at mid-latitudes are able to drive local Joule heating enhancements similar to those observed at high-latitudes. Their most dominant Joule heating values were coincident with the auroral region, where ion velocities are typically much higher, often in excess of $1000 \mathrm{ms}^{-1}$, particularly during geomagnetically intense periods (such as in their studies). Although we cannot compare our values with studies calculating height-integrated Joule heating rates, studies of the global Joule heating pattern (Billett et al., 2018; Lu et al., 2016; Zhang et al., 2005) indicate higher magnitudes in the auroral region, with the difference of at least an order of magnitude being fairly common. Our values being an order of magnitude smaller than those in the high-latitude studies is reasonable. If we consider the fact that the high-latitude studies

occured during geomagnetically intense periods, while our mid-latitude study is during a quiet time period, our Joule heating values may be closer than expected, indicating that even small transient events can result in a significant Joule heating deposition in the mid-latitudes.

Baloukidis et al. (2023) compared statistical high-latitude Joule heating distributions estimated by using the European incoherent scatter scientific association (EISCAT) radars with TIEGCM. Their EISCAT Joule heating estimations ranged from altitudes of $80 - 150$km altitude and did not include the neutral wind contributions, so are not directly comparable to our estimations in this study, but their comparisons to TIEGCM are still useful. They found that during low Kp, TIEGCM's modelled Joule heating was higher than their observed estimates. If we can assume that fast moving ion patches were averaged out in their low Kp statistical analysis, then our results of TIEGCM modelling higher Joule heating during low velocity ion events during the quieter preiods of our interval agrees with the findings from their study. At higher Kp, Baloukidis et al. (2023) also found TIEGCM's observed Joule heating was lower than their observed estimates. Although our study is a low Kp event, our periods of significant ion enhancements are more often associated with high levels of geomagnetic activity, so we can compare our fast moving ion patches to their high Kp analysis, whereby we also agree that TIEGCM's modelled Joule heating is lower than observed estimations. Similar to our findings, Baloukidis et al. (2023) remark that the difference in their discrepancies between TIEGCM and their observations are due to small-scale effects that amount to sub-grid variability within TIEGCM that it cannot resolve. Due to this sub-grid variability, TIEGCM includes an empirically-derived multiplication factor named JOULEFAC to increase its internal Joule heating by a fixed factor of 1.5 (NCAR, 2016) in order for its neutral temperatures to better agree with statistical observations. One solution Baloukidis et al. (2023) propose is to adjust JOULEFAC with Kp so that different values are used for different levels of geomagnetic activity. Previous studies have manually adjusted the value

of JOULEFAC to better reproduce realistic Joule heating values (Emery et al., 1999). Although there may be differences between optimised JOULEFAC values for high and mid-latitudes, optimised JOULEFAC values may work on a statistical level, however it could not account for small scale spatial or temporal events such as in this study. A better JOULEFAC for low Kp may bring TIEGCM's modelled Joule heating in line with our observed estimations for low velocity patches, however there would still be a large and potentially greater difference for excited ion motion, such as patch B between 0430 and 0500 UT in this study. Furthermore, adjusting JOULEFAC may "correct" the numerical Joule heating value, however it might not solve discrepancies between whether the ions or neutrals drive the Joule heating as occurs in this study. Rather, if focusing on localised studies, improvements should be made for TIEGCM to better model the microscale electrodynamics of the mid-latitude ionosphere.

4.6 Summary

The observed and modelled ion and neutral velocities during the interval of 16 July 2014 from the previous chapter (3) were used to estimate the full two-dimensional ion velocities and three dimensional neutral velocities during the same interval. We used a method similar to L-shell fitting, where we fit a cosine curve to the LOS velocities to regions of uniform velocity scatter, against their beam azimuths recorded by the BKS radar. We performed the fits to manually tracked patches of scatter both temporally and spatially, giving us greater control to fine tune the fits to regions of consistent scatter. Three main patches were active during the interval with patch B rising from $150\,\mathrm{ms}^{-1}$ at 0400 UT to its peak value of $250\,\mathrm{ms}^{-1}$ at 0500 UT. Patch C hovered between $150\ \mathrm{ms}^{-1}$ to $200\ \mathrm{ms}^{-1}$ between 0500 UT and 0700 UT while patch D ranged from $0\ \mathrm{ms}^{-1}$ to $100\ \mathrm{ms}^{-1}$ between 0500 and 0600 UT. Across all patches, the RMSE of the fits were $< 20\,\mathrm{ms}^{-1}$, indicating the technique performed excellently. We additionally ran the often used technique of spherical harmonic

fitting of SuperDARN data and found that its fitted velocities were $< 40\ \mathrm{ms}^{-1}$ throughout the entire period. The spherical harmonic fitted velocities were trended towards zero so that the fit was consistent with a zero-value equipotential at the boundary of the high-latitude twin-cell convection pattern, which was placed close to the location of the ANN FPI. We conclude that the spherical harmonic fitting method is only appropriate for flows that are certain to be due to the high-latitude convection pattern, and that L-shell fitting methods are far more appropriate for determining sub-auroral ion velocities.

Three-dimensional neutral wind velocities gradually increased from $\sim 40\ \mathrm{ms}^{-1}$ at 0330 UT to $150\ \mathrm{ms}^{-1}$ at 0800 UT. The neutral wind velocities alongside the ion velocities for each patch and the Pedersen conductivity from TIEGCM were used to calculate the Joule heating rates of each patch and an average Joule heating rate across the FPI area. The ion motion drove significant Joule heating enhancements to the region, peaking at over $200\,\mathrm{pWm}^{-3}$, a similar magnitude to results from high-latitude studies and only a single order of magnitude less than under high-latitude geomagnetically active periods, despite this interval being a geomagnetically quiet period. The neutral wind was shown to have a significant impact on the overall heating rate, accounting for on average between 24% and 43% of the total heating, while at the extremes increasing or decreasing the total heating rate by in excess of 75%.

Comparisons with modelled ion and neutral velocities from TIEGCM indicate that TIEGCM does not model equivalent enhancements in the Joule heating, due to a lack of sub-auroral driving, as discussed in chapter 3, resulting in an approximate 8 times smaller Joule heating rate than during the peak observed estimates. The mid-latitude Joule heating reported by the model was neutral wind driven rather than ion driven in contrast to our observations. The strong neutral winds in TIEGCM also resulted in a greater modelled Joule heating rate than our observational estimates during quieter periods of the interval.

The combined findings from this and the previous chapter suggest that significant

Joule heating can be produced in the sub-auroral mid-latitude ionosphere, even during geomagnetically quiet times. Furthermore, enhanced Joule heating rates may not be modelled in TIEGCM due to its inability to model enhanced ion velocities in the sub-auroral zone. We are left with a significant question, how often does this occur and what is the possible magnitude that TIEGCM can underestimate the ion velocities and Joule heating? We aim to answer these by performing a statistical analysis of observed ion velocities and compare them to outputs from TIEGCM in the next chapter.

Chapter 5

Statistical Analysis of Mid-Latitude Ion Scatter

5.1 Introduction

In the previous two chapters we showed how misrepresentations of the ion and neutral velocities in TIEGCM resulted in Joule heating estimations that conflicted with observed estimations at the location of the ANN FPI. TIEGCM's ion velocities were shown to be severely limited compared to the magnitude of the observed ion velocities due to a lack of mid-latitude microscale electrodynamic drivers within the TIEGCM model. This prevented TIEGCM from modelling Joule heating enhancements equivalent to our observations, both in terms of magnitude and due to the dependency on either the ion or neutral drivers.

During the interval studied, 16 July 2014. The observations were deemed to be sub-auroral. While TIEGCM has no magnetospheric sub-auroral driver, the F-region dynamo, caused by neutral wind motion is present in the model and is responsible for most of the sub-auroral ion motion in TIEGCM. The geomagnetic drivers during the interval studied were weak. Comparisons of the performance at higher, or different levels of geomagnetic activity are not possible due to no availability of high-quality co-located ion and neutral wind observations at any other

times. We can however investigate how often there is a disparity between observed sub-auroral ion velocities and TIEGCM modelled ion velocities. If we remove the necessity for co-located observations to the neutral winds, then we can perform a large scale statistical analysis on the sub-auroral ion velocities based on geomagnetic activity and compare them to TIEGCM.

Works by Maimaiti et al. (2018, 2019) have previously studied the morphology of sub-auroral ion motion. Maimaiti et al. (2018) carried out a statistical study on 2 years of SuperDARN data on the nightside quiet time mid-latitude ionospheric convection and found ion flows to typically travel in a westwards direction between $20 - 55\,\mathrm{ms}^{-1}$. Their study does not however, separate the data between auroral and sub-auroral ion motion neither does it study the convection at the dayside or during non-quiet times. A follow-up study, (Maimaiti et al., 2019), surveyed 7 years of data $(2011 - 2017)$ to identify the morphology of the sub-auroral ionospheric convection due to dependencies on monthly, seasonal and geomagnetic activity and found that peak ion velocities ranged from $60\,\mathrm{ms}^{-1}$ at low Kp to $150\,\mathrm{ms}^{-1}$ at high Kp. While that survey is sub-auroral, they only consider the nightside region. Their range of geomagnetic activities also peaked at Kp = 3, which is still a fairly low level of geomagnetic activity. The aim of this study is to compare statistical sub-auroral ion motion to outputs from TIEGCM over low to high geomagnetic activities and across all MLT sectors. We therefore perform a statistical analysis of SuperDARN data ourselves (although we focus less on the SuperDARN velocities themselves compared to Maimaiti et al. (2018) and Maimaiti et al. (2019)) instead we run TIEGCM for equivalent geomagnetic activity levels and compare the modelled and observed ion velocities.

5.2 Solar Inputs

The geomagnetic drivers for TIEGCM are the f10.7cm solar radio flux, the IMF B_x, B_y and B_z (in GSM coordinates), the solar wind speed in the x-direction (IMF V_x)

and the proton density. TIEGCM's background high-latitude electric field is driven by either the Heelis (Heelis et al., 1982) or Weimer (Weimer, 2005) electric potential models. We used the Weimer model (Weimer, 2005), where the equatorward extent of the Weimer electric potential is used to define the boundary between the high-latitude convection and sub-auroral latitudes as discussed in section 2.7. The IMF B_y, B_z solar wind density and IMF V_x are used as inputs for the background Weimer model.

We define our geomagnetic activity ranges using the Kp index. We handle Kp ranges in integer steps of 1 e.g. Kp 0-1, 1-2.... 7-8, 8-9. In principle, it is possible to run TIEGCM using the recorded solar inputs for every day between 2012-2018, however the computation requirements to do so are excessive. Instead we run an instance of TIEGCM for a single day using representative inputs for each given Kp range. For each index e.g. IMF B_y we obtain all values that occur for a given Kp range between 2012-2018. We then take the median of all values that occur during a negative IMF B_z. If we took all values (regardless of IMF B_z orientation) then occurences of both positive and negative values would result in the median values trending towards zero, instead of capturing enhanced activity. We choose to use IMF B_z as tests indicated that the equatorward extent of the Weimer boundary was most sensitive to changes in that index.

Figure 5.1 shows the median values of each index during negative IMF B_z for every Kp range. (a) Shows the f10.7cm solar radio flux intensity, (b, c, d) show the IMF B_x, B_y and B_z respectively. (e) is the IMF velocity in the x direction and (f) is the solar wind proton density. All parameters show increased magnitudes for greater geomagnetic activities except for the IMF B_x, B_y, B_z and V_x at the Kp8-9 which all have decreased magnitudes. This is likely due to only a limited number of Kp 8-9 events occuring, providing a poor sample size. Tests indicated that the Weimer model is most sensitive to IMF B_z and V_x, while the other parameters have little effect on the equatorward expansion of the model. The IMF B_z starts close to 0 nT for Kp 0-1 while its magnitude increases to 15 nT for Kp 7-8. The IMF V_x

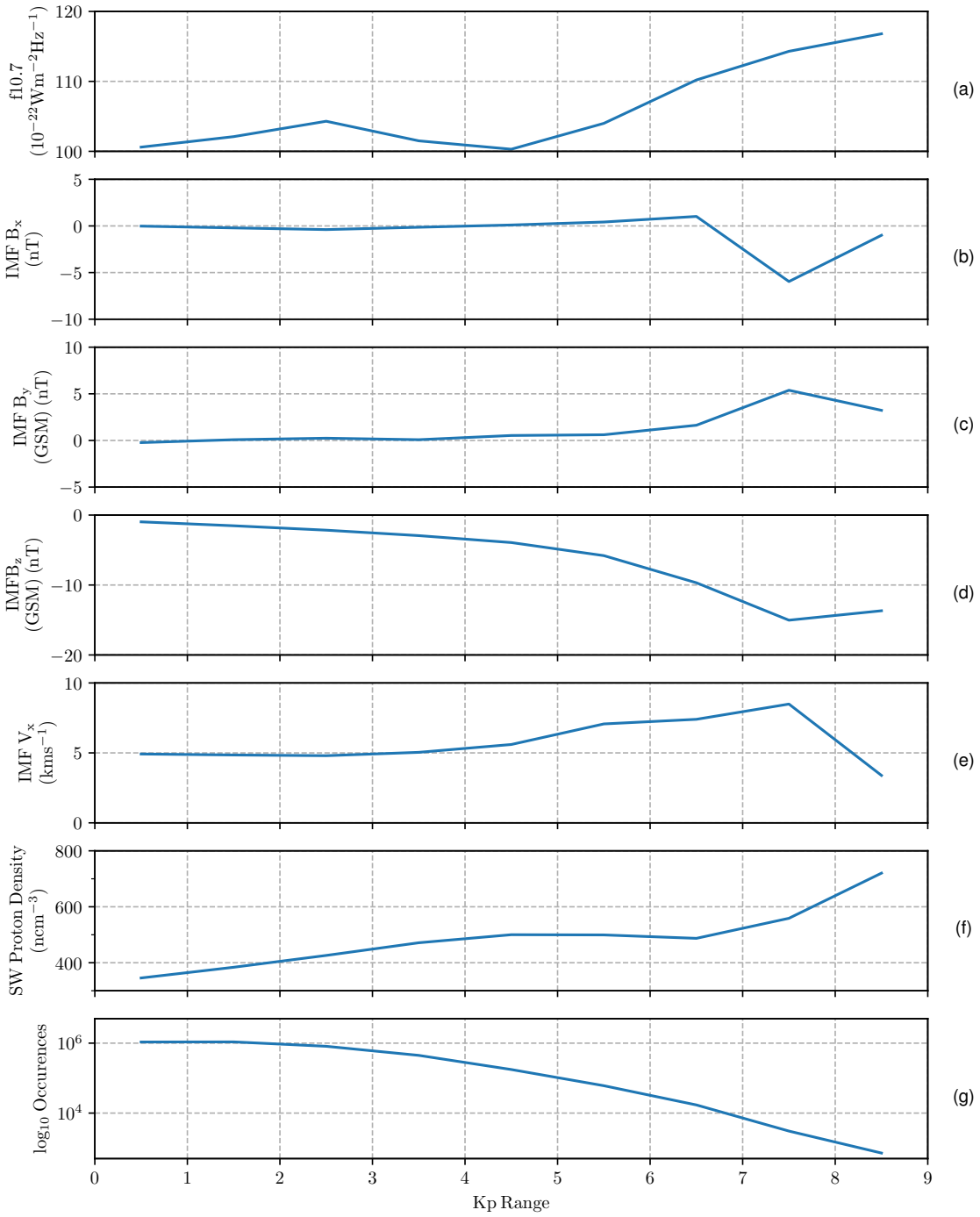

Figure 5.1: Median solar indices during negative IMF B_z between 2012-2018. (a) shows f10.7cm solar radio flux intensity. (b) IMF B_x, (c) IMF B_y, (d) IMF B_z, (e) IMF V_x and (f) the solar wind proton density. (g) Shows the number of occurences for each Kp range.

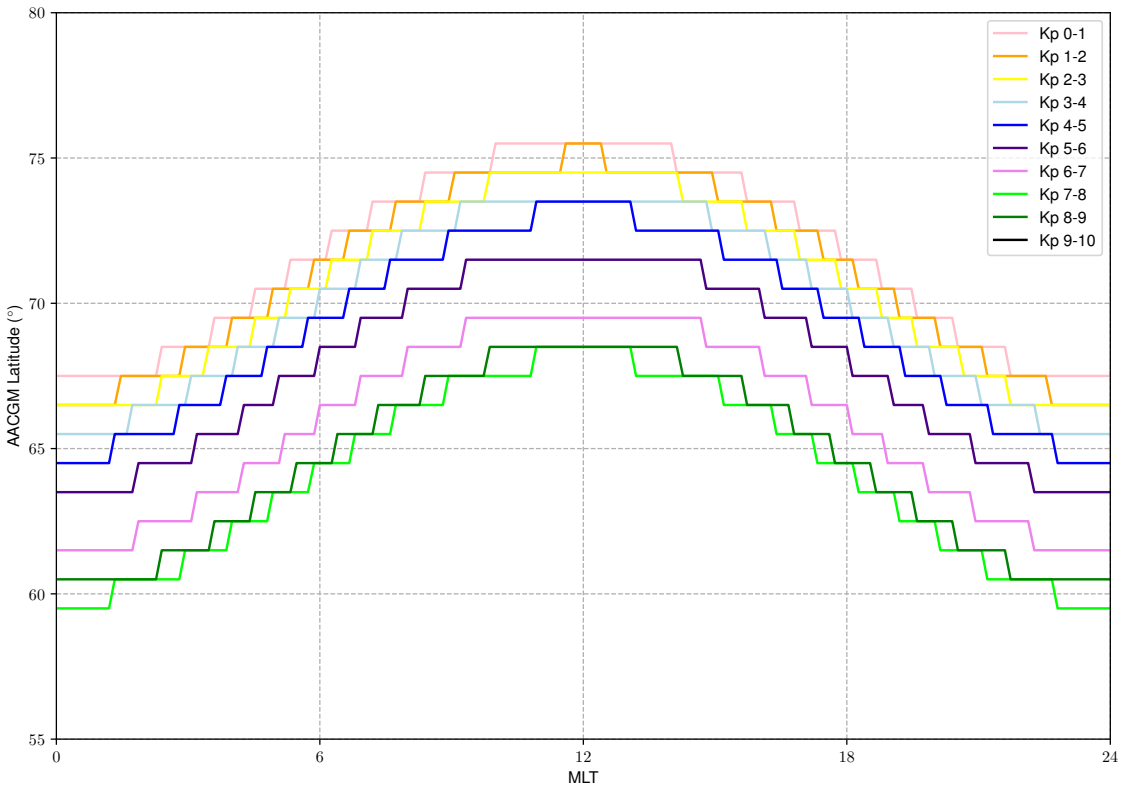

Figure 5.2: Latitudes where the Weimer model's electric potential goes to zero for the different Kp ranges using the driving conditions presented in Figure 5.1.

steadily increases from approximately 500 kms^{-1} to roughly 800 kms^{-1} for Kp 7-8.

5.3 The Sub-Auroral Boundary

Figure 5.2 shows the magnetic latitude where the electric potential of the Weimer model goes to zero for all MLTs, using the statistical solar inputs shown in Figure 5.1.

For the lowest geomagnetic activity range, the pattern extends to approximately 67° magnetic latitude at MLT midnight. As geomagnetic activity increases, the boundary expands to just below 60° at MLT midnight. The boundary expands only slightly at low Kp ranges (Kp $0-1$, $1-2$ and $2-3$), however the rate of expansion increases as geomagnetic activity increases, with the greatest expansion occuring

when the Kp steps up from $5-6$ to $6-7$. After the $7-8$ Kp range, the boundary saturates and does not expand further with increased activity, this could however be a symptom of poor solar input values for Kp $8-9$.

We survey for data from all of the northern hemisphere mid-latitude SuperDARN radars between 2012-2018. We split the data by Kp range and then filter to only select recorded data equatorward of the zero-value electric potential boundary of the Wiemer model for each geomagnetic activity as shown in Figure 5.2. We also cut data above this boundary in TIEGCM. It is important to note that for TIEGCM, the boundary of the Weimer model is not the same as the auroral boundary in TIEGCM (see section 2.7), therefore this cutoff may include some auroral data/exclude some sub-auroral data in the model. We split the velocities into bins of 2° latitude by 25ms^{-1}. Although the Ribeiro et al. (2011) algorithm is optimal for determining groundscatter without eliminating too much ionospheric scatter, it is a computationally intense algorithm to perform and we have a sufficiently large database of recorded ionospheric scatter that discarding some ionospheric scatter, especially as we are not focusing on slow moving ionospheric scatter such as in Maimaiti et al. (2018), is not of great concern. We therefore exclude velocities $< 25\,\mathrm{ms}^{-1}$ to eliminate groundscatter. To investigate the dependence of ionospheric scatter by MLT, we further split the remaining statistical data and the data from TIEGCM into noon (0900 MLT - 1500 MLT), dusk (1500 MLT - 2100 MLT), midnight (2100 UT - 0300 UT) and dawn (0300 UT - 0900 UT) MLT sectors.

5.4 Results

5.4.1 Comparison of SuperDARN and TIEGCM ion velocities

Figure 5.3 shows the probability of observed LOS velocities falling within a particular 2° latitude by $25\,\mathrm{ms}^{-1}$ cell for each MLT sector during low Kp $(1-2)$ according to

the colour bar on the right. The scale on the X-axis has been limited to 600 ms^{-1} for visual clarity but the measurements extend past 2000 ms^{-1}. Past 600 ms^{-1} the probability of seeing velocities greater than this magnitude are negligible and so can be considered to be zero. As we are collating a range of longitudes into each sector, the displayed probabilites are effectively the average probability at each sector. The black line in each plot is the average ion velocity from the TIEGCM run for the same Kp level located at 250 km altitude at the central MLT of each sector i.e. 1200 MLT for the noon sector. The TIEGCM runs used the same geomagnetic inputs as shown from Figure 5.1. White space is where no observed data has been kept, either for being excluded as groundscatter (where LOS velocity is $< 25\,\mathrm{ms}^{-1}$) or from being at latitudes which have been considered to be auroral due to being located poleward of the Weimer boundaries derived in Figure 5.2.

Figure 5.3 shows that the majority of ion scatter is either in the $25 - 50\mathrm{ms}^{-1}$ range or the $50 - 75\mathrm{ms}^{-1}$ range. The highest probabilities of ion scatter are in the $25 - 50\mathrm{ms}^{-1}$ at a latitude of 40° with an occurrence of approximately 45% at noon, 55% at midnight, 52% at dawn and 36% at dusk. All sectors show that roughly 20% less scatter is contained within the $25 - 50\mathrm{ms}^{-1}$ range at the highest latitude compared to 36°. The probability of ion scatter decreases exponentially with increased velocity range magnitudes.

Figure 5.4 which shows the same SuperDARN data as Figure 5.3, but plotted with cumulative probability on the y axis for lines of different latitude. We can see the he cumulative probability of scatter being less than 100 ms^{-1} to be 70% for noon, 84% for midnight 79% for dawn and 60% for dusk at 36° latitude. Across each sector the likelihood of velocities less than 100 ms^{-1} at 66° latitude is between $30 - 35\%$ lower than at 36° latitude. The dusk sector shows the highest likelihood of fast ion motion past velocity ranges of 200 ms^{-1}, with most latitude velocity bins having a probability of around 1%, while midnight, dawn and noon all have streaks of probabilities an order of magnitude less, 0.1%, at around 40° and 50° latitude.

The average TIEGCM ion velocity stays between $25 - 75$ ms^{-1} for both noon

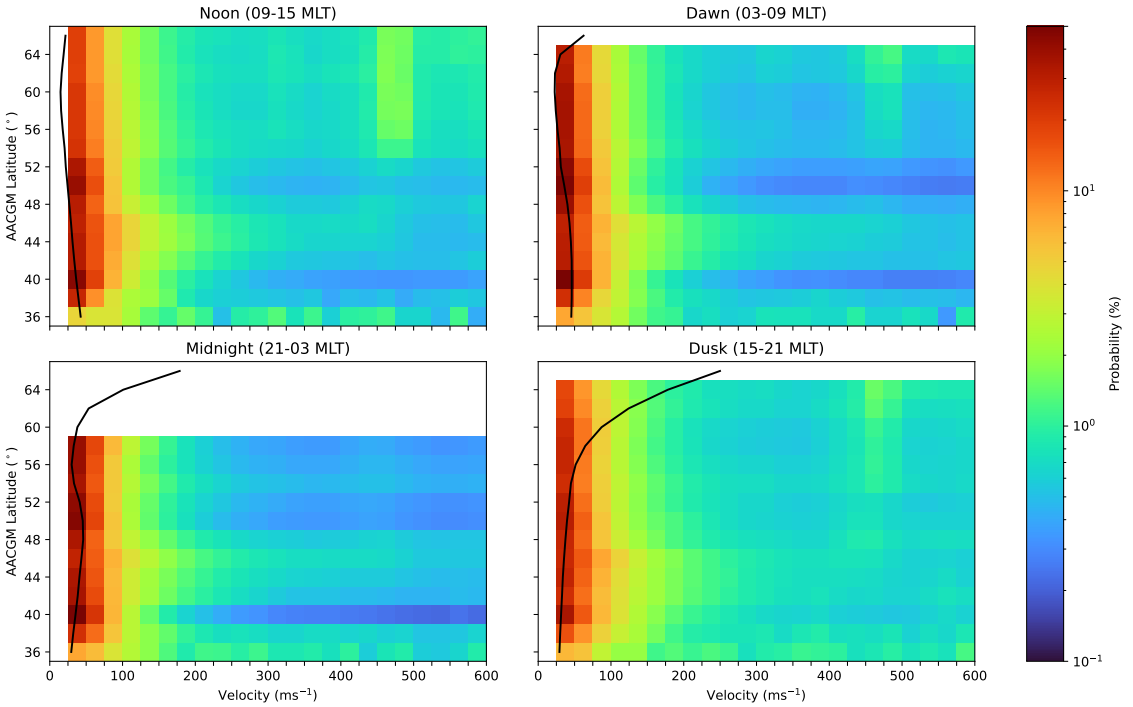

Figure 5.3: Probabilities of observed ionospheric scatter during Kp 0-1 in 2° latitude by 25 ms^{-1} bins according to the colour bar on the right. Top (right) is for the noon (dawn) and bottom (right) is for the midnight (dusk) MLT sectors, given by the MLT range at the top of each panel. The black line is the average TIEGCM velocity for the same Kp activity. White space is where no data has been collected, either for being excluded for groundscatter or due to being considered as from auroral latitudes.

and dawn which is in line with 70% and 79% of the ion scatter having velocities $< 100\ \mathrm{ms}^{-1}$ at noon and dawn respectively. In the midnight sector, the TIEGCM velocities remain at $25 - 50\ \mathrm{ms}^{-1}$ across all latitude ranges where data has been recorded. At dusk however, the TIEGCM velocities are between $25 - 50\ \mathrm{ms}^{-1}$ except poleward of 55° latitude, where the velocity increases by approximately two velocity bins (50 ms^{-1}) for every 2 degrees of latitude, resulting in modelled ion velocities in excess of 200 ms^{-1} at 64° latitude. According to the observations, the probability of these observations are only of the order of 1%. This may be due to

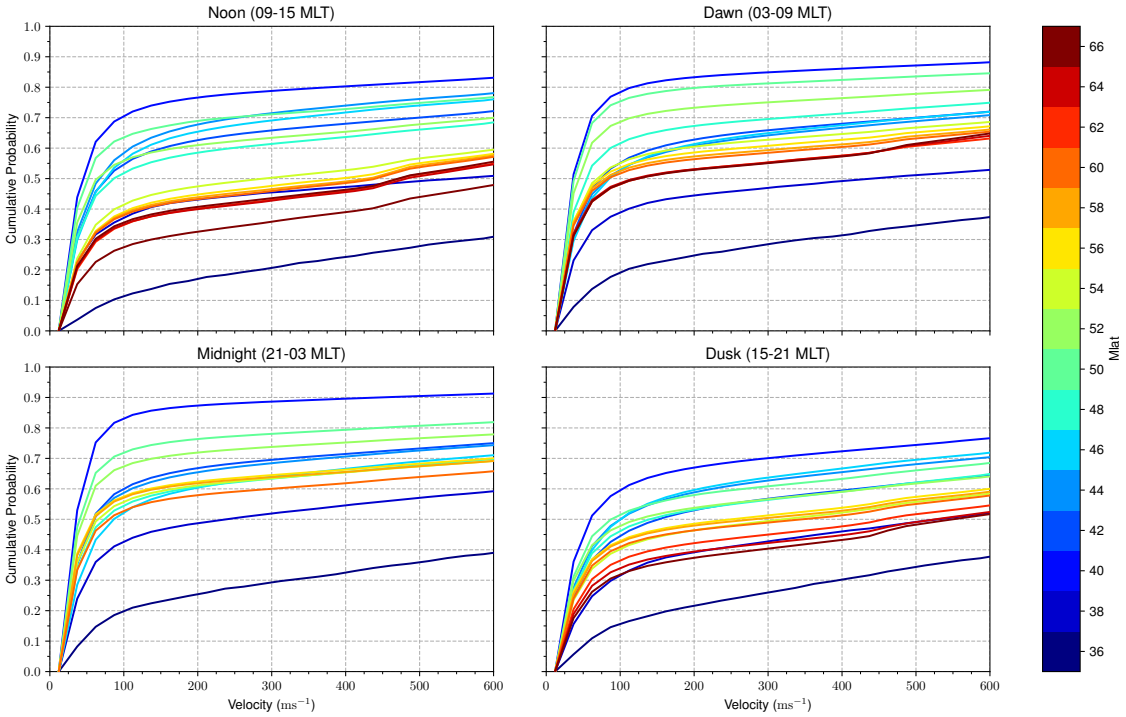

Figure 5.4: Cumulative probabilities of observed ionospheric scatter during Kp 0-1 in 2° latitude by 25 ms^{-1} bins according to the colourbar on the right. Top (right) is for the noon (dawn) and bottom (right) is for the midnight (dusk) MLT sectors, given by the MLT range at the top of each panel. The black line is the average TIEGCM velocity for the same Kp activity. White space is where no data has been collected, either for being excluded for groundscatter or due to being considered as from auroral latitudes.

the disconnect between the TIEGCM auroral boundary and the Weimer boundary resulting in contamination of high-latitude ion velocities in the TIEGCM dataset.

Figure 5.5 shows the same as Figure 5.3, but for a Kp range of $6-7$ while Figure 5.6 shows the SupderDARN data in the same cumulative format as Figure 5.4. The latitudinal limit of these figures is much lower due to the expanded Weimer pattern, with the poleward limit occurring at 52° latitude at midnight. The equatorward limit at low Kp is 36° latitude, whereas At high Kp the equatorward latitude limit is 40° due to fewer intervals occuring at this Kp range. Apart from the change in

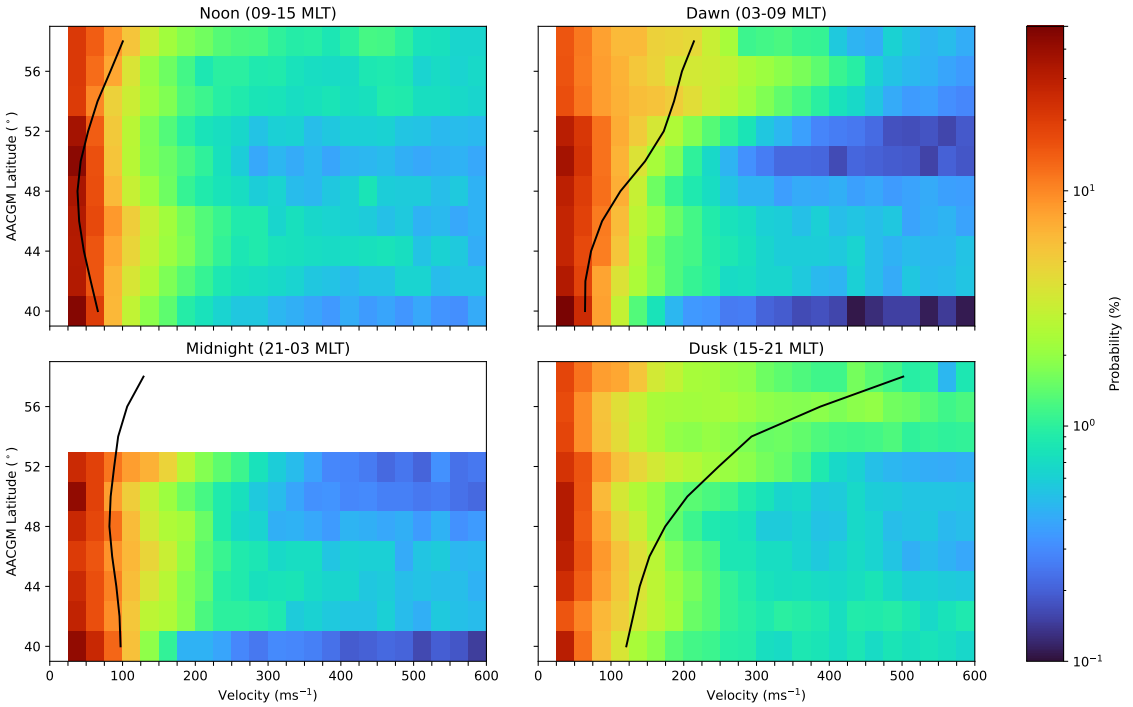

Figure 5.5: The same as Figure 5.3 except for during Kp 6-7.

latitudinal spread, noon sees little difference in the statistical likelihoods compared to the low Kp map. The lowest latitude still has a probability of 45% of scatter between 25 and 50 ms^{-1} and the highest latitude has a likelihood of 22% less than at 40°. Midnight sees the highest latitude of scatter (52°) have a 25% probability of the lowest velocity bin while the cumulative probability of observing velocities $> 100\,\mathrm{ms}^{-1}$ increases from 16% at low Kp to 45% for high Kp at the lowest latitude of recorded scatter (36° at low Kp, 40° at high Kp). The $25-50\,\mathrm{ms}^{-1}$ velocity range still has the highest likelihood of containing scatter across all MLT sectors and latitudes. An interesting feature of both dawn and dusk is the increased probability of higher velocity scatter, of the order around 5% above 52° latitude compared to lower latitudes. At dusk the probability of scatter at a lower latitude than 52° is around 1%, while at dawn this decreases closer to 0.1%.

The TIEGCM velocities are generally shifted towards higher velocity bins across all sectors at higher Kp. At Noon, TIEGCM's velocity is within the $25-50\,\mathrm{ms}^{-1}$

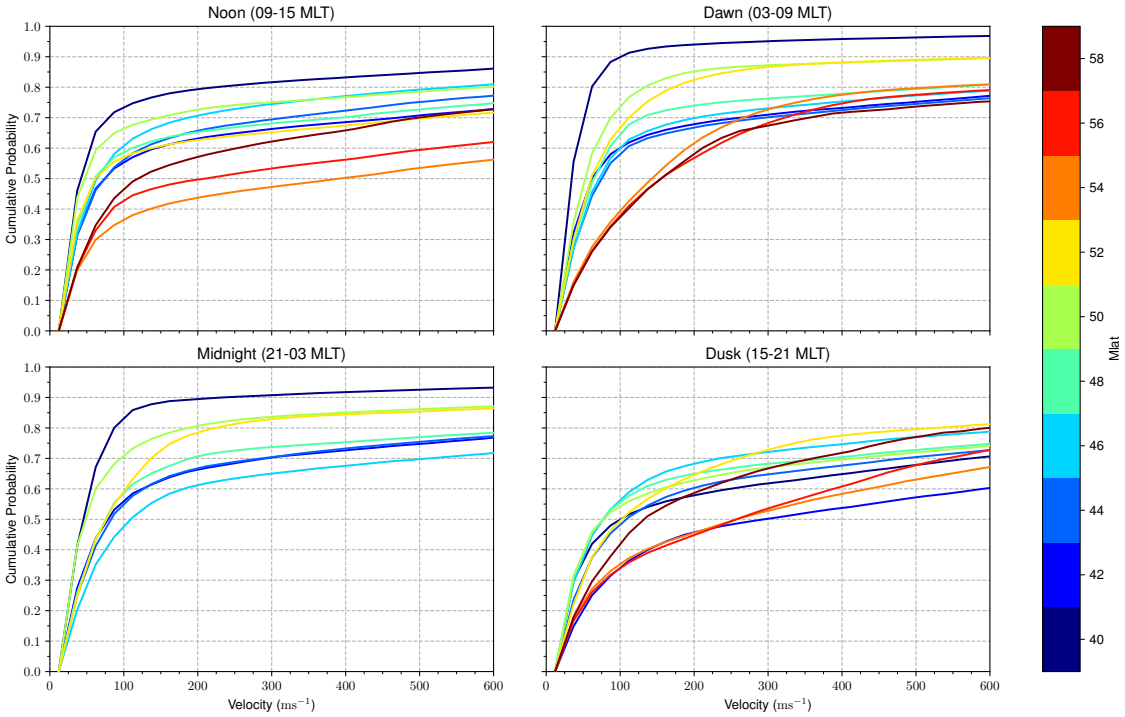

Figure 5.6: The same as Figure 5.4 except for during Kp 6-7.

range from $40° - 42°$ latitude ($32\% - 52\%$ observation likelihood respectively) and $52° - 56°$ latitude (each with a 22% observation likelihood) but dips in between so that it is within the $25 - 50$ ms^{-1} bin at around $48°$ latitude, where 48% of the scatter is located. The observed data shows an increased likelihood at the centre of the noon latitude range, the velocity line from TIEGCM appears to "bend" so that it behaves similarly to the observations. This same effect appears in the midnight sector, although it occurs over greater velocity magnitudes, with the upper and lower latitudes modelling the velocities towards the upper end of the $75 - 100$ ms^{-1} bin while the velocities at the central latitudes are modelled towards the lower end of the $75 - 100$ ms^{-1} velocity bin. In both dawn and dusk, the velocities at the lowest latitudes start off at a lower velocity bin, $50 - 75$ ms^{-1} ($\sim 25\%$ observed data probability) for dawn and $100 - 125$ ms^{-1} ($\sim 5\%$ observed data probability) for dusk. In both the dawn and dusk sectors, the modelled velocity increases with latitude, so that at $58°$ latitude in the dawn sector the TIEGCM velocity is modelled in the

$200 - 225\,\mathrm{ms}^{-1}$ velocity bin ($\sim 4\%$ observed data probability). In the dusk sector, TIEGCM increases its velocity aggressively, following an inverse exponential and actually appears to follow the trends from the observed data, with increased latitude and reaching a velocity bin of $500 - 525\,\mathrm{ms}^{-1}$ ($\sim 2\%$ observed data probability). Although the likelihood of observed data being placed in the $500 - 525\,\mathrm{ms}^{-1}$ bin is small, the cumulative probability of velocities $\geq 500\,\mathrm{ms}^{-1}$ at 58° latitude in the dusk sector for high-Kp is around 20%.

5.4.2 Implications of ion velocity distributions for Joule heating estimates

For a closer investigation on the how the differing ion velocities affect the Joule heating across different geomagnetic activities, Figure 5.7 plots the Joule heating rate against geomagnetic activity using the deciles of observed ion velocity distributions at a single point, where the magnitude of the ion flows are taken at the centre of each velocity range i.e. velocities in the $25 - 50\,\mathrm{ms}^{-1}$ velocity range have a magnitude of $37.5\,\mathrm{ms}^{-1}$. We take the probabilities from 48° latitude at the centre of each MLT sector, which is the highest latitude that is deemed sub-auroral for all sectors and Kp ranges. The Joule heating rate for each decile velocity was calculated by using the TIEGCM neutral wind velocity magnitudes and directions, conductivities, and magnetic field values for all times at each point and then averaged over all times. The ion velocity directions are also taken from TIEGCM such that only the velocity magnitude is varied. The coloured background of each sector shows the magnitude of the ion velocity required to achieve the Joule heating rate according to the green-blue colour bar. The background velocity values were calculated by rearranging equation 1.83 into

$$\mathbf{v} = \frac{1}{\mathbf{B}}\left[\sqrt{\frac{Q_j}{\sigma_p}} - (\mathbf{u} \times \mathbf{B})\right] \tag{5.1}$$

and averaging the output velocities.

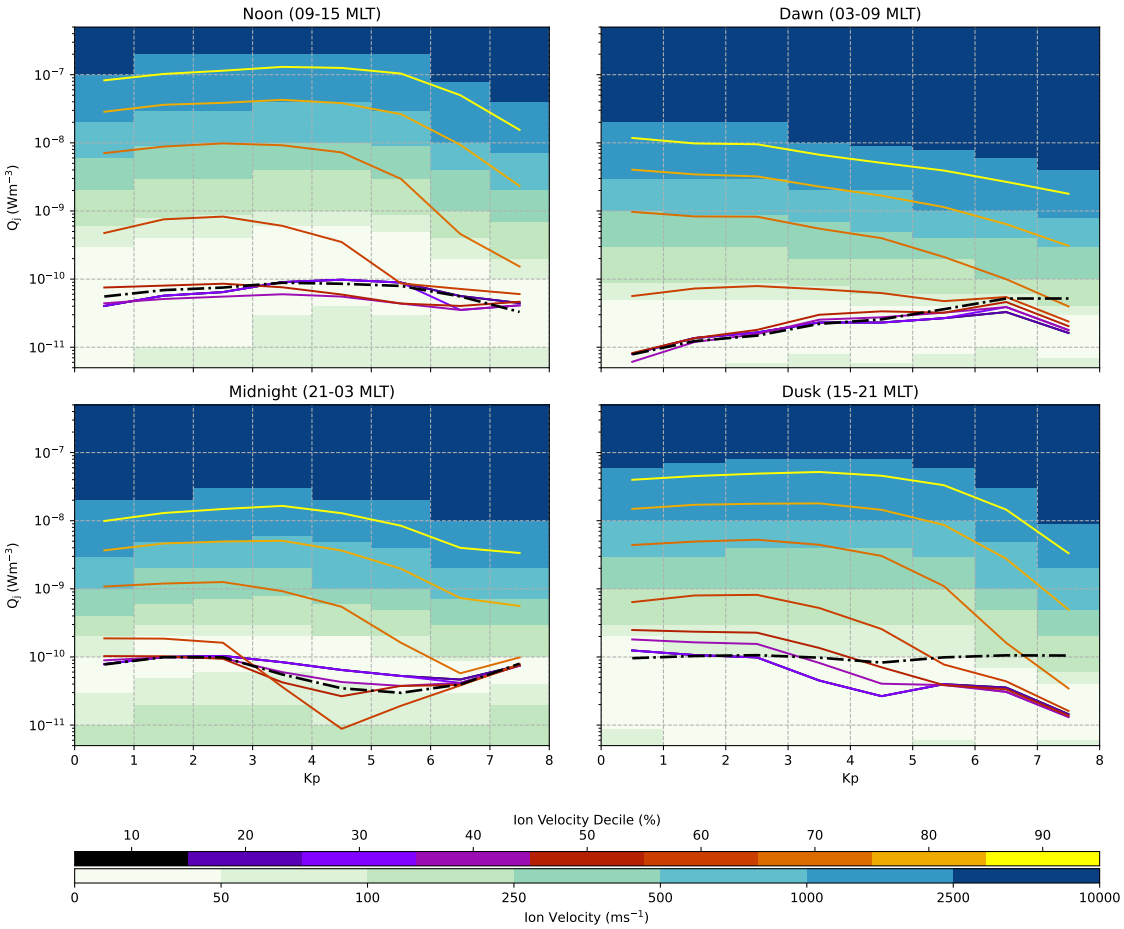

Figure 5.7: Lines show the Joule heating for the decile ion velocities for each Kp range at 48° AACGM latitude for the noon (top left), midnight (bottom left) dawn (top right) and dusk (bottom right) sectors. Backgrounds show the ion velocity required to result in the Joule heating magnitude (y axis) for each Kp range (X-axis) according to the green-blue colour bar. The dashed black line shows the Joule heating magnitude modelled by using TIEGCM's ion velocity.

Because so much of the ion velocity scatter is located in the lowest velocity range ($25 - 50\,\mathrm{ms}^{-1}$), the 1st, 2nd, 3rd and sometimes 4th deciles all produce the same velocity value of $37.5\,\mathrm{ms}^{-1}$, perfectly overlapping each other and resulting in only 6 lines being visible. The dashed black line shows the magnitude of the Joule heating modelled by TIEGCM, using its own ion velocity magnitude. Aside from dusk, the TIEGCM line closely follows some of the decile lines. At midnight, TIEGCM shows a magnitude that is very similar to the decile marking 50% of the observations across all Kp ranges with velocities between $0\,\mathrm{ms}^{-1}$ and $50\,\mathrm{ms}^{-1}$ at Kps between 0-3, and velocities between $50\,\mathrm{ms}^{-1}$ and $100\,\mathrm{ms}^{-1}$ for Kps 3-6. Despite a slight dip in magnitude for the 6th and 7th deciles, the 1st to 7th deciles all report the same Joule heating magnitude from velocity magnitudes of less than $100\,\mathrm{ms}^{-1}$. The 8th and 9th deciles are generally 2 orders of magnitude higher than modelled by TIEGCM, based on velocity magnitudes exceeding $250\,\mathrm{ms}^{-1}$ at low Kp and $100\,\mathrm{ms}^{-1}$ at high Kp for the 8th decile, while the 9th decile from velocity magnitudes in excess of $1000\,\mathrm{ms}^{-1}$ throughout (except for Kp 7-8).

The noon and dawn sectors portray similar results to midnight. Although not as closely aligned with a decile line for the entire set of Kp ranges, TIEGCM closely matches the 4th and 5th decile at middling Kp in the noon and dawn regions respectively. The TIEGCM line and the 1st to 6th deciles generally report velocities in the range of $0\,\mathrm{ms}^{-1}$ to $50\,\mathrm{ms}^{-1}$, resulting in Joule heating rates of the order of $10^{-10}\,\mathrm{Wm}^{-3}$ at noon and dawn. Compared to midnight, noon and dawn show a greater difference between the 7th decile and the lower deciles. Noon especially, shows Joule heating rates an order of magnitude higher for low-mid Kp. While dawn shows similar differences in the Joule heating magnitudes from the 8th and 9th deciles (two orders of magnitudes higher than TIEGCM ion velocities), at noon, the 8th and 9th deciles are up to 3 orders of magnitude higher than TIEGCM. If we investigate the background ion velocity colourmap, it is interesting to note that the extra Joule heating magnitude is not due to higher ion velocities, instead the same velocity values result in higher Joule heating rates at noon than in the

midnight, dawn and dusk sectors indicating that other factors affect the heating which shall be discussed in section 5.5 In general, the noon sector outputs the highest heating with the lowest ion velocities, whereas the dawn sector requires the highest velocities to achieve the same heating. For example, between Kp 4-5, Noon only requires velocities of $500-1000\,\mathrm{ms}^{-1}$ to result in Joule heating rates of the order of $10^{-8}\,\mathrm{Wm}^{-3}$, while to achieve the same heating at Dawn, velocities $> 2500\,\mathrm{ms}^{-1}$ are required.

TIEGCM exhibits the greatest difference between the deciles at dusk, although it follows a similar pattern to the 4th decile for Kps $0-3$, with velocities between $0\,\mathrm{ms}^{-1}$ and $50\,\mathrm{ms}^{-1}$. Each of the 1st to 7th decile lines tend to produce lower Joule heating magnitudes at greater geomagnetic activity, where velocities from the 7th decile drops from a range of $100\,\mathrm{ms}^{-1}$ to $250\,\mathrm{ms}^{-1}$ down to just $0\,\mathrm{ms}^{-1}$ to $50\,\mathrm{ms}^{-1}$. While at dusk the 8th and 9th decile starts with Joule heating rates 2 and 3 orders of magnitude higher than modelled by TIEGCM, from velocities exceeding magnitudes of $500\,\mathrm{ms}^{-1}$ and $1000\,\mathrm{ms}^{-1}$ respectively, each decreases with Kp so that at Kp 7-8, the 8th decile shows Joule heating magnitudes lower than modelled by TIEGCM. While most profound at dawn, the decreased Joule heating and velocity magnitudes with increased Kp is present for nearly all observed decile values in every sector.

Of particular interest is how the variation of ion velocities affects the overall Joule heating magnitude. At midnight, the lowest Joule heating magnitudes of the order of $10^{-11}\,\mathrm{Wm}^{-3}$ are not produced by the lowest velocity magnitudes of up to $50\,\mathrm{ms}^{-1}$, instead they are the result of velocity values between $100\,\mathrm{ms}^{-1}$ and $250\,\mathrm{ms}^{-1}$. In fact, velocity values of up to $250\,\mathrm{ms}^{-1}$ result in Joule heating values of the order of either $10^{-11}\,\mathrm{Wm}^{-3}$ or up to $10^{-9}\,\mathrm{ms}^{-1}$. We see this also manifesting in the statistical data, where the 5th and 6th velocity deciles result in lower Joule heating than the preceding deciles. Although to a lesser degree, all sectors show this feature of similar velocities resulting in different magnitudes of Joule heating, suggesting that other factors than the ion velocity magnitudes, such as the ion direction relative to the neutrals, the Pedersen conductivity or the neutral velocity

magnitudes have a significant impact on the resulting Joule heating magnitudes.

Whereas Figure 5.7 indicates how TIEGCM's ion velocities compare to the statistical data, Figure 5.8 specifically shows how the Joule heating is affected by variations based on TIEGCM's ion velocity. Using the probability data shown in Figures 5.3 and 5.5, we have calculated the Joule heating for each 25 ms^{-1} velocity bin, taking the centre value from each bin e.g. 37.5 ms^{-1} for 25 ms^{-1} to 50 ms^{-1}. Similarly to previously, the Joule heating rate for each velocity bin was calculated by using the TIEGCM neutral wind velocity magnitudes and directions, conductivities, and magnetic field values for all times at each bin and then averaged over all times. The resulting Joule heating value has the same probability as the corresponding velocity bin for the specific Kp range and magnetic latitude. The background of Figure 5.8 shows the Joule heating probability across different levels of geomagnetic activity calculated at 48° magnetic latitude according to the bottom colour bar. It should be noted that because of the features shown in Figure 5.7, where the same velocity results in different levels of Joule heating due to factors other then the ion velocity magnitude, the reverse happens here, where different ion velocity magnitudes can result in the same Joule heating value, which has the effect of the probabilities (or the "pixels" in the colourmap) at least partially overlapping each other. In these cases, where the probabilities (or "pixels") overlap, we sum the overlapping regions. The result is that at dawn and midnight, despite the lowest velocity bins being the most probable, the most probable Joule heating magnitudes are often not the minimum Joule heating magnitudes possible, especially at middling Kp ranges. At midnight for Kp $4-5$ the lowest Joule heating of $9^{-12}\,\mathrm{Wm}^{-3}$ has a probability of around 2%, whereas the most probable Joule heating magnitudes are around $7^{-11}\,\mathrm{Wm}^{-3}$ with a probability of $\sim 50\%$. For both noon and midnight the most probable Joule heating magnitudes typically hover between $10^{-11}\,\mathrm{Wm}^{-3}$ and $10^{-10}\,\mathrm{Wm}^{-3}$ for all Kp ranges. The dawn sector starts with the most probable Joule heating magnitudes occuring with the order of $10^{-12}\,\mathrm{Wm}^{-3}$ at low Kp , while increasing almost linearly to around $5^{-11}\,\mathrm{Wm}^{-3}$ with geomagnetic activity. The

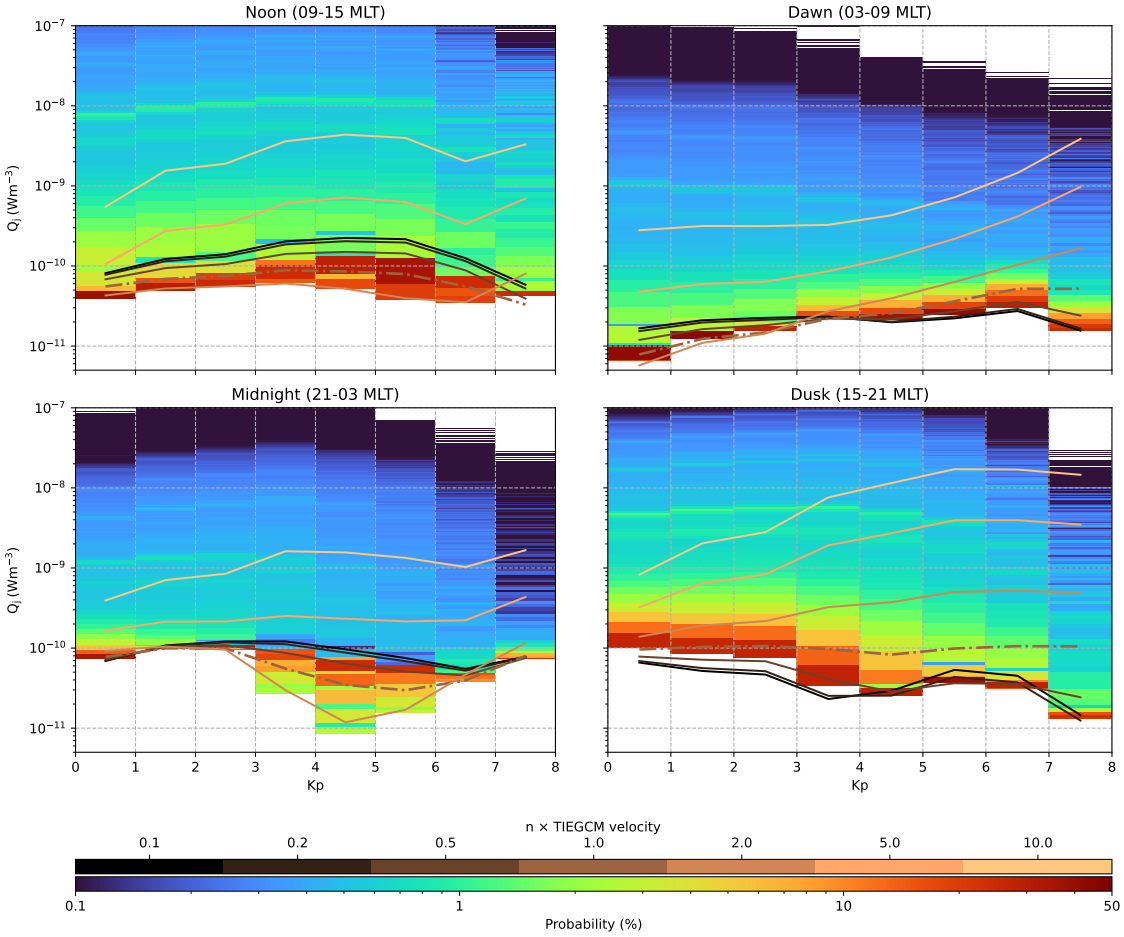

Figure 5.8: Lines show the Joule heating for multiples, n, of the TIEGCM ion velocity, where n is given by the top colour bar for the noon (top left), midnight (bottom left), dawn (top right) and dusk(bottom right) sectors. TIEGCM's Joule heating ($n = 1$) has also been dashed. Backgrounds show the probability of Joule heating magnitude (y axis) for each Kp range (X-axis) using the statistical observed velocity probabilities according to the bottom colour bar.

dusk sector shows the opposite effect of dawn. Low Kp sees most Joule heating depositing with magnitudes of the order of $10^{-10}\,\mathrm{Wm}^{-3}$, while decreasing with increasing geomagnetic activity to around $5^{-11}\,\mathrm{Wm}^{-3}$ for Kp $6-7$.

Plotted on top of the Joule heating colourmaps in Figure 5.8 is the Joule heating magnitude calculated using multiples, n, of the modelled TIEGCM ion velocity at 48° magnetic latitude, at the center of each MLT sector for each Kp range, where n is a value according to the top colour bar above the probability colour bar. TIEGCM's actual modelled ion velocity (given as $n = 1$) has been plotted as a dashed line to help distinguish it from other values of n. At both noon and dawn, TIEGCM's ion velocity results in Joule heating that is mostly contained within the most probable Joule heating values from the data. Since the ion velocities are the only variable between the modelled and observed data, it indicates that in these sectors, TIEGCM does produce the most probable Joule heating. At midnight and dusk between Kp's $0-3$, TIEGCM's ion velocity also results in Joule heating rates that are mostly probable according to the data, however from Kps 3 and above, TIEGCM ion velocities of $n \leq 0.5$ actually result in the most probable Joule heating. At midnight, the line corresponding to $n = 0.5$ especially shows a strong correlation with the most probable Joule heating values, suggesting that on a statistical level, half of TIEGCM's ion velocity would produce more realistically probable Joule heating outputs. The low velocities ($n < 1$) in each sector all result in quite similar Joule heating magnitudes. If the ion velocity is small enough relative to the neutral wind motion then the ion contribution to the Joule heating will be negligible. Thus, past some threshold, lowering the ion velocities will have no discernible impact on the output Joule heating.

At midnight (and noon), the $n = 2$ TIEGCM ion velocity produces lower Joule heating magnitudes of $\sim 10^{-11}\,\mathrm{Wm}^{-3}$ compared to $\sim 5 \times 10^{-11}\,\mathrm{ms}^{-1}$ of TIEGCM's velocity at Kp4-5. This falls in line with the findings from Figure 5.7, where velocities slightly larger than TIEGCM's result in lower Joule heating, due to other factors than the ion velocity magnitude. When the ion velocities are sufficiently

large ($n \geq 5$), the ion velocity magnitude overcomes the other factors and produces greater Joule heating. In all sectors and Kp ranges, TIEGCM's modelled ion velocity produces Joule heating magnitudes of the order of 10^{-11} Wm^{-3}. Generally, across all sectors and Kp ranges, $n = 5$ and $n = 10$ TIEGCM ion velocities each produce Joule heating magnitudes one, and two orders of magnitudes higher than TIEGCM's respectively.

Figures 5.7 and 5.8 report that at midnight some higher ion velocities can result in lower Joule heating being produced, however other sectors, such as dusk do not show this. To identify the causes of this, Figure 5.9 plots the individual contributors to the Joule heating (a) σ_p, (b) the angle between the ions and neutrals $\mathbf{u} - \mathbf{V}$, (c) the neutral wind velocity, $\mathbf{u}$, the ion velocity (d) $\mathbf{V}$ and the individual Joule heating components (e) $\mathrm{Q_{w2}}$, (f) $\mathrm{Q_c}$, (g) $\mathrm{Q_{w1}}$ and (h) $\mathrm{Q_j}$ for the (left) midnight and (right) dusk sectors at 48° magnetic latitude. The ion velocities correpsonding to $n = 0.5$, $n = 1$ and $n = 2$ and resulting $\mathrm{Q_c}$, $\mathrm{Q_{w1}}$ and $\mathrm{Q_j}$ are shown according to the legend in panel d. Note that there is a slight disconnect between the plotted contributors (panels a - d) and the Joule heating components (panels e - h). The contributors are plotted as their average value over time for each Kp, however these average values are not used to calculate the components. The components are calculated for all values at all times and are then averaged. The difference is subtle, but important when square terms are involved (such as Q_c and Q_{w2}) since $\overline{(\mathbf{a} \times \mathbf{b})^2} \neq \left(\overline{\mathbf{a}} \times \overline{\mathbf{b}}\right)^2$. The total Joule heating (panel h) shows that at midnight, two times TIEGCM's ion velocity results in a lower Joule heating between Kps 3 to 6 and half of the TIEGCM ion velocity actually results in higher Joule heating than the actual modelled velocity. Compared to dusk, two times the ion velocity results in greater Joule heating than the modelled value, and half results in lower heating. Following the panels up to $\mathrm{Q_{w1}}$ (panel g) we can see that at midnight, twice the TIEGCM ion velocity results in a more negative value, while half the velocity results in the most positive. The principle reasons being this can be found in panel b, which shows the angle between the ions and neutrals. An angle of 0° indicate the two flows are parallel

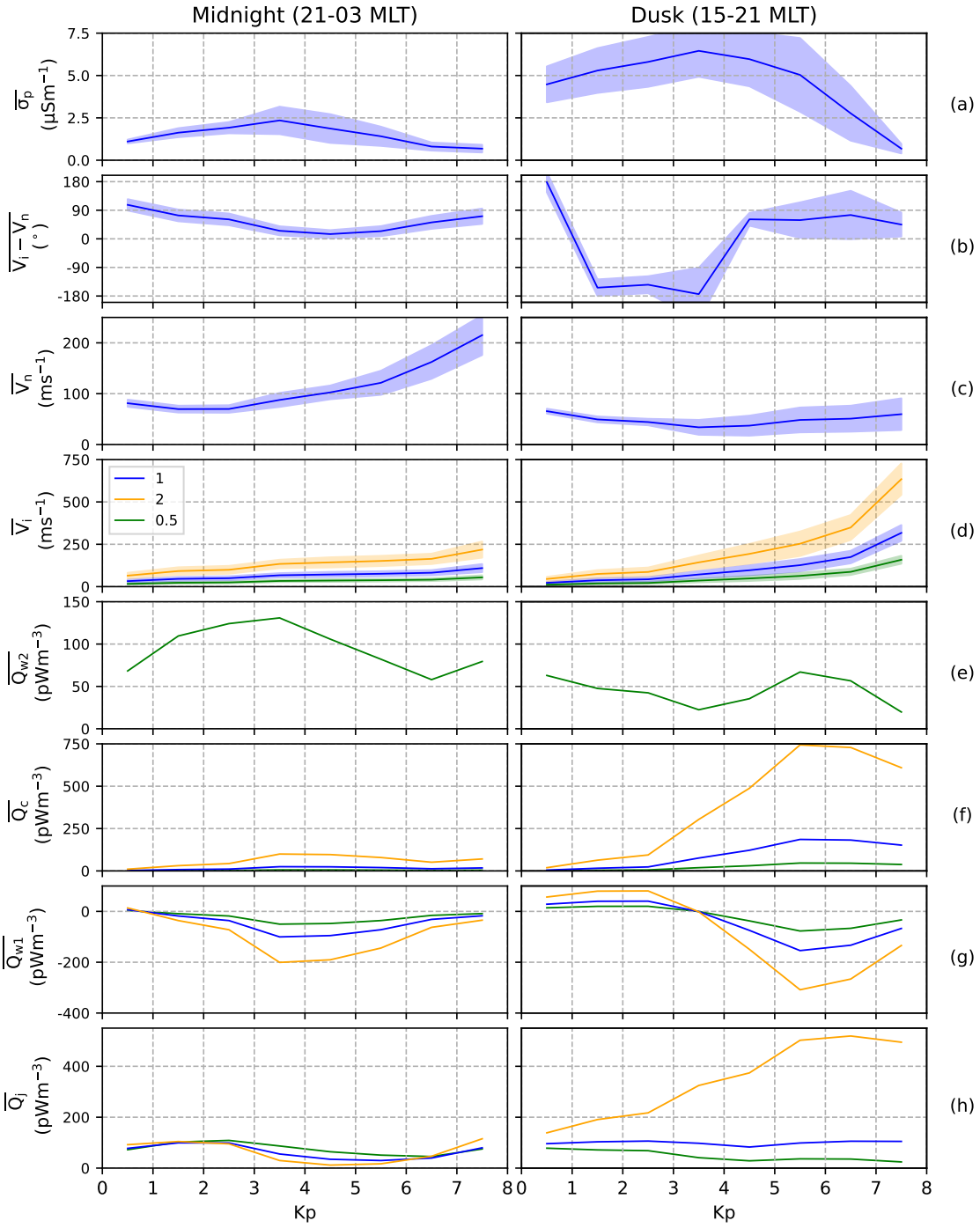

Figure 5.9: Panels a, b, and c show the TIEGCM Pedersen conductivity (σ_p), angle between the ions and neutral flows ($\mathbf{u} - \mathbf{V}$) and neutral wind velocity ($\mathbf{u}$) against Kp at 48° magnetic latitude and averaged over time respectively. Shaded regions indicate the standard deviation. Panel d shows the average of TIEGCM's and half and twice TIEGCM's ion velocity ($\mathbf{V}$). Panels e, f, g and h show the average Joule heating components, Q_{w2}, Q_c, Q_{w1} and Q_j against Kp at 48° magnetic latitude respectively. The left hand side shows data from the midnight sector while the right hand side shows dusk.

and travelling in the same direction, $\pm 90°$ indicate that they are perpendicular to each other, while $\pm 180°$ would show that they are antiparallel, travelling in opposing directions. At midnight, we can see that between Kps 3 to 6, where the Joule heating is decreased the most, the ion-neutral flow angle trends to $0°$, indicating that the flows are travelling approximately the same direction. The amount of Joule heating produced is then solely due to the difference in the ion and neutral velocities. Panel e shows the Joule heating contribution due to the neutrals (Q_{w1}) and panel f shows the contribution due to the ions (Q_{w2}). The neutral contribution between Kp 3 and 4 is around $125 \times 10 \times \mathrm{Wm}^{-12}$ and the ion contribution is comparitively small at half and one times the TIEGCM ion velocity. At twice the TIEGCM ion velocity the ion contribution to the Joule heating is around $150\mathrm{pWm}^{-3}$. Because the ions and neutrals are in the same direction and are so similar, the ion and neutral contributions are effectively cancelled out. Physically, this represents the fact the very few collisions occur between the neutrals and ions because their velocities are so similar. Interestingly, at dusk from Kps 4 and above, the neutral and ion directions are actually quite similar, and the value of Q_{w1} shows that the Joule heating is decreased because their directions are fairly aligned, however the ion velocities, especially two times TIEGCM's ion velocity, are so much higher than the neutrals, the sheer magnitude of the ion velocity overcomes the fact that they are travelling in the same direction as the neutrals (essentially, the ions are driving the heating) and significant Joule heating is deposited. These results show that the neutrals effectively act as a modulator and set how the ion velocities affect the heating. If the ion velocities are too similar to the neutrals, then regardless of the magnitude of the flow velocities, the Joule heating will be low, the more different the two are (both direction and magnitude) the greater the Joule heating will be, changing whether the neutrals or ions drive the heating.

5.5 Discussion

At all sub-auroral latitudes and levels of geomagnetic activity, low velocity ion scatter, of $< 100\,\mathrm{ms}^{-1}$ and predominantly $< 50\,\mathrm{ms}^{-1}$ are the most probable. The fact that most ion scatter is of low velocity, even at high levels of geomagnetic activity, tells us that the primary drivers of sub-auroral ion motion must be those that produce the low velocity scatter. Maimaiti et al. (2019) reported that a combination of high latitude penetrating electric fields and neutral wind dynamo action drives statistical sub-auroral ion motion of $20 - 90\,\mathrm{ms}^{-1}$. They suggest that the ionospheric conductivity modulates the relative dominance of each mechanism, where pre-midnight flows are typically due to the electric fields, while postmidnight, motion is primarily driven by neutral wind dynamo action. Greenwald et al. (2006) suggested that common occurences of $30 - 90\,\mathrm{ms}^{-1}$ during low to moderate Kp are due to the pressure gradient instabilities formed at the equatorward boundary of the ionospheric trough. Fast ion motion, of $> 200\,\mathrm{ms}^{-1}$, is instead likely to be produced by sub-auroral polarisation streams, which trigger when the equatorward ion precipitation boundary moves equatorward of the electron precipitation boundary (Gussenhoven et al., 1987; Heinemann et al., 1989). A key consideration for these mechanisms is that while all are susceptible to changes in the solar wind-magnetosphere-ionosphere system, the mechanisms which drive penetrating electric fields, the neutral wind dynamo and and pressure gradient drifts are more prevalent than those which drive stronger ion flows such as SAPS, which require more specific magnetosphere-ionosphere configurations to trigger. This means that even at higher levels of geomagnetic activity, the low-velocity ion drivers and resulting low velocity ion motion are still more frequent than high-velocity drivers.

There is likely to be a disconnect between data that we have labelled sub-auroral and whether the data is actually sub-auroral due to parametrising the sub-auroral latitudes rather identifying the sub-auroral boundary for each data point. The result is that our "sub-auroral" data is likely to contain some data from the auroral regions driven by the high-latitude convection pattern. It is hard to confirm how this would

affect the distribution of catalogued ion scatter. If the real boundary is slightly equatorward of our parametrised boundary, then low ion velocities at the boundary of the pattern would contaminate our dataset, if however, the actual equatorward extent of the pattern is significantly equatorward of our parametrised boundary, then high velocity observations would contaminate the dataset. While contamination of low-velocity, high-latitude scatter is important to consider, it does not result in the inclusion of velocity magnitudes that may be impossible to achieve by sub-auroral drivers and, since the majority of our recorded scatter is of low velocity, small amounts of contamination of low-velocity scatter from the high-latitudes should have little impact on the distributions. High-velocity, high-latitude contamination may instead result in velocity magnitudes which are otherwise improbable being included in the dataset. Some of the high-velocity probabilities in the dataset may not be an accurate representation of the sub-auroral ion velocities. Although we have no hard data on where this disconnect occurs, Figure 5.5, in the dusk sector particularly, shows an almost uniform increased likelihood of high-velocity ion scatter above 52° magnetic latitude, which may be due to the actual auroral boundary being equatorward of our parameterised boundary. Confirmation of this would require an analysis of the auroral boundary for each collected data point, which may be a potential area for future improvement. The reverse of the disconnect may also be occuring, where the equatorward extent of the real auroral boundary is poleward of our defined boundary, however this only excludes some sub-auroral population and does not result in high-latitude contamination of the dataset so is of less concern.

The deciles report the magnitude of the velocities (and resulting Joule heating) for the bottom n% of the data, where n is a multiple of 10. Although the comparisons provided by Figure 5.7 do not state how often TIEGCM models Joule heating values correctly, it is an indicator of how often TIEGCM over/underestimates compared to the observations. A perfectly balanced model would then have 50% of the observed data above, and the other 50% of the data below of its modelled value. At noon and dawn, TIEGCM closely tracks the bottom five deciles, where their magnitudes

are quite similar, we can say that in these sectors, across all geomagnetic activities TIEGCM produces Joule heating estimations in line with the observations for the bottom 50% of occurrences. The top 40% of velocities however, show differences of orders of magnitude between TIEGCM and the observational data. Although TIEGCM tracks the bottom 50% less well at midnight and dusk, it tracks them much more closely than the top 30% of ion velocities at midnight and 40% at dusk. This shows that in most cases, TIEGCM models Joule heating magnitudes similar to what we can observe. When TIEGCM is unable to accurately match the observational heating, the velocity magnitudes are usually $> 200\ \mathrm{ms}^{-1}$, which from looking at Figures 5.3 and 5.5, rarely occurs except for in the higher-latitude sub-auroral dawn and dusk sectors. What we have discussed as the drivers of strong ion motion in the observed data, SAPS, and leakage of the high-latitude twin-cell convection pattern are not modelled within TIEGCM and may be the reason for the difference between the TIEGCM simulations and the high-velocity deciles. Furthermore the TIEGCM model was ran using constant inputs, which may result in some alignment of the ions and neutrals over time, thus reducing the Joule heating whereas in reality sudden changes to the solar wind and geomagnetic drivers occur which then de-align the ions and neutrals.

Another interesting feature of Figure 5.7 is that except for the bottom 50% of deciles at dawn, the velocity of the nth deciles all decrease with increased geomagnetic activity. As discussed previously, the statistical dataset show that even at high levels of geomagnetic activity, low ion velocity events are still more frequent than high ion velocity events. We can assume that even at high Kp, there will always be some part of the SuperDARN radar observations that record slow moving ionospheric scatter, however there may not be strong ion motion always occuring. The fewer number of observed high geomagnetic activity datasets (~ 1.5 million datapoints for Kp $1-2$, compared to ~ 30 thousand datapoints for Kp $6-7$), means that the high-Kp dataset may be more prone to "noise" in the occurence rate of fast ion velocity events. There is the possibility that instrument, or "salt and

pepper" noise (Chisham et al., 2007) in the SuperDARN data may be responsible for the decreased velocities. Usually such noise produces extremely high velocities $> 1000\,\mathrm{ms}^{-1}$ and is present in SuperDARN data over all levels of geomagnetic activity. Due to the higher number of datapoints in the low Kp dataset, there are more occurences of extreme ($> 5000\,\mathrm{ms}^{-1}$) datapoints than at high Kp, which may skew the deciles towards higher values, however whether these are due to salt and pepper noise, instrument errors, other artifiacts, or whether they are physical values is difficult to know. Unlike in the previous chapters, the SuperDARN data used in this study has not been median filtered, therefore unphysical values do remain. Future work may instead include this step as a possible method to determine if the decreased decile velocities with Kp is actually a physical phenomena.

Another interesting detail that comes from Figure 5.7 is that in all sectors, as geomagnetic activity increases, higher ion velocities are required to achieve the same level of Joule heating as lower levels of geomagnetic activity. For example, in the midnight sector for a Kp range of $1-2$, The Joule heating rate of $10^{-9}\,\mathrm{Wm}^{-3}$, is between the boundaries requiring $250-500\,\mathrm{ms}^{-1}$. However for Kp ranges of 6 and above, velocities of at least $500\,\mathrm{ms}^{-1}$ are necessary to achieve the same levels of Joule heating. Figure 5.9 shows that the neutrals and ion flow directions are mostly aligned across Kp ranges, while the neutral wind magnitude increases with Kp. The result is that higher ion velocities are required in order to overcome the faster neutrals. The dusk side of Figure 5.9 shows that while the neutral wind velocities do not increase with Kp, they do become more aligned with the ion flow direction. The fact that all sectors of Figure 5.7 show that higher ion velocities are required to achieve the same level of heating, suggest that the neutral winds play an important role in modulating the sub-auroral Joule heating rates. The background of Figure 5.8 actually shows that extreme levels of Joule heating are actually less likely to occur at higher levels of geomagnetic activity. For example, at midnight, there is a $\sim 0.8\%$ likelihood of heating of $> 10^{-9}\,\mathrm{Wm}^{-3}$ at Kp $0-1$, while for Kp $7-8$, this decreases to around 0.1% and at dusk, the same level of

heating has an approximate 5% probability for Kp $0-1$ while for Kp $7-8$, it is nearly ten times less likely with a roughly 0.5% likelihood. This is not to say the Joule heating generally decreases with increased geomagnetic activity, the dawn side of Figure 5.9 does show that Joule heating steadily increases with Kp. The ion velocities however, are not necessarily the controlling factor that effects the Joule heating rate, and while we have shown that greater ion velocities are recorded with increased geomagnetic activity, the neutral wind velocities and directions also change in a manner which require the ion velocities to increase at a greater rate to actually increase the Joule heating. The behaviour of the neutral wind is also likely responsible for the difference in ion velocities required to reach a specific heating in each sector. Coriolis forces and solar pressure gradients are the primary drivers of neutral wind motion in the thermosphere (Rishbeth, 1977). The solar pressure gradients are greatest at noon and drives neutral wind flows against the direction of typical plasma circulation (Billett, 2019), thus requiring lower ion velocities for high levels of Joule heating. At midnight, the solar pressure gradients are minimised and aside from ion-neutral drag, corotation plays a significant factor in the neutral motion which is less dependent on Kp and results in lower neutral velocities. The effect on the Joule heating can also be seen by how "wide" the Joule heating range is for ion velocities $< 50\,\mathrm{ms}^{-1}$, which is rather narrow at midnight, producing Joule heating rates of around $10^{-11}\,\mathrm{Wm}^{-3}$ across Kp ranges, while at Noon, ion velocities of $< 50\,\mathrm{ms}^{-1}$ produces Joule heating rates ranging from $5 \times 10^{-12}\,\mathrm{Wm}^{-3}$ up to $6 \times 10^{-10}\,\mathrm{Wm}^{-3}$. Corotation, which drags the neutrals eastwards, is responsible for many dawn-dusk asymmetries observed in the ionosphere/thermosphere. At high-latitudes, plasma generally circulates westwards in the dusk region and eastwards at dawn (Grocott & Milan, 2014; Grocott et al., 2012; Thomas & Shepherd, 2018) while Kervalishvili and Lühr (2013) showed that the neutral densities are generally higher at dusk than at dawn. A combination of opposing plasma and neutral directions and higher neutral densities in the dusk sector may be responsible for the lower ion velocities producing greater Joule heating than at dawn.

5.6 Summary

The TIEGCM model was run for representative geomagnetic activities over 2011-2018. The different levels of geomagnetic activity were keyed by Kp and the necessary solar wind inputs (F10.7, IMF B_z, IMF B_y, IMF B_x, IMF V_x and solar wind proton density) which were determined by their median values during negative IMF Bz. The Weimer model, which was used as the background model for TIEGCM in this study, was run using the same inputs and its zero-value electric potential latitude was obtained as the auroral/sub-auroral boundary. All the north-American mid-latitude SuperDARN radars were surveyed over the same period and geomagnetic activities for sub-auroral ionospheric scatter and statistical distributions of sub-auroral ion velocities were obtained.

Statistical patterns of the observed ion velocities show that for all levels of geomagnetic activity, low velocity scatter ($< 100\ \mathrm{ms}^{-1}$), driven by penetrating electric fields and the F-region neutral wind dynamo, more commonly occur compared to faster scatter driven by SAPS and leakage of the high-latitude twin-cell convection pattern. The modelled TIEGCM ion velocities follow the trends in the statistical maps fairly well and although at high Kp it models ion velocities greater than the observed data suggests, the likelihood of observed velocity magnitudes do portray increases similar to the TIEGCM distributions. Using the neutral wind and Pedersen conductivity parameters modelled by TIEGCM, statistically, the Joule heating modelled by TIEGCM generally agrees with the bottom 6 deciles of the observed ion velocity distributions over all Kp ranges. The top $3-4$ deciles of the observed ion velocity distributions however, each produce Joule heating magnitudes sequential orders of magnitude greater than what TIEGCM models.

The neutral winds have an important impact on the rates of Joule heating produced. The direction of the neutrals and ions modulates the amount of Joule heating produced for all but extreme ($\geq 250\ \mathrm{ms}^{-1}$) ion velocities and causes the Joule heating to range from orders of $10^{-12}\ \mathrm{Wm}^{-3}$ when the flows are aligned up to $10^{-8}\ \mathrm{Wm}^{-3}$ when they are opposed. For equivalent ion velocities, the noon and

dusk sectors produce greater Joule heating rates than dawn and midnight as solar pressure gradients and corotation drives the neutrals into directions opposite to the plasma motion. Furthermore, because of the neutral winds and their directions, at midnight and noon, the most probable Joule heating rates are up to half a magnitude higher than the lowest possible Joule heating rates, despite the lowest ion velocities being the most probable.

Chapter 6

Conclusions

This thesis has investigated the co-located localised mid-latitude sub-auroral ion and neutral winds in the F-region ionosphere and how interactions between the two influences the Joule heating rates deposited in this region.

In Chapter 3 we identified 16 July 2014 as an interval where ion drift measurements from the BKS SuperDARN were co-located with neutral wind measurements from the ANN FPI. Despite low levels of geomagnetic activity during this event, relatively high ion velocities for the mid-latitudes were recorded (> 200 ms^{-1}) alongside significant neutral wind flows. Analysis from particle precipitation data from the POES satellites and FAC densities from the AMPERE dataset indicate the flows to be sub-auroral. TEC data from GNSS shows the ion drifts to be located at the equatorward boundary of the mid-latitude ionospheric trough and we suggest that the ion flows are driven by pressure gradient forces often found in this region.

Comparisons of the observations to the TIEGCM modelled data show that TIEGCM's ion velocities were almost uniform across the entire interval (~ 50 ms^{-1}) compared to the highly dynamic nature of the observations. While the TIEGCM simulation modelled the meridional neutral velocities well compared to the observations, TIEGCM's zonal neutral velocities were significantly overestimated compared to the observations. Imposing a large scale mid-latitude SAPS model

into TIEGCM had a negligible effect on the ion velocities despite the close spatial proximity to the FPI location. We reason that TIEGCM's lack of sub-auroral dynamic ion drivers was the principle reason for TIEGCM's inability to accurately model the ion and neutral winds compared to the observations and a better representation of the small-scale forces at the mid-latitudes is needed for more accurate model simulations.

In Chapter 4 we continued with the observations from 16 July 2014. We compared two methods of estimating the two-dimensional ion velocities from the line-of-sight observations, a variant of L-shell fitting, whereby we manually tracked patches of "high-velocity" ion scatter across the FOV of the BKS radar and fit the LOS velocities against azimuth to a cosine and the often used technique of spherical harmonic fitting of SuperDARN data. The spherical harmonic fitting method conflicted with the data and reduced the magnitude of their LOS velocities towards zero, whilst the L-shell fitting technique conformed well to the observations. We concluded that the L-shell fitting method was more appropriate for determining two-dimensional sub-auroral ion velocities.

Joule heating estimations using the two-dimensional ion and neutral velocities show significant Joule heating enhancements of over 200 pWm^{-3} occured due to strong ion motion, which is of a similar magnitude to results from high-latitude studies, despite the fact the the interval occured during a geomagnetically quiet period. The neutral winds were shown to have a strong effect on the overall Joule heating rate, accounting for on average between 24% and 43% of the total Joule heating for the different patches of ion scatter. Due to the lack of strong ion motion in TIEGCM, equivalent Joule heating enhancements were not produced by the model and during the peak Joule heating observations, TIEGCM's Joule heating was approximately 8 times lower. Furthermore, the Joule heating modelled by TIEGCM was primarily driven by neutral wind motion compared to ion motion in the observations and, where the observed ion motion was slower during this interval, TIEGCM's overestimation of the neutral winds resulted in TIEGCM overestimating

the Joule heating rate.

The greatest difference between the observed and modelled Joule heating occured when TIEGCM could not model ion velocity enhancements, which lead to the question of how often does this occur, and what is the possible magnitude of this difference? This brings us to Chapter 5 where we ran a statistical survey on the mid-latitude sub-auroral ion velocities observed by the whole mid-latitude SuperDARN network over different gomagnetic activity (Kp) ranges and compared them to TIEGCM. The statistical patterns of observed ion velocities showed that ion velocity scatter of $< 100\,\mathrm{ms}^{-1}$, driven by penetrating electric fields and the F-region neutral wind dynamo was most common across all geomagnetic activity ranges. This further shows the rarity of the fast flows observed in Chapters 3 and 4. While TIEGCM did not match exactly with the ion observations in the statistical survey, it does follow the same trends of increased velocity magnitudes with higher geomagnetic latitudes and greater geomagnetic activity. Furthermore estimations of the Joule heating indicate that TIEGCM generally agrees with the bottom 6 deciles of the statistical ion dataset, however the top $3-4$ deciles of the observed ion velocity distributions produce Joule heating magnitudes that are sequential orders of magnitude greater than TIEGCM.

Variations in the Joule heating magnitudes from similar ion velocities indicate that the neutral winds have an important role in modulating the Joule heating produced. Except for extreme ion velocities ($\geq 250\,\mathrm{ms}^{-1}$), the direction of the neutral winds relative to the ions are responsible for determining the Joule heating rate, which varies from $10^{-12}\,\mathrm{Wm}^{-3}$ when the flows are aligned, up to $10^{-8}\,\mathrm{Wm}^{-3}$ when the flows are opposed. Furthermore, due to solar pressure gradient and corotation which drive the neutrals to a greater extent in the noon and dusk sectors, the noon and dusk sectors produce greater Joule heating magnitudes than at dawn and dusk for equivalent ion velocities.

6.1 Future Work

The focus of this thesis has been on the mid-latitude sub-auroral Joule heating and due to the results from Chapters 3 and 4 the ion motion that drives them. While a statistical analysis of the ion velocities were performed in Chapter 5, the neutral winds used to estimate the heating were pulled from TIEGCM. A similar survey of the mid-latitude sub-auroral neutral winds could be performed using the full network of NATION FPI's. Rather than using the LOS ion velocities, two-dimensional ion velocities within MLAT-MLT grids could be estimated using L-shell fitting techniques as shown by Maimaiti et al. (2018). Two-dimensional estimations of statistical neutral flows within co-located MLAT-MLT cells could allow us to produce statistical maps of mid-latitude Joule heating at a much greater (longitudinal) spatial resolution, while also providing a more accurate statistical representation of the mid-latitude Joule heating by using observational rather than modelled neutral wind data.

Previous studies have shown that TIEGCM can be modified to better improve its performance. Zhang et al. (2021) used a SAPS model to modify TIEGCM's mid-latitude behaviour and Wu et al. (2015) replaced TIEGCM's high-latitude background electric field model with convection maps derived from high latitude SuperDARN data. There is the possibility then that TIEGCM's mid-latitude ionosphere can be modified. The results from Chapter 5 provide a basis for statistical patterns of ion observations. A more detailed statistical mapping could produce a model that may be able to be injected within TIEGCM to provide a more representative mid-latitude sub-auroral ionosphere.

While TIEGCM does account for climatology from the lower atmosphere, it cannot fully model the coupling between the thermosphere and lower levels of the atmosphere that may affect the neutral wind patterns and by proxy, the electric field dynamo. Other models, such as the Whole Atmosphere Community Climate Model with thermosphere and ionosphere extension (WACCM-X) uses comprehensive models of each layer of the atmosphere and couples them together at

their boundaries. WACCM-X may then be able to provide more accurate estimation of the neutrals due to bottom forcing below the thermosphere. WACCM-X could also be studied to identify it it provides better estimations of the mid-latitude ionosphere than TIEGCM.

Appendix A

Mathematical Derivations

A.1 E × B Drift

If we consider the perpendicular component of equation 1.7, $\mathbf{v}_\perp$, then we have:

$$\frac{d\mathbf{v}_\perp}{dt} = \frac{q}{m}(\mathbf{E} + \mathbf{v}_\perp \times \mathbf{B}) \tag{A.1}$$

The time derivative of equation A.1 becomes

$$\frac{d\mathbf{v}_\perp^2}{dt^2} = \frac{q}{m}\left(\frac{d\mathbf{E}}{dt} + \frac{d(\mathbf{v}_\perp \times \mathbf{B})}{dt}\right) \tag{A.2}$$

And then applying the vector chain rule, $d/dt(\mathbf{A}\times\mathbf{B}) = d/dt(\mathbf{A})\times\mathbf{B} + \mathbf{A}\times d/dt(\mathbf{B})$,

$$\frac{d\mathbf{v}_\perp^2}{dt^2} = \frac{q}{m}\left(\frac{d\mathbf{E}}{dt} + \frac{d\mathbf{v}_\perp}{dt} \times \mathbf{B} + \mathbf{v}_\perp \times \frac{d\mathbf{B}}{dt}\right) \tag{A.3}$$

as the electric and magnetic field are constant, we can eliminate the time varying components,

$$\frac{d\mathbf{v}_\perp^2}{dt^2} = \frac{q}{m}\left(\frac{d\mathbf{v}_\perp}{dt} \times \mathbf{B}\right) \tag{A.4}$$

We can substitute equation 1.7 back into A.5,

$$\frac{d\mathbf{v}_\perp^2}{dt^2} = \frac{q^2}{m^2}\left((\mathbf{E} + \mathbf{v}_\perp \times \mathbf{B}) \times \mathbf{B}\right) \tag{A.5}$$

expanding and applying the vector triple product, $(\mathbf{A}\times\mathbf{B})\times\mathbf{B} = (\mathbf{A}\cdot\mathbf{B})\mathbf{B} - \mathbf{A}|B|^2)$, and since $\mathbf{v}_\perp$ and $\mathbf{B}$ are perpendicular, $(\mathbf{v}_\perp \cdot \mathbf{B})$ reduces to zero, leaving

$$\frac{d\mathbf{v}_\perp^2}{dt^2} = \frac{q^2}{m^2}\left((\mathbf{E} \times \mathbf{B}) - \mathbf{v}_\perp B^2\right) \tag{A.6}$$

If we assume that $\mathbf{v}_\perp = \tilde{\mathbf{v}_\perp} + \mathbf{v_E}$, where $\tilde{\mathbf{v}_\perp}$ is time varying and $\mathbf{v_E}$ is constant.

Under time independent conditions, $\tilde{\mathbf{v}_\perp}$ goes to zero such that $\mathbf{v}_\perp = \mathbf{E} = const.$. We can then write

$$\frac{d\mathbf{v}_\perp^2}{dt^2} = 0 = \frac{q^2}{m^2}\left((\mathbf{E}\times\mathbf{B}) - \mathbf{v_E}B^2\right) \tag{A.7}$$

which can be rearranged to,

$$\mathbf{v_E} = \frac{\mathbf{E}\times\mathbf{B}}{B^2} \tag{A.8}$$

A.2 Magnetic Gradient Drift

In an inhomogeneous magnetic field, $\mathbf{B}$ can be written as

$$\mathbf{B} = \mathbf{B_0} + (\mathbf{r}\cdot\nabla)\mathbf{B_0}) \tag{A.9}$$

where $\mathbf{B_0}$ is the magnetic field strength at the guiding center of the particle motion and $\mathbf{r}$ is the distance from the guiding center. Inserting A.9 into equation 1.6 gives

$$\frac{d\mathbf{v}}{dt} = \frac{q}{m}(\mathbf{v}\times\mathbf{B_0}) + \frac{q}{m}(\mathbf{v}\times(\mathbf{r}\cdot\nabla)\mathbf{B_0}) \tag{A.10}$$

If we consider the motion of a charged particle as it gyrates through a magnetic field of increasing strength, the gyroradius of the particle will decrease at the stronger end of the magnetic field, while increasing at the bottom end, causing a drift perpendicular to both $\mathbf{B}$ and $\nabla\mathbf{B}$.

We can note the total velocity as the velocity of the gyration perpendicular to the magnetic field, $\mathbf{v}_\perp$, and the drift velocity $\mathbf{v}_\nabla$.

$$\mathbf{v} = \mathbf{v}_\perp + \mathbf{v}_\nabla \tag{A.11}$$

Substituting this into equation A.10 gives us

$$\frac{d\mathbf{v}_\perp}{dt} + \frac{d\mathbf{v}_\nabla}{dt} = \frac{q}{m}(\mathbf{v}_\perp\times\mathbf{B_0} + \mathbf{v}_\nabla\times\mathbf{B_0}) + \frac{q}{m}(\mathbf{v}_\perp\times(\mathbf{r}\cdot\nabla)\mathbf{B_0} + \mathbf{v}_\nabla\times(\mathbf{r}\cdot\nabla)\mathbf{B_0}) \tag{A.12}$$

As we are considering the drift of an inhomogenous magnetic field, we can ignore the terms describing gyration in a homogenous field, $d\mathbf{v}_\perp/dt$ and $\mathbf{v}_\perp\times\mathbf{B}$. $\mathbf{v}_\nabla\times(\mathbf{r}\cdot$

$\nabla)\mathbf{B_0}$ is a small quantity, so can also be neglected, leaving us with

$$\frac{d\mathbf{v}_\nabla}{dt} = \frac{q}{m}(\mathbf{v}_\nabla \times \mathbf{B_0}) + \frac{q}{m}(\mathbf{v}_\perp \times (\mathbf{r}\cdot\nabla)\mathbf{B_0}) \tag{A.13}$$

We generally consider scales much larger than one gyroperiod, therefore we can average for a single gyration. The left side then goes to 0, since the acceleration from moving to the weak side of a field is balanced by deceleration from moving to the strong side, leaving us with

$$0 = \mathbf{v}_\nabla \times \mathbf{B_0} + \langle \mathbf{v}_\perp \times (\mathbf{r}\cdot\nabla)\mathbf{B_0}\rangle \tag{A.14}$$

where angular brackets denote averaging over one gyroperiod. Using equation 1.14 and taking x_0 and y_0 to be zero, we split the radial distance from the guiding center into it's x and y components,

$$\mathbf{r_g} = \begin{bmatrix} x \\ y \end{bmatrix} = \frac{v_\perp}{\Omega}\begin{bmatrix} \sin\Omega_g t \\ \cos\Omega_g t \end{bmatrix} \tag{A.15}$$

using $r_g = v_\perp/\Omega$ from equation 1.13. Differentiating to get the velocity perpendicular to $\mathbf{B}$ produces

$$\mathbf{v_g} = \begin{bmatrix} v_x \\ v_y \end{bmatrix} = \begin{bmatrix} \frac{dx}{dt} \\ \frac{dy}{dt} \end{bmatrix} = v_\perp \begin{bmatrix} \cos\Omega_g t \\ -\sin\Omega_g t \end{bmatrix} \tag{A.16}$$

If we assume that $\nabla\mathbf{B_0}$ acts entirely in the x direction, the right most side from equation A.14 becomes

$$\mathbf{v_g} \times (\mathbf{r_g}\cdot\nabla)\mathbf{B_0} = v_\perp \begin{bmatrix} v_x x\frac{dB}{dx} \\ v_y x\frac{dB}{dx} \end{bmatrix} \tag{A.17}$$

and by substituting in equations A.15 and A.16 into A.17:

$$\mathbf{v_g} \times (\mathbf{r_g}\cdot\nabla)\mathbf{B_0} = \frac{{v_\perp}^2}{\Omega}\frac{dB}{dx}\begin{bmatrix} \sin\Omega_g t\cos\Omega_g t \\ -\sin^2\Omega_g t \end{bmatrix} \tag{A.18}$$

Where $\sin\Omega_g t\cos\Omega_g t = 0$ and $\sin^2\Omega_g t = 1/2$, therefore the x component goes to zero and there is only drift in the y direction. If we revert back to vector notation so that the direction of the magnetic field is not arbitrary,

$$\mathbf{v_g} \times (\mathbf{r_g}\cdot\nabla)\mathbf{B_0} = -\frac{1}{2}\frac{{v_\perp}^2}{\Omega}\nabla B \tag{A.19}$$

substituting and rearranging this into equation A.14, results in

$$\mathbf{v}_\perp \times \mathbf{B} = \frac{1}{2}\frac{{v_\perp}^2}{\Omega}\nabla B \tag{A.20}$$

If we then cross product equation A.20, and using the vector triple product, the result is

$$-\mathbf{v}_\nabla = \frac{1}{2}\frac{{v_\perp}^2}{\Omega}\frac{\mathbf{B}\times\nabla B}{B^2} \tag{A.21}$$

Finally, if we substitute in $\Omega = qB/m$ we arrive at the equation describing magnetic field gradient drift

$$\mathbf{v}_\nabla = \frac{mv_\perp^2}{2qB^3}(\mathbf{B}\times\nabla B) \tag{A.22}$$

Appendix B

Fitting Over Multiple Latitudinally Narrow Areas

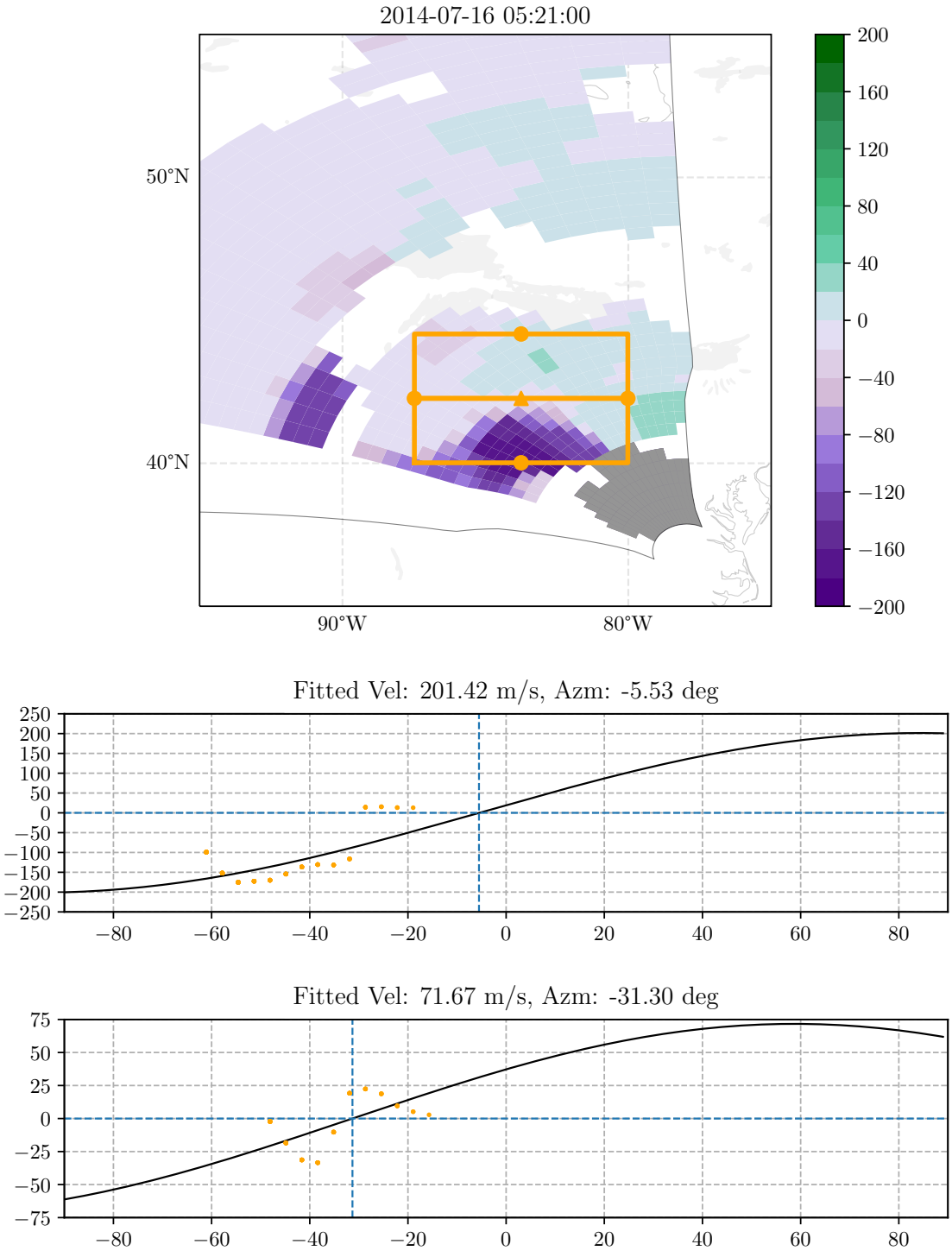

Figure B.1: Same as Figure 4.3, except the overall fitting area has been latitudinally split into two separate fitting areas. The top (bottom) panel showing the LOS velocities against azimuth with accompanying fit corresponds to the top (bottom) fitting area show in the FOV plot.

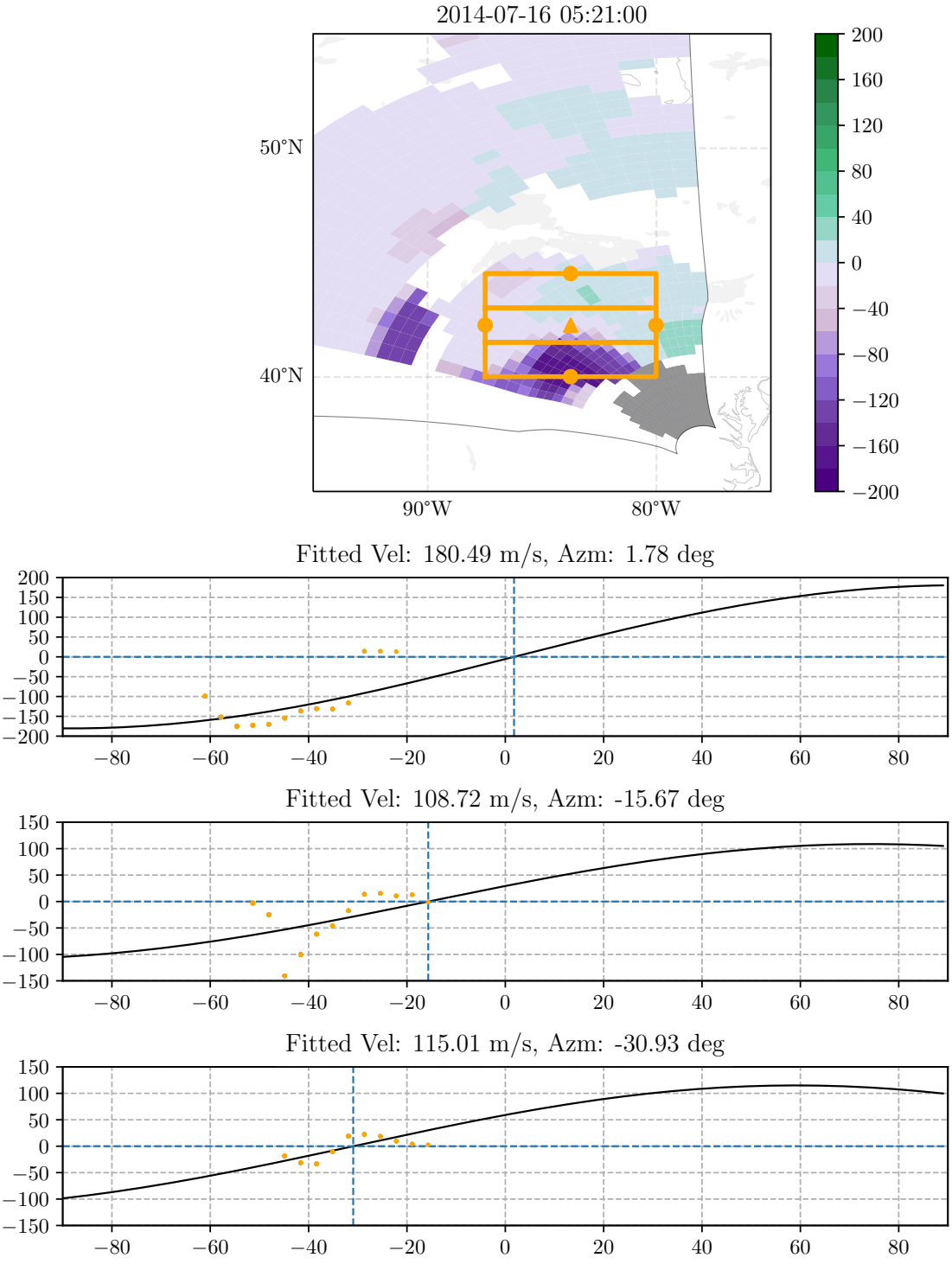

Figure B.2: Same as Figure B.1, except for three separate fitting areas.

Bibliography

Alken, P., Thébault, E., Beggan, C. D., Amit, H., Aubert, J., Baerenzung, J., Bondar, T. N., Brown, W. J., Califf, S., Chambodut, A., Chulliat, A., Cox, G. A., Finlay, C. C., Fournier, A., Gillet, N., Grayver, A., Hammer, M. D., Holschneider, M., Huder, L., ... Zhou, B. (2021). International geomagnetic reference field: The thirteenth generation. *Earth, Planets and Space*, *73*. https://doi.org/10.1186/s40623-020-01288-x

Anderson, B. J., Korth, H., Waters, C. L., Green, D. L., Merkin, V. G., Barnes, R. J., & Dyrud, L. P. (2014). Development of large-scale birkeland currents determined from the active magnetosphere and planetary electrodynamics response experiment. *Geophysical Research Letters*, *41*, 3017–3025. https://doi.org/10.1002/2014GL059941

Anderson, B. J., Takahashi, K., Kamei, T., Waters, C. L., & Toth, B. A. (2002). Birkeland current system key parameters derived from iridium observations: Method and initial validation results. *Journal of Geophysical Research: Space Physics*, *107*. https://doi.org/10.1029/2001JA000080

Anderson, B. J., Angappan, R., Barik, A., Vines, S. K., Stanley, S., Bernasconi, P. N., Korth, H., & Barnes, R. J. (2021). Iridium communications satellite constellation data for study of earth's magnetic field. *Geochemistry, Geophysics, Geosystems*, *22*. https://doi.org/10.1029/2020GC009515

Anderson, C., Kosch, M. J., Nicolls, M. J., & Conde, M. (2013). Ion-neutral coupling in earth's thermosphere, estimated from concurrent radar and optical

observations above alaska. *Journal of Atmospheric and Solar-Terrestrial Physics*, *105-106*, 313–324. https://doi.org/10.1016/j.jastp.2013.04.005

Anderson, H. R., & Vondrak, R. R. (1975). Observations of birkeland currents at auroral latitudes. https://doi.org/10.1029/RG013i001p00243

Anderson, P. C., Hanson, W. B., Heelis, R. A., Craven, J. D., Baker, D. N., & Frank, L. A. (1993). A proposed production model of rapid subauroral ion drifts and their relationship to substorm evolution. *Journal of Geophysical Research: Space Physics*, *98*, 6069–6078. https://doi.org/10.1029/92ja01975

Andersson, L., Peterson, W. K., & McBryde, K. M. (2004). Dynamic coordinates for auroral ion outflow. *Journal of Geophysical Research: Space Physics*, *109*. https://doi.org/10.1029/2004JA010424

Aruliah, A. L., Griffin, E. M., Aylward, A. D., Ford, E. A. K., Kosch, M. J., Davis, C. J., Howells, V. S. C., Pryse, S. E., Middleton, H. R., & Jussila, J. (2005). First direct evidence of meso-scale variability on ion-neutral dynamics using co-located tristatic fpis and eiscat radar in northern scandinavia.

Baloukidis, D., Sarris, T., Tourgaidis, S., Pirnaris, P., Aikio, A., Virtanen, I., Buchert, S., & Papadakis, K. (2023). A comparative assessment of the distribution of joule heating in altitude as estimated in tie-gcm and eiscat over one solar cycle. *Journal of Geophysical Research: Space Physics*, *128*. https://doi.org/10.1029/2023JA031526

Barclay, L., Hall, M., Bacon, D., Hewitt, T., Mehler, M. J., Craig, K. H., Constantinou, C. C., Saunders, S. R., Goddard, J. W. F., Middleton, J., Beach, M. A., Allpress, S. A., Rishbeth, H., Cannon, P. S., Milson, J., & Howell, R. G. (2003). *Propogation of radio waves* (L. Barclay, Ed.; 2nd ed.).

Bauer, S. J. (1973). *Physics of planetary ionospheres*. Springer-Verlag.

Baumjohann, W., & Treumann, R. (1996). *Basic space plasma physics*. Imperial College Press.

Billett, D. D., Grocott, A., Wild, J. A., Walach, M. T., & Kosch, M. J. (2018). Diurnal variations in global joule heating morphology and magnitude due to

neutral winds. *Journal of Geophysical Research: Space Physics*, *123*, 2398–2411. https://doi.org/10.1002/2017JA025141

Billett, D. D. (2019). The great space weather washing machine: Examining the dynamics of high-latitude ionosphere-thermosphere coupling.

Billett, D. D., Mcwilliams, K. A., Kerr, R. B., Makela, J. J., Chartier, A. T., Ruohoniemi, J. M., Kapali, S., Migliozzi, M. A., & Riccobono, J. (2022). Mid-latitude neutral wind responses to sub-auroral polarization streams. *Annales Geophysicae*, *40*, 571–583. https://doi.org/10.5194/angeo-40-571-2022

Blanc, M., Amayenc, P., Bauer, P., & Taieb, C. (1977). Electric field induced drifts from the french incoherent scatter facility. *Journal of Geophysical Research*, *82*, 87–97. https://doi.org/10.1029/ja082i001p00087

Blanchard, G. T., Sundeen, S., & Baker, K. B. (2009). Probabilistic identification of high-frequency radar backscatter from the ground and ionosphere based on spectral characteristics. *Radio Science*, *44*. https://doi.org/10.1029/2009rs004141

Bristow, W. A., Hampton, D. L., & Otto, A. (2016). High-spatial-resolution velocity measurements derived using local divergence-free fitting of superdarn observations. *Journal of Geophysical Research: Space Physics*, *121*, 1349–1361. https://doi.org/10.1002/2015JA021862

Buonsanto, M. J., Foster, J. C., & Sipler, D. P. (1992). Observations from millstone hill during the geomagnetic disturbances of march and april 1990. *Journal of Geophysical Research: Space Physics*, *97*, 1225–1243. https://doi.org/10.1029/91ja02428

Burrell, A. G., Perry, G. W., Yeoman, T. K., Milan, S. E., & Stoneback, R. (2018). Solar influences on the return direction of high-frequency radar backscatter. *Radio Science*, *53*, 577–597. https://doi.org/10.1002/2017RS006512

Cai, L., Aikio, A. T., & Nygrén, T. (2014). Solar wind effect on joule heating in the high-latitude ionosphere. *Journal of Geophysical Research: Space Physics*, *119*, 10, 440–10, 455. https://doi.org/10.1002/2014JA020269

Carpenter, L. A., & Kirchhoff, V. W. J. H. (1975). Comparison of high-latitude and mid-latitude ionospheric electric fields. *Journal of Geophysical Research*, *80*, 1810–1814. https://doi.org/10.1029/ja080i013p01810

Chisham, G., Lester, M., Milan, S. E., Freeman, M. P., Bristow, W. A., Grocott, A., McWilliams, K. A., Ruohoniemi, J. M., Yeoman, T. K., Dyson, P. L., Greenwald, R. A., Kikuchi, T., Pinnock, M., Rash, J. P., Sato, N., Sofko, G. J., Villain, J. P., & Walker, A. D. (2007, January). A decade of the super dual auroral radar network (superdarn): Scientific achievements, new techniques and future directions. https://doi.org/10.1007/s10712-007-9017-8

Chisham, G., Yeoman, T. K., & Sofko, G. J. (2008). Mapping ionospheric backscatter measured by the superdarn hf radars – part 1: A new empirical virtual height model. *Annales Geophysicae*, *26*, 823–841. https://doi.org/10.5194/angeo-26-823-2008

Clausen, L. B., Baker, J. B., Ruohoniemi, J. M., Greenwald, R. A., Thomas, E. G., Shepherd, S. G., Talaat, E. R., Bristow, W. A., Zheng, Y., Coster, A. J., & Sazykin, S. (2012). Large-scale observations of a subauroral polarization stream by midlatitude superdarn radars: Instantaneous longitudinal velocity variations. *Journal of Geophysical Research: Space Physics*, *117*. https://doi.org/10.1029/2011JA017232

Cousins, E. D., & Shepherd, S. G. (2010). A dynamical model of high-latitude convection derived from superdarn plasma drift measurements. *Journal of Geophysical Research: Space Physics*, *115*. https://doi.org/10.1029/2010JA016017

Cowley, S. W. H. (2000). Magnetosphere-ionosphere interactions: A tutorial review. American Geophysical Union (AGU). https://doi.org/https://doi.org/10.1029/GM118p0091

Cowley, S. W. H., & Lockwood, M. (1992). Excitation and decay of solar wind-driven flows in the magnetosphere-ionosphere system. *Copernicus*, *10*, 103–115.

Dang, T., Li, X., Luo, B., Li, R., Zhang, B., Pham, K., Ren, D., Chen, X., Lei, J., & Wang, Y. (2022). Unveiling the space weather during the starlink satellites destruction event on 4 february 2022. *Space Weather*, *20*. https://doi.org/10.1029/2022SW003152

Day, E. K., Grocott, A., Walach, M.-T., Wild, J. A., Lu, G., Ruohoniemi, J. M., & Coster, A. J. (2024). Observation of quiet-time mid-latitude joule heating and comparisons with the tiegcm simulation. *Journal of Geophysical Research: Space Physics*, *129*. https://doi.org/10.1029/2024JA032578

Deng, W., Killeen, T. L., Burns, A. G., Roble, R. G., Slavin, J. A., & Wharton, L. E. (1993). The effects of neutral inertia on ionospheric currents in the high-latitude thermosphere following a geomagnetic storm. *Journal of Geophysical Research*, *98*, 7775–77790.

Dungey, J. W. (1961). Interplanetary magnetic field and the auroral zones. *Phys. Rev. Lett.*, *6*, 47–48.

Dungey, W. (1965). The length of the magnetospheric tail. *J. Geophys. Res*, *70*, 503.

Elvidge, S., & Angling, M. J. (2019). Using the local ensemble transform kalman filter for upper atmospheric modelling. *Journal of Space Weather and Space Climate*, *9*. https://doi.org/10.1051/swsc/2019018

Emery, B. A., Lathuilere, C., Richards, P. G., Roble, R. G., Buonsanto, J., Knipp, J., Wilkinson, P., Sipler, P., & Niciejewski, R. (1999). Time dependent thermospheric neutral response tothe 2–11 november 1993 storm period. *Journal of Atmospheric and Solar-Terrestrial Physics*, *61*, 329–350. https://doi.org/10.1016/S1364-6826(98)00137-0

Fang, T.-W., Kubaryk, A., Goldstein, D., Li, Z., Fuller-Rowell, T., Millward, G., Singer, H. J., Steenburgh, R., Westerman, S., & Babcock, E. (2022). Space weather environment during the spacex starlink satellite loss in february 2022. *Space Weather*, *20*. https://doi.org/10.1029/2022SW003193

Foster, J. C., & Vo, H. B. (2002). Average characteristics and activity dependence of the subauroral polarization stream. *Journal of Geophysical Research: Space Physics*, *107*. https://doi.org/10.1029/2002JA009409

Fuller-Rowell, T. J., Codrescu, M. V., Roble, R. G., & Richmond, A. D. (1997). How does the thermosphere and ionosphere react to a geomagnetic storm? https://doi.org/10.1029/GM098p0203

Gold, T. (1959). Motions in the magnetosphere of the earth. *Journal of Geophysical Research*, *64*, 1219–1224. https://doi.org/10.1029/jz064i009p01219

Greenwald, R. A., Baker, K. B., Dudeney, J. R., Pinnock, M., Jones, T. B., Thomas, E. C., Villain, J.-R., Cerisier, J.-C., Senior, C., Hanuise, C., Hunsucker, R. D., Sofko, G., Koehler, J., Nielsen, E., 1, R. P., Walker, A. D. M., Sato, N., & Yamagishi, H. (1995). Darn/superdarn. *Space Science Reviews*, *71*, 761–796.

Greenwald, R. A., Oksavik, K., Erickson, P. J., Lind, F. D., Ruohoniemi, J. M., Baker, J. B. H., & Gjerloev, J. W. (2006). Identification of the temperature gradient instability as the source of decameter-scale ionospheric irregularities on plasmapause field lines. *Geophysical Research Letters*, *33*, n/a–n/a. https://doi.org/10.1029/2006GL026581

Grocott, A., & Milan, S. E. (2014). The influence of imf clock angle timescales on the morphology of ionospheric convection. *Journal of Geophysical Research: Space Physics*, *119*, 5861–5876. https://doi.org/10.1002/2014JA020136

Grocott, A., Milan, S. E., Baker, J. B., Freeman, M. P., Lester, M., & Yeoman, T. K. (2011). Dynamic subauroral ionospheric electric fields observed by the falkland islands radar during the course of a geomagnetic storm. *Journal of Geophysical Research: Space Physics*, *116*. https://doi.org/10.1029/2011JA016763

Grocott, A., Milan, S. E., Imber, S. M., Lester, M., & Yeoman, T. K. (2012). A quantitative deconstruction of the morphology of high-latitude ionospheric convection. *Journal of Geophysical Research: Space Physics*, *117*. https://doi.org/10.1029/2012JA017580

Gussenhoven, M. S., Hardy, D. A., & Heinemann, N. (1983). Systematics of the equatorward diffuse auroral boundary. *Journal of Geophysical Research*, *88*, 5692–5708. https://doi.org/10.1029/JA088iA07p05692

Gussenhoven, M. S., Hardy, D. A., & Heinemann, N. (1987). The equatorward boundary of auroral ion precipitation. *Journal of Geophysical Research: Space Physics*, *92*, 3273–3283. https://doi.org/10.1029/ja092ia04p03273

Hagan, M. E., & Forbes, J. M. (2002). Migrating and nonmigrating diurnal tides in the middle and upper atmosphere excited by tropospheric latent heat release. *Journal of Geophysical Research Atmospheres*, *107*, ACL 6-1-ACL 6–15. https://doi.org/10.1029/2001JD001236

Hagan, M. E., & Forbes, J. M. (2003). Migrating and nonmigrating semidiurnal tides in the upper atmosphere excited by tropospheric latent heat release. *Journal of Geophysical Research: Space Physics*, *108*. https://doi.org/10.1029/2002JA009466

Hall, G. E. (1997). Super dual auroral radar network observations of meteor echoes. *Journal of Geophysical Research: Space Physics*, *102*, 14603–14614. https://doi.org/10.1029/97JA00517

HAO. (2018). Tiegcm v1.94 model description. https://www.hao.ucar.edu/modeling/tgcm/doc/description/model_description.pdf

Hapgood, M. A. (1992). Space physics coordinate transformations : A user guide.

Hardy, D. A., Gussenhoven, M. S., & Brautigam, D. (1989). A statistical model of auroral ion precipitation. *Journal of Geophysical Research: Space Physics*, *94*, 370–392. https://doi.org/10.1029/ja094ia01p00370

Hargreaves, J. (1992). *The solar-terrestrial environment: An introduction to geospace - the science of the terrestrial upper atmosphere, ionosphere and magnetosphere* (Vol. 7). Cambridge Atmospheric; Space Science Series.

He, M., Liu, L., Wan, W., & Zhao, B. (2011). A study on the nighttime midlatitude ionospheric trough. *Journal of Geophysical Research: Space Physics*, *116*. https://doi.org/10.1029/2010JA016252

Heelis, R. A., Lowell, J. K., & Spiro, R. W. (1982). A model of the high-latitude ionospheric convection pattern. *Journal of Geophysical Research*, *87*, 6339. https://doi.org/10.1029/ja087ia08p06339

Heinemann, N. C., Gussenhoven, M. S., Hardy, D. A., Rich, F. J., & Yeh, H.-C. (1989). Electron/ion precipitation differences in relation to region 2 field-aligned currents. *Journal of Geophysical Research: Space Physics*, *94*, 13593–13600. https://doi.org/10.1029/ja094ia10p13593

Heppner, J. P., & Maynard, N. C. (1987). Empirical high-latitude electric field models. *Journal of Geophysical Research: Space Physics*, *92*, 4467–4489. https://doi.org/10.1029/ja092ia05p04467

Hinteregger, H. E., Hall, L. A., & Schmidtke, G. (1965). Solar xuv radiation and neutral particle distribution in july 1963 thermosphere. *Space Research Conference*, 1175.

Holzworth, R. H., & Meng, C. .-. (1975). Mathematical representation of the auroral oval. *Geophysical Research Letters*, *2*, 377–380. https://doi.org/10.1029/GL002i009p00377

Howell, D. C. (2005). Median absolute deviation. John Wiley; Sons, Ltd. https://doi.org/https://doi.org/10.1002/0470013192.bsa384

Huang, C. S., & Foster, J. C. (2007). Correlation of the subauroral polarization streams (saps) with the dst index during severe magnetic storms. *Journal of Geophysical Research: Space Physics*, *112*. https://doi.org/10.1029/2007JA012584

Hudson, M. K., & Kelley, M. C. (1976). The temperature gradient drift instability at the equatorward edge of the ionospheric plasma trough. *J Geophys Res*, *81*, 3913–3918. https://doi.org/10.1029/JA081i022p03913

Ishida, T., Ogawa, Y., Kadokura, A., Hiraki, Y., & Häggström, I. (2014). Seasonal variation and solar activity dependence of the quiet-time ionospheric trough. *Journal of Geophysical Research: Space Physics*, *119*, 6774–6783. https://doi.org/10.1002/2014ja019996

Joshi, P. P., Baker, J. B. H., Ruohoniemi, J. M., Makela, J. J., Fisher, D. J., Harding, B. J., Frissell, N. A., & Thomas, E. G. (2015). Observations of storm time midlatitude ion-neutral coupling using superdarn radars and nation fabry-perot interferometers. *Journal of Geophysical Research A: Space Physics*, *120*, 8989–9003. https://doi.org/10.1002/2015JA021475

Kelley, M. C., Fejer, B. G., & Gonzales, C. A. (1979). An explanation for anomalous equatorial ionospheric electric fields associated with a northward turning of the interplanetary magnetic field. *Geophysical Research Letters*, *6*, 301–304. https://doi.org/10.1029/GL006i004p00301

Kelley, M. (2009). *The earth's ionosphere: Plasma physics and electrodynamics* (Second Edition, Vol. 96). International geophysics series.

Kervalishvili, G. N., & Lühr, H. (2013). The relationship of thermospheric density anomaly with electron temperature, small-scale fac, and ion up-flow in the cusp region, as observed by champ and dmsp satellites. *Annales Geophysicae*, *31*, 541–554. https://doi.org/10.5194/angeo-31-541-2013

Kiene, A., Bristow, W. A., Conde, M. G., & Hampton, D. L. (2019). High-resolution local measurements of f region ion temperatures and joule heating rates using superdarn and ground-based optics. *Journal of Geophysical Research: Space Physics*, *124*, 557–572. https://doi.org/10.1029/2018JA025997

Kilcommons, L. M., Redmon, R. J., & Knipp, D. J. (2017). A new dmsp magnetometer and auroral boundary data set and estimates of field-aligned currents in dynamic auroral boundary coordinates. *Journal of Geophysical Research: Space Physics*, *122*, 9068–9079. https : / / doi . org / 10 . 1002 / 2016JA023342

Knipp, D. J., Emery, B. A., Engebretson, M., Li, X., McAllister, A. H., Mukai, T., Kokubun, S., Reeves, G. D., Evans, D., Obara, T., Pi, X., Rosenberg, T., Weatherwax, A., McHarg, M. G., Chun, F., Mosely, K., Codrescu, M., Lanzerotti, L., Rich, F. J., ... Wilkinson, P. (1998). An overview of the early

november 1993 geomagnetic storm. *Journal of Geophysical Research: Space Physics*, *103*, 26197–26220. https://doi.org/10.1029/98ja00762

Knipp, D. J., Tobiska, W. K., & Emery, B. A. (2004). Direct and indirect thermospheric heating sources for solar cycles 21-23.

Knudsen, W. C. (1974). Magnetospheric convection and the high-latitude f 2 ionosphere. *Journal of Geophysical Research*, *79*, 1046–1055. https://doi.org/10.1029/ja079i007p01046

Kosch, M. J., Cierpka, K., Rietveld, M. T., Hagfors, T., & Schlegel, K. (2001). High-latitude ground-based observations of the thermosphericion-drag time constant. *Geophysical Research Letters*, *28*, 1395–1398. https://doi.org/10.1029/2000GL012380

Kunduri, B. S., Baker, J. B., Ruohoniemi, J. M., Coster, A. J., Vines, S. K., Anderson, B. J., Shepherd, S. G., & Chartier, A. T. (2021). An examination of magnetosphere-ionosphere influences during a saps event. *Geophysical Research Letters*, *48*. https://doi.org/10.1029/2021GL095751

Kunduri, B. S., Baker, J. B., Ruohoniemi, J. M., Nishitani, N., Oksavik, K., Erickson, P. J., Coster, A. J., Shepherd, S. G., Bristow, W. A., & Miller, E. S. (2018). A new empirical model of the subauroral polarization stream. *Journal of Geophysical Research: Space Physics*, *123*, 7342–7357. https://doi.org/10.1029/2018JA025690

Kunduri, B. S., Baker, J. B., Ruohoniemi, J. M., Thomas, E. G., Shepherd, S. G., & Sterne, K. T. (2017). Statistical characterization of the large-scale structure of the subauroral polarization stream. *Journal of Geophysical Research: Space Physics*, *122*, 6035–6048. https://doi.org/10.1002/2017JA024131

Larquier, S. D., Ponomarenko, P., Ribeiro, A. J., Ruohoniemi, J. M., Baker, J. B., Sterne, K. T., & Lester, M. (2013). On the spatial distribution of decameter-scale subauroral ionospheric irregularities observed by superdarn radars. *Journal of Geophysical Research: Space Physics*, *118*, 5244–5254. https://doi.org/10.1002/jgra.50475

Laundal, K. M., & Richmond, A. D. (2017, March). Magnetic coordinate systems. https://doi.org/10.1007/s11214-016-0275-y

Lejosne, S., & Mozer, F. S. (2016). Typical values of the electric drift e × b/b2 in the inner radiation belt and slot region as determined from van allen probe measurements. *Journal of Geophysical Research: Space Physics*, *121*, 12, 014–12, 024. https://doi.org/10.1002/2016JA023613

Lin, D., Wang, W., Garcia-Sage, K., Yue, J., Merkin, V., McInerney, J. M., Pham, K., & Sorathia, K. (2022). Thermospheric neutral density variation during the "spacex" storm: Implications from physics-based whole geospace modeling. *Space Weather*, *20*. https://doi.org/10.1029/2022SW003254

Liu, Y., Xiong, C., Wan, X., Lai, Y., Wang, Y., Yu, X., & Ou, M. (2021). Instability mechanisms for the f-region plasma irregularities inside the midlatitude ionospheric trough: Swarm observations. *Space Weather*, *19*. https://doi.org/10.1029/2021SW002785

Lockwood, M., Cowley, S. W. H., & Freeman, M. P. (1990). The excitation of plasma convection in the high-latitude ionosphere. *Journal of Geophysical Research: Space Physics*, *95*, 7961–7972. https://doi.org/10.1029/ja095ia06p07961

Lu, G., Baker, D. N., McPherron, R. L., Farrugia, C. J., Lummerzheim, D., Ruohoniemi, J. M., Rich, F. J., Evans, D. S., Lepping, R. P., Brittnacher, M., Li, X., Greenwald, R., Sofko, G., Villain, J., Lester, M., Thayer, J., Moretto, T., Milling, D., Troshichev, O., ... Hayashi, K. (1998). Global energy deposition during the january 1997 magnetic cloud event. *Journal of Geophysical Research: Space Physics*, *103*, 11685–11694. https://doi.org/10.1029/98ja00897

Lu, G., Emery, B. A., Rodger, A. S., Lester, M., Taylor, J. R., Evans, D. S., Ruohoniemi, J. M., Denig, W. F., de la Beaujardière, O., Frahm, R. A., Winningham, J. D., & Chenette, D. L. (1996). High-latitude ionospheric electrodynamics as determined by the assimilative mapping of ionospheric electrodynamics procedure for the conjunctive sundial/atlas 1/gem period

of march 28-29, 1992. *Journal of Geophysical Research: Space Physics*, *101*, 26697–26718. https://doi.org/10.1029/96ja00513

Lu, G., Richmond, A. D., Emery, B. A., & Roble, R. G. (1995). Magnetosphere-ionosphere-thermosphere coupling: Effect of neutral winds on energy transfer and field-aligned current. *Journal of Geophysical Research*, *100*, 19643. https://doi.org/10.1029/95ja00766

Lu, G., Richmond, A. D., Lühr, H., & Paxton, L. (2016). High-latitude energy input and its impact on the thermosphere. *Journal of Geophysical Research: Space Physics*, *121*, 7108–7124. https://doi.org/10.1002/2015JA022294

Lyons, L. R., Killeen, T. L., & Walterscheid, R. L. (1985). The neutral wind "flywheel" as a source of quiet-time, polar-cap currents. *Geophysical Research Letters*, *12*, 101–104. https://doi.org/10.1029/GL012i002p00101

Maimaiti, M., Baker, J. B., Ruohoniemi, J. M., & Kunduri, B. (2019). Morphology of nightside subauroral ionospheric convection: Monthly, seasonal, kp, and imf dependencies. *Journal of Geophysical Research: Space Physics*, *124*, 4608–4626. https://doi.org/10.1029/2018JA026268

Maimaiti, M., Ruohoniemi, J. M., Baker, J. B., & Ribeiro, A. J. (2018). Statistical study of nightside quiet time midlatitude ionospheric convection. *Journal of Geophysical Research: Space Physics*, *123*, 2228–2240. https://doi.org/10.1002/2017JA024903

Makela, J. J., Meriwether, J. W., Huang, Y., & Sherwood, P. J. (2011). Simulation and analysis of a multi-order imaging fabry–perot interferometer for the study of thermospheric winds and temperatures. *Appl. Opt.*, *50*, 4403–4416. https://doi.org/10.1364/AO.50.004403

Makela, J. J., Meriwether, J. W., Ridley, A. J., Ciocca, M., & Castellez, M. W. (2012). Large-scale measurements of thermospheric dynamics with a multisite fabry-perot interferometer network: Overview of plans and results from midlatitude measurements. https://doi.org/10.1155/2012/872140

Martin, C. J., Shi, X., Schmidt, M. T., Day, E. K., Bland, E. C., Khanal, K., Billett, D. D., Kunduri, B. S. R., Tholley, F., Frissell, N., Coyle, S., R, A. R., T, J. K., & K, J. K. (2023). Pydarn. https://doi.org/10.5281/zenodo.7767590

McHarg, M., Chun, F., Knipp, D., Lu, G., Emery, B., & Ridley, A. (2005). High-latitude joule heating response to imf inputs. *Journal of Geophysical Research: Space Physics*, *110*. https://doi.org/10.1029/2004JA010949

Milan, S. E., Carter, J. A., Korth, H., & Anderson, B. J. (2015). Principal component analysis of birkeland currents determined by the active magnetosphere and planetary electrodynamics response experiment. *Journal of Geophysical Research: Space Physics*, *120*, 10415–10424. https://doi.org/10.1002/2015JA021680

Milan, S. E., Clausen, L. B., Coxon, J. C., Carter, J. A., Walach, M. T., Laundal, K., Østgaard, N., Tenfjord, P., Reistad, J., Snekvik, K., Korth, H., & Anderson, B. J. (2017, March). Overview of solar wind–magnetosphere–ionosphere–atmosphere coupling and the generation of magnetospheric currents. https://doi.org/10.1007/s11214-017-0333-0

Milan, S. E., Lester, M., Cowley, S. W. H., Oksavik, K., Brittnacher, M., Greenwald, R. A., Sofko, G., & Villain, J.-P. (2003). Annales geophysicae variations in the polar cap area during two substorm cycles.

Nagano, H., Nishitani, N., & Hori, T. (2015). Occurrence characteristics and lowest speed limit of subauroral polarization stream (saps) observed by the superdarn hokkaido east radar. *Earth, Planets and Space*, *67*. https://doi.org/10.1186/s40623-015-0299-7

NCAR. (2016). Tiegcm documentation release 2.0 ncar high altitude observatory. https://www.hao.ucar.edu/modeling/tgcm/tiegcm2.0/userguide/userguide.pdf

Nishitani, N., Ruohoniemi, J. M., Lester, M., Baker, J. B. H., Koustov, A. V., Shepherd, S. G., Chisham, G., Hori, T., Thomas, E. G., Makarevich, R. A., Marchaudon, A., Ponomarenko, P., Wild, J. A., Milan, S. E., Bristow,

W. A., Devlin, J., Miller, E., Greenwald, R. A., Ogawa, T., & Kikuchi, T. (2019, December). Review of the accomplishments of mid-latitude super dual auroral radar network (superdarn) hf radars. https://doi.org/10.1186/s40645-019-0270-5

Oceanographic, N., & Administration, A. (n.d.). Noaa space weather scales. https://www.swpc.noaa.gov/noaa-scales-explanation

Palmroth, M., Grandin, M., Sarris, T., Doornbos, E., Tourgaidis, S., Aikio, A., Buchert, S., Clilverd, M. A., Dandouras, I., Heelis, R., Hoffmann, A., Ivchenko, N., Kervalishvili, G., Knudsen, D. J., Kotova, A., Liu, H. L., Malaspina, D. M., March, G., Marchaudon, A., ... Yamauchi, M. (2021). Lower-thermosphere-ionosphere (lti) quantities: Current status of measuring techniques and models. *Annales Geophysicae*, *39*, 189–237. https://doi.org/10.5194/angeo-39-189-2021

Parker, E. N. (1958). Dynamics of the interplanetary gas and magnetic fields. *Astrophysical Journal*, *128*, 664. https://doi.org/10.1086/146579

Peterson, W. K., Andersson, L., Callahan, B. C., Collin, H. L., Scudder, J. D., & Yau, A. W. (2008). Solar-minimum quiet time ion energization and outflow in dynamic boundary related coordinates. *Journal of Geophysical Research: Space Physics*, *113*. https://doi.org/10.1029/2008JA013059

Qian, L., Burns, A. G., Emery, B. A., Foster, B., Lu, G., Maute, A., Richmond, A. D., Roble, R. G., Solomon, S. C., & Wang, W. (2014, March). The ncar tie-gcm. https://doi.org/10.1002/9781118704417.ch7

Redmon, R. J., Peterson, W. K., Andersson, L., Kihn, E. A., Denig, W. F., Hairston, M., & Coley, R. (2010). Vertical thermal o+ flows at 850 km in dynamic auroral boundary coordinates. *Journal of Geophysical Research: Space Physics*, *115*. https://doi.org/10.1029/2010JA015589

Ribeiro, A. J., Ruohoniemi, J. M., Baker, J. B., Clausen, L. B., Greenwald, R. A., & Lester, M. (2012). A survey of plasma irregularities as seen by the midlatitude

blackstone superdarn radar. *Journal of Geophysical Research: Space Physics*, *117*. https://doi.org/10.1029/2011JA017207

Ribeiro, A. J., Ruohoniemi, J. M., Baker, J. B., Clausen, L. B., Larquier, S. D., & Greenwald, R. A. (2011). A new approach for identifying ionospheric backscatter in midlatitude superdarn hf radar observations. *Radio Science*, *46*. https://doi.org/10.1029/2011RS004676

Richmond, A. D., Ridley, E. C., & Roble, R. G. (1992). A thermosphere/ionosphere general circulation model with coupled electrodynamics. *Geophysical Research Letters*, *19*, 601–604. https://doi.org/10.1029/92GL00401

Richmond, A. D., & Roble, R. G. (1997). Elect od a c cooling effexzts in the e osp onosp system.

Rideout, W., & Coster, A. (2006). Automated gps processing for global total electron content data. *GPS Solutions*, *10*, 219–228. https://doi.org/10.1007/s10291-006-0029-5

Rishbeth, H. (1971). The f-layer dynamo. *Planetary Space Science*, *19*, 263–267.

Rishbeth, H. (1977). Drifts and winds in the polar f region. *Journal of Atmospheric and Terrestrial Physics*, *39*, 111–116.

Rishbeth, H., Moffett, R. J., & Bailey, G. J. (1969). Continuity of air motion in the mid-latitude thermosphere.

Roble, R. G., & Ridley, E. G. (1987). An auroral model for the ncar thermospheric general circulation model (tgcm). *Annales Geophysicae*, *5*, 369–382.

Ruohoniemi, J. M., & Baker, K. B. (1998). Large-scale imaging of high-latitude convection with super dual auroral radar network hf radar observations. *Journal of Geophysical Research: Space Physics*, *103*, 20797–20811. https://doi.org/10.1029/98ja01288

Ruohoniemi, J. M., & Greenwald, R. A. (1996). Statistical patterns of high-latitude convection obtained from goose bay hf radar observations. *Journal of Geophysical Research: Space Physics*, *101*, 21743–21763. https://doi.org/10.1029/96ja01584

Ruohoniemi, J. M., Greenwald, R. A., Baker, K. B., Villain, J.-P., Hanuise, C., & Kelly, J. (1989). Mapping high-latitude plasma convection with coherent hf radars. *Journal of Geophysical Research*, *94*, 13463. https://doi.org/10.1029/ja094ia10p13463

Russell, C., Luhmann, J., & Strangeway, R. (2016). *Space physics, an introduction*. Cambridge University Press.

Schunk, R., & Nagy, A. (2009). *Ionospheres: Physics, plasma physics, and chemistry*. Cambridge University Press.

Shepherd, S. G. (2014). Altitude-adjusted corrected geomagnetic coordinates: Definition and functional approximations. *Journal of Geophysical Research: Space Physics*, *119*, 7501–7521. https://doi.org/10.1002/2014JA020264

Solomon, S. C., & Qian, L. (2005). Solar extreme-ultraviolet irradiance for general circulation models. *Journal of Geophysical Research: Space Physics*, *110*. https://doi.org/10.1029/2005JA011160

SpaceX. (2022, February). Spacex - updates.

Spiro, R. W., Heelis, R. A., & Hanson, W. B. (1978). Ion convection and the formation of the mid-latitude f region ionization trough. *J Geophys Res*, *83*, 4255–4264. https://doi.org/10.1029/JA083iA09p04255

Thomas, E. G., Baker, J. B., Ruohoniemi, J. M., Clausen, L. B., Coster, A. J., Foster, J. C., & Erickson, P. J. (2013). Direct observations of the role of convection electric field in the formation of a polar tongue of ionization from storm enhanced density. *Journal of Geophysical Research: Space Physics*, *118*, 1180–1189. https://doi.org/10.1002/jgra.50116

Thomas, E. G., Reimer, A. S., Bland, E. C., Burrell, A. G., Grocott, A., Ponomarenko, P. V., Schmidt, M. T., Shepherd, S. G., Sterne, K. T., & Walach, M.-T. (2022). Superdarn radar software toolkit (rst). https://doi.org/https://zenodo.org/doi/10.5281/zenodo.801458

Thomas, E. G., & Shepherd, S. G. (2018). Statistical patterns of ionospheric convection derived from mid-latitude, high-latitude, and polar superdarn

hf radar observations. *Journal of Geophysical Research: Space Physics*, *123*, 3196–3216. https://doi.org/10.1002/2018JA025280

Vierinen, J., Coster, A. J., Rideout, W. C., Erickson, P. J., & Norberg, J. (2016). Statistical framework for estimating gnss bias. *Atmospheric Measurement Techniques*, *9*, 1303–1312. https://doi.org/10.5194/amt-9-1303-2016

Villain, J. P., Greenwald, R. A., Baker, K. B., & Ruohoniemi, J. M. (1987). Hf radar observations of e region plasma irregularities produced by oblique electron streaming. *Journal of Geophysical Research*, *92*, 12327. https://doi.org/10.1029/ja092ia11p12327

Voss, H. D., & Smith, L. G. (1979). Nighttime ionization by energetic particles at wallops island in the altitude region 120 to 200 km. *Geophysical Research Letters*, *6*, 93–96. https://doi.org/10.1029/GL006i002p00093

Voss, H. D., & Smith, L. G. (1980). Rocket observations of energetic ions in the nighttime equatorial precipitation zone. *Low Latitude Aeronomic Processes*.

Walach, M. T., & Grocott, A. (2019). Superdarn observations during geomagnetic storms, geomagnetically active times, and enhanced solar wind driving. *Journal of Geophysical Research: Space Physics*, *124*, 5828–5847. https://doi.org/10.1029/2019JA026816

Walach, M. T., Grocott, A., & Milan, S. E. (2021). Average ionospheric electric field morphologies during geomagnetic storm phases. *Journal of Geophysical Research: Space Physics*, *126*. https://doi.org/10.1029/2020JA028512

Wand, R. H., & Evans, J. V. (1981). The penetration of convection electric fields to the latitude of millstone hill (magnetic latitude=56°). *Journal of Geophysical Research: Space Physics*, *86*, 5809–5814. https://doi.org/10.1029/ja086ia07p05809

Wang, W., Burns, A., Lei, J., Solomon, S., Killeen, T., & Wiltberger, M. (2008). Neutral winds and ionospheric electrodynamics during geomagnetic storms. *37th COSPAR Scientific Assembly*.

Wang, W., Talaat, E. R., Burns, A. G., Emery, B., Hsieh, S. Y., Lei, J., & Xu, J. (2012). Thermosphere and ionosphere response to subauroral polarization streams (saps): Model simulations. *Journal of Geophysical Research: Space Physics*, *117*. https://doi.org/10.1029/2012JA017656

Wang, X., Miao, J., Aa, E., Ren, T., Wang, Y., Liu, J., & Liu, S. (2020). Statistical analysis of joule heating and thermosphere response during geomagnetic storms of different magnitudes. *Journal of Geophysical Research: Space Physics*, *125*. https://doi.org/10.1029/2020JA027966

Weimer, D. R. (2005). Improved ionospheric electrodynamic models and application to calculating joule heating rates. *Journal of Geophysical Research: Space Physics*, *110*. https://doi.org/10.1029/2004JA010884

Werner, S., & Prelss, G. W. (1997). The position of the ionospheric trough as a function of local time and magnetic activity.

Weygand, J. M., Zesta, E., & Troshichev, O. (2014). Auroral electrojet indices in the northern and southern hemispheres: A statistical comparison. *Journal of Geophysical Research: Space Physics*, *119*, 4819–4840. https://doi.org/10.1002/2013JA019377

Winch, D. E., Ivers, D. J., Turner, J. P., & Stening, R. J. (2005). Geomagnetism and schmidt quasi-normalization. *Geophysical Journal International*, *160*, 487–504. https://doi.org/10.1111/j.1365-246X.2004.02472.x

Wu, Q., Emery, B. A., Shepherd, S. G., Ruohoniemi, J. M., Frissell, N. A., & Semeter, J. (2015). High-latitude thermospheric wind observations and simulations with superdarn data driven ncar tiegcm during the december 2006 magnetic storm. *Journal of Geophysical Research A: Space Physics*, *120*, 6021–6028. https://doi.org/10.1002/2015JA021026

Wu, Q., Jee, G., Lee, C., Kim, J. H., Kim, Y. H., Ward, W., & Varney, R. H. (2017). First simultaneous multistation observations of the polar cap thermospheric winds. *Journal of Geophysical Research: Space Physics*, *122*, 907–915. https://doi.org/10.1002/2016JA023560

Zhang, K. D., Wang, H., Wang, W. B., Liu, J., Zhang, S. R., & Sheng, C. (2021). Nighttime meridional neutral wind responses to saps simulated by the tiegcm: A universal time effect. *Earth and Planetary Physics*, *5*, 52–62. https://doi.org/10.26464/epp2021004

Zhang, S. R., Erickson, P. J., Zhang, Y., Wang, W., Huang, C., Coster, A. J., Holt, J. M., Foster, J. F., Sulzer, M., & Kerr, R. (2017). Observations of ion-neutral coupling associated with strong electrodynamic disturbances during the 2015 st. patrick's day storm. *Journal of Geophysical Research: Space Physics*, *122*, 1314–1337. https://doi.org/10.1002/2016JA023307

Zhang, X. X., Wang, C., Chen, T., Wang, Y. L., Tan, A., Wu, T. S., Germany, G. A., & Wang, W. (2005). Global patterns of joule heating in the high-latitude ionosphere. *Journal of Geophysical Research: Space Physics*, *110*. https://doi.org/10.1029/2005JA011222

Zhang, Y., & Paxton, L. J. (2008). An empirical kp-dependent global auroral model based on timed/guvi fuv data. *Journal of Atmospheric and Solar-Terrestrial Physics*, *70*, 1231–1242. https://doi.org/10.1016/j.jastp.2008.03.008

Zou, Y., & Nishitani, N. (2014). Study of mid-latitude ionospheric convection during quiet and disturbed periods using the superdarn hokkaido radar. *Advances in Space Research*, *54*, 473–480. https://doi.org/10.1016/j.asr.2014.01.011